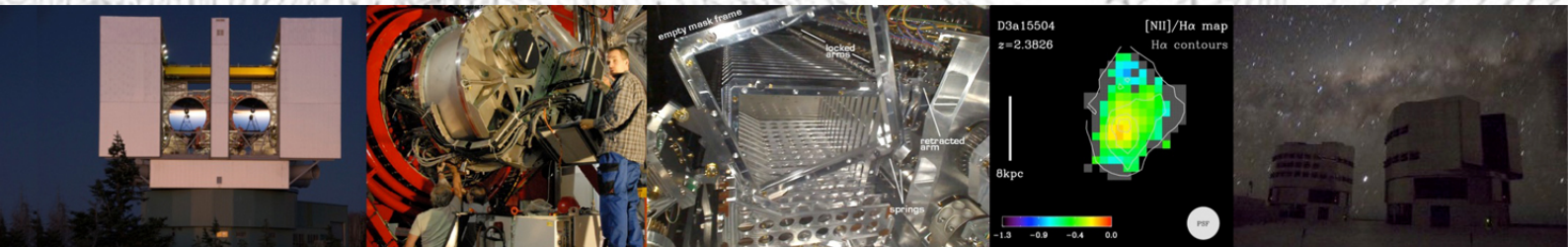


**The LUCIFER multi-object spectroscopy unit**  
and  
**Line excitation, metallicity, and dust extinction in massive star-forming galaxies at high redshift**

Peter Buschkamp



München 2012



---

**The LUCIFER multi-object  
spectroscopy unit**

and

**Line excitation, metallicity, and  
dust extinction in massive star-  
forming galaxies at high redshift**

---

Dissertation  
an der Fakultät für Physik  
der Ludwig-Maximilians-Universität  
München

vorgelegt von  
Peter Buschkamp  
aus Bielefeld

München, den 26.7.2012

Erstgutachter: Prof. Dr. Reinhard Genzel

Zweitgutachter: Prof. Dr. Ralf Bender

Tag der mündlichen Prüfung: 22. November 2012

# Zusammenfassung

Das frühe Universum bei einer Rotverschiebung  $z \sim 1-3$  ist ein faszinierendes und herausforderndes Feld astrophysikalischer Forschung in Wissenschaft und Instrumentierung. In dieses Weltalter fällt das Maximum der Sternentstehung, der Aktivität von major mergern (Verschmelzen von Galaxien ähnlicher Masse) und der Quasaraktivität. Die Epoche markiert aber auch einen wichtigen evolutionären Übergang, das beginnende Auftreten der Hubblesequenz der Galaxien, wie wir sie im heutigen Universum beobachten. Jedoch erscheinen –durch die riesigen Distanzen und die kosmologische Verringerung der Flächenhelligkeit– Galaxien bei hoher Rotverschiebung sehr lichtschwach und sehr klein. Ihre routinemäßige Beobachtung ist erst seit einigen Jahren möglich, dank hocheffizienter Nahinfrarotspektrometer an Teleskopen der 8-10m Klasse. Damit eröffneten sich neue Wege in der Erforschung des frühen Universums, welche zu neuen Erkenntnissen über die treibenden Prozesse der Entstehung und Entwicklung von Galaxien führten. Diese Dissertation erstrebt einen Beitrag zu beidem, mit einem Instrumentierungsprojekt und einer astrophysikalischen Studie.

In Teil 1 stellen wir unseren Beitrag für das neuartige voll-kryogene Multi-Objekt Nahinfrarot-Spektrometer “LUCIFER” vor, die Multi-Objekt-Einheit “MOS” zur Manipulation der Spektrographenmasken. Ziel dieses Teils der Arbeit war die Fertigstellung und Inbetriebnahme der MOS-Funktions- und Kontroll- Hard- und Software. Mehrere signifikante Hardwareänderungen infolge dieser Arbeit waren der Schlüssel für eine erfolgreiche Inbetriebnahme der Einheit. Ebenso wurden im Zuge dieser Arbeit komplexe situationsadaptive Kontroll- und Bewegungssequenzen für den Betrieb der MOS entwickelt. Um die Leistung des Spektrographen im K und H+K Band zu erweitern, wurden von uns zwei zusätzliche Reflexionsgitter hoher Effizienz gerechnet und getestet. Mit der MOS wurden seit ihrer Inbetriebnahme vor 2 Jahren mittlerweile mehrere tausend Maskenwechsel während Beobachtungen durchgeführt. Allerdings führten einige wenige Funktionsfehler auch zu Reparaturen vor Ort, sowie Auf- und Umrüstungen. LUCIFER sticht durch seine vielseitigen Betriebsmodi heraus und liegt mit seiner Systemtransmission und Leistung gleich auf mit anderen Instrumenten oder übertrifft diese. Die Leistungsfähigkeit wird teilweise eingeschränkt durch die Komplexität des Instruments, den Instrument- und Teleskop-Betriebsmodus sowie die häufigen Schlechtwetterperioden.

Teil 2 bildet eine detaillierte Studie der Anregung, Metallizität und Extinktion in massiven Galaxien mit Sternentstehung bei  $z \sim 2$ . Beobachtungen mit dem Integralfeldspektrometers SINFONI am Very Large Telescope ermöglichten eine vollständige zweidimensionale räumliche Auflösung der Galaxien bis herunter auf wenige Kiloparsec, während gleichzeitig die bei (Lang-)Spaltspektroskopie vorhandenen Probleme wie Lichtverlust am Spalt vermieden wurden. Unsere Analyse basiert auf Messungen der Emissionslinien  $H\alpha$ ,  $H\beta$ , [NII] und [OIII] in unserem Hauptsample von 12 Galaxien, sowie  $H\alpha$  und [NII] in einem größeren Sample von 26 Galaxien.

Wir beobachten merkbliche Unterschiede in der Morphologie in den verschiedenen Emis-

sionslinien bei einigen Objekten, was auf räumliche Variationen der Anregungsmechanismen, der Elementhäufigkeiten und/oder der Extinktion hindeuten könnte. Vergleiche der Kinematik zeigen hingegen größtenteils Übereinstimmungen. Wir nutzen die Relationen  $[\text{OIII}]/\text{H}\beta$  und  $[\text{NII}]/\text{H}\alpha$  zur Analyse der Anregungsmechanismen. Unsere Galaxien zeigen Anregungsmechanismen dominiert von reiner Sternentstehung bis hin zu AGN-Dominanz. In vielen Fällen messen wir höhere Anregung im Vergleich zum Gros der Galaxien bei  $z\sim 0$  in Übereinstimmung mit Studien anderer kleiner Sample bei  $z\sim 1-3$ . In einigen Fällen kann die höhere Anregung durch das Vorhandensein eines AGN erklärt werden. In anderen Fällen ohne Anzeichen für AGN ist die höhere Anregung vermutlich begründet durch unterschiedliche physikalische Bedingungen (Metallizität, Elektronendichte, Ionisationsparameter) und/oder das Vorhandensein von Schocks. Unsere Galaxien folgen einer ähnlichen Masse-Metallizitäts-Relation wie der in der Literatur bei  $z\sim 2$  beschriebenen, zeigen aber Hinweise auf einen Trend erhöhter Metallizität für röttere Objekte mit höherem Staubanteil bei gleichen stellaren Massen. Die beobachteten Metallizitäten erscheinen konsistent mit der kürzlich vorgeschlagenen fundamentalen Metallizitätsrelation (FMR), die  $M_*$ , SFR und Metallizität verbindet. Unsere Objekte zeigen ausschließlich flache, negative Metallizitätsgradienten jedoch keine Anzeichen für positive Gradienten wie in anderen Arbeiten bei  $z\sim 3$  bzw.  $z\sim 1$  berichtet. Wir finden Hinweise für eine erhöhte Extinktion im Bereich von Sternentstehungsgebieten im Vergleich zum Gros der Sterne, die das UV- und optische-Kontinuum (Ruhezustand) dominieren. Eine solche "differentielle Extinktion" wird in lokalen Starburst-Galaxien beobachtet und für  $z>1$  diskutiert. Unsere Fallstudie räumlich aufgelöster Extinktion zeigt klare räumliche Variationen mit einem Anstieg der Extinktion im Zentralbereich, wo die Metallizität erhöht und molekulares Gas konzentriert ist.

# Abstract

The universe at redshift  $z \sim 1-3$  is a fascinating and challenging field of astrophysical research – both in science and in instrumentation. The peak of star formation, major mergers, and quasar activity occurred at these times. These epochs further correspond to the emergence of the Hubble sequence of galaxies as observed in the present-day universe. However, the large distances and cosmological surface brightness dimming make high-redshift galaxies appear both very faint and very small. These systems became routinely accessible to detailed spectrally- and spatially-resolved studies only recently with the advent of high-throughput near-IR spectrographs at 8-10m class telescopes. These developments have opened exciting avenues providing new and crucial insights into the processes driving their formation and early evolution. This thesis aims to contribute to both; with an instrumentation project and an astrophysical study.

In part one, we present our contribution to the the novel full cryogenic near-infrared imager and multi-object spectrograph “LUCIFER”, the multi-object spectroscopy “MOS” unit that handles the spectroscopic multi-object slit-masks. The aim of this thesis work was to finalize and commission the MOS’s function- and control-hard- and software. We have introduced several mechanical hardware changes during this work, which were key for the unit’s successful completion. We have also developed and put forward the complex situation-adaptive control- and motion-sequences needed for operating the unit. To enhance the spectrograph’s K- and H+K-band performance, we have successfully designed and tested two additional high efficiency reflection gratings for LUCIFER. The MOS is meanwhile successfully in use, having served several thousand mask exchanges, albeit a small number of errors that required extended debugging and led to upgrades to the unit. LUCIFER stands out in its versatility; its system efficiency and general performance compares or exceeds other competing NIR multi object spectrometer to date. Observing efficiency gets however limited by the instrument’s complexity, by the current modes of instrument- and facility-operation, and by the frequent periods of bad weather on site.

In part 2, we present a detailed investigation of line excitation, metallicity, and extinction in massive  $z \sim 2$  star-forming galaxies. Observations with the integral-field spectrometer SINFONI at the Very Large Telescope, allowed full two dimensional spatially-resolved mapping, down to a few kiloparsecs, without the limitations inherent to slit (single- or multi-object) spectroscopy such as slit-losses. The analysis is based on measurements of key rest-frame optical nebular emission lines, including all of  $H\alpha$ ,  $H\beta$ , [NII], and [OIII] for the main sample of 12 sources, and  $H\alpha$  and [NII] for a larger set of 26 objects. We find noticeable differences in morphology between different emission lines in several cases, suggesting spatial variations in line excitation mechanism, nebular oxygen abundances and/or extinction. The kinematics observed for the different lines, however, are generally very similar. Based on the diagnostic [NII]/ $H\alpha$  and [OIII]/ $H\beta$  line ratios,

our main sample galaxies span a range of excitation, from purely-star-forming to AGN-dominated objects. Many of the objects exhibit slightly higher excitation than the bulk of  $z \sim 0$  star-forming galaxies, similar to results reported for other small samples at  $z \sim 1-3$ . In some cases, we find the offset could be due to the presence of a central AGN. In other cases with no sign of an AGN, the offset could be due to different nebular conditions (metallicity, ionization parameter, electron density) and/or contributions by shocks. Our sample follows a similar mass-metallicity relation as reported previously at  $z \sim 2$ . Our analysis reveals in addition trends of higher metallicities for redder, dustier systems, at a given stellar mass. The metallicities appear to be broadly consistent with the fundamental metallicity relation (FMR) relating  $M_*$ , SFR, and metallicity that has been recently proposed. Our objects show shallow, negative metallicity gradients but no positive gradients, as has been reported for some  $z \sim 1$  and  $z \sim 3$  galaxies. We find evidence for extra attenuation towards HII regions with respect to the bulk of stars, stars that dominate the rest-UV to optical continuum light. This “differential extinction” is seen in local starburst galaxies but has been debated at  $z > 1$ . Our case study of spatially-resolved  $H\alpha/H\beta$  measurements reveals spatial variations with an increase in nebular extinction towards the central regions where the metallicity is enhanced and molecular gas concentrated.

# Contents

<b>Zusammenfassung</b>	<b>I</b>
<b>Abstract</b>	<b>III</b>
<b>I. The MOS - LUCIFER's cryogenic multi-object spectroscopy unit</b>	<b>1</b>
<b>1. Introduction</b>	<b>3</b>
1.1. Scope of this thesis in the LUCIFER project . . . . .	3
1.2. Summary of the contribution to the project . . . . .	4
1.3. LUCIFER: Instrument layout and functionality . . . . .	6
<b>2. Multi Object Slitmask Unit (MOS)</b>	<b>13</b>
2.1. General function and purpose of the MOS . . . . .	13
2.2. Focal plane masks . . . . .	21
2.3. Focal Plane Unit (FPU) . . . . .	24
2.4. Mask Handling Unit (MHU) . . . . .	30
2.4.1. Grabber . . . . .	30
2.4.2. Rotator . . . . .	32
2.4.3. Translator . . . . .	34
2.5. Mask Storage . . . . .	35
2.5.1. Mask Cabinet and cabinet drive . . . . .	35
2.5.2. Retainer . . . . .	37
2.6. Mask Cabinet Exchange components . . . . .	42
2.6.1. Auxiliary Cryostats . . . . .	42
2.7. Radiation Shield Shutter . . . . .	43
2.8. Upgrade path . . . . .	44
<b>3. MOS unit control, function- and motion sequences</b>	<b>47</b>
3.1. MOS control hardware . . . . .	47
3.1.1. Auxiliary cryostat control . . . . .	50
3.2. Control-Software . . . . .	51
3.3. MOS function and motion sequences . . . . .	52
3.4. Main function sequences . . . . .	54
3.4.1. Mask exchange sequence details . . . . .	55

3.5. Auto correction and recovery sequences . . . . .	61
3.5.1. Correcting motions . . . . .	61
3.5.2. Error recovery . . . . .	63
3.5.3. Motion pausing and skipping . . . . .	63
<b>4. Design of two high performance gratings for LUCIFER</b>	<b>65</b>
4.1. Existing grating . . . . .	65
4.2. Requirements on the new gratings . . . . .	66
4.2.1. Scientific requirements . . . . .	66
4.2.2. Technical requirements and constraints . . . . .	67
4.3. Design process . . . . .	68
4.3.1. Optical principles . . . . .	68
4.3.2. Grating simulations . . . . .	71
4.3.3. The designed gratings . . . . .	71
4.4. Lab tests . . . . .	76
4.4.1. Test setup and measurements . . . . .	77
4.4.2. Grating test results . . . . .	78
4.5. On sky tests . . . . .	78
<b>5. Commissioning and performance of LUCIFER and the MOS</b>	<b>83</b>
5.1. Commissioning and selected results . . . . .	83
5.1.1. Detector performance . . . . .	84
5.1.2. System efficiency in spectroscopic mode . . . . .	85
5.2. Deep faint object spectroscopy . . . . .	90
5.2.1. Observations and data reduction . . . . .	90
5.2.2. Results . . . . .	91
5.3. Performance of the MOS unit hardware . . . . .	94
5.3.1. General performance . . . . .	94
5.3.2. Encountered, observation-stopping function errors of the MOS . . . . .	95
5.3.3. Cabinet Transfer . . . . .	97
5.4. Lucifer compared to other NIR MOS spectrographs . . . . .	97
5.4.1. MOIRCS . . . . .	98
5.4.2. MOSFIRE . . . . .	100
5.4.3. FLAMINGOS-2 . . . . .	102
5.4.4. SINFONI . . . . .	103
5.4.5. KMOS . . . . .	104
5.5. Lessons learnt . . . . .	104
5.5.1. The LUCIFER MOS based high-z galaxy survey project . . . . .	104
5.5.2. Lessons learnt during observation . . . . .	106
5.6. Summary and Outlook . . . . .	107
5.6.1. Summary . . . . .	107
5.6.2. Outlook to future use, science project planning and upgrades . . . . .	109

<b>II. Massive star-forming galaxies at high-redshift: a study of spectrally- and spatially-resolved line excitation, metallicity and extinction</b>	<b>113</b>
<b>6. The universe at <math>z \sim 1-3</math></b>	<b>115</b>
6.1. Galaxy formation and evolution over cosmic time . . . . .	115
6.2. Recent developments and the emerging picture . . . . .	116
6.3. Spatially- and spectrally-resolved studies . . . . .	120
6.3.1. Near-IR integral field spectroscopy . . . . .	120
6.3.2. The SINS survey . . . . .	122
6.4. Motivation for this work . . . . .	126
6.4.1. Overview of Part II of this thesis . . . . .	128
<b>7. Observations, sample selection and data reduction</b>	<b>131</b>
7.1. Integral-field spectroscopic observations with SINFONI . . . . .	131
7.2. Sample Selection for this study . . . . .	133
7.2.1. General constraints and strategy for target selection . . . . .	133
7.2.2. The SINS sample . . . . .	134
7.3. SINFONI observations . . . . .	137
7.4. Data reduction . . . . .	140
7.4.1. Reduction steps . . . . .	140
7.5. Emission line measurements . . . . .	145
7.5.1. Emission line fit . . . . .	145
7.5.2. Spatially-integrated line fluxes . . . . .	146
7.5.3. Inter-band alignment of emission line and ratio maps . . . . .	148
<b>8. The SINS multi-line data sets</b>	<b>151</b>
8.1. Overview and data quality . . . . .	151
8.2. Morphologies and kinematics from the different emission lines . . . . .	155
<b>9. Excitation mechanisms and metallicity at high redshift</b>	<b>167</b>
9.1. Optical nebular line emission . . . . .	167
9.1.1. H recombination lines . . . . .	167
9.1.2. Forbidden line emission . . . . .	168
9.2. Sources as a whole: integrated measurements . . . . .	169
9.2.1. Integrated emission line fluxes . . . . .	169
9.2.2. The BPT diagram at $z \sim 2$ . . . . .	172
9.2.3. Integrated line ratios and metallicities . . . . .	181
9.3. Zooming in: spatially-resolved line ratios and metallicity . . . . .	196
9.3.1. Metallicity profiles from discrete apertures and annuli . . . . .	198
9.3.2. Line ratio and metallicity maps . . . . .	202
9.4. Spatially-resolved BPT diagnostics . . . . .	207
9.4.1. Pixel-to-Pixel BPT diagram . . . . .	207
<b>10 Interstellar extinction at high redshift</b>	<b>211</b>

## Contents

---

10.1 Extinction . . . . .	211
10.1.1 Measuring extinction . . . . .	213
10.1.2 Differential extinction towards HII regions and stars . . . . .	214
10.2 Nebular extinction and comparison with extinction from broad-band SED modeling . . . . .	214
10.3 Case study: spatially-resolved extinction in BX610 . . . . .	217
<b>11 Summary and outlook</b>	<b>219</b>
11.1 Summary . . . . .	219
11.2 Outlook for future studies . . . . .	222
<b>A. Near-IR atmospheric OH line emission: origin and properties</b>	<b>223</b>
<b>B. Plots - Apertures and Annuli used for the radial and axis profiles in emission line ratios</b>	<b>225</b>
<b>C. Adaptive Optics</b>	<b>233</b>
<b>Bibliography</b>	<b>254</b>

# List of Figures

1.1.	LUCIFER at the telescope . . . . .	7
1.2.	LUCIFER optical layout . . . . .	8
2.1.	MOS Unit System Sketch . . . . .	16
2.2.	MOS Unit CAD drawing . . . . .	17
2.3.	MOS Unit components assembled 1 . . . . .	18
2.4.	MOS Unit components assembled 2 . . . . .	19
2.5.	MOS components 3 . . . . .	20
2.6.	Mask frame . . . . .	21
2.7.	Mask sheet . . . . .	22
2.8.	Mask sheet close up . . . . .	23
2.9.	Laser Cut quality . . . . .	23
2.10.	Mask preparation software screenshot . . . . .	24
2.11.	Mask Postscript file . . . . .	25
2.12.	FPU . . . . .	26
2.13.	FPU Pins . . . . .	28
2.14.	FPU scratched pin . . . . .	29
2.15.	FPU pins CAD . . . . .	29
2.16.	Grabber . . . . .	30
2.17.	Grabbing a mask . . . . .	31
2.18.	MHU . . . . .	33
2.19.	MHU-Translator . . . . .	34
2.20.	Mask storage area . . . . .	36
2.21.	Mask Cabinet . . . . .	37
2.22.	Retainer, partly disassembled . . . . .	39
2.23.	Retainer . . . . .	40
2.24.	Retainer . . . . .	41
2.25.	LUCIFER with attached auxiliary cryostat . . . . .	43
2.26.	View along cabinet rails . . . . .	44
3.1.	MOS Camera . . . . .	49
3.2.	MOS vibration monitoring . . . . .	50
3.3.	MOS Engineering GUI . . . . .	53
3.4.	MOS unit init sequence tree . . . . .	54
3.5.	Seq. Storage-to-Turnout . . . . .	57

## List of Figures

---

3.6.	Mask takeout . . . . .	58
3.7.	Seq. Turnout-to-FPU . . . . .	59
3.8.	Storage to FPU . . . . .	60
4.1.	Theoretical reflectivity zJHK grating . . . . .	66
4.2.	Theoretical reflectivity H+K grating . . . . .	72
4.3.	Theoretical reflectivity Ks grating . . . . .	73
4.4.	Grating comparison . . . . .	74
4.5.	Grating efficiency company measurments . . . . .	76
4.6.	Test setup grating efficiency measurement . . . . .	77
4.7.	Grating . . . . .	80
4.8.	Gratingwheel . . . . .	81
5.1.	System efficiency H, K, Grating 1, old det. . . . .	87
5.2.	System efficiency H, K, Grating 2, old det. . . . .	88
5.3.	System efficiency H, K, Grating 2, new det. . . . .	89
5.4.	System efficiency J Grating 1, old det. . . . .	90
5.5.	Lucifer BX610 spectrum . . . . .	92
5.6.	MOIRCS efficiency . . . . .	100
5.7.	MOSFIRE efficiency . . . . .	102
5.8.	SINFONI efficiency . . . . .	103
5.9.	preliminary BPT with LUCIFER data . . . . .	112
6.1.	Outline of the evolution of cosmic star formation rate density . . . . .	117
6.2.	Stellar mass and star formation rate distribution of the SINS/zC-SINF samples at $z \sim 2$ . . . . .	123
6.3.	Kinematics mix of massive star-forming galaxies at $z \sim 2$ . . . . .	125
8.1.	MD41: morphologies and kinematics . . . . .	157
8.2.	BX482: morphologies and kinematics . . . . .	158
8.3.	BX389: morphologies and kinematics . . . . .	159
8.4.	ZC782941: morphologies and kinematics . . . . .	160
8.5.	ZC782941, AO: morphologies and kinematics . . . . .	161
8.6.	ID7: morphologies and kinematics . . . . .	161
8.7.	D3a6004: morphologies and kinematics . . . . .	162
8.8.	D3a6397: morphologies and kinematics . . . . .	163
8.9.	BX610: morphologies and kinematics . . . . .	164
8.10.	ID5: morphologies and kinematics . . . . .	165
8.11.	D3a15504: morphologies and kinematics . . . . .	166
9.1.	The BPT diagram . . . . .	173
9.2.	BPT diagram, source-integrated ratios . . . . .	176
9.3.	BPT diagram including $H\beta$ absorption . . . . .	180
9.4.	Mass-Metallicity (M-Z) relation . . . . .	189

9.5.	N2 versus. O3N2 metallicity . . . . .	190
9.6.	N2 versus. O3N2 metallicity including $H\beta$ absorption . . . . .	190
9.7.	M - $\Delta Z$ residuals . . . . .	191
9.8.	BK - $(\Delta)Z$ plot . . . . .	193
9.9.	$A_{V,SED}$ - $(\Delta)Z$ plot . . . . .	194
9.10.	$\mu$ -Z relation . . . . .	195
9.11.	[NII]/ $H\alpha$ in aperture axis cuts and annuli profiles I . . . . .	200
9.12.	[NII]/ $H\alpha$ in aperture axis cuts and annuli profiles II . . . . .	201
9.13.	[NII]/ $H\alpha$ in aperture axis cuts and annuli profiles III . . . . .	202
9.14.	D3a-15504: Line ratio maps . . . . .	203
9.15.	D3a-6004: Line ratio maps . . . . .	204
9.16.	D3a-6397: Line ratio maps . . . . .	205
9.17.	ZC-782941: Line ratio maps . . . . .	206
9.18.	BX610: Line ratio maps . . . . .	206
9.19.	D3a15504: Pixel-to-pixel BPT . . . . .	208
9.20.	ZC782941: Pixel-to-pixel BPT . . . . .	209
10.1.	$A_{V,neb}$ versus $A_{V,SED}$ . . . . .	216
10.2.	Spatially-resolved $A_{V,neb}$ in BX610 . . . . .	218
A.1.	OH lines at different resolutions . . . . .	224
B.1.	D3a-15504: [NII]/ $H\alpha$ in aperture cuts & annuli profiles . . . . .	226
B.2.	D3a-6004: [NII]/ $H\alpha$ in aperture cuts & annuli profiles . . . . .	227
B.3.	D3a-6397: [NII]/ $H\alpha$ in aperture cuts & annuli profiles . . . . .	228
B.4.	ZC782941: [NII]/ $H\alpha$ in aperture cuts & annuli profiles . . . . .	229
B.5.	ZC782941-AO: [NII]/ $H\alpha$ in aperture cuts & annuli profiles . . . . .	230
B.6.	BX610: [NII]/ $H\alpha$ in aperture cuts & annuli profiles . . . . .	231
B.7.	ID7: [NII]/ $H\alpha$ in aperture cuts & annuli profiles . . . . .	232
C.1.	Adaptive optics system block diagram . . . . .	235

# List of Tables

1.1.	LUCIFER observing modes . . . . .	9
1.2.	Basic characteristics of the LBT . . . . .	10
1.3.	Characteristics of the LUCIFER-1 filters . . . . .	10
4.1.	Technical requirements for the gratings . . . . .	67
4.2.	Optical specifications affecting the design . . . . .	67
4.3.	Final specifications for both gratings . . . . .	72
4.4.	Observation modes for the gratings at the two camera configurations . . . . .	75
4.5.	Results of the grating tests . . . . .	78
4.6.	Grating characteristics measured on sky . . . . .	79
4.7.	Measured wavelength coverage . . . . .	79
4.8.	Physical limits of the tilt unit for central wavelength on the detector . . . . .	80
5.1.	Characteristics of the detector . . . . .	84
5.2.	Noise sources . . . . .	93
5.3.	NIR MOS instruments to date . . . . .	99
6.1.	Strongest nebular rest-frame optical emission lines . . . . .	121
6.2.	Commonly used strong line diagnostics . . . . .	121
7.1.	List of observed targets . . . . .	135
7.2.	General target properties . . . . .	136
7.3.	Observation modes and dates . . . . .	139
8.1.	Overview over the data quality, derived data products and quantities I . . . . .	153
8.2.	Overview over the data quality, derived data products and quantities II . . . . .	154
9.1.	Measured line fluxes in $H\alpha$ , $[\text{NII}]\lambda 6584$ , $H\beta$ , and $[\text{OIII}]\lambda 5007$ . . . . .	170
9.2.	Calculated $\text{NII}/H\alpha$ and $\text{OIII}/H\beta$ ratios . . . . .	171
9.3.	$\text{N2}$ and $\text{O3N2}$ metallicities . . . . .	183
9.4.	$H\alpha$ , $\text{NII}$ , and $\text{NII}/H\alpha$ for the SINS $H\alpha$ sample . . . . .	186
9.5.	$\text{N2}$ based metallicity gradients . . . . .	199
10.1.	Measured Balmer decrements and $A_{V,\text{neb}}$ . . . . .	215

**Part I.**

**The MOS -  
LUCIFER's cryogenic multi-object  
spectroscopy unit**



# Chapter 1.

## Introduction

LUCIFER, the **L**arge **B**inocular **T**elescope **S**pectroscopic **U**tility with **C**amera and **I**ntegral **F**ield **U**nit for **E**xtragalactic **R**esearch <sup>1 2</sup>, is the new fully cryogenic near-infrared multi object spectrograph and imager at the Large Binocular Telescope, located in an altitude of 3221m on top of Mt. Graham, Arizona, USA.

The MOS unit is LUCIFER's unique full cryogenic mask exchange unit for storing and loading slitmasks. It is a joint development by the Max Planck Institute for extraterrestrial Physics for all hardware parts and the Astronomical Institute of the University of Bochum for the control software.

### 1.1. Scope of this thesis in the LUCIFER project

Most of the MOS unit's basic development of mechanical and electrical parts had been completed by the time the thesis work started. Some of the sub units and components had been fabricated and assembled. Basic function- and proof-of-concept tests were ongoing in ambient and starting in cryogenic conditions. Most of the components, however, were not fully assembled, and some were still lacking parts. For some components, it was not even clear if the intended functionality could be implemented with the designed parts simply because of the novelty and unique functionality of this instrument.

Scope of the instrumentation work of this thesis was to finalize the unit, setup and test it, develop operation scenarios and the corresponding motion sequences, and finally integrate and commission the unit inside the instrument at the telescope. In short, turning it into a working piece of equipment, making it available to the scientific community.

Multi-object spectroscopy opens new observational possibilities and scientific opportunities for near infrared astronomy. Early science case discussions quickly showed the need

---

<sup>1</sup>The IFU got replaced by the MOS but is still in the name.

<sup>2</sup>As of 2011 LUCIFER is named LUCI following a court settlement in a law suit between the LBT and various Mt. Graham forrest reservation interest groups.

## 1.2. Summary of the contribution to the project

---

for additional spectroscopic gratings in the LUCIFER instrument. Their development was also a part of this thesis.

## 1.2. Summary of the contribution to the project

As just mentioned, the MOS unit was developed and built by a larger group. We summarize the contributions of this thesis to the MOS and the LUCIFER project in a concise list below. A more detailed description of the contributions and the work can be found in the corresponding chapters.

### **MOS unit hardware**

1. Test and optimization of the mask frame for maximum thermal contact, minimum stray light and accurate mask sheet positioning
2. Development and testing of the mask position detection mechanism in the focal plane unit (FPU)
3. Revision and update of the mask alignment mechanism in the FPU
4. Revision and update of the clamp arm drive mechanism in the FPU
5. Revision of the mask handling unit (MHU) grabber limit switches
6. Revision of the locking mechanism of the MHU rotator
7. Design of the update of the MHU rotator to an angular encoder assisted drive
8. Re-design of the mask-cabinet's mask guides
9. Revision and update of the position sensing mechanism for the mask retainer arms
10. Update of the shutter to an angular encoder assisted drive mechanism
11. Test and revision of various state and limit switches and their mechanical actuation scheme
12. Development and testing of the MOS unit debugging camera
13. Test and optimization of the cold coupling in the auxiliary cryostats

### **MOS unit control**

14. Test and revision of the switch box logics
15. Development of the interlock schemes for the cabinet exchange
16. Introduction of the motion and vibration monitoring

17. Design of the orientation monitoring
18. Co-Design of the auxiliary cryostat micro controller programming
19. Development of the motion correction and auto-debug process charts
20. Co-Development of reliable motion sequences of the MHU for the sequence server from ground up
21. Co-Development of the 'auto-debug by initialize' scheme
22. Co-Development of the mask cabinet exchange procedures

### **Testing and commissioning**

23. Significant contribution to the instrument commissioning especially the MOS unit
24. Testing and optimizing the MOS unit functions and motion parameters
25. Planning of and participation in yearly and ad-hoc maintenance campaigns
26. Co-Supervision and planing of the MOS-2 work package for LUCIFER-2

### **LUCIFER gratings**

27. Design and testing of two additional spectroscopic gratings

### **Overview of part I of this thesis**

The main instrument, LUCIFER, and the overall functionality will be described in the next paragraph. The MOS unit's details and all work related to assembling, adjusting and testing the unit are the scope of part one's main chapter 2. In addition to the description of the instrument hardware components, we describe important hardware changes and the contribution of this thesis to the various aspects of the instrument. In chapter 3 we describe the MOS control hard- and software and our developed MOS unit control- and motion sequences. The development and performance tests of two additional spectroscopic gratings are presented in chapter 4. Chapter 5 contains selected results from the commissioning phase of both the MOS unit and LUCIFER, presents the performance of the MOS unit and shows a comparison of LUCIFER to other near-infrared spectrographs. We also present some of the lessons learnt during the first two years of operation and close with summarizing the current state and give an outlook to future operations and forthcoming upgrades.

### 1.3. LUCIFER: Instrument layout and functionality

LUCIFER is a non-interferometric instrument; each eye, i.e. primary mirror, of the LBT has its own LUCIFER. Both instruments are identical in functionality and available observation modes. They can operate independently or in sync in binocular mode. LUCIFER-1 had first light on 6 September 2008 and is in operation on sky. LUCIFER-2 is currently undergoing lab tests and is scheduled for installation in late 2012 with commissioning in early 2013.

LUCIFER provides both seeing-limited and high-order AO corrected “diffraction limited” near-infrared imaging and spectroscopy on a field of view of  $4' \times 4'$  (seeing limited) or  $30'' \times 30''$  (diffraction limited). The maximum angular separation of the two instruments FOVs on sky is 40 arcsec. This is due to the binocular mount design of the LBT where the placement of the FOVs is limited by the working range of the primary mirror active optics system and the secondary mirror hexapod support. The adaptive optics correction for diffraction limited observations is provided by a deformable secondary mirror. LUCIFER is mounted on the telescope at the bent Gregorian focal station between the two primary mirrors. Telescope guiding and wavefront sensing using a natural AO star is done by a dedicated guiding and wavefront sensing unit, the ‘AGW’, it precedes LUCIFER in the optical train. Laser-cut cryogenic longslit and multi slit masks are placed in the focal plane for spectroscopic observations. The user-designed slit masks that are used for multi-object spectroscopy (MOS) are exchanged using auxiliary cryostats while preserving cryogenic conditions. These cryostats temporarily attach to the main cryostat during the mask cabinet exchange. A bridge like structure between the two LUCIFER focal stations provides support for the auxiliary cryostats. Key performance figures, as measured during commissioning, are presented in chapter 5

Lucifer is a rather compact instrument. The cryostat has a diameter of 2m and a height of 1.8m. The optical path is folded with four folding mirrors in total. The dichroic entrance window is tilted by 15 degrees and reflects light with  $\lambda < 0.87\mu\text{m}$  towards the wavefront sensor in the guider unit. Light with  $\lambda > 0.87\mu\text{m}$  passes into the instrument. The useful unvignetted FOV of the Telescope has a diameter of  $\sim 7'$ . This FOV is stopped down to a usable FOV of  $4' \times 4'$  in the instrument’s focal plane. The focal plane can be equipped with longslit and multi-object slitmasks for spectroscopy. Unlike most other spectrographs and cameras, LUCIFER has no slit viewer and no atmospheric dispersion corrector. The cold pupil stop is at the imaging mirror or grating depending on the observing mode. LUCIFER features a lookup table driven mechanical flexure compensation by adjusting the angle and tilt of folding mirror no. 4. The imaging onto the detector can be done with three different cameras with different focal lengths. The two cameras for seeing limited observations are refractive systems, the diffraction limited camera is a Cassegrain design. The ‘N3.75’ camera images the FOV on the full  $2\text{k} \times 2\text{k}$  pixel Hawaii-2 detector, which results in a resolution of 0.12 arcsec/pixel (0.25'' Nyquist sampled resolution). The ‘N1.8’ camera images the FOV on a quarter of the detector centered on the detector ( i.e. 0.25 arcsec/pixel = 0.5'' resolution). It looks beyond the instrument FOV,

partly imaging the (dark) 'inside of the instrument' This is on purpose as it is used for spectroscopic applications, where the full spectral band (J, H or K) needs to be recorded and whose angular dispersion in turn extends beyond the  $4' \times 4'$  field (assuming a slit centered in the FOV and the grating tilt adjusted such that the band's central wavelength is at the center of the detector).

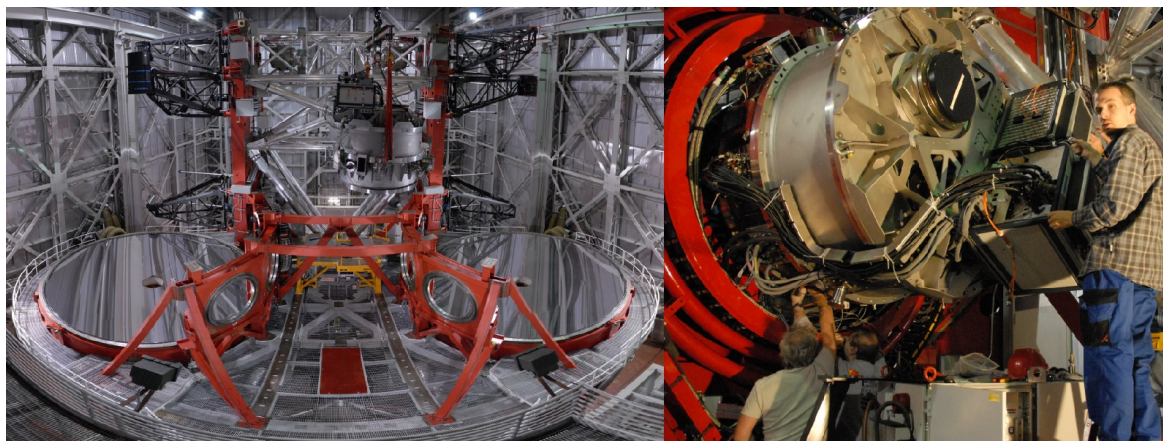


Figure 1.1.: LUCIFER-1 at the telescope, Summer 2010.

The left image shows a birds eye view of the telescope. The two primary mirrors are visible on the left and right side. The black swing arms that hold the tertiary mirrors, the prime focus cameras and the secondary mirrors can be seen above both primary mirrors. The swing arms are moved in and out of the optical train depending on the desired instrument configuration. The red 'gallery', located in the middle between the two primaries, are the six focal stations of the bent Gregorian focus. There exist three stations at each primary mirror. LUCIFER-1 is mounted at the rear bent Gregorian focal station of the left primary. At that position, the yellow painted bridge that mechanically supports the auxiliary cryostats is partly visible. In the image LUCIFER-1 is hanging down from the crane in the upper middle. It is re-installed after the yearly maintenance.

The right image shows LUCIFER-1 as it is attached to the instrument rotator and AGW unit (guider and wave front sensing unit). The AGW is embedded inside the red 'ring' -which is the de-rotator- on the left. One of the electronics racks is visible below LUCIFER. The detector read out electronics and the MOS Motion control electronics are mounted on the back of LUCIFER (towards the author, standing on a ladder on the right). Looking towards the top, a black lid (with a white stripe) can be seen. It covers the vacuum interface for attaching the Auxiliary cryostat. The MOS unit is located just behind that vacuum interface inside the cryostat (see next chapter). The yellow bridge that is present in the left image is not installed in this image.

### 1.3. LUCIFER: Instrument layout and functionality

---

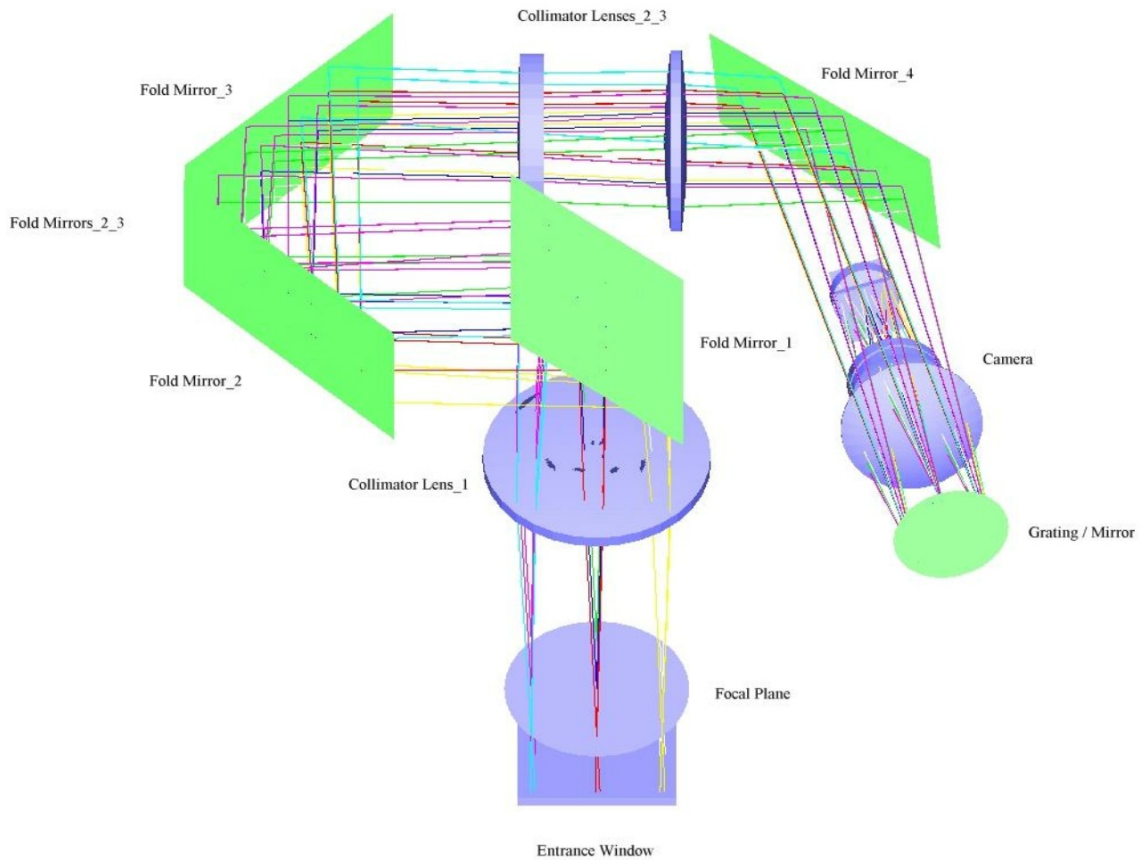


Figure 1.2.: Optical layout of LUCIFER. The light enters from below through the entrance window. The entrance window is tilted by  $15^\circ$ . It has a dichroic coating. Visible light gets reflected towards the wavefront sensor inside the AGW (for natural guide star AO). IR radiation ( $\lambda > 870\text{nm}$ ) is passed through into the instrument. The focal plane is left empty for imaging. For spectroscopy the long slit or multi-object masks are placed in the focal plane. After passing the first calcium fluoride collimator lens, the optical path is folded four times by gold coated folding mirrors ('FM', green). FM1 and FM4 are movable to correct for instrument flexure and pupil position misalignment. FM4 reflects the light towards the grating/mirror (round green element on the right). From there, the light enters the camera that focusses the FOV onto the detector (not shown). The camera shown in the figure is the N1.8 camera. The filter wheel that houses wide and narrow band filters (listed in table 1.3) is not shown. It is positioned between the camera and the detector. The camera field lens is positioned after the filter wheel. Image taken from the LUCIFER Final Design Report Optics.

Two filter wheels, housing a set of 18 broad- and narrowband filters, are located in the converging beam between the camera and the detector. A pupil imaging lens can be flipped into the beam to check uniformity of illumination and alignment. Table 1.1 lists the operation modes of lucifer and table 1.3 summarizes the available filters. The detector is a HAWAII-2, its main characteristics as measured during lab tests and commissioning are summarized in table 5.1.

Table 1.1.: LUCIFER observing modes

Camera	N1.8	N3.75	N30 (non available yet)
Scale ("/ pixel)	0.25	0.12	0.015
Imaging			
FOV (arcminute)	4 × 4	4 × 4	0.5 × 0.5
Comments	on central quarter	on full detector	FOV limited by anisoplanatism
Spectroscopy			
FOV (arcminute)	4 × 2.8	4 × 2.8	0.5 × 0.5
Resolution (2pix) <sup>(c)</sup>	1900 ... 8500	3800 ... 17000	10000 ... 40000
Comments	LSS & MOS <sup>(a)</sup> full coverage of z,J,H,K,H+K band <sup>(b)</sup>	LSS & MOS limited band coverage	LSS only narrow band useable

<sup>(a)</sup>LSS: long slit spectroscopy, MOS: multi object spectroscopy

<sup>(b)</sup>Assuming a slit centered on the detector

<sup>(c)</sup>Nyquist sampling resolution

In spectroscopic mode, the user can chose between three gratings depending on the desired resolution and wavelength coverage. The grating replaces the imaging mirror in this mode. Chapter 4 describes in detail the available gratings and the design process for two of them, a work which was a part of this thesis. In summary, a multi purpose grating covers z, J, H and K band at resolutions  $\sim 7000$  for a 2-pixel (Nyquist sampled) slit. Depending on the camera the bands extend partly beyond the detector area. The two other gratings serve a special purpose: One acts as an H+K grating at a resolution of  $\sim 2000$  for seeing limited or as an H or K grating for AO assisted observations at  $R \sim 4000$  (again 2-pixel slit). The third one is a single purpose grating: delivering a resolution of  $\sim 4000$  at a high efficiency in Ks for a seeing limited  $0.5''$  slit.

Spectroscopy can either be done in longslit or multi-object-slitmask (MOS) mode. For longslit observations, the MOS unit provides the instrument with MOS masks that contain only one longslit. In MOS mode, 23 custom made exchangeable multi-slit masks can be stored and used in the instrument. The masks are laser cut and are exchanged usually monthly prior to an observation run.

### 1.3. LUCIFER: Instrument layout and functionality

---

Table 1.2.: Basic characteristics of the LBT

effective primary aperture $D_{\text{Tel}}$	8251 mm
focal length $f_{\text{Tel}}$	123420 mm
effective system focal ratio $N_{\text{Tel}}$	15.0
primary spacing	14417 mm center-to-center
image scale	0.6 mm/arcsec
$\varnothing$ FOV	7'
field curvature $r_{\text{Tel}}$	1043 mm
AO System	Secondary Mirror

Table 1.3.: Characteristics of the filters installed in LUCIFER-1

Name	$\lambda_{\text{C,air}}/\mu\text{m}$	FWHM/ $\mu\text{m}$	$\tau_{\text{peak}}$	$\tau_{\text{average}}$
z	0.957	0.195	98.4 %	94.3 %
J	1.247	0.305	91.2 %	83.2 %
H	1.653	0.301	95.0 %	90.5 %
K	2.194	0.408	90.1 %	85.7 %
K <sub>s</sub>	2.163	0.270	90.7 %	86.8 %
H+K	1.950	0.981	95.0 %	86.3 %
Brackett- $\gamma$	2.170	0.024	79.4 %	76.5 %
FeII	1.646	0.018	91.2 %	89.5 %
H <sub>2</sub>	2.124	0.023	87.9 %	84.9 %
HeI	1.088	0.015	65.2 %	64.6 %
J-high	1.303	0.108	95.9 %	93.3 %
J-low	1.199	0.112	95.4 %	93.3 %
OH_1060	1.065	0.009	68.6 %	66.8 %
OH_1190	1.193	0.010	80.4 %	78.0 %
Paschen- $\beta$	1.283	0.012	86.1 %	85.5 %
Paschen- $\gamma$	1.097	0.010	81.1 %	80.0 %
Y1	1.007	0.069	67.3 %	64.2 %
Y2	1.074	0.065	94.2 %	89.5 %

## **Planned upgrades**

### **Normal, Wide-Field and Ground Layer Adaptive Optics**

The adaptive optics correction is realized through an adaptive secondary mirror. Therefore all instruments on the Cassegrain and bent Gregorian focal stations can benefit from the facility AO system. 672 electro-magnetic force actuators manipulate the shape of the adaptive secondary mirror shell that has a diameter of 0.91m while it is only 1.5mm thick. Wavefront sensing, reconstruction and corrections are carried out at a rate of 1kHz (Esposito et al. 2003; Gallieni et al. 2003).

As an upgrade, the ground layer adaptive optics facility 'ARGOS' is currently built at MPE and various partner institutes. ARGOS utilizes three pulsed lasers per primary mirror to project multiple Rayleigh laser guide stars onto the sky for homogeneous field correction. The green 532nm lasers, pulsed at 10 kHz, are focussed to an altitude of around 12km in the atmosphere. The returning scattered photons are electro-optically range-gated to  $\pm 300\text{m}$  around the focussing altitude before entering the wavefront sensing unit. A separate tip-tilt sensing unit provides the necessary correction of the tilt introduced by the atmosphere, taking the light from an additional natural tip-tilt star.

The correction of the science light wavefront does not fully achieve the diffraction limit. It rather yields a decrease of the PSF FWHM and an increase of the encircled energy by a factor 2-3 over the full field of view of  $4' \times 4'$ . This yield corresponds to a gain of a factor 4-9 in integration time.

In a further step, ARGOS can be upgraded with an additional 589nm sodium laser guide star to achieve diffraction limited observations in a multi-conjugated adaptive optics setup. Since the wavefront is already pre-corrected by the GLAO, resulting in an increase in  $r_0$  (see appendix C, p.233ff.), less laser power is needed which greatly facilitates this possible upgrade (Rabien et al. 2010).

### **Detector upgrade to Hawaii-2 RG**

On 12 October 2011 the Hawaii-2 detector of LUCIFER was lost due to human error and technical malfunctions while in cryogenic condition. Subsequently the LUCIFER-2 detector was put into LUCIFER-1 as an interim solution. As LUCIFER-2 therefore lacks a detector, it was decided to upgrade both instruments to the newest 'Hawaii-2 RG'  $2\text{k} \times 2\text{k}$  detector within the next 1.5 years. The new detectors feature a  $\sim 20\%$  increased quantum efficiency in J, H and K band. This and the technical need for a completely different back end electronics will introduce significant changes to the measured performance presented in chapter 5.

### 1.3. LUCIFER: Instrument layout and functionality

---

## **Chapter 2.**

### **Multi Object Slitmask Unit (MOS)**

In this chapter we describe the MOS unit's hardware details and all work related to assembling, adjusting and testing the unit. In addition to the description of the instrument hardware components, we present important hardware changes and the contribution of this thesis to the various aspects of the instrument.

The LUCIFER MOS Unit is the only full cryogenic mask exchange unit for a near infrared spectrograph to date. It features a unique design which allows to store, handle and exchange masks inside the instrument at the working temperature of 77K. All mask manipulations are done by a novel cryogenic mask handling robot that can individually address up to 10 fixed and 23 user-provided masks and place them in the focal plane with high accuracy. A complete mask exchange cycle is done in less than five minutes. It can be run in every instrument position and state. This reduces the instrument setup time during science observations to a minimum. Exchange of old and new MOS masks is likewise done under cryogenic conditions using a unique exchange drive mechanism and two auxiliary cryostats that attach to the main instrument cryostat.

The MOS unit replaced the Integral Field Unit which was removed from the design at an intermediate stage of the project. All the other components were fixed at that design stage. Thus the MOS had to fit into the space envelope intended for the IFU. This added significant complications to the design of the MOS.

Nonetheless, the MOS could be built successfully. The unit is offered for science users since beginning of 2010. Over 4500 mask exchanges have been run so far during commissioning, test and science nights.

#### **2.1. General function and purpose of the MOS**

The MOS serves a number of different tasks to provide the functionality of placing long slit and user cut multi-object masks in the focal plane and exchanging the used multi-

## 2.1. General function and purpose of the MOS

---

object masks with new ones. Specifically, the tasks of the MOS unit are:

1. storage of up to 33 masks in a stationary (10 masks) and an exchangeable cabinet (23 masks). Fixed masks are for alignment and long slit spectroscopy, exchangeable masks are used for multi object spectroscopy.
2. reproducible positioning of a mask in the focal plane unit with an accuracy better than  $30\ \mu m$ ,
3. transport of a mask between the storage cabinets and the focal plane unit in every instrument and telescope orientation,
4. temporary removal of a mask from the focal plane (e.g. for pointing checks and target acquisition),
5. replacement of the exchangeable mask cabinet under vacuum and at cryogenic temperature to load new user science multi object masks.

### **System components overview**

The functions listed above are provided by the interplay of numerous components. Specifically these components are:

1. **Slitmasks**, mounted in a frame that can a) be handled inside the instrument and b) be reproducibly positioned in the focal plane.
2. a **focal plane unit** (FPU) to position and clamp a mask in the telescope focal plane during observation with high accuracy,
3. a **structure** providing the interface to the LUCIFER structure that carries all other MOS-components,
4. a **stationary and an exchangeable mask cabinet** together with a drive unit, rails and a locking mechanism for the exchangeable cabinet to store fixed masks (e.g. long slit masks) and user provided multi object masks,
5. a **mask retainer** for locking the masks in the cabinets and for releasing one mask at a time for transport to the FPU or for releasing all masks at the same time during a cabinet exchange,
6. a **mask handling unit** (MHU, called 'robot') which takes the mask out of the cabinet, carries it to the FPU and inserts it into the FPU and back.

For the mask cabinet exchange the following additional components are required:

1. a **radiation shield shutter** opening a port in the LUCIFER radiation shield through which the cabinet is transferred,
2. a **gate valve** with 32 cm clear diameter attached to the LUCIFER cryostat back cover through which the cabinet is transferred,
3. two **auxiliary cryostats** equipped with drive units for the cabinet transfer and vacuum gate valves identical to the one attached to LUCIFER,
4. a **rail system** on which the cabinet can slide out and into the cryostats and a drive system to drive that motion. To account for the thermal contraction and displacement of the cabinet rails in the cold cryostats the short cabinet rails in the warm vacuum interface are positioned such to fit the cold rails inside the two cryostats.

The following figures 2.1 to 2.5 show the arrangement of the MOS unit components with respect to each other. Figure 2.1 shows a sketch of the MOS and auxiliary cryostat system. Figure 2.2 depicts an overview of the MOS unit as a CAD drawing. The next three figures 2.3 to 2.5 show the real components that have been built. We refer to the figure captions for a detailed explanation.

We describe the individual components in the subsequent sections, starting with the focal plan masks in section 2.2, p.21 ff.. For each subunit the general description is given, followed by important design details and changes introduced during this work.

## 2.1. General function and purpose of the MOS

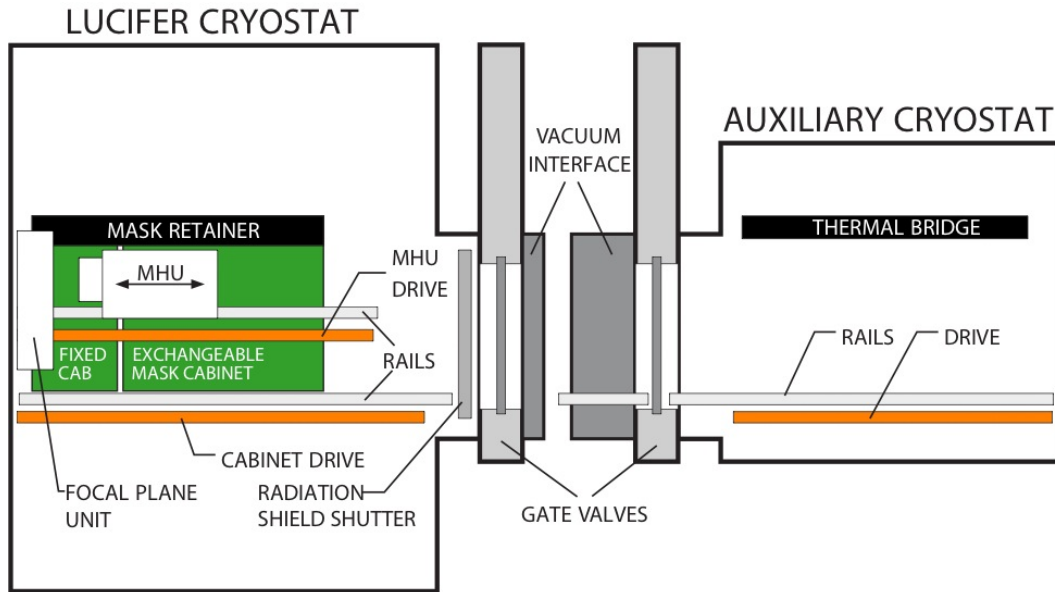


Figure 2.1.: Sketch of the MOS and auxiliary cryostat system.

On the left: The LUCIFER cryostat which houses all instrument components and the MOS unit; on the right: the auxiliary cryostat which is used for extracting and inserting the MOS mask cabinet. The auxiliary cryostat is placed on a support structure (the 'bridge', not drawn) during mask cabinet transfer. This is to keep the vacuum interface (in the middle) free of shearing forces. The MOS unit in the LUCIFER cryostat is oriented such that the exchangeable cabinet (right green box) can be moved in and out of the cryostat on the cabinet drive rails which are located underneath. The two lower drive units (orange, LUCIFER and aux cryostat) move the mask cabinet during cabinet transfer. The upper 'MHU' drive unit inside LUCIFER (orange) drives the mask handling unit ('MHU' or 'robot'). It moves the robot along the two mask cabinets to the one mask that shall be picked up or to the empty slot where a used masks shall be put down. The mask retainer in LUCIFER (black) secures the masks or frees the individual one that was selected by the observer. On the very left the focal plane unit 'FPU' is drawn as a white box inside the LUCIFER cryostat. The MHU moves a mask into the FPU for spectroscopic observation. The radiation shield shutter on the right inside LUCIFER blocks the thermal radiation from the gate valve (which is at ambient temperature) during normal operations. It opens during cabinet transfer for a brief time. Likewise the vacuum gate valves open once the vacuum interfaces of the two cryostats have been connected and the interface pumped to  $< 10^{-4}$  mbar. A short pair of rails is built into the vacuum interface for the cabinet to cross the gap between the two cryostats. The thermal bridge in the aux cryo on the right is only for increased thermal coupling during cooldown. It also prevents the masks from moving inside the cabinet during aux cryo handling.

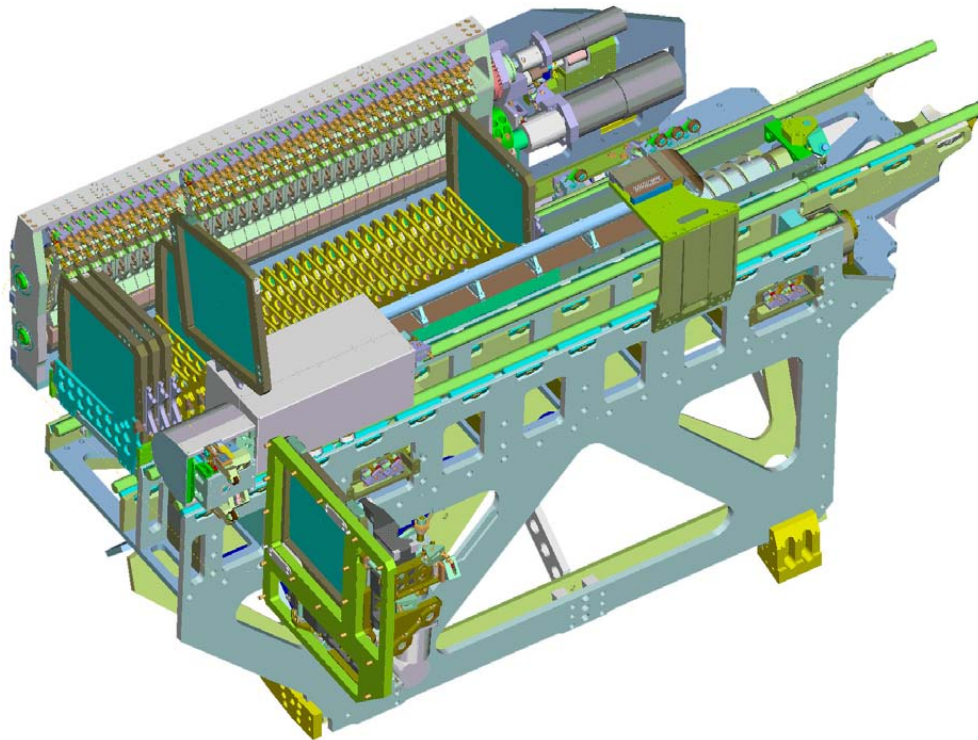


Figure 2.2.: Overview of the MOS unit as a CAD drawing.

From left to right, the orientation of the components is the same as in figure 2.1, without the auxiliary cryostat. The focal plane unit ('FPU', bright green) is located on the left front towards the bottom of the figure. A mask (dark cyan) is inside the FPU. Above the FPU, the MHU robot is shown as a gray box. The robot's rotating head, the grabber (left side of the grey box), is rotated towards the FPU. The mask cabinet (dark yellow) is populated with five mask frames (dark cyan), four in the fixed cabinet to the left and one at the very last position #32 on the very right in the exchangeable cabinet. The rails for the cabinet (bright green) protrude towards the right. The mask retainer is located behind the cabinet. The figure shows masks in the three possible mask rotation positions, in 'storage' (i.e. inside the cabinet), in 'turnout/transport' and inside the 'FPU'. One mask is drawn hovering in mid air above the robot. This is the 'turnout/transport' position. The grabber holds a mask upwards in this position while the MHU robot moves a mask along the cabinet towards the FPU or towards the mask's slot. When near the FPU, the MHU's rotating head rotates the grabber -and thus the mask- from the shown 'turnout/transport' position into the focal plane unit. Likewise the mask is 'turned back out' of the FPU into this position. Note that -unlike in the figure- there are *never* two or more masks outside the cabinet at the same time in the real unit. The bottom of the unit consists of a brace framework which supports the functional components. The real unit as seen from a similar angle is shown in the next figure (2.3).

## 2.1. General function and purpose of the MOS

---

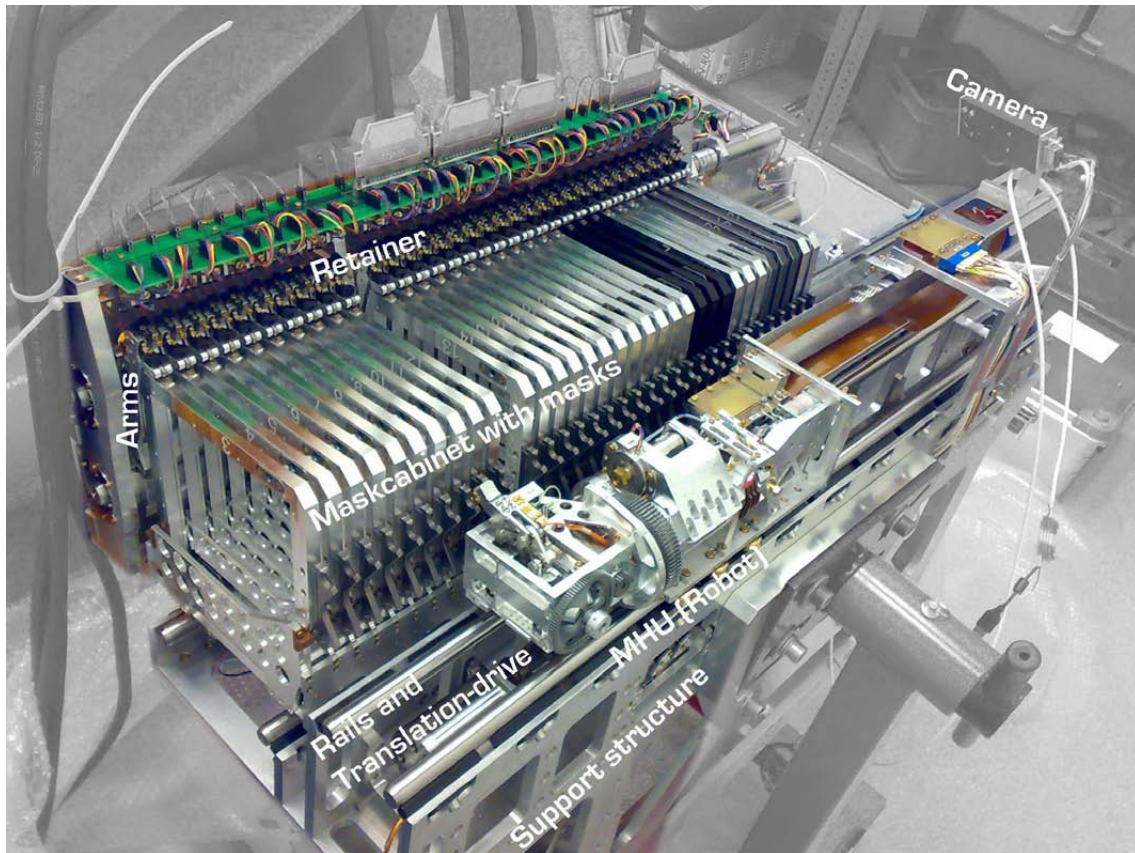


Figure 2.3.: The real MOS unit seen from roughly the same viewing angle as the CAD drawing in figure 2.2. The storage, retainer and Mask Handling Unit are shown during maintenance outside the main cryostat. The Focal Plane unit is not visible in this image as it is attached to the LUCIFER main structure. The MHU rotating head is in storage position with the grabber open, ready to grab a mask. The MHU robot is electrically connected to the MOS base via a ribbon cable that is custom made to be flexible in cryogenic conditions. It can be seen as a brown stripe towards the right. A small modified USB visual CCD camera is mounted where the ribbon cable attaches to the base structure. The camera can be used to monitor, fine-tune and debug the unit in cryogenic conditions. The MHU translation drive and the robot's rails can be seen on the left of the MHU robot. The mask retainer is visible below a green electronics board towards the top of the figure. The cabinet with the masks is located between the retainer and the robot. It is completely filled with (empty) mask frames for testing purposes. All masks are locked in their cabinet slot, each retainer arm is in contact with its respective mask. The silver mask frames shown in this image have meanwhile all been replaced with blackened ones (similar to the ones in the rear of the cabinet) to reduce reflexions.

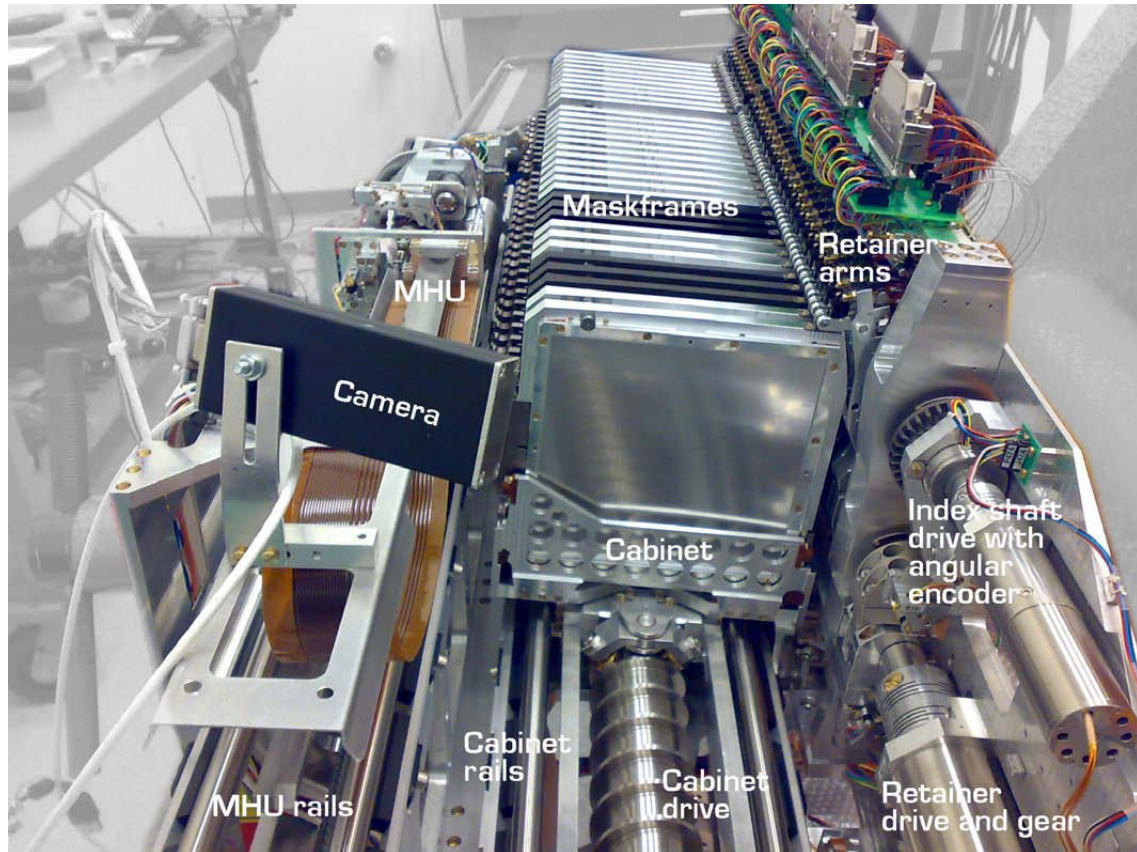


Figure 2.4.: View of the MOS unit seen from the LUCIFER vacuum gate valve. The setup is the same as in figure 2.3. The mask cabinet filled with mask frames is visible in the middle. The cabinet drive worm gear and the cabinet rails can be seen below it towards the bottom of the image. The motors and gears for the index- and drive shaft of the retainer are located on the cabinet's right. The retainer is closed, the retainer arms hold all mask frames in place. The arm's position sensing switches are located above the arms and are connected with a green printed circuit board. On the left of the cabinet, the USB vis-CCD 'debug' camera is visible. The brown electrical ribbon cable can be seen below the camera. Further down one can see the rails on which the MHU moves. The MHU itself is in the background on the left of the mask cabinet.

## 2.1. General function and purpose of the MOS

---



Figure 2.5.: The MOS as seen by the modified USB camera which is placed above the MHU ribbon cable (see figure 2.4). This is an actual image taken with the camera in cryogenic conditions. Except the FPU, all critical moving sub units can be observed with this camera. The camera needs to be warmed up slightly before it can be used. As the camera is  $\sim 80\text{K}$  warmer than the cryostat, it can readily be seen as an ambient glow in the K band on the science detector. It is therefore only put into operation for special debugging or during the instruments yearly maintenance for fine tuning the grabber position for each mask, so it can be used in every instrument/telescope orientation. During the camera's operation three high brightness LEDs illuminate the scenery in the otherwise dark cryostat.

The mask cabinet, filled with black mask frames, can be seen in the center of the image. As the (test-) mask frames hold no mask sheets, one can see the dividers between the individual mask slots inside the cabinet. They have holes drilled in for light-weighting. The robot and its ribbon cable is on the left. The retainer arms are on the right. A part of the index drive and the retainer drive are visible on the very right, enough to check their functions.

## 2.2. Focal plane masks

The focal plane slit masks are the essential components of the MOS-unit. Up to 33 masks can be stored inside LUCIFER at a time. The masks are distributed over two cabinets. One cabinet is fixed inside LUCIFER. It houses 10 permanent masks. These are longslit masks with slit widths of 0.25, 0.50, 0.75, 1.0, 1.5, and 2.0 arcsec on sky and masks for tests and optical and spectral alignment. The second cabinet is exchangeable and has 23 storage slots for multi object 'MOS' masks that are laser cut to the specifications given by the observer. A cabinet exchange is usually done monthly prior to the science nights block.



Figure 2.6.: An empty mask frame as one would see it from the outside of the instrument looking towards the focal plane. The handle where the MHU-head grabs the mask is on the left. The mask-fpu-alignment holes are in the top right and bottom left of the frame. These are coated stainless steel insets mounted into the aluminum frame. The frame identification number '37' is at the bottom. Above it, the gap between the base-frame and the cover-frame is visible in which the mask sheet is inserted. The gap's curvature follows the telescopes focal plane in one direction, giving the mask sheet a cylindrical shape. The metal insets on the right side and top left of the frames align the frame inside the storage cabinet. This ensures that the frame is always at the same position in the cabinet, i.e. the grabber position can be the same irrespective of telescope and instrument orientation. The recess in the frame on the left side is for securing the frame in the cabinet together with the retainer when the instrument is rotated upside down.

## 2.2. Focal plane masks

---

A mask consists of the mask frame and the mask sheet which is held therein. The side facing the instrument (i.e the side 'seen' by the detector) of both the mask frame and the mask sheet are blackened. This is to reduce and diffuse light originating from reflections on optical surfaces. The mask frame has interfaces to the Mask Handling Unit (a 'handle'), to the Focal Plane Unit (two inside cones for centering the mask on the FPU's alignment pins) and to the storage unit (hardened surfaces for guiding and locking). The frames are  $180 \times 180 \text{mm}^2$  in size, having a clear aperture of  $144 \times 144 \text{mm}^2$ , which corresponds to  $4 \times 4 \text{arcmin}^2$  on sky. All masks are cylindrically curved perpendicular to the dispersion direction following the telescopes field curvature in one dimension. The radius of curvature of 1030mm. A full 2D spherical correction requires spherical masks. These are expensive to manufacture and it is difficult to maintain their shape under cryogenic conditions given the thickness of the stainless steel mask sheet of only 120 microns, see section 2.8. The cylindrical curvature is defined and ensured by the shape of the frames which are machined accordingly. We limit the slit distance from the optical axis to  $\pm 1.25 \text{ arcmin}$  in dispersion direction and place the mask center 0.5mm behind the telescope focal point to reduce the defocus on the edge of the mask and to get an overall more uniform focus. Following the field curvature in only one direction reduces the usable FOV from  $4' \times 4'$  to  $4' \times 2.5'$  in dispersion direction. This limitation is not too severe for practical applications on sky as the spectrum of slits near to the mask's edge is clipped by the detector area. This is because the optical layout is such that the spectrum extends equally to both sides measured from the slit position on the detector. First year operation has shown that no science program suffered from this limitation.

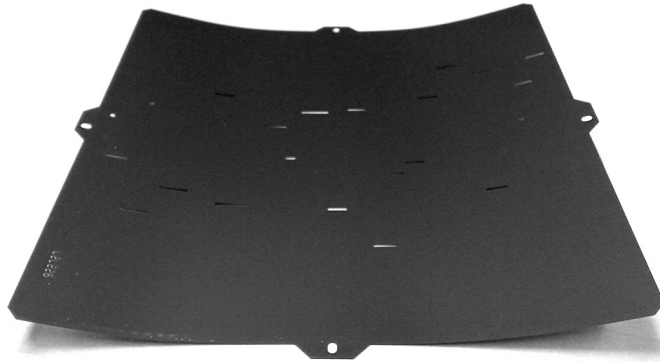


Figure 2.7.: Mask sheet with multi object slits. Four alignment holes are visible on all four sides along the outer edge. The mask ID number can be seen on the front left. It identifies the mask and can be checked during on sky acquisition. The side of the mask which is facing the instrument is blackened to reduce stray light. The curvature of the mask sheet follows the telescopes focal plane curvature in one direction. The slits are laser cut to the specifications of the science user. A special mask planning software is used to design the mask.

During labtests, stainless steel material of various thickness and surface properties was tested for their performance in the cold. The final material has been tested in the lab and showed only diffuse reflections in the near infrared.



Figure 2.8.: Close up on the mask sheet with mask ID number and mechanical alignment hole on top. The little holes in line below the ID number are for spectral alignment. With the help of these holes one can check the masks orientation with respect to the detector. Three MOS slits are visible on the sheet. The one square hole on the top right is one of several used for alignment of the mask during on-sky acquisition. Field stars are placed in them for alignment.

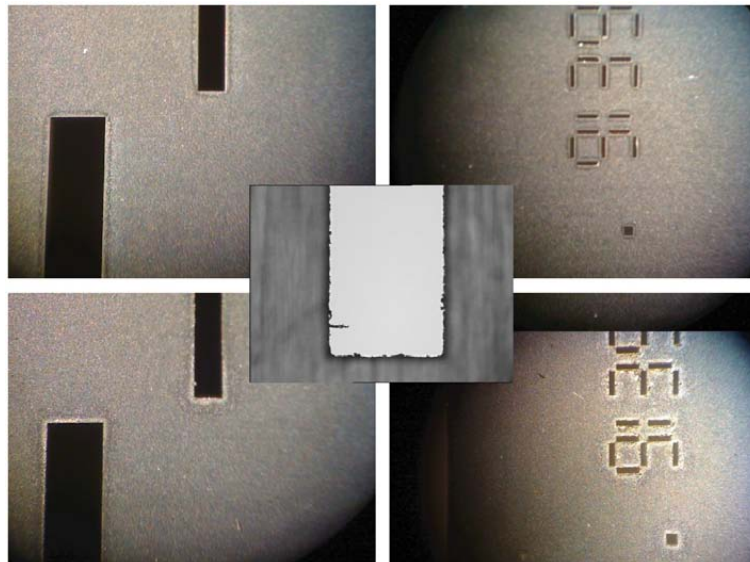


Figure 2.9.: Comparison of cuts with different cutting parameters (e.g. laser power and shielding gas pressure). Top row: Parameters adjusted. The cut edges are clean, Bottom Row: Laser power and gas flow not yet optimized. Molten material has re-solidified in an irregular shape on the edges, making it unusable as an entrance slit for a spectrometer. Inset: Close up of the recast material.

## 2.3. Focal Plane Unit (FPU)

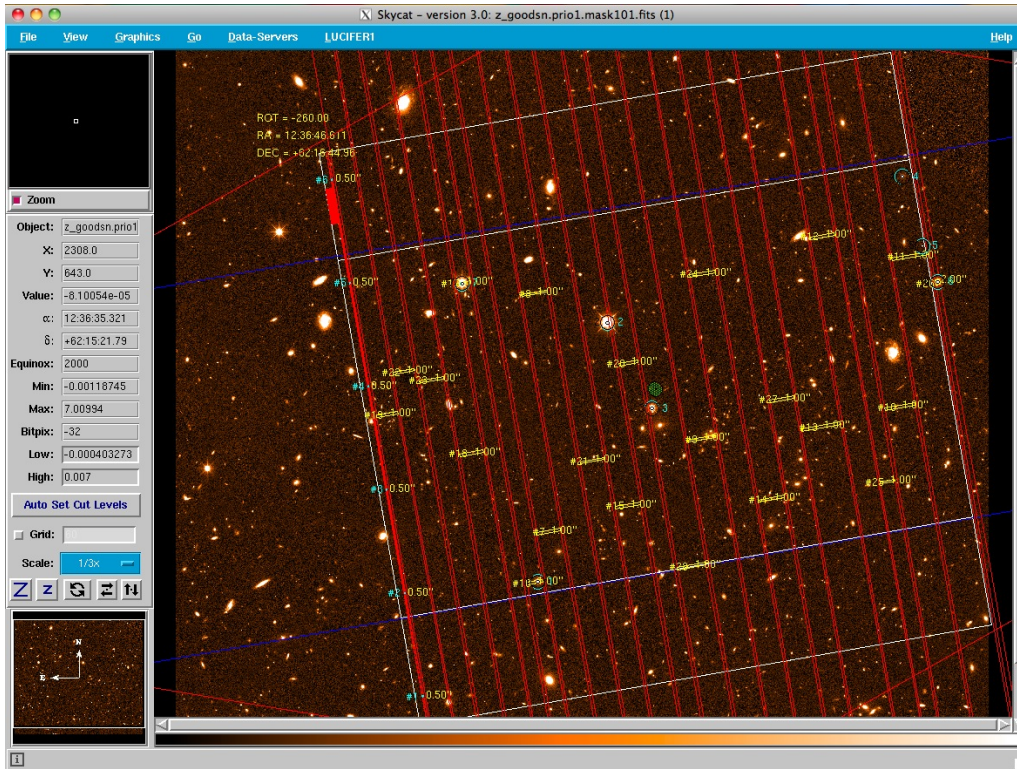


Figure 2.10.: Screenshot of the mask preparation software. The white square is the FOV the smaller rectangle inside the allowed area for slit placement. The slits are labeled in yellow. The red lines indicate the direction and length of the spectra for the selected grating/filter combination.

Mask creation is done via the mask-planning software shown in figure 2.10. It was programmed by MPE as a plug in to the widely used skycat software.

Figure 2.11 shows the postscript converted output of the mask-planning software. Since the mask is cut from a larger sheet of steel, also the outer edge and alignment holes are cut by the lasercutter. The mask shown is an actual science mask used in the ongoing MOS survey of our group.

## 2.3. Focal Plane Unit (FPU)

The Focal Plane Unit (FPU) holds and positions the mask in the focal plane. Masks are held and positioned using clamping arms and centering pins. In x-y-direction the masks can be reproducibly placed at the nominal position with an accuracy of  $< 30$  microns, corresponding to  $< 0.05''$  on sky. In z-direction along the optical axis, the positioning accuracy is better than 100 microns.

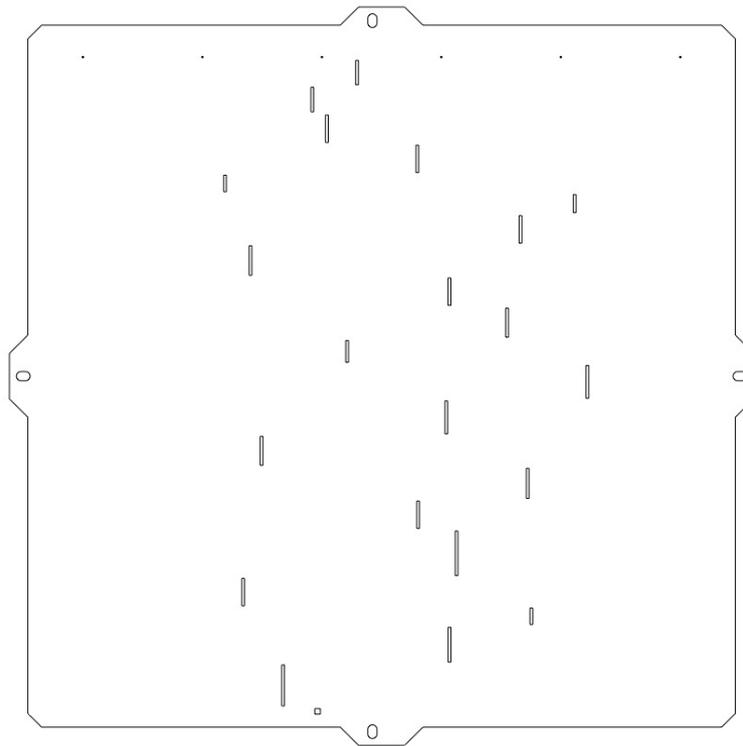


Figure 2.11.: Postscript file of the mask as it is output from the mask preparation software. A laser-cutter readable machine file ('gerber file') is also generated and is used to cut the mask.

The FPU has three operating states: OPEN, HOLD and LOCKED:

In OPEN position, a mask is either inserted into or removed from the FPU. When a mask is put into the focal plane, it is first rotated into the FPU by the Mask Handling Unit (MHU, see next section) into a gap between the fully retracted mask clamping-arm tips and the mask centering pins of the FPU. In this state, a mask is always grabbed and held by the MHU grabber.

The HOLD position is the mask-hand-over position between the MHU and the FPU. After the mask's has reached the OPEN position, the MHU moves the mask  $\sim 5$ mm out of the open position and into the HOLD position in the direction of the focal plane. The mask frame touches four spring loaded pads after this move. Also, the tips of the two centering pins extend into the alignment holes in the mask frame as they have a smaller diameter at their tip. In this position the centering pins serve as support pins only. Figure 2.13 shows a close up of this FPU part. From the other side (direction of the inside of the instrument), the two clamp arms now approach the mask frame. In the hold-position, these arms press only slightly against the frame so it is held between the spring-loaded-pads on one side and the spring-loaded tips of the clamping arms on the other side. In

### 2.3. Focal Plane Unit (FPU)

---

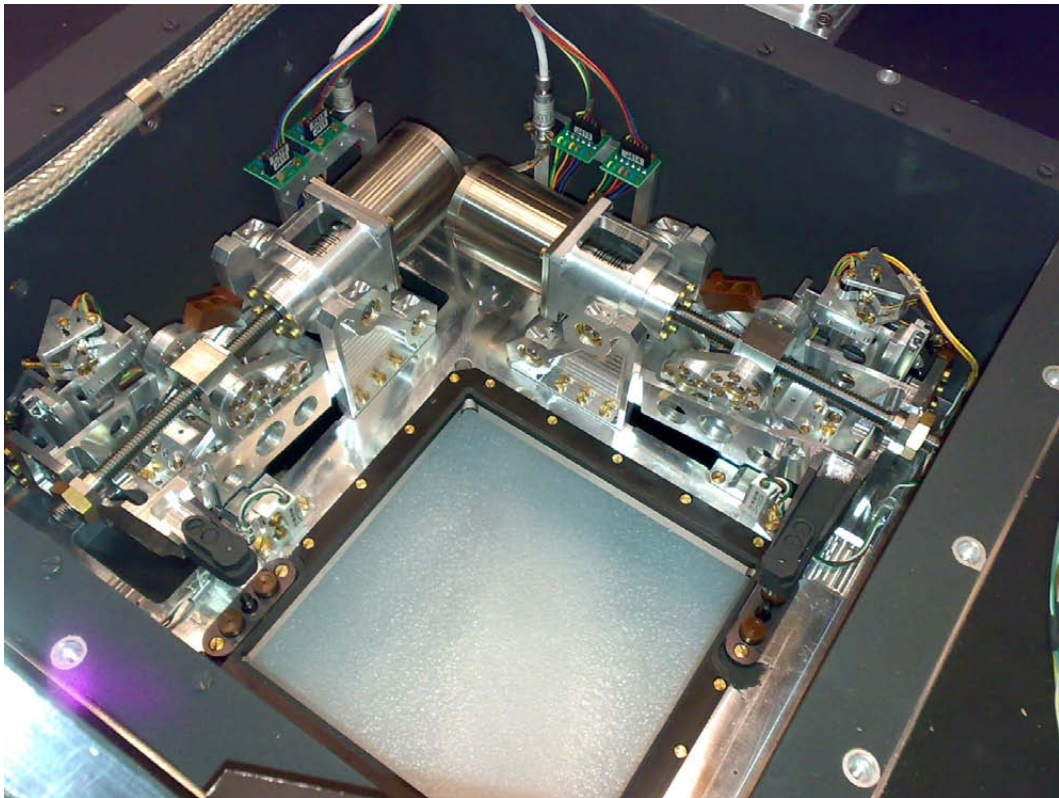


Figure 2.12.: Focal Plane Unit inside its housing mounted in the base plate of LUCIFER's inner structure.

The two stepper motors which drive the clamping arms can be seen in the upper part, their electrical connections leaving the image on the top. Arm-'X' is to the left and arm-'Y' to the right. The stepper motors drive two ball screws which in turn move a knee joint (attached to the ball screw's nut) to which the arms are bolted. The open black square in the center is the border of the  $4 \times 4 \text{ arcmin}^2$  FOV. The spring loaded pads and the alignment pads that are used for the mask alignment are located in the left and right corner. Their corresponding clamping arms are visible above them. Small reed contact switches next to the arms sense the mask frame position in open, hold and locked state.

this configuration the MHU grabber can now securely release the mask frame. The slight push of the clamping arms against the pads and the tips of the centering pins prevent the mask from falling out of place.

The LOCKED position is the final position where the mask is in the focal plane and can be used for observations. After the grabber has released the mask in the HOLD position, the clamp arms move further down, pushing the mask frame onto the centering pins. The motion stops when the mask frame has been fully pushed onto the centering alignment

pins and the spring loaded pads are fully pushed into the FPU's base plate. Now the alignment-surfaces, which center the mask, are in contact and align the mask correctly inside the FPU.

The FPU clamps are elbow joints driven by ball screws. The mechanism provides self-locking of the clamps in LOCKED position without the need for a hold current on the motors which would generate additional heat over long periods of observation time. Extensive tests and usage have shown that the ballscrews' dimensions are too small and abrasion can block the motion. Thus the ballscrews were revised during the thesis' work and now have a bigger diameter. The motion's error rate has dropped significantly.

### **Clamp motion control and mask position detection**

Both clamp arm drives have three micro switches attached to them which indicate the OPEN, HOLD, and LOCKED position. They act as motion limit switches in OPEN and LOCKED position. In HOLD position, a position-reference switch is activated. Reed contacts are installed in the FPU to monitor the actual mask movement. The contacts are positioned next to the mask frame and are actuated by two 3mm diameter Nd-magnets that are glued into the mask frames. Each reed contact has two switchover points, switching from 'on' to 'off' and back 'on' when a magnet is moved along the contact. The contacts are aligned such that they are 'on' in 'OPEN', 'off' in 'HOLD' and 'on' again in 'LOCKED' position. With this arrangement, the mask position can be determined to an accuracy of 1mm in z-direction. This is sufficient to reliably judge if the mask is in the proper position for grabbing. This information, together with the arms' state switches, is used to evaluate whether it is safe to grab or release the mask in HOLD position.

In an earlier hardware version, the mask frame position check was done using a lever-actuated switch. This setup proved to be prone to errors. As the solution the magnet actuated reed-contacts were introduced in this thesis work.

### **Alignment of the masks in the focal plane**

Proper and reproducible lateral alignment of the masks in the focal plane is crucial for successful science observations. Masks need to be inserted and taken out of the FPU smoothly and reliably to not wear out or damage the mechanical components. During MOS science field acquisition and pointing correction, the mask needs to be (repeatedly) put in and out of the focal plane. A reproducible positioning is of utmost importance in this case.

In earlier hardware versions described in Hofmann et al. 2004, lateral mask alignment was done by moving two hollow centering cylinders located in diagonal positions inside

### 2.3. Focal Plane Unit (FPU)

---

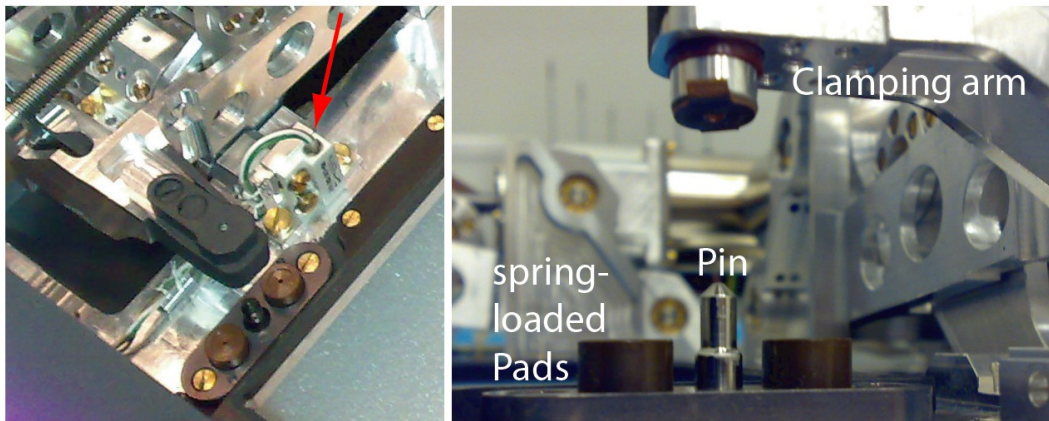


Figure 2.13.: Close up view of the clamping mechanism. The left view is from top. The blackened clamping arm and the pin/pad array below are visible. They protrude from the mask position reference surface. The arrow points at the reed-contact that is used for mask position detection. Right: Clamping arm and pin/pad viewed from side in FPU 'OPEN' position. During mask-insertion and -removal, the mask is rotated in and out of the gap between the arm and the pin, perpendicular to the paper plane.

the mask frames onto centering pins with fitting diameter anchored in the FPU base-plate. The fitting travel range was a few millimeter. All parts were hardened and coated with the dry-lubricant DICRONITE<sup>®</sup>. During extended cold tests, canting between the frame and the pins was observed, mostly when a mask was locked in the focal plane for an extended period of time. Differential thermal expansion of the mask (which is fully exposed to thermal radiation through the entrance window of the instrument) was suspected to be an issue in these cases because of the small thermal contact (the pins are the only thermal contact between the mask and the FPU). Also, we observed that in some cases the push-springs that are used to push the mask out of the locked position did not move sufficiently in sync which lead to canting of the frames on the alignment pins, causing damage to the pins (see figure 2.14).

Consequently, a new design emerged from this thesis: Now the clamping arms drive inside-cones in the mask frames against positioning ball-cups in the FPU base plate. Figure 2.15 shows a CAD drawing of the new pin design. This setup makes canting impossible. Extended cold test proved this setup to be very reliable and accurate.

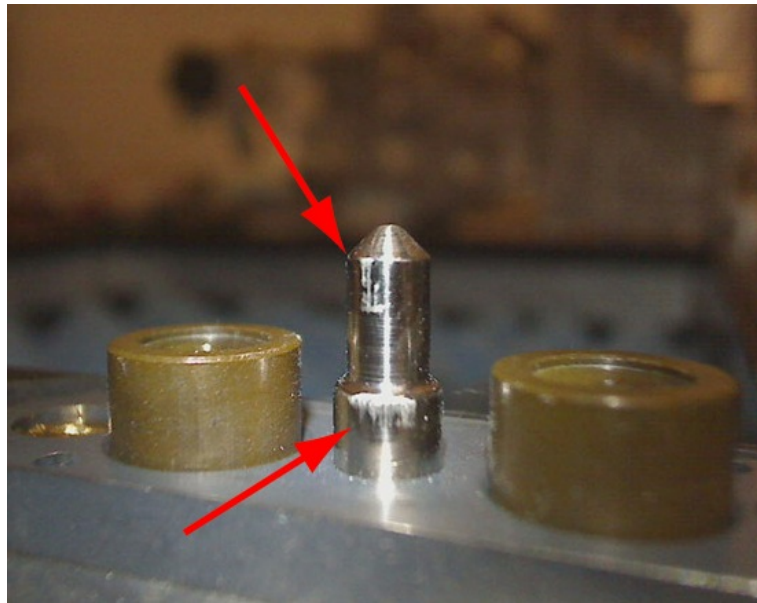


Figure 2.14.: Old version of the alignment pin with scratch marks due to canting and off-axis insertion of the mask. The spring loaded pads are located to the left and right of the pin. The three elements protrude from the mask position reference surface. In 'LOCKED' position the mask rests on this surface.

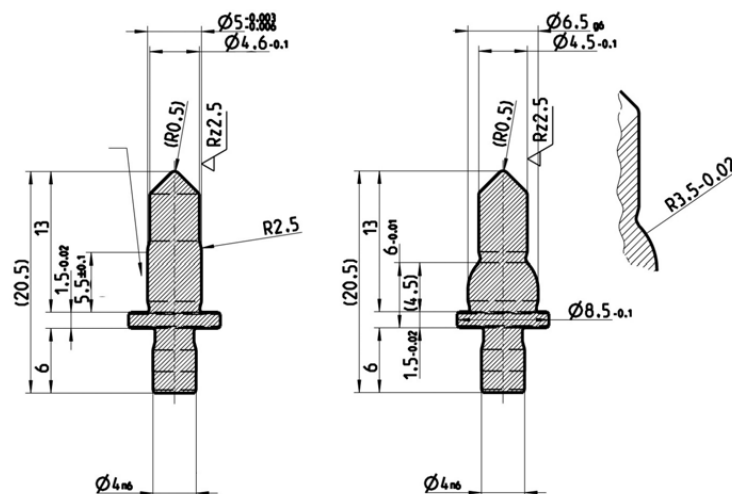


Figure 2.15.: Old version of the alignment pin (left) and new version (right) as CAD drawing. In the new version canting between pin and mask can no longer occur.

## 2.4. Mask Handling Unit (MHU)

The Mask Handling Unit (MHU), or 'robot', is the central component to move and manipulate the masks between the FPU and the mask storage. The MHU has three degrees of freedom, (i) grabbing the mask, (ii) rotating the mask into the FPU and the storage cabinet and (iii) moving along the cabinet to the corresponding storage place or the FPU position. These three functions are implemented in three subsystems: the grabber, the rotating head ('rotator') and the body ('translator').

### 2.4.1. Grabber

The MHU grabber picks or places masks from or into the mask cabinet or the FPU. It grabs a mask frame by its handle which is mounted on the side of each mask frame. The grabber's mechanic works similar to locking pliers. This ensures a secure transport of the mask between storage and FPU.

#### Grabber mechanics

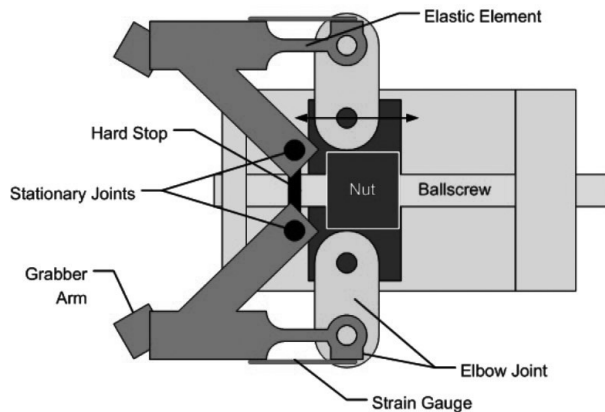


Figure 2.16.: Schematic drawing of the grabber in dead center configuration. Moving the nut slightly to the left from this position selflocks the grabber.

The system is build up from a ballscrew driven elbow joint which is self-locking when the mask is grabbed. A ball screw drives a nut to which an elbow joint is bolted, one joint for each of the two jaws/arms of the grabber. The arms are attached to the grabber body with a stationary joint and the elbow joint. This configuration (see figure 2.16) results in a closing or opening motion of the arms of the grabber when the ball screw moves the nut. For the self locking, the elbow joint requires elastic parts which are implemented as thinned bars. The nut is driven slightly beyond the dead center for securely grabbing the

mask. When the grabber has grabbed a mask, the two thinned bars are bent and exert a force on the nut, pushing it further to the left against a mechanical stop. The mechanism is self locked in this configuration. The motion stops as soon as the nut hits a limit switch at either end of the ballscrew. Two strain gauges affixed to the elastic part detect if a mask is grabbed. These strain gauges measure the deformation of the elastic part of each elbow joint. The deformation is slightly higher once a mask is grabbed and we measure the differential deformation between the open and closed state of the grabber. Therefore the sensors are calibrated (i.e 'zeroed') before each grabbing motion.

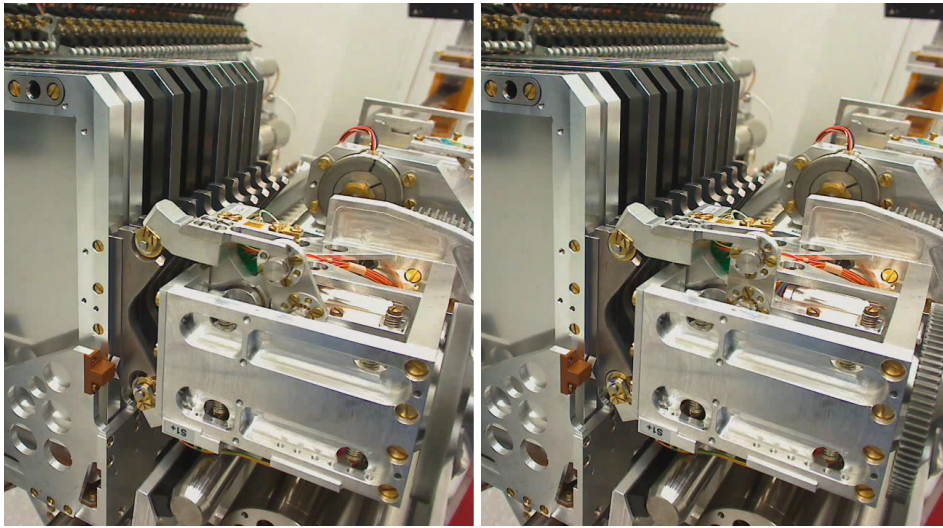


Figure 2.17.: The grabber grabs a mask. Left: the grabber has not yet finished grabbing, the clamps are closing. A small gap is still visible between the grabber arms and the mask frame handle. Right: The grabbing sequence has finished. Clamps are fully closed and the elbow joint is self-locked in 'strait up' position, cf. figure 2.16.

### Mask grabbing complexities and peculiarities

Grabbing and releasing the mask are very delicate phases in a mask exchange sequence. The mask frame and grabber arms need to be in line to prevent damage to the grabbing mechanism while grabbing. We have found two main situations can lead to a misalignment of the mask and the grabber:

(i) The mask frame is tilted out of the grabber plane in the FPU HOLD position. The grabber then tries to grab the mask under a certain angle. In this case, the grabber arms miss the mask handle and the closing arms of the grabber tilt the mask even more. This either moves the mask even further out of place (possibly making it stuck and preventing another grabbing attempt) or the grabber jaws are damaged significantly.

## 2.4. Mask Handling Unit (MHU)

---

(ii) Mask and grabber are parallel but there is a displacement in translation direction because the position of the MHU is measured incorrectly or the motion was not correctly initialized, i.e. nulled. In this case, the grabber does not grab the mask handle at all if the displacement is sufficiently large, or it grabs the mask with the jaw's sides to which some screws protrude. In this second case, the grip is firm as long as the mask is not moved. The strain gauges would indicate a successful grab. However, once the mask is moved, it would break free from the grip. The mask is then lost inside the instrument, possibly causing damage to other components.

We therefore monitor the MHU-translation and the masks position in the FPU and correct it when necessary. The translator features an auto correction sequence which checks the absolute position of the translator within one revolution. If the translator offset is greater than one turn of the spindle, the calculated position inferred from the incremental encoder will be sufficiently off for the sequence to stop. Both the grabber position (i.e. MHU-translator) and the mask frame position are checked when the mask is manipulated inside the FPU. The MHU position is checked as just described, the mask position is checked using the reed contacts as described in section 2.3. The contacts are read out after and prior to grabber- and translator motions to check the software-defined post- and preconditions for the current or the next motion in the sequence.

### 2.4.2. Rotator

The overview in figure 2.2 shows how the FPU and mask storage area are located opposite to each other, with the rail system of the robot translator between them. The mask is rotated out of the mask cabinet (see figure 3.6 for a snapshot of this motion) to get it into a position from where it can be moved along the cabinet and into the FPU. The rotation is done with the robot's head which also houses the grabber. The rotation axis is parallel to the translation direction.

Three rotator angles are defined for the three situations where the rotation is stopped and locked (cf. figure 2.2):

1. The storage angle is the rotator angle where masks are grabbed and released while they are taken out or put back into the storage cabinet.
2. The transport angle defines the rotator position when a mask is moved along the cabinet. The mask is also rotated into transport position for a short time when the mask is temporarily removed from the FPU for pointing checks or acquisition.
3. The FPU angle is where the mask is moved into 'hold' position, released, and grabbed while inside the FPU.

The rotation head is locked in storage, transport, or FPU position. In an earlier hardware version, this lock was a mechanical latch. This setup proved to be prone to errors and got stuck several times which prevented further mask manipulation. It was replaced during this thesis work by an electrical 'lock': the motor holding current is now active as long as a mask is grabbed. The additional dissipated heat was found in extensive tests to be negligible.

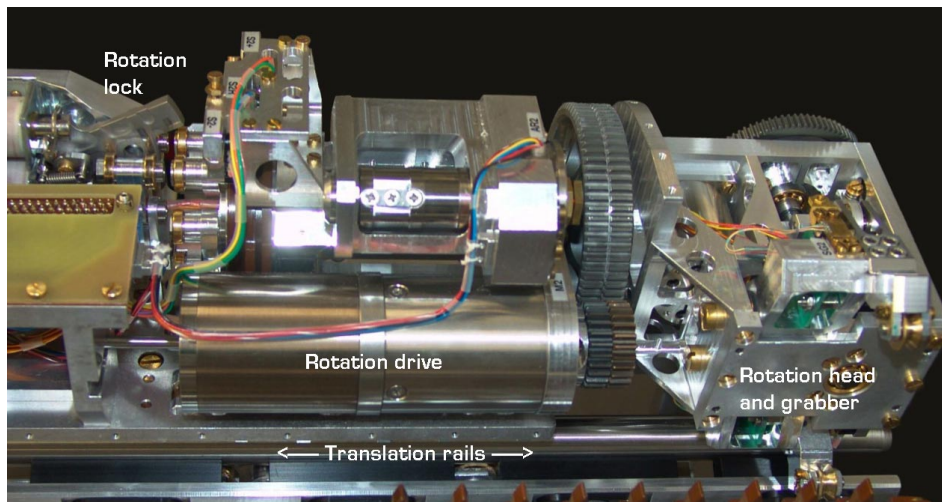


Figure 2.18.: MHU in storage position.

The rotation head and the grabber arms are visible on the right. It is connected to the rotation drive with a spring-loaded double wheel gear which is the next element to the left. The rotation drive stepper motor can be seen in the middle. The angular encoder is mounted above it. The translation rails are visible at the bottom. The (now replaced) mechanical rotation lock latch is shown on the top left. The green board on the left is where the robot's ribbon cable is connected.

A spring-loaded double wheel gear ensures that the motion is backlash free. An angular encoder monitors the motion. The gear ratio is 1:60 which gives us enough torque to rotate the mask in every instrument orientation (e.g. against gravity when upside down) and at the same time allows us to control the position angle down to 0.1 degree. We use absolute angles to address the rotator position as the total angle between storage and FPU is 185 degrees.

In earlier hardware versions, limit switches defined the three rotator positions. An angular encoder now replaces these switches since different instrument position-dependent torques on the rotator-head and grabber require a more flexible control solution.

### 2.4.3. Translator

The translator drive moves the robot along the cabinet. It is fixed to the support structure. The drive mechanism consists of a stepper motor that drives a ball screw to which the robot is attached by a nut. The robot rides on two cylindrical stainless steel rods, the “rails”, with gold-coated ball bearings as 15 wheels in 3 pairs. Their arrangement on the two rails is two fold: One the one rail three “guiders”, that each consist of 3 wheels mounted in 120° separation to one another, ensure a precise movement. On the other rail is a two-wheel arrangement that defines the azimuth angle. This arrangement is insensitive to slight changes in the separation of the rails due to differential thermal contraction in cryogenic conditions.

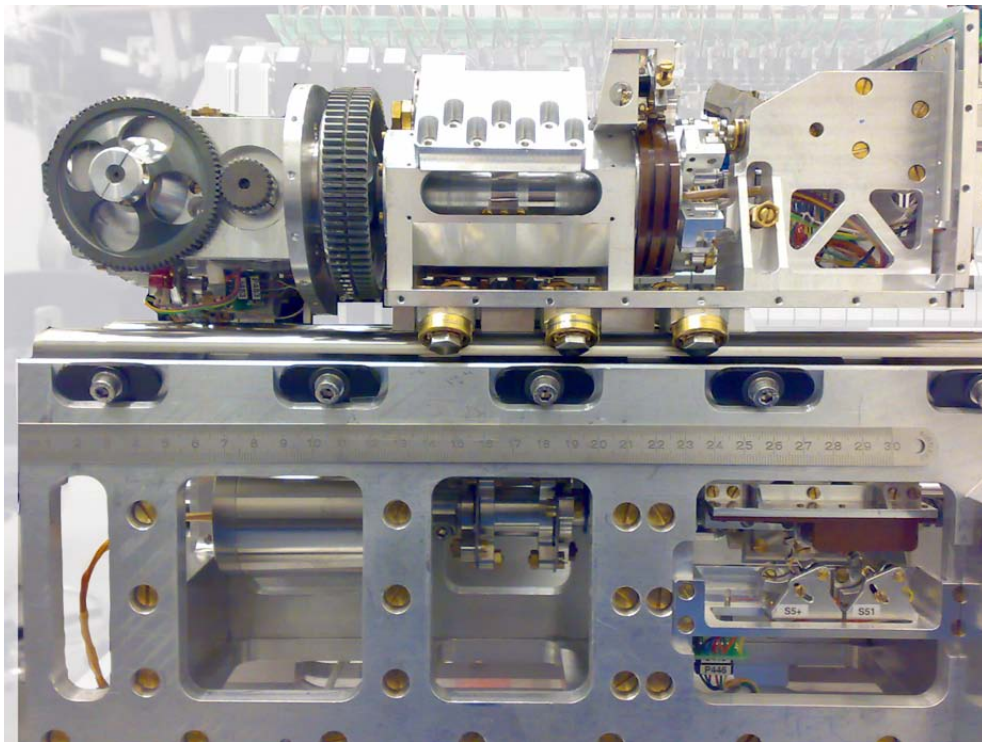


Figure 2.19.: MHU on its rails with the translation drive underneath.

The upper part is the moving robot: (from left to right) the rotating head with grabber gear and grabber motor seen face on, the rotator-double gear seen from the side, the body with the rotation motor and three gold-coated wheels underneath and the old version of the rotation blocking mechanism. Below the rails and the ruler (for size comparison) are the translation stepper motor (left), the clutch (middle) and the mechanical limit switches (right, labeled S5+ and S51) that are used for initializing the translator. The translator drive's angular encoder is not visible as it is located at the ball screw's far end (see figure 2.20 on the left).

The translator motion is monitored through an angular- and incremental encoder which is affixed to the ball screw. Motion limit switches are located at either end of the rails. The limit switches are used to calibrate the translation zero point (i.e. to 'initialize' the MHU position along the translation direction) and to measure the contraction between the warm and cold instrument, which can then be accounted for by the control software.

The mask positions are defined as absolute stepper motor steps from the zero point. To ensure that the robot has reached its intended position, we check the number of steps that were sent to the motor against the number of steps that have actually been moved. The number of moved steps is calculated from the angular encoder signal by (i) counting full revolutions (incremental encoder value) and (ii) the absolute angle (direct encoder readout) of the last revolution. For each mask position the position lookup table also holds the absolute target angle. Thus we can correct small deviations -if encountered- easily. Similar to the rotator, the translation can be locked at two angles per revolution using an electromagnetic actuated latch. The two locking angles are set up such that the translator drive can be locked in OPEN and HOLD position when manipulating a mask inside the FPU. The mechanical latch will be replaced in the near future with a motor holding-current 'lock'.

## 2.5. Mask Storage

The masks are stored in a mask cabinet similar to those used in slide projectors. As mentioned above, the masks are distributed over two cabinets. One cabinet is fixed inside LUCIFER and houses 10 permanent masks. The cabinet can only be replaced during maintenance of the instrument when the cryostat is open at ambient temperature. The second cabinet features 23 slots for user-provided MOS masks. This cabinet can be removed and replaced with the help of the auxiliary cryostats while the instrument is in operating condition, i.e. under vacuum at 77K. Masks in the permanent cabinet can be replaced, too, by swapping masks between the cabinets. This, however, can only be done in instrument engineering mode and not by the normal user.

The mask storage consists of two subunits: the mask cabinet(s) for storing the masks and the retainer which holds the masks in place and allows access to individual masks in every instrument rotation position or tilt.

### 2.5.1. Mask Cabinet and cabinet drive

The mask cabinet stores the masks and is used to transfer masks in and out of the LUCIFER cryostat. The slots have a nominal pitch of 17mm which corresponds to 680 steps (or 3.4 revolutions) of the MHU translator. Like the robot, the cabinet runs on rails with

## 2.5. Mask Storage

---

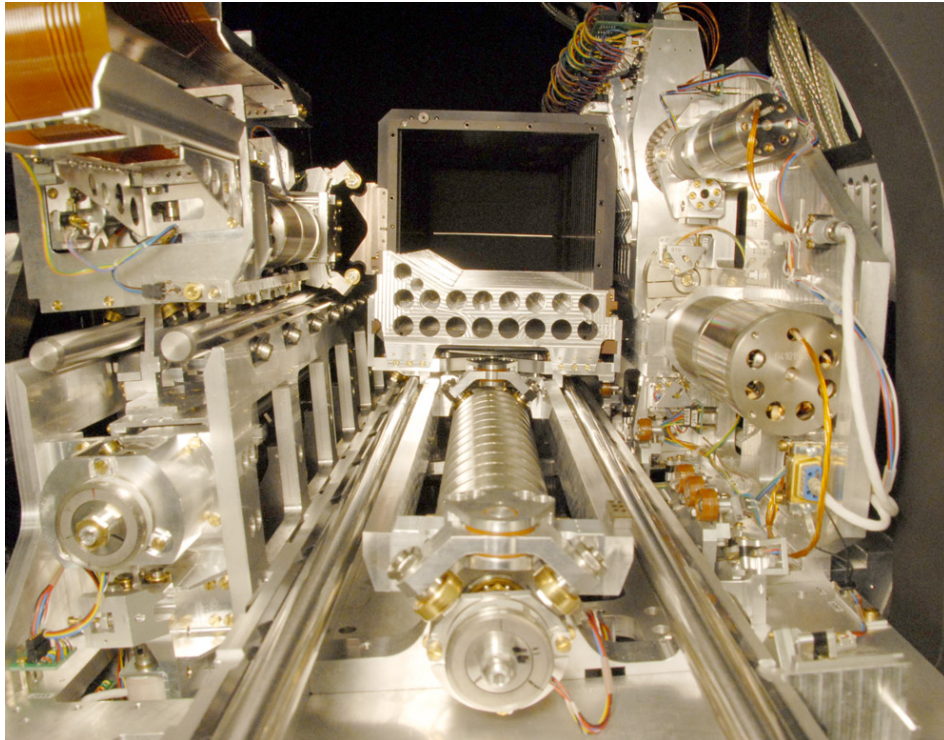


Figure 2.20.: View of the mask storage area, with the mask cabinet (containing some black mask frames) and its worm gear in the middle. A “draw bar” with two gold coated ball bearing wheels at its end extends from the cabinet to the front. It is used during handover between the LUCIFER and auxiliary cryostat during cabinet transfer to cross the gap in between where there is no drive mechanism. The two drives need to rotate in sync for this maneuver to work. The angular encoder of the cabinet drive that ensures a synchronous motion can be seen at the end of the worm gear, below the draw bar wheels. The mask retainer with mask index- (upper part) and retainer-drive-motor (lower part) is shown on the right. On the left is the robot and its rails with the angular encoder for the translator drive below.

wheels built in the same arrangement as on the robot. The cabinet has to attach to and detach from the driving mechanism during cabinet transfer. We therefore do not use a ballscrew but a worm gear to drive the cabinet. The cabinet attaches to the worm gear with another set of wheels (see figure 2.20 in the middle below the cabinet and the draw bar). The worm gear has an angular encoder attached to synchronize its motion with the other worm gear inside the auxiliary cryostats during cabinet exchange. The cabinet structure is soft against torsion about its long axis to reduce stress during the cabinet exchange. Such torsion can be introduced by misalignment of the three sets of rails: in LUCIFER, in the vacuum interface and in the auxiliary cryostat. A clamping mechanism ensures that the cabinet is locked the same end position after cabinet insertion inside

LUCIFER. The mask positions in robot-translation direction are therefore fixed and can be stored in a simple lookup table. The mask slots are separated by light weighted aluminum bars. Small plastic guides made from Vespel<sup>®</sup> (brown parts on the side of the bars in figure 2.21) guide the mask frame in and out of the cabinet when handled by the robot. These guides have been revised several times during this work to ensure secure mask extraction and insertion in every instrument orientation.

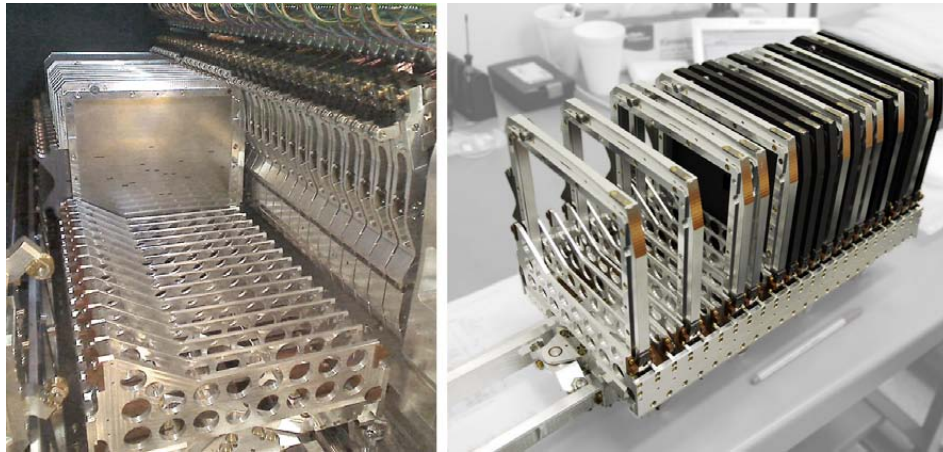


Figure 2.21.: Mask cabinet inside LUCIFER (left) and outside on a lab table (right). In the cabinet on the left only the slots towards the front are filled with masks. Higher number slots are empty. One can see the slot dividers and the brown mask frame guides on each divider to the left. The cabinet in the right image shows some empty slots and a mix of new (black) and old (bare aluminum) masks. The cabinet's draw bar is visible on the left side of the cabinet.

### 2.5.2. Retainer

To exchange masks in every instrument orientation, masks that are not in use need to be held in place in the cabinet. At the same time masks must be unlockable individually when a certain mask shall be put in the FPU. This is the task of the retainer. It consists of 33 aluminum arms, one for each mask, which hold the masks in place or unlock one selected mask. For the cabinet exchange, all masks can be unlocked simultaneously.

A retainer arm consist of two parts, a bottom part and a top part. The bottom part is bolted to the retainer drive shaft, the top part is attached to the bottom part with a flexible joint supported by springs (see figure 2.24). The top part has a fork like structure with a bar built in that is used for selecting the correct arm during unlocking (see below). This arrangement is combined with an index shaft that selects which arm is retracted during unlocking. Behind every arm there is a circumferential bar on the index shaft

## 2.5. Mask Storage

---

with a notch at a specific azimuth angle. The notches are rotationally offset by 10.6 degrees between neighboring circumferential bars, with one additional notch on each bar at the same azimuth angle for all arms. To select a mask arm, the index shaft is rotated to an angle that corresponds to a specific arm so that the blocking bar of the arm's top part can fit into the notch (see detailed description below). Figure 2.22 shows the location of drive and index shaft and figure 2.23 (right) shows a close up on the notches and circumferential bars.

### **Lock- and unlock motion**

To unlock a mask, the corresponding retainer arm needs to retract, i.e. it has to move backwards. At the same time, all other arms need to stay in place, i.e. must not move backwards. The drive shaft has two functional positions, 'locked' and 'unlocked'. A rotation of the drive shaft of 10° clock- or counterclockwise drives the arms back and forth, i.e. from locked to unlocked position and vice versa.

As all arms are bolted with their bottom part to the one drive shaft, all arms bottom parts move when the drive shaft is rotated. Thus all arm's top parts move backwards against the index shaft, against their corresponding circumferential bar. Only for the one arm that got selected, the notch in the circumferential bar is now in the correct position so that the blocking bar in the arm's top part can move into this notch. Therefore only this one arm moves backwards and frees its mask. The blocking bars of all other arms can not slide into their respective notches at that point because their notches are not at the selected index shaft azimuth angle. The bottom and top part of the 'non-selected' arms flex around their joint, as the bottom part is moved by the drive shaft. The springs around the joint are compressed (see figure 2.24, left) Consequently, the non-selected arms do not retract when the drive shaft turns to the 'unlocked' position, i.e these arms do not free their respective masks but stay in locked position.

All arms have magnets attached to their top part which activate reed contacts to monitor the locked and unlocked state. In the hardware version prior to this work, mechanically actuated micro switches were used. We observed that the spring tension of the switches can be sufficient to block the arms motion, which could then not fully retract, i.e. the mask could not be unlocked. We exchanged the micro switches with the new magnets and reed switches. A second electromechanical micro switch on each arm gets actuated upon mask contact, indicating the presence of a mask in a given slot. This one was not changed.

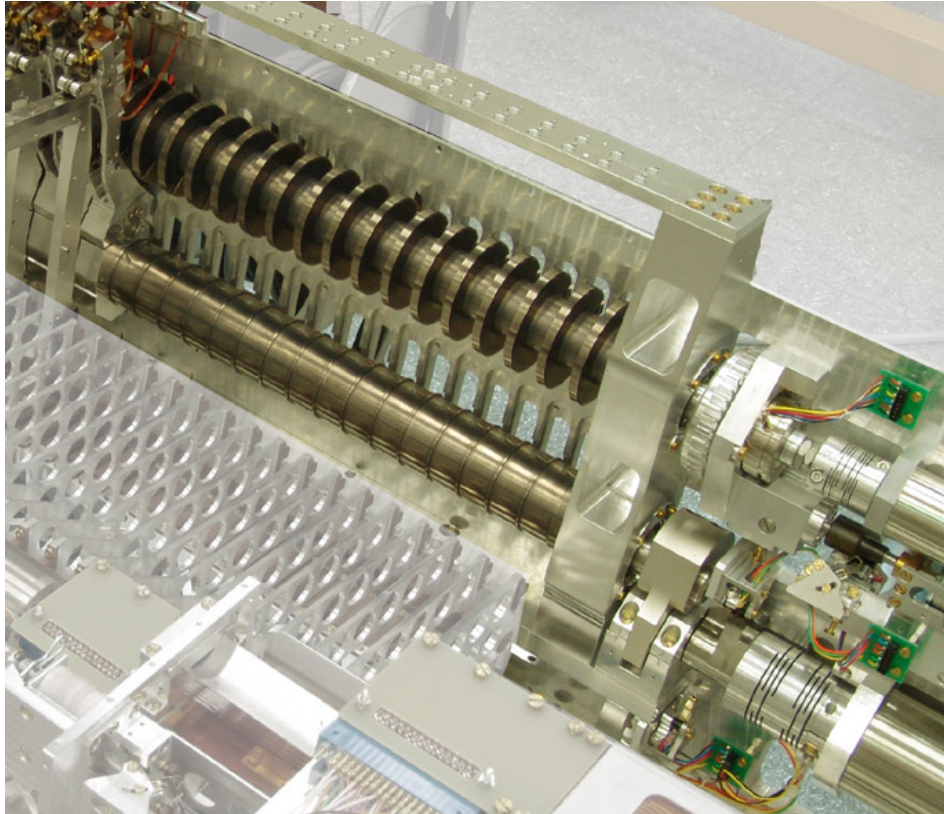


Figure 2.22.: Retainer mechanism with most of the arms removed. The lower drive shaft and the upper index shaft of the retainer which are normally hidden behind the arms are visible in the middle. On the right, top: the index shaft with its stepper motor, gear and angular encoder. The stepper motor, gear and eccentric tapper for the drive shaft is located below. One test arm and a mask frame can be seen on the very left. The green electronics board, that is visible in figure 2.23 on top of the retainer, is missing in this image.

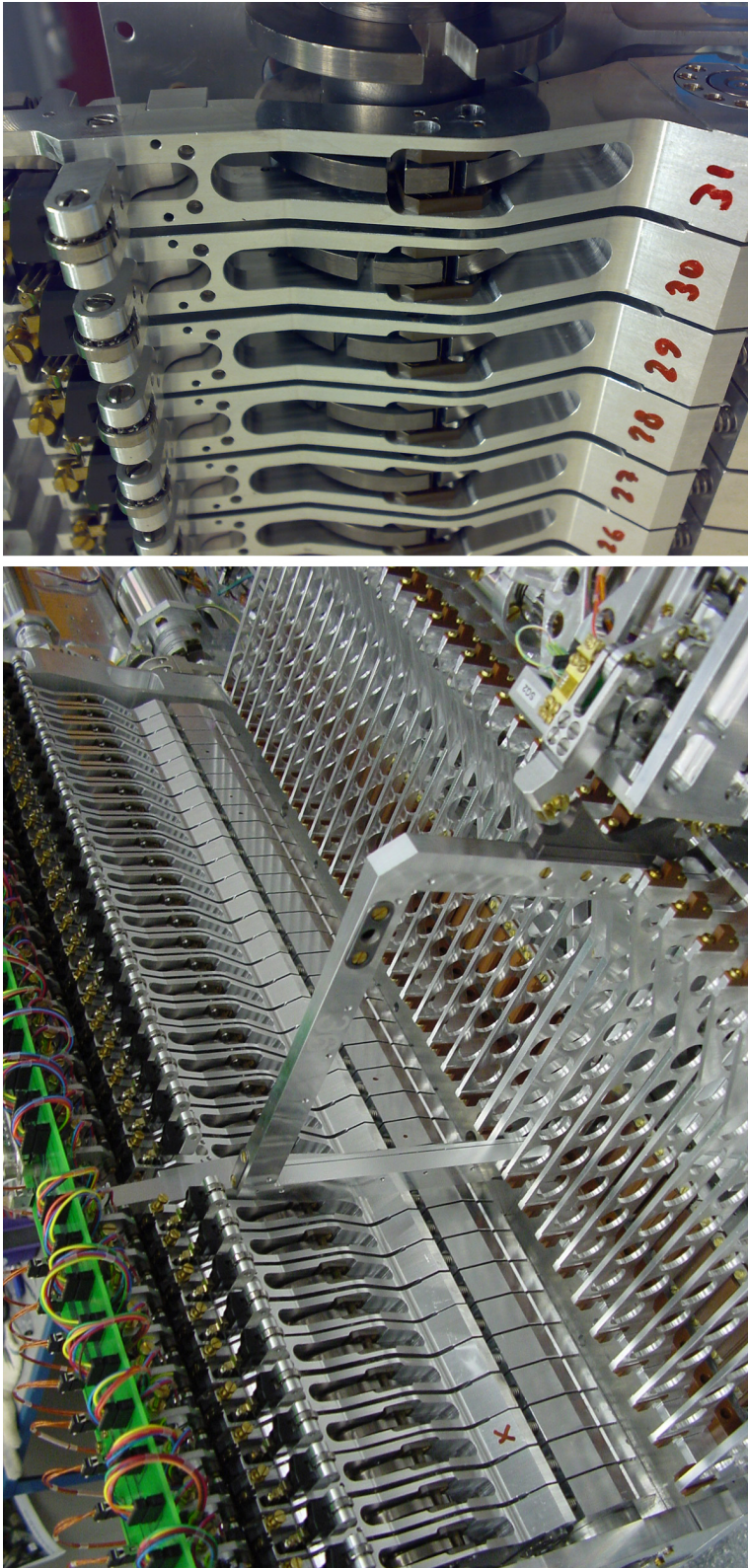


Figure 2.23.: Left: Overview of the retainer with all 32 arms in place. One empty mask frame is in the last slot of the fixed cabinet. Right: Close up of the arms and the indexshaft in 'select-all' position. The arms are all retracted, their index bars fit into the common 'select all notch' in the index shaft. The notches for individual mask selection can be seen for arm 29, 30 and 31. At the bottom of arm 31 the joint between the bottom and top part of the arm can be seen. The springs between the bottom and the top part are visible for arm 16-19. The small finger with ball bearing at the top of the arm touches the mask in locked positions. Arm 32 is removed.

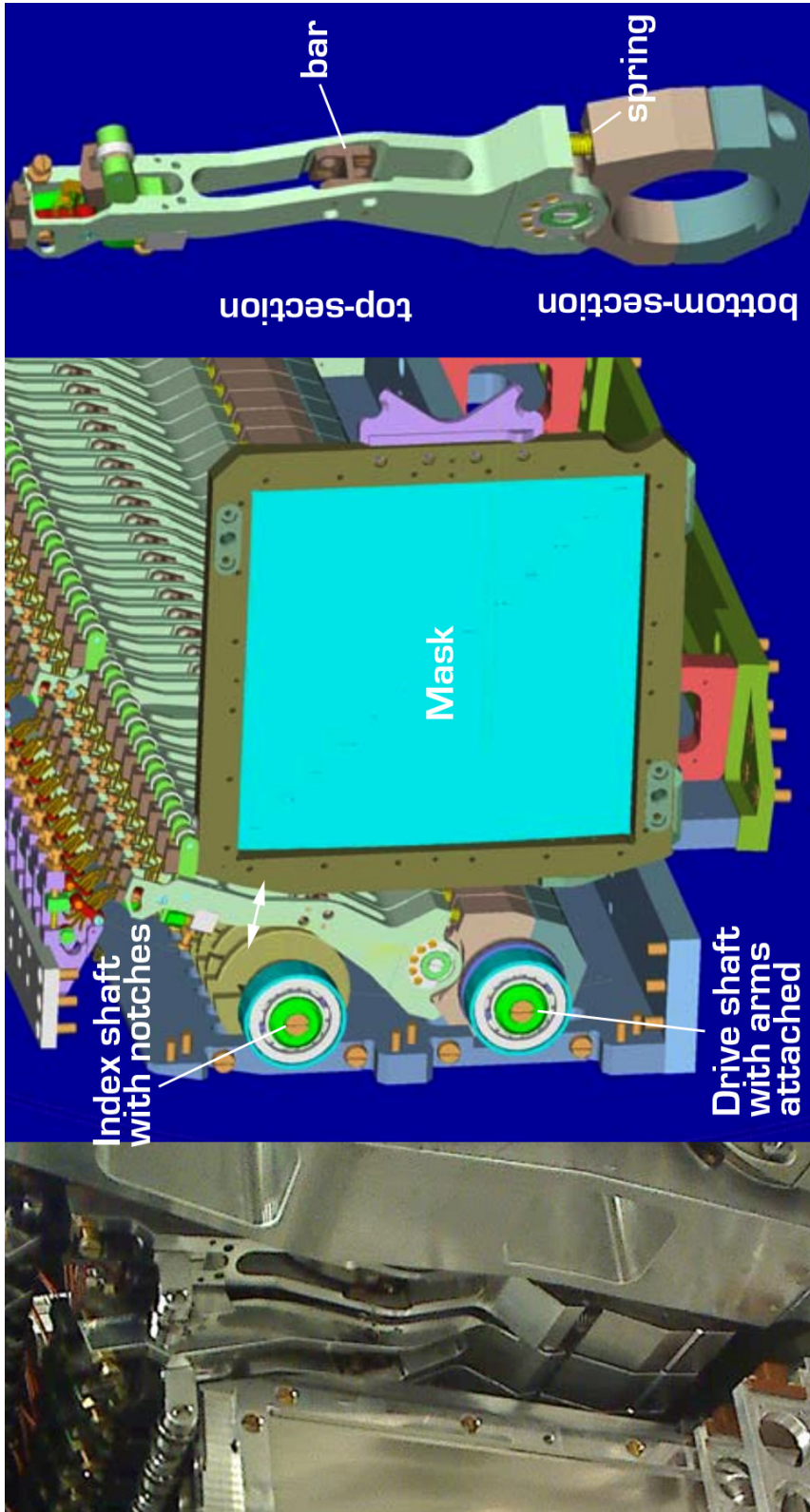


Figure 2.24.: Left: Retainer arms in locked and unlocked position. Note the compressed and expanded springs in the bottom section. Middle: CAD overview of the retainer with drive and index shaft. Right: a single retainer arm.

## 2.6. Mask Cabinet Exchange components

One of the outstanding features of the LUCIFER MOS is the possibility to exchange MOS masks while preserving full cryogenic conditions within one day of daytime engineering, i.e. between two science nights. The mask cabinet is driven in and out of the LUCIFER cryostat using a worm gear as described above. Cabinets are supplied and received by an auxiliary cryostat that attaches to the main instrument cryostat.

### 2.6.1. Auxiliary Cryostats

The auxiliary cryostats are built into a support structure of roughly 80x80x160 cm in size, having a total weight of about 400kg. They attach to the Lucifer cryostat through a vacuum interface with a free diameter of 30cm. The auxiliary cryostats are supported and guided by rails built on top of a bridge-like structure which is permanently bolted to the telescope in between the two LUCIFERs (see figure 1.3 and 2.25).

There are no retainer or other storage structures integrated into the auxiliary cryostats as they are only used for cooldown, transport, and warmup of the mask cabinets. We have implemented a thermal coupling that can be lowered onto the masks for faster cooldown or warmup. An electronics rack is mounted on top of the outer support structure. It controls the vacuum system and the LUCIFER and auxiliary cryostat gate valves. Unintentional opening and closing of the gate valves is protected by various software and hardware interlocks. The auxiliary cryostats have the same rail and worm gear system as in LUCIFER to drive the mask cabinets in and out (figure 2.26). During the actual transfer, the LUCIFER electronics controls all movements, since the motions of the LUCIFER and the aux-cryostat cabinet drive need to run synchronously during the cabinet handover between the two units. The cabinet drive can be operated manually from the aux-cryo-control electronics when a new cabinet is inserted into the aux-cryostat or the old one is removed in the lab in ambient conditions. The aux-cryostats hold up to 30 liters of liquid nitrogen in a tank coupled to its internal structure. Cooldown takes about 24h. The masks are at LUCIFER operating temperature another 18-24h later. For rapid warmup heaters can be switched on. The cryostats are equipped with all vacuum equipment needed to pump the cryostats as well as the vacuum interface between the auxiliary and LUCIFER gate valve. Communication to the main instrument is done via digital lines which the support staff at the telescope needs to connect to LUCIFER manually. Interlocks ensure that all cabling and preparation steps have been completed successfully before a transfer can be run from a dedicated software GUI. For operation both the LUCIFER and the auxiliary cryostat gate valve need to be connected to pressurized air. A pressure leak is potentially dangerous as the gate valves could close during transfer.

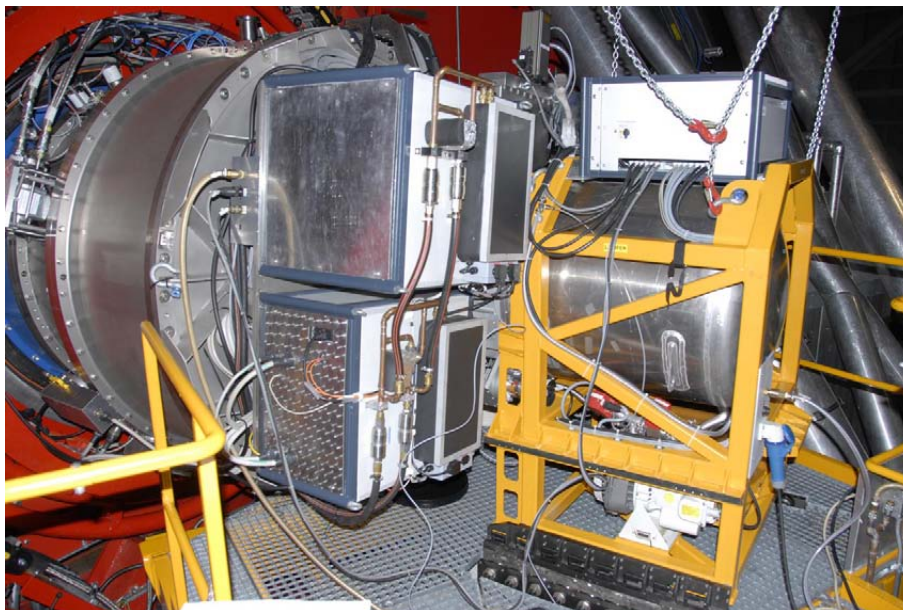


Figure 2.25.: LUCIFER (left) with an auxiliary cryostat attached (right, in its yellow support frame) during a cabinet transfer. The white box on top of the auxiliary cryostat is its control electronics. A part of the vacuum system is visible in the lower part of the yellow aux-cryostat frame. The black bars at the bottom of the aux. cryostat structure are the rails on which the cryostat is moved towards the vacuum flange and which support the weight of the unit. The communication cables are attached to the LUCIFER system on the left. The vacuum flange is not visible from this viewing angle, it is behind the electronics boxes on top of LUCIFER.

## 2.7. Radiation Shield Shutter

During a cabinet exchange, an opening of roughly 30x30cm in the radiation shield of the main LUCIFER cryostat is required such that the cabinet can exit the cryostat. This opening exposes the cold volume to a high thermal radiation load. Therefore, a shutter closes the opening during normal LUCIFER operation. The shutter consists of the shutter blade, a clamp system, and the drive unit. The shutter blade covers the opening in the radiation shield. The clamps close around the two rails on which the cabinet rides, and which protrude beyond the radiation shield towards the gate valve. The drive unit is powered by a stepper motor connected to a ballscrew. The linear motion is converted into a rotation by a gear-rod / gear-wheel combination. The micro-switch based detection of the open and closed state turned out to be prone to errors. We have now added an angular encoder to the shutter blade axle to monitor the shutter movement and check the open and close state.

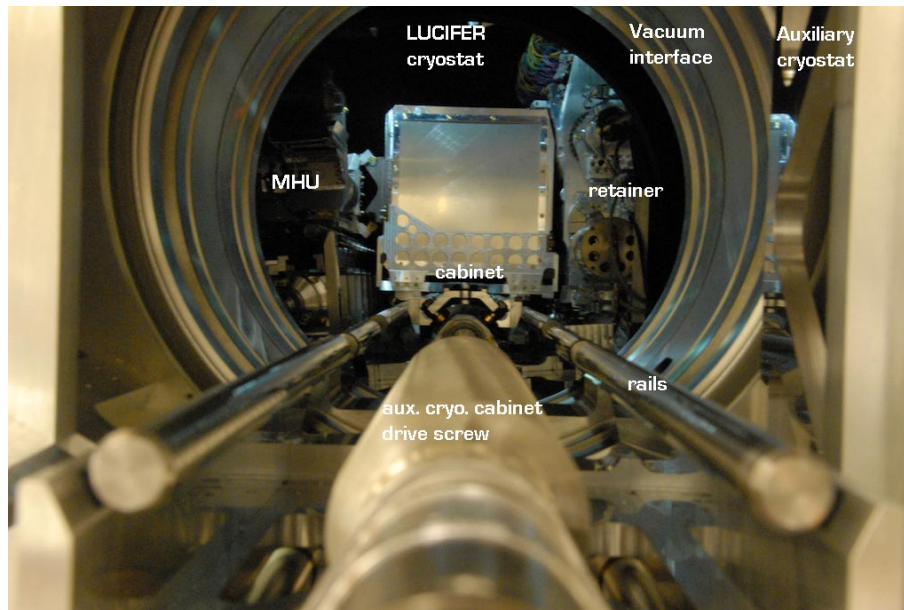


Figure 2.26.: View along the cabinet drive and rails from the auxiliary cryostat towards the LUCIFER cryostat. During transfer, the cabinet is handed over from the LUCIFER cabinet drive to the auxiliary cryostat cabinet drive in a synchronous motion of the two worm gears. The three pairs of rails are visible in the center.

## 2.8. Upgrade path

Various upgrades are possible to improve the efficiency of science observations and to make operations more secure. From the experience gathered during the first year of operations following upgrades appear promising:

### Spherically curved masks

For now the curved focal plane of the telescope is corrected in one dimension only. This reduces the usable field of view in multi object slit masks from  $4 \times 4$  arcmin<sup>2</sup> to  $\sim 4 \times 2.5$  arcmin<sup>2</sup>. With spherically curved masks the whole FOV would be usable for MOS observations. Spectra would however be severely truncated at the edges, but for narrow band observations having a full FOV is still desirable. The laser cutting facility already provides the functionality of cutting spherical shaped mask material, since MODS, the optical waveband counterpart to LUCIFER at the LBT, is already using spherical masks. The masks require special mask frames and are fabricated by galvanic deposition of nickel to a reference surface. First tests with spherical LUCIFER masks have been carried out in early 2011 giving inconclusive results. Alignment problems of the f/3.78 camera led

to a defocus at the FOV edge, preventing a robust comparison. We will investigate this option further especially in the light of the upcoming ground layer laser AO that covers the whole FOV.

### **OH filtertstacks**

The Lucifer mask frames are sufficiently thick that special 'masks' with OH-line suppression filter-stacks (e.g. similar to the ones presented in Günster et al. 2011) for a small FOV or even arrays of such stacks are conceivable. These OH suppression field masks could then be used in imaging observations to greatly reduce OH line contamination allowing for deeper exposures in the near infrared before the sky-limit is reached.

### **Gate valve pressure reservoir**

To make the effect of a potential loss in pressurized air during a mask cabinet transfer less severe, pressurized air reservoirs could be integrated into the auxiliary cryostats holding the gate valves open until the transfer has been completed. This is also beneficial since controlled and complete closing of the gate valves requires pressurized air to be present.

## 2.8. Upgrade path

---

## Chapter 3.

# MOS unit control, function- and motion sequences

In this chapter we present the control hard- and software and the motion sequences that are used to control the MOS unit. As part of this work the needed function- and motion sequences presented here were advanced or developed from scratch. In the first part we discuss the control hardware, followed by a brief overview over the control software. After that we present in detail the software based function- and motion sequences for normal operation and error handling.

### 3.1. MOS control hardware

#### Motion control unit

The control electronics for the MOS unit is mounted in a rack on top the main LUCIFER cryostat. Communication between the LUCIFER server and the instrument is done through a fiberline interface over RS232. The motion control unit electronics is divided into four sections:

The **motor controller**, developed by the MPI for Astronomy in Heidelberg, controls the stepper motors, which drive all the MOS unit motions. The MOS version has been extended by our group so we can control the needed number of 12 motors. The motor controller receives commands from the control software, monitors the angular encoders attached to some of the motors, and calculates the current motor position based on the commanded steps and/or the angular encoder signal. Motor-limit-switch signals are directly passed to the motor controller to shut off motions before hard mechanical limits are reached. The motor controller creates a pulse-width-modulated TTL signal for the stepper motor amplifiers (see below).

The FPGA based **switchbox** is another section. The signals of all micro- and reed-switches, i.e. limit-, state- and position-indicating switches, are fed into this component. The limit switches are directly passed through to the motor controller. State- and position-switch information is parsed and translated into switch states. As every switch is a toggle switch, a state change requires two signals to change (i.e. one from high to low, the other from low to high). Is the state change detected within a timeframe of 2 microseconds a valid output ('on' or 'off') is generated. Otherwise the switch state is flagged with an error bit. The switchbox also performs Boolean operations on various switch inputs that are needed for interlocks. The switchbox logic can be altered if needed (e.g. if a switch shows a defect and the current logic breaks) by re-programming the FPGA. The switchbox is queried and read by the control software to check pre- and postconditions of sequences.

The **motor amplifiers** translate the control signal into the needed modulated sine and cosine signals for the stepper motor coils. The motor current needs to be optimized for cryogenic conditions. It can be adjusted via potentiometers. Three amplifiers are grouped on one amplifier board which can be easily accessed and exchanged if a malfunction occurs.

The **angular encoder driver boards** generate the reference signal for the angular encoders. They also read the return signal. From there the angle is calculated. An incremental encoder counts full revolutions. This allows to calculate the travel distance of the MHU robot or the mask cabinet.

## Interlocks

Hard- and software interlocks have been implemented for functions and movements of the MOS unit components. Both ballscrews of the grabber and the translator are equipped with limit switches on both ends. Likewise, both the 'locked' and 'unlocked' position of the retainer feature limit switches. The limit switches are hard-wired to the motor controller and shut of the motion instantaneously when hit. Also from the software engineering panel further movement is then prohibited to prevent permanent damage to the unit. They can only be overridden using a cable break out box.

The pre- and post-conditions of every software sequence are software interlocks. They cannot be overridden by the normal science user / observer or the high level control software. In engineering mode these conditions can however be overridden for debugging purposes. The two vacuum gate valves cannot be automatically opened or closed. They need to be activated using push buttons secured by mechanical caps. Additionally certain criteria must be fulfilled (e.g the units must be evacuated and at cryogenic temperatures *or* warm and at atmospheric pressure) before the opening pulse is led through to the valves.

### Motion and vibration monitoring

To inspect and monitor the MOS unit motions in more detail under cryogenic conditions, we have built and added a camera (see figure 2.3, 2.5, and 3.1) and a vibration monitor. The camera is monitoring the storage side of the unit including the cabinet and the retainer as well as the robot. It is based on a commercial USB VIS-CCD webcam and is temporarily warmed up to working temperature ( $\sim 80\text{K}$  above instruments temperature) when needed. It features high brightness LEDs to illuminate the otherwise dark cryostat. We have modified the sound input to record structure-borne sound via a piezo-electric transducer to analyze and check mechanical vibrations on a regular basis. An example of a spectrogram generated from recorded structure-borne sound is shown in figure 3.2. This setup has proven to be extremely useful. It was used in several occasions to debug the unit in cryogenic conditions during daytime between two science nights.

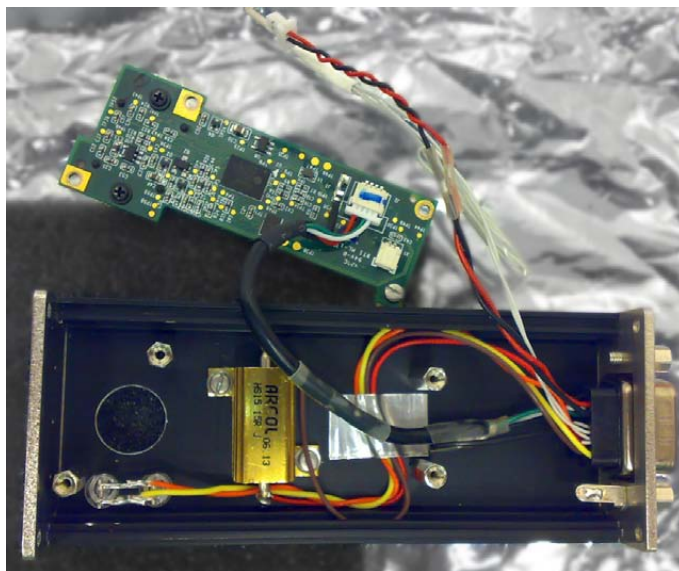


Figure 3.1.: Inside the modified USB VIS-CCD camera. The camera's PCB is on top. The housing is shown below. Inside the heater resistor (gold) and the LEDs for illumination are visible. The connector for the piezo-electric solid-borne sound transducer protrudes towards the top.

### Orientation monitoring

During this work we have also added a MEMS (microelectromechanical systems) based accelerometer and gyroscope, that allows for orientation monitoring of the instrument. It is integrated in the MOS electronics rack on top of LUCIFER but is not yet used in software. We plan to use the information to detect instrument orientations that lead to

### 3.1. MOS control hardware

---

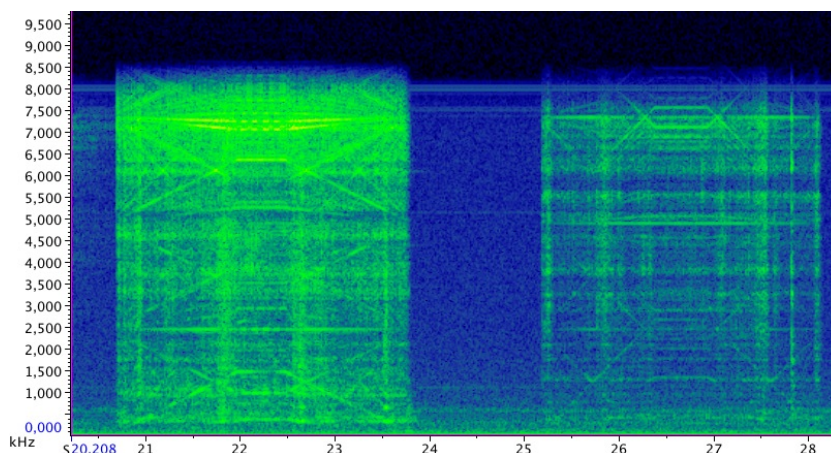


Figure 3.2.: Sound spectrogram of two MOS motions. On the x-axis is the time in seconds, on the y-axis the frequency in kHz. Color coded from black to yellow is the amplitude/intensity. The left motion is the open-to-hold motion of the translator, the right motion are the FPU arms moving from open to hold. The motion ramps (increasing and decreasing velocity) of the stepper motors are visible as 'diagonal stripes'. In between the spectral signature is 'flat'.

mask and MHU positions which are known to need correcting motions. If the instrument reaches such a position, the correcting motion could be speeded up by directly reading from a lookup table instead of being adaptive and therefore slower.

#### 3.1.1. Auxiliary cryostat control

The auxiliary cryostats have their own control electronics for driving the cabinet worm gear in the lab. One can mount and remove mask cabinets into and from the auxiliary cryostats at room temperature and normal atmospheric pressure without LUCIFER attached. The control electronics further controls the vacuum pumps, the vacuum valves, and the heater. During the mask transfer to and from the LUCIFER main cryostat, the LUCIFER electronics takes over the control over the cabinet drive. In this situation the engineer has to manually connect two controller cables between the aux- and the LUCIFER cryostat. A software interlock ensures the cables are connected before the exchange is initiated. The auxiliary electronics continues to control the vacuum pumps of the auxiliary cryostat and the vacuum interface during the cabinet transfer.

A programmable micro controller monitors the cryostats state and evaluates limit switches and pressure sensors inside the cryostat to put interlocks to the different functions. Venting of the cryostat is e.g. not possible during a cabinet transfer, likewise the gate valves can not be opened if there is ambient pressure on one side of the gate valve while the

other side is evacuated. Critical operations like opening the gate valves, venting the cryostat or switching on and off vacuum pumps cannot be controlled by software. These functions are wired to push buttons on the auxiliary electronics control panel. The switches are secured by plastic caps against accidental pushing and are also wired to electronic interlocks.

## 3.2. Control-Software

The motions of the MOS unit are not static. They have to adapt to slight changes in the geometry of the unit due to flexure of the instrument when it is rotated and tilted during observations. Since mask- and other positions can therefore slightly change, motions cannot be hardwired or executed as end to end movement between limit or position switches. Also motions might fail as e.g. a position switch is not triggered or an angle is not reached after the first try. In that case it is desirable to have auto-correcting/debugging capabilities of the unit. All movements are therefore initiated and monitored by a complex control software.

The Lucifer control software is a Java based multi level service architecture developed by the Astronomical Institute of the University of Bochum (Polsterer 2011). There are three main MOS unit services which are called from higher services or graphic user interfaces:

1. MCU (motion control unit) service:

This service implements the communication with the motion control unit, that part of the control electronics which drives the hardware. It issues all motion commands, operates magnetic locks and reads out angular position encoders.

2. Switchbox service:

Queries and reads out the FPGA-based switchbox. The state of each limit switch can be 'on' or 'off' and can additionally carry an error flag when the hardware has detected a failure in the electrical signal as described above. The switchbox service is called to check if pre- and postconditions of sequences are fulfilled or have been reached.

3. Sequence server:

The Sequence Server holds the scripts and the information in which order the sub units have to work together to carry out the desired function, e.g. put a mask to the focal plane unit. This service provides all motion sequences for the MOS unit, ranging from so called 'atomic' sequences, i.e. single motor motions, to the most top level sequences for complete mask and cabinet exchanges. It allows to pause sequences and carry on interrupted sequences in a process called 'motion pausing and skipping'

### 3.3. MOS function and motion sequences

---

The MCU and switchbox service can both be directly accessed through an engineering GUI to override the motion sequences. It enables direct access to the hardware, i.e it provides direct motor control. Motion limit switches can not be overridden as their signals are directly passed to the motion control electronics. In case a debug is necessary which involves overriding these, breakout boxes have to be used to electrically simulate the desired state. Additionally, the engineering GUI allows to check the state of the unit and execute the available motion sequences. The MOS Unit is completely transparent to the science user and higher-ranking instrument control service. It is operated using a simple GUI (or internal software calls respectively) which only select the mask and end-position and request the start of the motion. Mask configuration (name, type, position, observation-ID) and the cabinet exchange procedure have their own GUIs for convenience. The cabinet exchange GUI automatically detects the current status of the attached auxiliary cryostat and guides the system engineer at the telescope through the delicate exchange procedure.

All motions are carried out in open loop. After a command is sent to the hardware, the software either waits until a switch-state is reached or until the motion controller signals that the commanded motion has been executed, e.g. the number of commanded steps was executed by the hardware. Then the actual state of the MOS is compared with the nominal state. Correcting motions are carried out or the sequence stops if there are deviations from the nominal state beyond a given tolerance limit.

### **3.3. MOS function and motion sequences**

The function- and motion sequences are completely transparent to the user for the instrument operation during science observation. The instrument manager service calls the sequences when a new mask or mask position is requested from the instrument user GUI. Function- and motion sequences are set up hierarchically. 'Atomic' transitions control individual motor movements between two states, e.g. 'move motor x (from here) into a limit switch' or 'move motor x (from here) y steps'. Transitions are grouped into sequences. Sequences can be grouped into higher level sequences. Therefore a sequence can represent any kind of motion from a simple one motor-transition motion to a tree of complex sub-sequences. The top-level sequences are the mask exchange sequences that describe a whole mask exchange to the focal plane unit and back to the storage unit or vice versa. Another set of top-level sequences group all the sequences that are needed to control the mask cabinet exchange.

Each sequence is bundled with a start- and an end-state called pre- and post-conditions. Pre-conditions are not only used to decide *if* a sequence can be run, but can also contain a decision tree to determine which sequence parameters to take and which sub sequences

### 3.3. MOS function and motion sequences

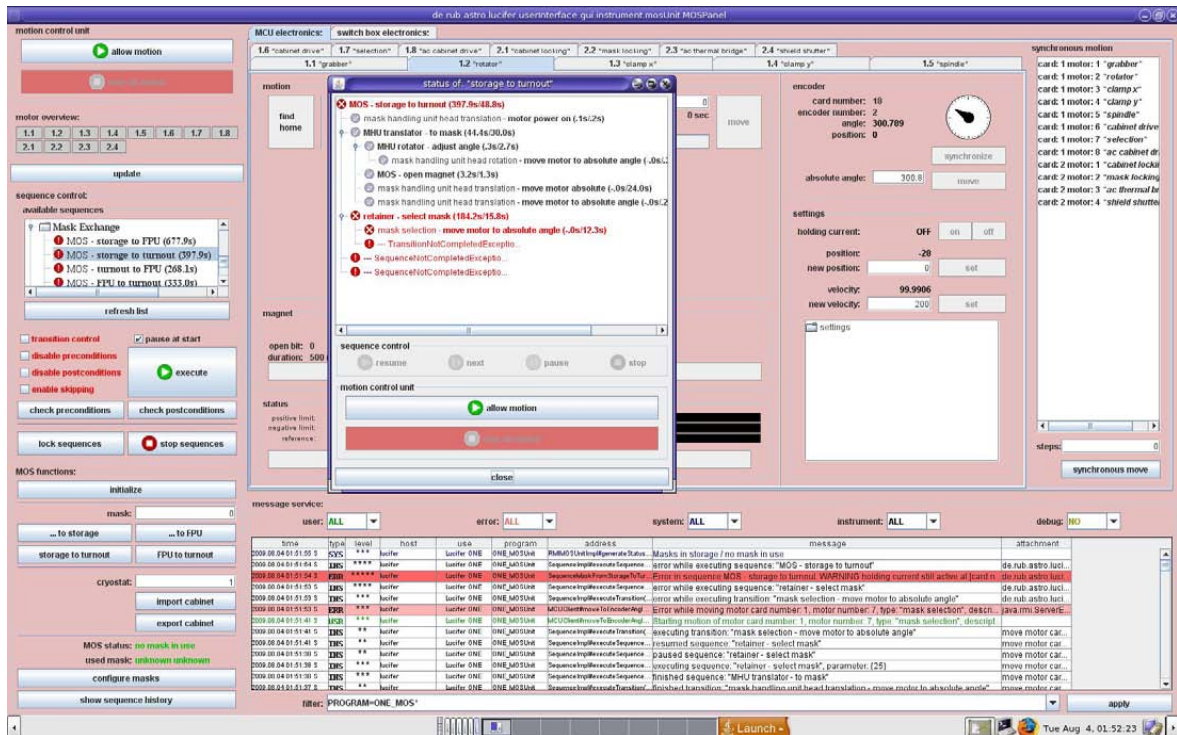


Figure 3.3.: The MOS Engineering GUI during error recovery. The main panel is visible in the background. The sequence-selection, -modification, and -parameter controls are on the left. An array of indicator lights shows when a motor is running. On its right, the motors and switches can be controlled and checked in individual panels. The latest entries from the system log are displayed on the bottom. In the foreground, a sequence tree window shows the progress of a running sequence and indicates in red that (and where) the sequence has just stopped. The system log shows the corresponding error(s) in the red lines.

(not) to run depending on the current instrument state. A state-transition model is used to guarantee a reliable transport of the masks. Only if a defined state has been reached the next sequence is called. Although some sequences could be carried out in parallel, as they do not interfere with each other, we have decided to carry out only one transition at a time. This extends the time for a set of sequences to finish, but lab-tests have shown that this greatly simplifies auto- and manual-recovery in case of errors.

Sequences are created 'on the fly' from their basic 'receipt' depending on the current state of the unit, the desired end-state and conditions encountered during execution. To keep track of how a sequence was executed and e.g. what subsequences were used and whether error-corrections were carried out, a sequence tree is created during sequence execution. This sequence-tree is a graphical log of the sequence "as executed".

### 3.4. Main function sequences

---

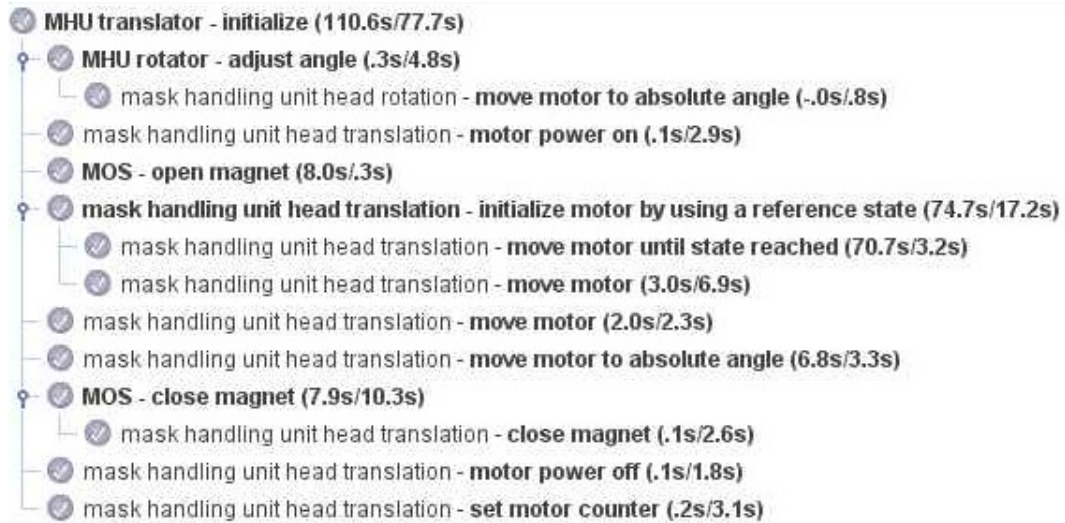


Figure 3.4.: A successfully completed sequence in sequence-tree view in the software.

The sequence for initializing the MHU translator is shown. Sequences (and sub sequences) are written in bold. The top line lists the name of the over all sequence, here 'MHU translator - initialize'. Next to it (and all other (sub)steps) the actual execution time and the maximum execution time (including possible error correction motions) are recorded. A branch extends downward from the first entry, i.e. the timeline is from top to bottom. In the second line, a branch extends to the right. This is the first subsequence of the over all sequence (here: 'MHU-rotator - adjust angle'). It has a child (line 3) which records the actual motor movement. Several other transitions and sub sequences are recorded along the main branch. All were carried out successfully as the gray tick mark denotes.

Figure 3.4 shows such a sequence tree, in this case a successfully executed MHU-translator initialization sequence. If a sequence stops due to an error, a tree like this can be used to locate the error (cf. figure 3.3).

### 3.4. Main function sequences

The MOS-unit functions are executed using essentially four top-level control sequences:

1. 'Storage to FPU' takes a mask from the mask storage cabinet, transports it to the FPU and locks it in the FPU
2. 'FPU to Storage' unlocks the masks and transports the mask back from the FPU to its storage slot in the mask storage cabinet

3. 'Cabinet to LUCIFER' transfers a mask storage cabinet from an attached auxiliary cryostat to the LUCIFER main cryostat
4. 'Cabinet to AUX' transfers a mask storage cabinet from the main instrument cryostat to an attached auxiliary cryostat

Three additional sequences are used for preparing the MOS-acquisition and for temporal removal of a mask from the FPU. All three are sub-sequences of the first two sequences listed above:

1. 'Storage to turnout' takes the mask out of the mask storage cabinet and transports it to the FPU insertion point but stops without insertion.
2. 'FPU to turnout' takes the mask temporarily out of the FPU and holds it outside the telescope field of view, normally for checking the pointing of the telescope
3. 'turnout to FPU' reinserts the mask into the FPU

### 3.4.1. Mask exchange sequence details

In this section we describe one of the developed mask exchange sequences in more detail. We use the 'Storage to FPU' sequence in this example. Figure 3.5 and 3.7 show the corresponding sequence tree and 3.8 shows this sequence in six snapshots (see caption for details).

We start out when there is no mask inside the FPU and all masks are in their respective slot in the mask cabinet. In the first step the user/observer selects a mask number and 'FPU' as the desired end position from the user GUI and commits the new instrument configuration.

The instrument manager service now calls the sequence server of the MOS unit, passing the two parameters (i.e. mask number and desired location) that the user provided. The sequence server starts to execute the sequence 'Storage-to-FPU' since no mask is in use. The first step in the sequence is the pre-condition check. Amongst diverse other items it is checked if the MHU-translator unit is initialized and if the FPU is empty. After the successful pre-condition check, the actual sequence starts to run.

'Storage-to-FPU' is divided in two big sub-sequences, 'MOS - storage to turnout' (cf. figure 3.5) and 'MOS - turnout to FPU' (cf. figure 3.7).

The first sub-sequence of 'MOS - storage to turnout' is 'Translator to mask'. It is called to move the robot to the selected mask using the translation drive. Being a sequence itself,

### 3.4. Main function sequences

---

this sequence has a pre- (and post-) condition. This pre-condition checks if the motion is allowed at all and if e.g., the robot head is in the correct rotation position to move along the cabinet. Subsequently it powers up the motor, opens the lock and moves the robot to the mask. The movement itself is an atomic transition 'move motor to absolute' that drives the translator stepper motor the calculated number of steps that are needed to reach the mask's absolute position which was read from a lookup table. After that, the stepper motor is turned to ball screw angle that is associated with the mask, 'move motor to absolute angle'.

After the motion has finished, we check in the post-condition if the measured steps (using the incremental angular encoder) correspond to the commanded steps, i.e. the motion was ok without the motion being blocked. If a small deviation is present (like that the target translator ballscrew angle is off), we check if the value is within in the set tolerance interval. If it is not, an auto correction is called and the position checked again.

This scheme of checking pre- and postconditions applies to all the next sub-sequences. For simplicity we omit the description of every condition check hereafter. If the mask position has been reached and the post-condition is fulfilled, the next sub sequence is called.

While the retainer is still closed and the masks are locked, the retainer index shaft now rotates to the angle corresponding to the selected mask ('retainer - select mask').

Next, the rotation head holding current is activated ('motor power on') so the rotation head does not move by accident (or because e.g. the gravity vector changes) and the grabber grabs the mask ('MHU picker arms - grab mask').

The grabber-motion is carried out according to a motor-step-lookup table that holds an array of motor steps and is run 'until state reached' (the state here being 'the limit switch is hit'). The first array entry holds a number of motor steps which is normally sufficient to reach the limit switch. The next entries are fewer motor steps (motion correction steps). These entries are only executed if the motion is not complete after the steps from the first entry have been executed.

The motion stops as soon as the state has been reached (the limit switch is hit) whether or not all array entries have been used. In case the limit switch has not been reached by the time all the lookup table entries (i.e ) have been executed, the sequence aborts. The error would then cascade to the top level and the whole Storage-to-FPU sequence would abort. The strain gauges are read to check if the mask was properly grabbed (post condition). In our example, the grabber has successfully grabbed and thus the sequence continues.

The retainer drive shaft now rotates to 'unlocked' position ('retainer - unlock mask(s)'). This moves the selected mask's locking arm backwards, unlocking the mask and leaving all other masks still locked. At this point the mask is held by the grabber but otherwise free and can be moved.

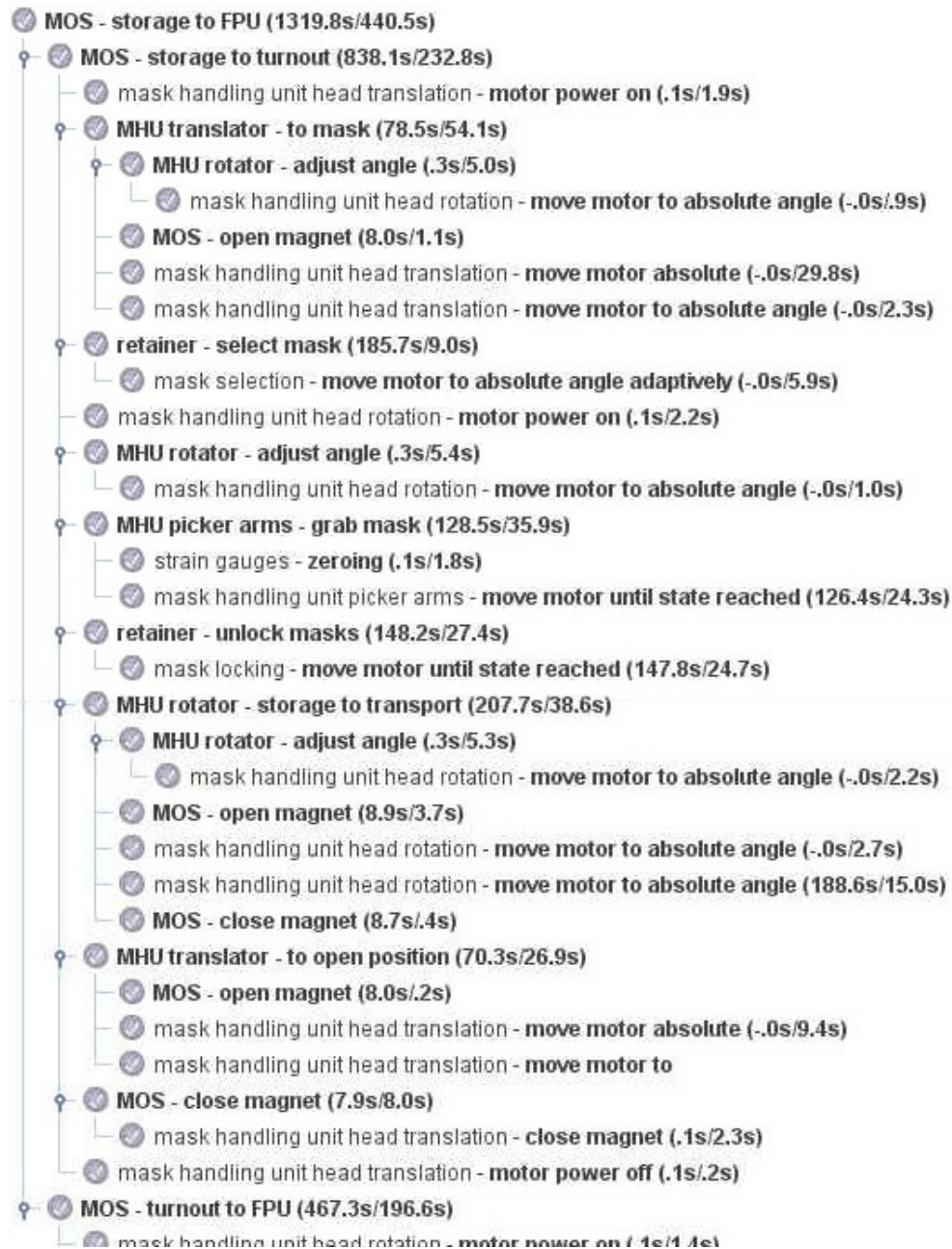


Figure 3.5.: First part of the Storage-to-FPU Sequence until 'Turnout'. The rest of the sequence from 'Turnout to FPU' is shown in figure 3.7

Next the mask is rotated ('MHU rotator - storage to transport') from the storage angle out of the storage cabinet into an extraction test position only 2 degrees away to check if the rotator motion is ok, and after that the rotator moves on to the transport position (cf. figure 3.6). The holding current is still on for the rotator as we need to make sure that the mask stays in this position when we move along the cabinet in the next sub sequence.

### 3.4. Main function sequences

---

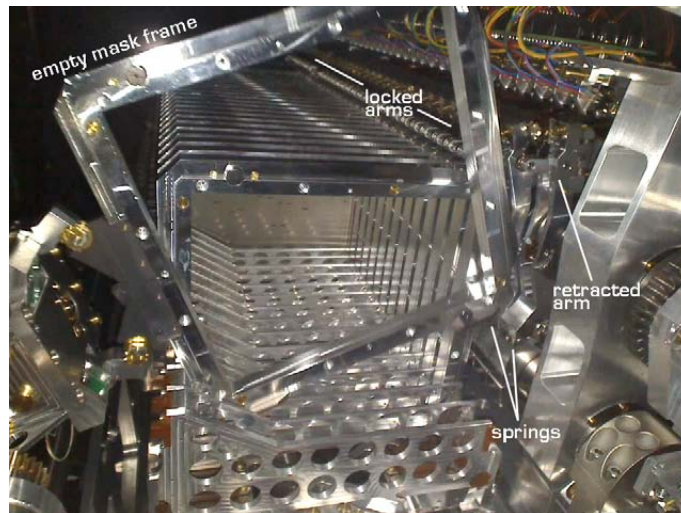


Figure 3.6.: The MHU takes a mask frame out of the cabinet. On the right: The corresponding arm of the retainer is retracted, all others stay locked.

The MHU moves now towards the FPU ('MHU translator - to open position') and it stops at the FPU's 'open' position. With this step, the first big subsequence ('MOS - storage to turnout', cf. figure 3.5) is complete and we jump to the second big subsequence 'MOS - turnout to FPU' (cf. figure 3.7).

At first we check the pre-condition of 'MOS - turnout to FPU', i.e. we test if the FPU is ready to receive the mask (and starting an auto correction if it is not). After that the MHU rotator rotates the MHU-head with the grabbed mask to the FPU rotator angle ('MHU rotator - transport to FPU', 'move motor to absolute angle'). Magnets inside the mask frame activate the reed contacts insider the FPU which indicate the presence of a mask inside the FPU in open position once the rotation has been successfully completed.

The MHU translator now moves the robot (and thus the grabbed mask) forward in the direction of the focal plane into the 'hold' position ('MHU translator - to hold position'). When the mask has reached the 'hold' position and the mask is in light contact with two spring loaded pads located to the left and right of each centering pin, the reed contacts switch to 'off' and indicate that the mask is in hold position.

Now the two FPU clamp arms move until their spring loaded tips hold down the mask from the other side ('FPU - open to hold'). If the motion is completed successfully, micro switches are now actuated and indicate that the FPU arms are 'hold' position.

Then the MHU grabber releases the mask ('MHU picker arms - release mask'). The grabber moves 'until state reached' just reversing the grabbing motion as described above.

The holding current of the rotator is switched off ('Motor power off'). Finally, the FPU clamps close completely ('FPU - hold to locked'), pushing the spring-loaded pads completely into the FPU base plate. The reed-contacts and clamp-arm limit switches are checked to see if the mask is in its final locked position.

Upon successful completion the MOS subsystem signals the high level software that the motion has completed successfully. The user/observer can now use the mask as desired. Putting the mask back to its storage slot follows a very similar sequence in reverse, pre-and post conditions are slightly different.

Figure 3.8 shows six snapshots from the Storage-to-FPU sequence.



Figure 3.7.: Second part of the Storage-to-FPU Sequence from 'Turnout' to 'FPU'. The beginning of the sequence from 'Storage' to 'Turnout' is shown in figure 3.5

### 3.4. Main function sequences

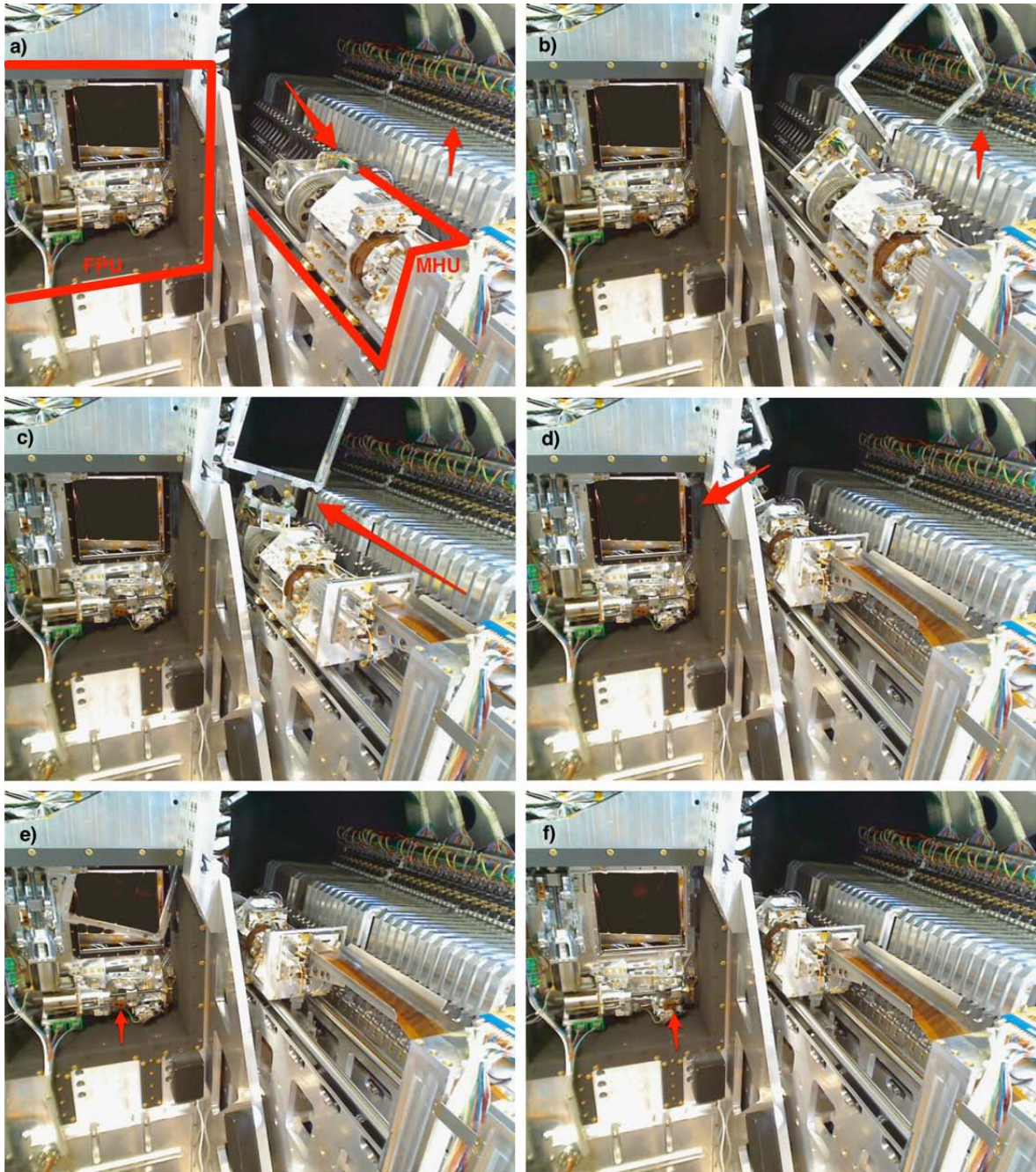


Figure 3.8.: Storage-to-FPU in 6 Snapshots:

a) The grabber (left arrow) is grabbing the mask, the mask's retainer arm (right arrow) is still locking the mask. b) The rotator rotates the mask out of the cabinet, the retainer arm is open (arrow) c) The MHU robot moves in arrow direction along the cabinet towards the FPU on the left. Along the way the mask is held up in 'transport' position d) The rotator rotates the mask into the FPU (arrow). e) The mask is nearing its FPU position, the FPU clamp arm drive is in 'open' position (arrow). f) The mask is in its final place in the focal plane. The clamp arm drive is in 'locked' position (arrow).

## **3.5. Auto correction and recovery sequences**

Auto correction and recovery sequences were added to the control system during the thesis work. Extensive tests in the lab showed that the unit needs much more flexibility in its motions than originally anticipated. E.g. the forces and torques from a changing gravity vector change the three position angles of the MHU-rotator by several tenths of a degree. In this situation a static lookup table would be useless.

Auto correction and recovery sequences are triggered by pre- and post conditions. Each motion sequence has a set of pre- and post-conditions which need to be fulfilled before or after the movement. Higher level sequences can have additional conditions. If these conditions are not met, motion correction sequences are called. The kind of correction depends on the high level sequence and the involved movement. In the case of rotating motions, for example, a target angle must be reached within a given tolerance ('target interval') to fulfill the post-condition. If only a larger pre-defined interval is reached, a correction motion sequence is called. If the larger 'correction possible' interval is not reached after the initial motion, the (sub)sequence is either aborted or the motion is reversed to get to the starting point.

Pre- and postconditions can be disabled manually for debugging. This can be useful for example when a position switch is known to be faulty but the motion cannot start without it being present.

### **3.5.1. Correcting motions**

Corrections are done by either commanding the same target position, i.e. a motion retry, or by running specialized debug sequences. As mentioned above different instrument positions (rotation and tilt) result in changing torques and force vectors on the various components of the MOS unit. Therefore it can be necessary to call different correction sequences. However, if condition-exceptions are encountered that could be caused by a critical instrument state and continuing the motion could result in permanent damage, the unit is stopped. A manual inspection of the MOS unit state is necessary if such a stop occurs to determine the best debug strategy. All auto correction motions are limited in their number of attempts and call for human intervention if the motion could not be completed successfully after the defined number of retries/attempts.

#### **Translator position correction**

As explained in section 2.4.3, positioning of the translator is done by commanding motor steps to the translator drive. The translator position is checked by comparing the commanded steps with the measured steps (i.e. travelled distance) that is calculated from the angular and incremental encoder signal. It became obvious during extended tests that this positioning scheme is not sufficient. The new developed positioning scheme is two fold. First, we move the robot to the desired position by moving a certain number motor steps. A lookup table holds the absolute steps measured from the init (zero) point for each translator position (all 33 mask storage places, FPU positions, other important positions) along with their corresponding spindle angles (modulus of  $2\pi$ ). The needed number of motor steps are the difference between the current position count and the target position count. If, after moving the calculated number of steps, the spindle angle corresponds to the angle stored in the LUT within a tolerance, the motion sequence stops. If not, the nominal angle is commanded and the translator drive rotates to this angle. The check and correction is repeated 3 times. Small step-losses can be reliably corrected with this motion scheme.

In some orientations of the MOS the translator position for grabbing a mask and the translator position for extracting the mask from the storage cabinet (rotating it to the transport position) are *not* the same. An adaptive motion has been developed for flexibility and to avoid lengthy lookup tables.

At first the mask is rotated to a test angle after the mask has been grabbed and the retainer has un-blocked the mask. The motion continues to transport position if this test extraction angle is reached. If the extraction test angle has not been reached, something is blocking the motion; in all practical cases the translator position is off where it should be. The translator position is then varied in a back and forth motion inside a given interval. A retry to rotate the mask to the test angle is done after each new translator position. If the boundaries of the interval are reached before the mask could be successfully extracted, the sequence stops, producing an error state.

#### **Rotator position correction**

The two gear wheels of the rotator drive are mounted twisted in respect to each other to avoid backlash in the rotating motion. Because of flexure in the rotation head and the robots body, it can occur, that the target angle for transport and the FPU angle are not reached in one go. Normally these positions are exactly defined by the target angle and in most cases one retry is sufficient. It can happen though, that the reached position is close to the target angle, but that flexure changes the position of the stepper motor axle in a way that commanding less than 5 motor-steps is not causing any motion. In this case the correcting sequence first moves farer away from the target position (into the direction the motion originated from) and does a retry using more steps.

### Other motors

We have found that stepper motors and drivetrains which have not been used for a long time in the cold tend to fail in the first motion. This is for example the case for the cabinet lock. The motion is commanded as 'move to limit switch' and the lookup table for the stepper motor steps contains a back-and-forth motion as the first entries.

The retainer drive has a similar lookup table that produces a back and forth motion if the limit switch has not been reached in the first go.

For the retainer selection motor an adaptive sequence was developed which analyzes the reached and nominal motion, compares with the previous motions and chooses the best strategy 'retry or move backwards and forward' according to the debug history so far. This enables to use the motor even if one turning direction fails, since the motion can be carried out clock- or counterclockwise.

### 3.5.2. Error recovery

The control software builds up an execution tree while executing a sequence or a collection of sequences to facilitate debugging. The tree contains all the completed, failed, and not completed steps. The reason why a sequence was stopped is explained. Additional debugging information for the system engineer is written to a detailed log file that also contains info on reached angles or positions if necessary. Also the complete communication between the instrument server and the MCU can be logged. The log file can be accessed via a specialized web interface which allows to search for events according to type, date, subunit, sequences, running processes and others. Also standard SQL-queries are allowed.

The initialization routine is adaptive in the sense that it produces an initialized state from which the unit can be restarted from the user panel. This one-button-auto-recovery is still under development.

### 3.5.3. Motion pausing and skipping

The sequence execution tree allows to pause sequences and also to run step-wise in order to test new parameter sets after hardware modifications. This is mostly needed during debugging, when single sequence steps are to be checked for errors. Pausing can happen on two levels. On sequence level the whole (sub)sequence is paused or continued. On the 'atomic' transition level all transitions, including the activation of holding currents, has to be acknowledged by the engineer.

### 3.5. Auto correction and recovery sequences

---

With the help of skipping, paused sequences or sequences that got interrupted by an error condition can be recovered and continued after the error has been corrected. To do so all steps are replayed and the current status of the instrument is checked against pre- and postconditions. When a matching state is found, the sequence is carried on from that point. Skipping, however, only works up to a sequence level. Additional conditions imposed by super sequences cannot be checked in this recovery scheme. Thus skipping is not a general cure-all debugging tool.

## Chapter 4.

# Design of two high performance gratings for LUCIFER

In this chapter we present the design and testing of two additional reflection gratings for LUCIFER that was done as a part of this thesis.

The need for additional gratings arose from the first science program planning in 2007, when it quickly became clear that the one existing grating of the instrument may not serve a large fraction of our groups interests in the near and middle future - especially since AO assisted observations would not be available from the start of LUCIFER operations and the availability of the laser guide star facility was scheduled for 2013+.

### 4.1. Existing grating

Grating 1 (the only existing grating for LUCIFER in 2007) is an aluminum substrate replica grating with 210 lines/mm blazed at 5.0 micron in 1st order,  $\Theta_{\text{Blaze}} = 31.7^\circ$ . It is identical to the grating used in the ISAAC instrument (Moorwood et al. 1998) on VLT UT1. It is used in 2nd, 3rd, 4th and 5th order for K, H, J and z band respectively. In seeing limited observing mode using a  $0.5''$  wide entrance slit, the grating provides a Nyquist sampled 2-pixel slit resolution of  $\sim 6600$ - $8400$  in J to K.

Figure 4.1 shows the calculated efficiency for grating No. 1 in the different orders. The calculation was done in Littrow configuration. In LUCIFER the efficiency is about 10-15% less because the grating is not mounted in Littrow configuration. The grating is available from Newport, Type: MR 35 53 \* 877.

## 4.2. Requirements on the new gratings

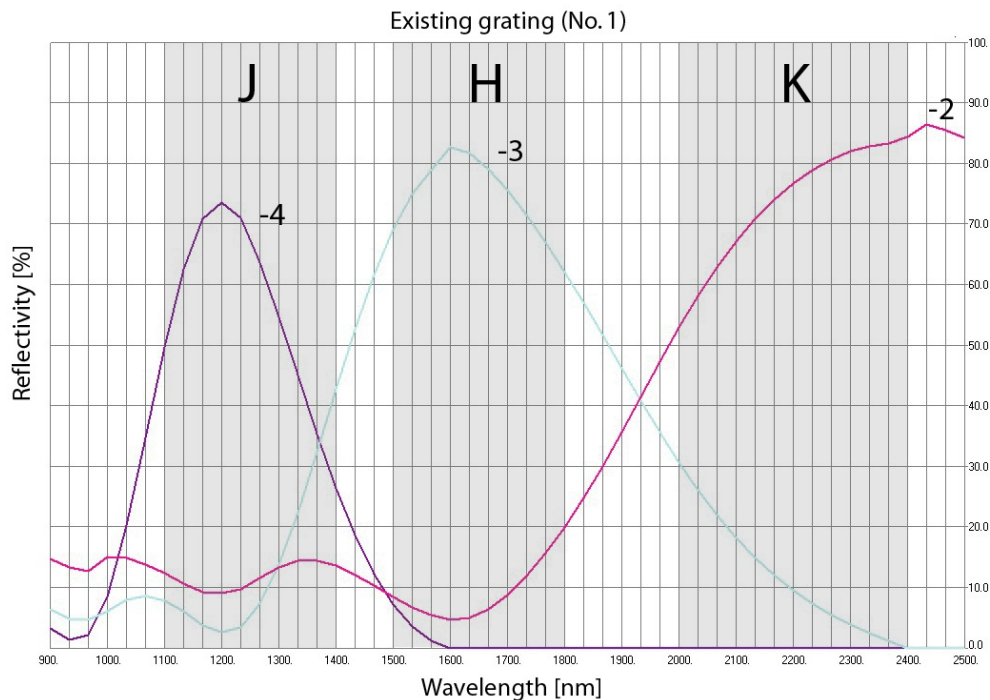


Figure 4.1.: Calculated reflectivity for the zJHK grating from 1800nm – 2500nm. The incident radiation is unpolarized. Shown are the reflectivity in -2nd to -4th order. Because it serves all three bands with different orders, it cannot deliver optimum performance in all bands.

## 4.2. Requirements on the new gratings

### 4.2.1. Scientific requirements

Especially from the ongoing SINS project in our group (Förster Schreiber et al. 2009), the near infrared survey of high redshift galaxies with SINFONI at the VLT, various requirements for the spectroscopic observation mode could be identified, e.g. the possibility of doing H+K survey type observations, the need for high performance in the  $K_s$  band, and low to moderate spectral resolution ( $R \sim$  a few thousands) in AO mode. These requirement could not be met by the existing grating. In detail the science requirements were:

- longslit and MOS spectroscopy at a resolution suitable for OH Line avoidance ( $R \sim 4000$ ) in seeing limited mode using a suitable slit width (i.e. 0.5-1.0 arcsec projected slit width on sky)
- enable 'survey type' or SINFONI-follow-up observations on a larger sample of galaxies using the MOS mode. For this no full OH-Line resolution is needed but more

emphasis on a wider wavelength coverage (H+K simultaneously) combined with the use of the fast  $f/1.8$  camera optics.

- get a high throughput ( $>70\%$  grating reflectivity) in the full  $K_s$  band, needed for high redshift observations, since the thermal background limits the use of the long end of the K-band
- provide better K band coverage in the intermediate pixel scale ( $f/3.75$  camera)
- use the  $f/3.75$  camera for AO-assisted observations (i.e. using a  $0.25''$  slit together with the  $f/3.75$  camera) at an intermediate resolution around  $R\sim 4000$  (and not at  $R\sim 10.000$  as for the existing grating no. 1)
- possibly support the use of drop-out technique for Ly- $\alpha$  beak galaxies at  $z\sim 5-7$  (i.e. z-band coverage).

#### 4.2.2. Technical requirements and constraints

From the existing optical and mechanical design of the telescope and the instrument some dimensions are fixed. These are listed in table 4.1 and 4.2. Central wavelength selection is done by slightly turning the gratings in their mount using linear coil actuators.

Table 4.1.: Technical requirements for the gratings

Wavefront	0.10 RMS @ 6328 Å with a goal of achieving 0.20 PV
Roughness	< 5nm RMS
Ruled Area	110x100mm
Free Aperture	105mm
Coating	Chrome bonded Gold
Grove alignment	parallel to reference surface +/- 2arcmin
Replica Substrate	6061-T6 AL
Operating temp.	-196°C, i.e. 77K
Storage temp.	+20°C, i.e. 293K

Table 4.2.: Optical specifications affecting the design

Detector size	2048pixel, $18\mu\text{m}$
Angle incident-emergent beam	35deg
Camera focal length	180 or 375mm
Slitwidth	$0.5''$ or $0.25''$
Collimator beam size	102mm
Collimator focal length	1500mm
Telescope focal length	123420mm

## 4.3. Design process

### 4.3.1. Optical principles

A diffraction grating is essentially a periodic structure that diffracts light into several beams propagating under different angles to the incident beam. The diffraction angles depend on the spacing of the periodic structure of the grating ('grooves') and the wavelength of the incident light. Gratings can be either transparent or reflective. Their periodic structure can for example be formed from parallel aligned grooves that have been machined onto a substrate or even consist just of periodic density variations of the crystal lattice in a transparent material (e.g. holographic gratings).

Fraunhofer's diffraction grating equation describes the relation between the wavelength  $\lambda$ , spacing of the grooves or the periodic structure  $d$ , and the angle of incident ( $\alpha$ ) and diffracted ( $\beta$ ) light, measured relative to the grating normal.

$$n\lambda = d(\sin \alpha + \sin \beta) \quad (4.1)$$

where  $n$  is an integer, the order number. If the incident light is collimated,  $\alpha$  is constant, while  $\beta$  is wavelength dependent. For practical reasons it is important to realize that the orders overlap increasingly with higher order  $n$ . If  $\alpha$  remains constant, then  $\beta$  is the same for  $\lambda_1 = 2\lambda_2 = 3\lambda_3 = \dots$

The intensity of the outgoing light can be calculated as

$$I = \frac{\sin^2 N\Phi \sin^2 \Psi}{\sin^2 \Phi \Psi^2} \quad (4.2)$$

(e.g. Jenkins and White 1976) where  $\Phi$  is the phase difference between adjacent grooves and  $\Psi$  is the phase difference between the edge and the center of one groove. The second term, the diffraction term, modulates the interference term, the first term. The envelope peaks in zero diffraction order. In astrophysical applications, where the incident light is already rather dim, it would be desirable not to put most of the light into zero order but rather to peak the intensity at some useful low order. This can be realized by *blazing* the grating. Blazing means creating the grating surface as periodic inclined facets, tilted to the grating normal at the blaze angle  $\Theta_B$  common for all facets such that  $\alpha + \beta = 2\Theta_B$ . In a real spectrograph the angle  $\gamma$  between the collimator axis and the camera axis is normally fixed and  $\gamma = \alpha - \beta$ . When the Grating is mounted in the optical path in Littrow condition ( $\gamma = 0$ ), i.e. in and outgoing light have the same angle to the grating normal, one can define the Littrow angle  $\Theta$  as a small deviation from this arrangement ( $\alpha \approx \beta$ ), and write  $\alpha = \Theta_B + \Theta$  and  $\beta = \Theta_B - \Theta$ . The peak of the blaze profile in a given order  $n$  is at  $\lambda_B(n = 1)/n$  and the width of the profile scales with  $1/n$  (Foy 2005). For the blaze condition where  $\lambda = \lambda_B$  the grating equation becomes

$$n\lambda_B = 2d \sin \Theta_B \cos \Theta = 2d \sin \Theta_B \cos(\gamma/2) \quad (4.3)$$

or for small  $\Theta$

$$n\lambda_B \approx 2d \sin \Theta_B. \quad (4.4)$$

Equation 4.2 uses a simplified diffraction model where  $d > \lambda$ . For the case where  $d \approx \lambda$  polarization and resonance effects complicate the situation. In the simple model the efficiency drops to 40% of the peak blaze value at  $\lambda_{\pm} = (2n\lambda_B)/(2n \mp 1)$  leading to a useful wavelength range of  $\lambda_+ - \lambda_- \approx \lambda_B/n$ . (Palmer and Loewen 2000; Foy 2005). For some wavelengths, however, the intensity can drop or rise sharply, while generally it only varies slowly with wavelength. This was first observed by R.W. Wood, 1902 and is due to Rayleigh and resonance anomalies. While Rayleigh anomalies are somewhat subtle, resonance anomalies are easily seen in efficiency calculations. They are caused by surface excitation effects (surface plasmon resonance, SPR) (Ritchie et al. 1968). Under certain conditions charge density oscillations can occur at the interface of an dielectric and a metal (here e.g. a gold coated epoxy replica grating). These oscillations transport energy away from the incident beam, lowering the diffraction intensity. The resonance condition is met by a specific combination of wavelength and incidence angles for a given groove profile and refractive index, and the effect is visible as a sharp drop in intensity in the efficiency vs. wavelength curve.

For the angular dispersion of the outgoing light ( $d\beta/d\lambda$ ), differentiating the grating equation leads to

$$\frac{d\beta}{d\lambda} = \frac{n}{d \cos \beta} \quad (4.5)$$

$$= \frac{\sin \alpha + \sin \beta}{\lambda \cos \beta} \quad (4.6)$$

$$\approx \frac{2 \tan \Theta_B}{\lambda}, \quad (4.7)$$

independent of the spacing of the grooves. The reason why a finer groove spacing is usually associated with a higher dispersion is, that a finer spacing will get a higher dispersion in the *same diffraction order* for a given  $\lambda$  and  $\beta$ .

The linear dispersion ( $dx/d\lambda$ ) measured on the surface of the detector in dispersion direction is

$$\frac{dx}{d\lambda} = \frac{nf_{\text{Cam}}}{d \cos \beta} \quad (4.8)$$

$$\approx \frac{2f_{\text{Cam}} \tan \Theta_B}{\lambda}, \quad (4.9)$$

where  $f_{\text{Cam}}$  is the focal length of the camera optics.

Another important characteristic of a spectrograph is the spectral resolution. For astronomical applications a high resolution can lead to long exposure times for faint objects,

### 4.3. Design process

---

while a too low resolution blends lines and makes it impossible to discern OH lines caused by the atmosphere in the NIR bands. The theoretical diffraction limited slit resolution is defined as

$$R_{\text{diff}} = \frac{mN}{\Delta} \left( \frac{\lambda}{D} \right) \quad (4.10)$$

where  $N$  is the number of grating lines (i.e grooves),  $m$  is the used order of the grating,  $\Delta$  is the slit width and  $\lambda/D$  the diffraction limit.

Using more readily available instrument and telescope parameters one can calculate the slit-limited resolution as follows: The projected width  $w'$  of the slit width  $w$  on the detector, taking the anamorphic magnification introduced by the grating into account, is

$$w' = w \frac{f_{\text{Cam}} D_{\text{Coll}}}{D_{\text{Cam}} f_{\text{Coll}}} = w \frac{f_{\text{Cam}} D_{\text{Tel}}}{D_{\text{Cam}} f_{\text{Tel}}} \quad (4.11)$$

with  $f_{\text{Coll}}, f_{\text{Cam}}$  the focal length of the collimator and camera and their diameters  $D_{\text{Coll}}$  and  $D_{\text{Cam}}$  the diameter of the telescope and camera beam. The spectral resolution is

$$\delta\lambda = \frac{d\lambda}{dx} w' = \frac{d \cos \beta}{n} \frac{D_{\text{Tel}}}{f_{\text{Tel}} D_{\text{Cam}}} w \quad (4.12)$$

$$= \frac{wd}{F_{\text{Tel}} W n} \quad (4.13)$$

With  $F_{\text{Tel}}$ , the telescope focal ratio and  $W = D_{\text{Cam}} / \cos \beta$ . The Resolving power  $R$ , is then:

$$R := \frac{\lambda}{\delta\lambda} = \frac{n\lambda F_{\text{Tel}} W}{dw} \quad (4.14)$$

$$= \frac{n\lambda W}{d\theta_s D_{\text{Tel}}} \quad (4.15)$$

where  $\theta_s$  is the angular slitwidth. If one takes the slit width on the detector  $w' = \theta_s f_{\text{eff}}$  where  $f_{\text{eff}} = f_{\text{Cam}} D_{\text{Tel}} / D_{\text{Coll}}$  in quasi Littrow mode (i.e incident and reflected beam are nearly in the same direction) and where the linear dispersion is given as  $2f_{\text{Cam}} \tan \Theta_B / \lambda$ , the slit-limited resolution is

$$R = \frac{2 \tan \Theta_B D_{\text{Coll}}}{\lambda \theta_s D_{\text{Tel}}} \quad (4.16)$$

$$= \frac{\tan \Theta_B}{41.2 \lambda \theta_s} \quad (4.17)$$

for LUCIFER at the LBT.

### 4.3.2. Grating simulations

A successful grating design requires the simulation of the effective reflectivity of the grating for the used wavebands for different grating orders. In this work the software 'PCGrate' was used for these simulations. The software calculates the efficiency of a reflexion grating in different orders and for S- and P-Polarization. The surface groove profile can be set arbitrarily (and thus the blaze angle), various coatings can be loaded. For the LUCIFER gratings the surface is a sawtooth profile with a 90deg angle at the tooth tip. For the calculations a Chrome linked Gold coating was assumed on a Aluminum substrate.

PCGrate can solve for best blaze angle when specifying a reflectivity for a certain wavelength but the various requirements listed made it necessary to optimize blaze and grating constants until all requirements were met.

When specifying the blaze angle it is important to keep the manufacturing process in mind: the maximum attainable accuracy for the blaze angle during the ruling process is only  $\sim 0.1^\circ$ . We therefore calculated the efficiency over an interval of blaze angles and chose the specification value after evaluating peak efficiency versus overall efficiency of the grating within the operating wavelength range. The blaze angle for the Ks grating was e.g. chose such that the blaze peak is not in the center of Ks. As the thermal background rises significantly beyond 2.3 micron, the far tail of the K band is of lower scientific interest. Therefore it makes more sense to set the blaze angle a bit off to ensure the Ks band is adequately covered even in the case the ruled grating does not have the exact specified blaze angle.

### 4.3.3. The designed gratings

The scientific and technical requirements could be met by designing two gratings, each one having a different purpose. Table 4.3 lists the final design specifications for the two gratings.

The H+K grating specifications are calculated primarily for seeing limited (i.e 0.5''slit) observations at a resolution  $\sim 2000$ . However it can also be used as a pure H or K grating in AO-assisted observations (i.e. 0.25''slit) at a resolution  $\sim 4000$ , see below.

The Ks grating was designed to have high reflection efficiency in the Ks band and for use in seeing limited observations (i.e 0.5''slit) observations at a resolution  $\sim 4000$ . It has no dual use. Table 4.4 lists the observation modes for all three gratings.

Figure 4.2 and 4.3 show the calculated reflectivity from  $1.8 \mu\text{m}$  to  $2.5 \mu\text{m}$  for the H+K and the Ks grating respectively. The calculations were done for unpolarized light and an angle of incidence to the grating normal of  $15^\circ$ .

### 4.3. Design process

Table 4.3.: Final specifications for both gratings

Grating No.	Lines/mm	Blaze angle $\Theta_B$	$\lambda_{\text{Blaze}}$
2 'H+K'	200	11.4°	1.97 in 1st order
3 'K <sub>s</sub> '	150	19.5°	4.45 in 1st order

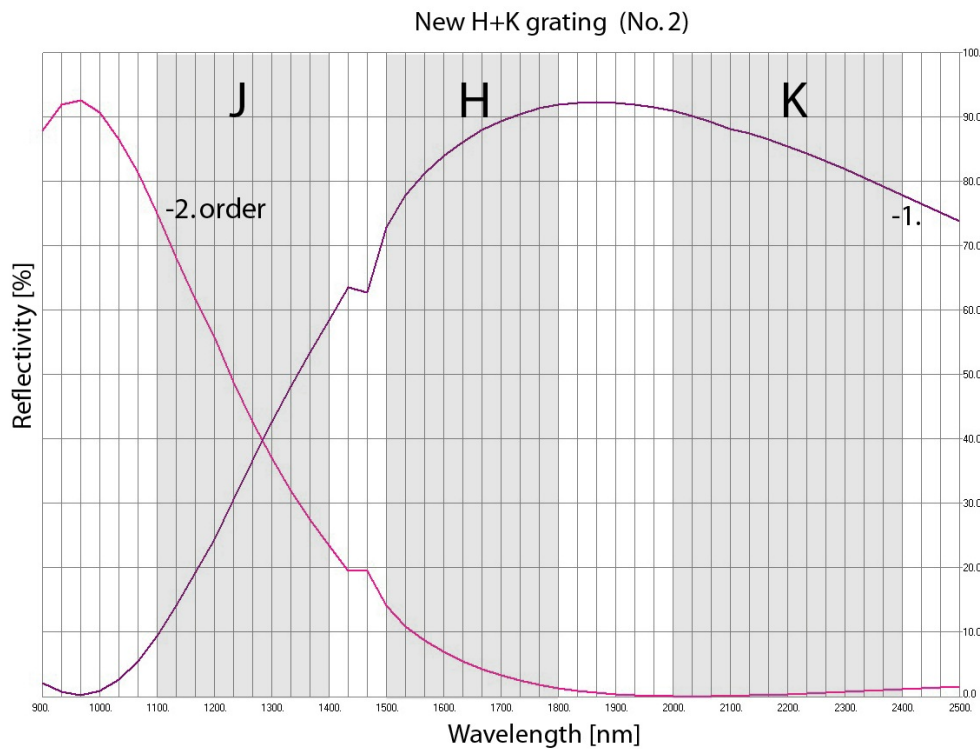


Figure 4.2.: Calculated reflectivity for the H+K grating from 900nm – 2500nm. The incident radiation is unpolarized. Shown are the reflectivity in -1st and -2nd order, assuming an incident angle of 15° to the grating surface normal. The kink in both curves around 1460 nm is a resonance anomaly due to a surface plasmon resonance which is not resolved in the coarse calculation steps. It is actually a dip with almost zero reflectivity.

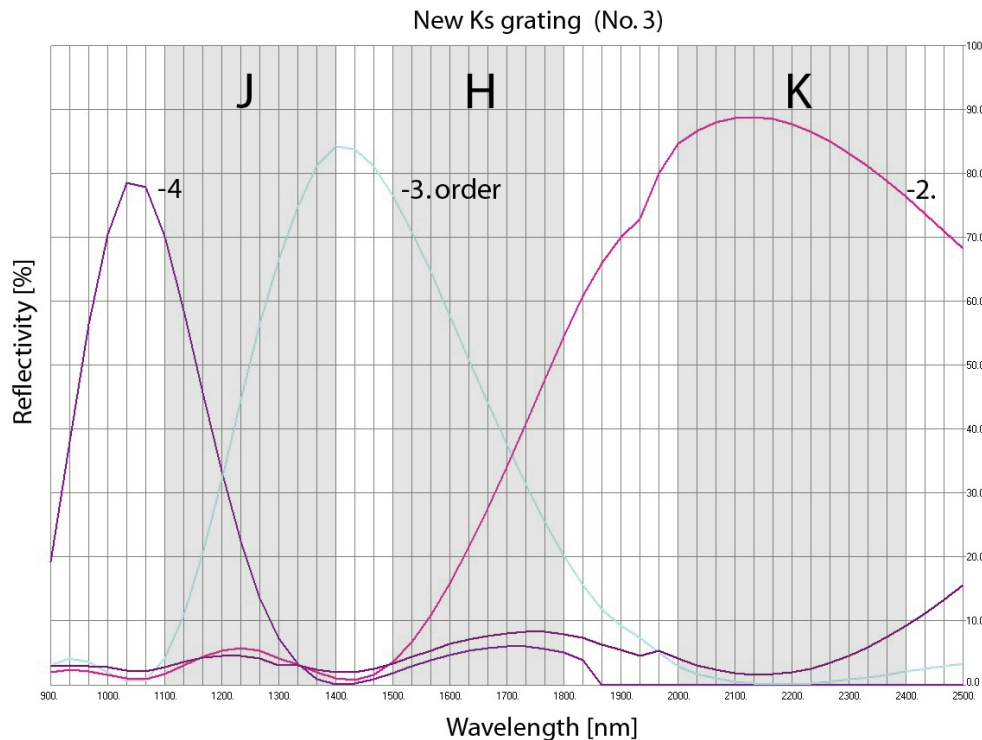


Figure 4.3.: Calculated reflectivity for the Ks grating from 900nm – 2500nm. The incident radiation is unpolarized. Shown are the reflectivity in -2nd, -3rd and -4th order, assuming an incident angle of  $15^\circ$  to the grating surface normal. The grey areas denote the FWHM of the band filters for J, H and K respectively. Note that J and H band are not met by the grating orders. This is a pure K/Ks grating.

### Built-in upgrade path

The new H+K grating, has double use: For AO-assisted observations this grating can be used as an H or K grating to achieve a resolution of  $\sim 4000$  when using the  $f/3.75$  camera in combination with a slitwidth of  $0.25''$  (i.e Nyquist sampled slit). Note that in this mode the wavelength coverage is half of the one in seeing limited  $f/1.8$  camera operations, i.e. either the full H or K band is projected onto the detector. That this 'trick' works at all is due to the design of the cameras: The  $f/1.8$  camera images the  $4' \times 4'$  FOV onto an area that is  $1/4$  of the detector area, centered on the detector (i.e a  $0.5''$  slit is imaged onto two pixel), while the spectrum can extend beyond the FOV and is still recorded by the detector (use with grating 2: spectroscopy of H+K at  $0.5''$  slit at  $R_{\text{slit}} \sim 2000$ ). The  $f/3.75$  camera images the  $4' \times 4'$  FOV on the full detector (i.e. a  $0.25''$  wide slit is imaged onto two pixel). This then reduces the spectral coverage to  $1/2$  of the coverage with the  $f/1.8$  camera (use with grating 2: spectroscopy of H or K at  $0.25''$  slit at  $R_{\text{slit}} \sim 4000$ )

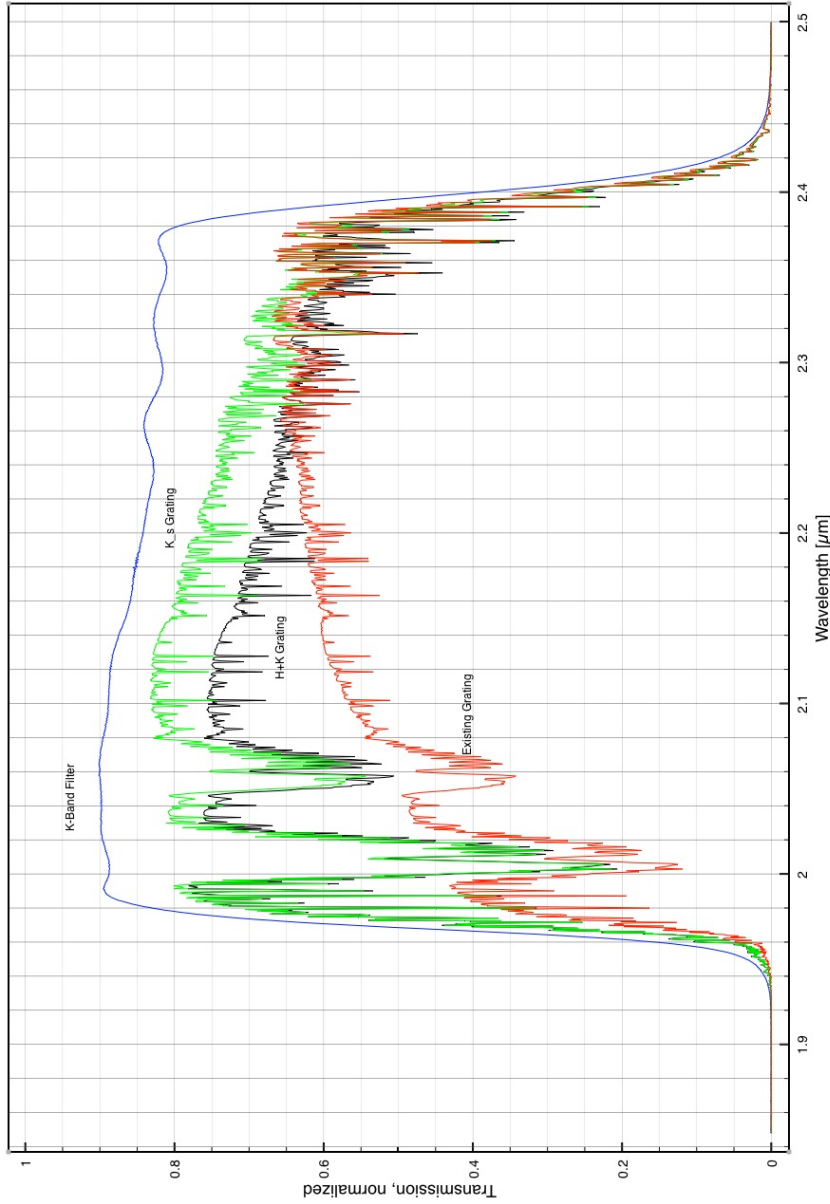


Figure 4.4.: Comparison of calculated K-band efficiency for all three gratings. The K-band filter envelope is shown in blue, the Ks grating in green, H+K in black, and the existing grating in red. The atmospheric transmission was calculated into the grating efficiencies. The advantage of the new K-band gratings can clearly be seen. The dedicated Ks grating is just a few percents more effective than the H+K grating. This however is no design or production failure. It is designed for a different spectral resolution and slit width (see text).

Table 4.4.: Observation modes for the gratings at the two camera configurations

<b>existing Grating '1'</b>		
	f/1.8 camera	f/3.75 camera
arcsec/pixel	0.25	0.12
Nyquist (2 pixel) slit	0.5''	0.25''
Resolution	~5000	~10000
spectral bandwidth	0.22 (J)	0.16(J)
on detector [ $\mu\text{m}$ ]	0.29(H) 0.45 (K)	0.14(H) 0.22(K)
observable bands	J, H, or K	J, H, or K (part)
orders used	-4, -3, -2	-4, -3, -2

<b>new H+K Grating '2'</b>		
	f/1.8 camera	f/3.75 camera
arcsec/pixel	0.25	0.12
Nyquist (2 pixel) slit	0.5''	0.25''
Resolution @ $\lambda_c$	2200(@1.95 $\mu\text{m}$ )	3700(@1.65 $\mu\text{m}$ ), 5100(@2.2 $\mu\text{m}$ )
R over spectr. range	1600–2900	3100–4300, 4400–5700
spectral range	1.45–2.45	1.40–1.89, 1.95–2.44
on detector [ $\mu\text{m}$ ]		
observable bands	H+K(full)	H or K(full)
orders used	-1	-1

<b>new Ks Grating '3'</b>		
	f/1.8 camera	f/3.75 camera
arcsec/pixel	0.25	0.125
Nyquist (2 pixel) slit	0.5''	0.25''
Resolution @ $\lambda_c$	4050(@2.15 $\mu\text{m}$ )	8100(@2.15 $\mu\text{m}$ )
spectral range	1.81–2.49	1.99–2.31
on detector [ $\mu\text{m}$ ]		
observable bands	Ks(full), K(full)	Ks(part), K(part)
orders used	-2	-2

## 4.4. Lab tests

The groove alignment relative to the substrate and the blaze angle were tested directly at the manufacturer. To achieve the correct blaze angle, test sections were ruled and measured. For one replica of each grating type the groove alignment was measured to be out of specs: 3.15arcmin for the Ks grating no.2 and 4.5arcmin for the H+K grating no. 2. However this misalignment is negligible compared to the angular alignment error that can occur when mounting the grating inside the grating mount and was thus of no concern.

A first test of the gratings efficiency was also done at the manufacturer. These measurements could not be carried out successfully since the test equipment was in part not working properly. Tests at the manufacturer were done using one He-Ne gas laser at  $1.15\mu\text{m}$  using different orders of the grating. The efficiency in the first and second order was calculated.

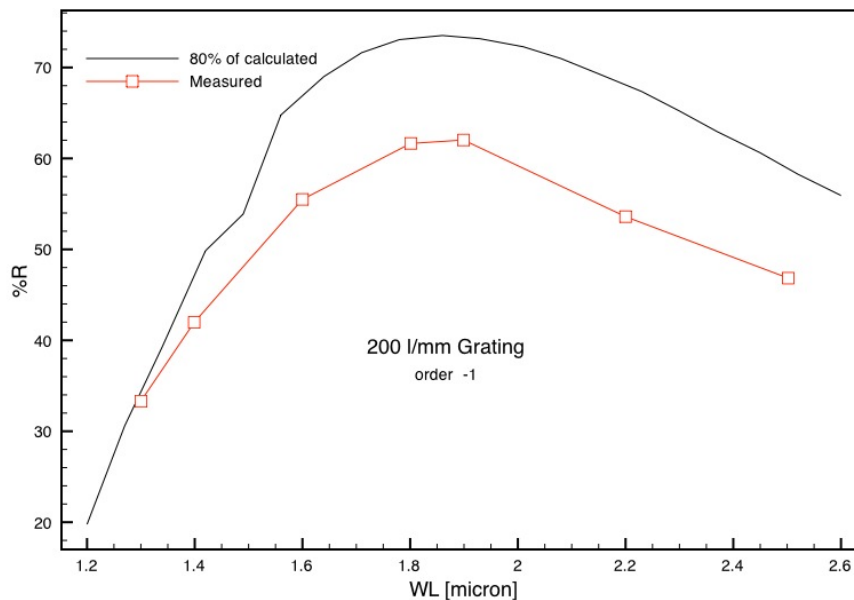


Figure 4.5.: Results from the reflectivity measurements at the manufacturer. Despite the difficulties in measuring the correct absolute flux, the shape of the curve follows the calculated curve quite nicely. Measurements for the 150l/mm Ks grating could not be carried out successfully.

#### 4.4.1. Test setup and measurements

For the tests done at the MPE lab, two lasers were used and efficiencies were directly measured in the first and second order. A He-Ar Gaslaser at  $2.39\mu\text{m}$  and a Thulium Fiber laser at  $1.908\mu\text{m}$  were used as light sources. Their light was single mode filtered and passed through a beam expander to widen the beam size to 10mm truncated by a baffle setup. The light was then directed onto either a gold coated flat mirror or the grating, both exchangeable mounted on a rotation stage. The reflected light was detected using a power meter and a near infrared camera for comparison. The test setup is further explained in figure 4.6. The He-Ar laser was thermally stabilized, the power output did however fluctuate over timescales of minutes and as such a second powermeter was used to monitor the laser output power. The actual measurement was carried out as a relative measurement comparing the reflected intensity from the grating in different orders with the intensity when using a gold-coated flat mirror as a standard.

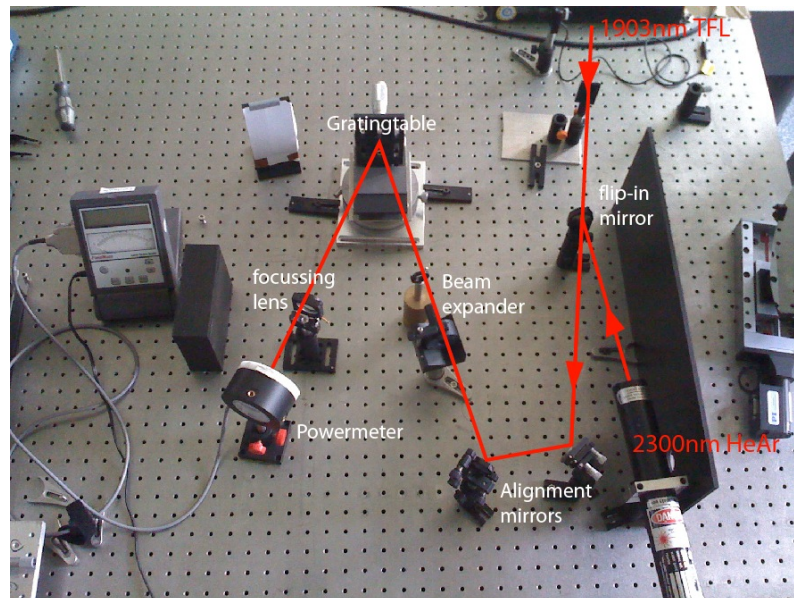


Figure 4.6.: Test setup for the grating efficiency measurements. The 1903nm laser enters from the upper right, the 2300nm He-Ar laser from the lower right. A flip-mirror can be used to inject the one or the other laser into the setup. Two alignment mirrors on the lower right ensure a beam that is in a plane perpendicular to the grating surface. A beam expander widens the beam to about 1cm. The light then falls on the grating. The angle between incident and reflected beam is  $35^\circ$  as in the LUCIFER spectrometer. The grating is mounted on a rotation stage to select the correct order of the reflected beam. A focussing lens focusses the reflected beam onto a power meter. The gold mirror against which the grating reflection efficiency is measured is mounted on the rotation stage instead of the grating.

#### 4.4.2. Grating test results

Table 4.5 shows the results from the reflectivity tests in the lab test setup as well as the measured groove alignment relative to the substrate side surface. For the reflectivity measurements only one grating of each kind was tested. This was because the other set was already mounted into LUCIFER. Since both replica for each grating type were cast from the same master grating each, efficiencies should be comparable. Cosmetics of all four gratings were inspected by eye. No scratches or digs were found on the grating surface.

Table 4.5.: Results of the grating tests

Parameter	Grating Ser.No.				Specification
	200-1	200-2	150-1	150-2	
%R @ 1903nm	91±6%	-( <sup>a</sup> )	77±5%	- <sup>1</sup>	>70%
%R @ 2300nm	73±5%	-( <sup>a</sup> )	-( <sup>b</sup> )	- <sup>1</sup>	>70%
Alignment	2'	4'.5	2'	3'.15	+/- 2arcmin

(<sup>a</sup>) The second replica of each grating was not tested in the lab setup at MPE since those replicas were already integrated into LUCIFER and undergoing cold tests.

(<sup>b</sup>) Too low SNR to get a robust value

The measured values are within the specification. Typically the efficiency of a flat reflection grating replica is ~5-10% lower than the theoretical calculations. For the 150l/mm grating no good measurements could be made. From the one datapoint that could be taken, the efficiency does appear within specs. The overall shape of the reflectivity vs wavelength curve can however not be confirmed by these tests.

## 4.5. On sky tests

The gratings were tested on sky using standard stars. Table 4.6 lists the maximum efficiencies at the denoted peak wavelength for all three gratings. The measured spectral resolution is also listed. It was measured using the f/1.8 camera and a 0.5''slit. The efficiency was calculated by comparing the measured detector counts with the expected number of photons collected by the telescope. The transmission, reflection and quantum efficiency curves of the optical surfaces and the detector are not available except for the band pass filters and thus were accounted for by single efficiency factors. The measurement does not account for slit losses, a problem inherent to slit-spectroscopy.

Their effect is minimized by taking 1 arcsec slits under good seeing conditions (FWHM  $\lesssim 1''$ )

Table 4.6.: Grating characteristics measured on sky

Order	$\lambda_{peak}$ [ $\mu\text{m}$ ]	$\text{Eff}_{max}$	50% Cut on [ $\mu\text{m}$ ]	50% Cut off [ $\mu\text{m}$ ]	Resolution
Grating 1 - 210 lines/mm					
-2.	2.44	68	2.02	3.18	6687
-3.	1.64	77	1.41	1.90	7838
-4.	1.24	76	1.09	1.41	8460
-5.	1.00	72	0.89	1.11	6877
Grating 2 'H+K' - 200 lines/mm					
-1.	1.87	83	1.38	>2.40	1881 (H) 2573 (K)
Grating 3 'Ks' - 150 lines/mm					
-2.	2.13	78	1.81	>2.40	4150

Table 4.7 lists the measured minimum and maximum wavelength on the detector given the noted central wavelength is used for the grating tilt. The resulting spectral width is also noted.

Table 4.7.: Measured wavelength coverage

Grating	Band	$\lambda_{min}$ [ $\mu\text{m}$ ]	$\lambda_c$ [ $\mu\text{m}$ ]	$\lambda_{max}$ [ $\mu\text{m}$ ]	bandwidth [ $\mu\text{m}$ ]
210 zJHK	K	2.025	2.200	2.353	0.328
210 zJHK	H	1.541	1.650	1.743	0.202
210 zJHK	J	1.169	1.250	1.319	0.150
210 zJHK	z	0.893	0.960	1.017	0.124
200 H+K	H+K	1.475	1.930	2.355	0.880
150 Ks	Ks	1.890	2.170	2.423	0.533

The grating tilt mechanism limits the usable range of central wavelengths. Table 4.8 lists the wavelength range from which the central wavelength can be selected.

#### 4.5. On sky tests

---

Table 4.8.: Physical limits of the tilt unit for central wavelength on the detector

Grating	Band	Wavelength range [ $\mu\text{m}$ ]
210 zJHK	z	0.87 ... 1.02
210 zJHK	J	1.05 ... 1.28
210 zJHK	H	1.40 ... 1.70
210 zJHK	K	2.10 ... >2.4
200 H+K	H+K	1.49 ... >2.4

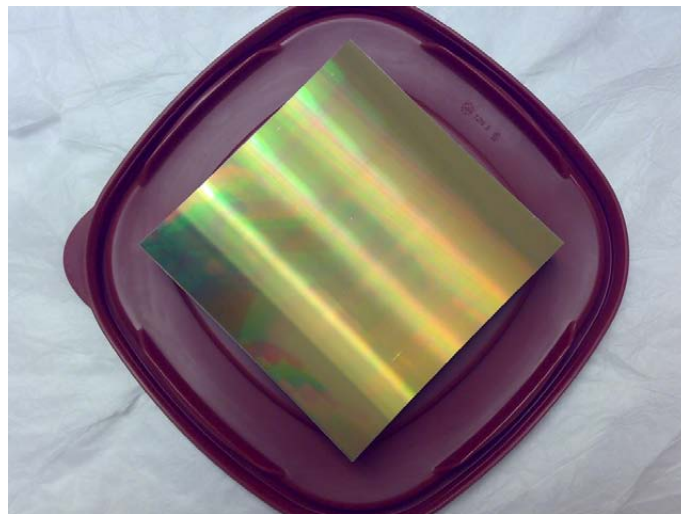


Figure 4.7.: One of the manufactured gratings screwed to its storage box. No major defects (i.e. digs or scratches) are visible by inspection with the naked eye.

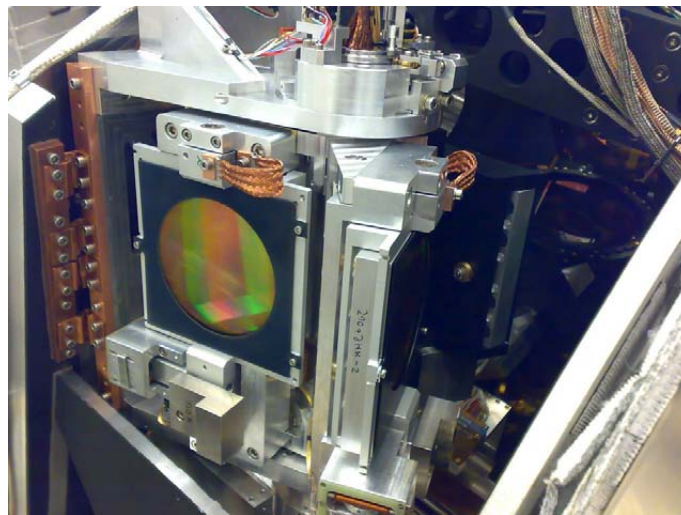


Figure 4.8.: Gratingwheel inside LUCIFER. The Ks 150l/mm grating is visible, the zJHK grating is mounted at the next grating position seen from the side on the right. A black pupil stop is mounted on top of the gratings. On the bottom of the zJHK grating slot the coils of tilting mechanism for the gratings can be seen.



## **Chapter 5.**

# **Commissioning and performance of LUCIFER and the MOS**

In the first two sections of this chapter we present selected results from the LUCIFER commissioning phase in 2008 and 2009, and show the spectroscopic performance of the LUCIFER instrument, especially in deep faint object spectroscopy. We compare the deep faint spectroscopy result with observations of the same object using the integral field spectrometer SINFONI which is used in part II of this thesis. After that we present the performance and reliability of the MOS unit in the first two years of operation. In the last section we present a short comparison of LUCIFER other multi-object near-infrared spectrometer that exist on 8–10m class telescopes to date, most notably 'MOIRCS' at Subaru and 'MOSFIRE' at the Keck observatory. We also present some of the lessons learnt during the first two years of operation and close with summarizing the current state and give an outlook to future operations and forthcoming upgrades.

### **5.1. Commissioning and selected results**

Re-integration of LUCIFER-1 at the telescope site, lab tests and installation took place from August 10th, 2008 till September 5th, 2008. The commissioning phase of LUCIFER-1 followed immediately afterwards, starting with LUCIFER's first light on September 6th 2008. Initial commissioning took until until March 2009 and was hampered by telescope commissioning which was ongoing in parallel. LUCIFER-1 was offered for seeing-limited imaging and long-slit spectroscopy from April 2009. MOS spectroscopy with user cut masks was commissioned thereafter and offered to observers from December 2009. Commissioning officially ended on December 23rd, 2009. LUCIFER-1 is in operation since then. The diffraction limited observing modes of LUCIFER will be commissioned once the f/30 AO-camera has been integrated into LUCIFER and the adaptive secondary has been commissioned. This is presently scheduled for the first half of 2013. Adaptive optics using the laser guide star will be commissioned after the installation of the ARGOS

## 5.1. Commissioning and selected results

laser system, i.e in late 2013. LUCIFER-2 will be brought to the LBT at the end of 2012, its commissioning will follow thereafter.

During commissioning we checked for proper functionality of the instrument in the telescope environment, i.e. hardware and software interfaces, determined basic performance parameters (e.g. image quality, image motion, MOS mask setting accuracy, efficiency) in all available observation modes, and verified the observation procedures including observations preparation, MOS mask manufacturing and calibrations. We refer to the commissioning report (LBT document 'LBT-LUCIFER-TRE-023') and Ageorges et al. (2010) and Seifert et al. (2010) for a detailed presentation of all commissioning results.

### 5.1.1. Detector performance

The LUCIFER detector has been exchanged since the commissioning. On 12 October 2011 the Hawaii-2 detector of LUCIFER-1 was lost due to human error and technical malfunctions while in cryogenic condition. Subsequently the LUCIFER-2 detector was put into LUCIFER-1 as an interim solution. Table 5.1 shows the performance characteristics of the LUCIFER detector.

Table 5.1.: Characteristics of the LUCIFER-1 detector

	old detector	new detector
Pixel size	18.0 $\mu\text{m}^2$	
Number of pixels	2048 $\times$ 2048 pixel <sup>2</sup>	
Fullwell	$\sim 235000 \text{ e}^-$	$\sim 257000 \text{ e}^-$
Linearity within 5%	up to 90% full well	up to 80% full well
Quantum efficiency <sup>(a)</sup> in obs. band	z=0.25, J=0.33, H=0.74, K=0.73	z=0.37, J=0.48, H=0.55, K=0.57
Readout modes	Double-Correlated Reads (DCR) Multiple-Endpoint Reads (MER, 10 samples)	
Min Exposure time	4sec (DCR), 12sec (MER)	
Gain (DCR)	4.08e <sup>-</sup> /ADU	4.5 e <sup>-</sup> /ADU
Read out noise	11.9 (DCR), 5.7(MER) e <sup>-</sup>	12.6(DCR), 7.6(MER) e <sup>-</sup>
Dark current (DCR)	0.06 e <sup>-</sup> /s/pix	0.04 e <sup>-</sup> /s/pix

<sup>(a)</sup> Values from detector data sheet; correctness questionable, see next section

The “new” (LUCIFER-2) detector shows some electronic artifacts which require a different readout scheme for double correlated readout. We read out the array *two* times before and after the integration and throw away the first pair and correlate the second. In that sense the current DCR is a modified MER with 4 reads. By this we get rid of some otherwise persisting electronic noise pattern near the borders of the readout channels which would -if present- severely hamper spectroscopic observations of faint sources.

Both LUCIFER-1 and LUCIFER-2 will be upgraded to Hawaii-2 RG detector arrays in late 2012. This will significantly change the values given above. Also, we expect the system efficiency (see next section) to raise by up to  $\sim 60\%$  in the H and K band as the new ‘RG’ detectors have a significantly increased quantum efficiency.

### 5.1.2. System efficiency in spectroscopic mode

The system efficiency in spectroscopic observing mode was measured on sky using standard stars under typical observing conditions for the LBT site (seeing  $\sim 0.9\text{-}1.1''$ ). We have used a  $2''$  slit so that slit losses are not affecting our measurement. The system efficiency measurements for grating 1 and 2 in H and K band are presented in figure 5.1 to 5.3. We show the *total* efficiency, i.e. it *includes* the telescope. As performance values for the telescope are not available these cannot be accounted for. The effect of the atmosphere is corrected for, however, since the exact observing conditions differ slightly from the model atmosphere, residuals are present.

We have calculated the system efficiency by comparing the measured flux with the calculated flux from a model star of the same stellar type and magnitude. The stellar model spectra were taken from Pickles (1998) and were multiplied with a model atmosphere generated in ‘atran’ (Lord 1992).

In all figures, the calculated efficiency is shown in black with its axis on the left. We also plot the atmospheric sky emission in orange and the atmospheric transmission in green. Both are normalized (axis on the right), the sky emission to the intensity of brightest OH line, and the atmosphere to 100% transmission within the respective wavelength range. Both are calculated for a spectral resolution of  $R=4000$ . This is to guide the eye when evaluating the efficiency in ‘usable’ wavelength intervals in the near-IR, i.e. between the OH line molecular series. The slight mismatch between the calculated and observed atmosphere introduces some small scale noise. The general shape of the efficiency is dominated by the filter-, the grating-, and the detector-efficiency curve. The measured system efficiencies are in very good agreement with the theoretical system efficiency calculated from the optical properties of the individual components.

Figure 5.1 shows the system efficiency for **grating no. 1** (the 210 lines/mm zJHK grat-

## 5.1. Commissioning and selected results

---

ing) in H- (left) and K-band (right) and the **old** detector. The dedicated H and K band filters were used. The maximum efficiency of  $\sim 20\%$  is in the middle of the H-band. This reflects the grating curve for the 3rd order of the grating, which peaks in the mid H-band. In the K-band, the efficiency is lowest on the blue end (around 15-20%) and increases towards the red end where it peaks at  $\sim 29\%$ . This behavior is again directly governed by the grating curve of the 2nd order. The comparably low efficiency in the blue K band was one of the drivers for the development of the new Ks and H+K grating.

Figure 5.2 shows the system efficiency for **grating no. 2** (the 200 lines/mm H+K grating) in H- (left) and K-band (right) and the **old** detector. The H+K filter was used. We have split into two graphs as the data reduction pipeline for H+K is not yet as advanced as for separated H and K. Plotted next to each other, one can see the overall shape of the gratings 1st order which peaks between the H and K band. In the H band the efficiency starts out comparably low around 10% and rises to  $\sim 22\%$  at the red end of the H-band. The efficiency in the K band is around  $\sim 23\%$ , starting out slightly higher in the blue K (i.e. Ks) and decreasing slowly to the red K band. As expected the efficiency in the Ks is about 10% higher with this grating compared to the 'all purpose grating' used in figure 5.1.

Figure 5.3 shows the system efficiency for **grating no. 2** (the 200 lines/mm H+K grating) in H- (left) and K-band (right) and the **new** detector. The H+K filter was used. Surprisingly, the efficiency in the H band is  $\sim 5\%$  higher, although the new detector should have a decreased quantum efficiency in the H band according to the detector's specification sheet. This lower efficiency of the detector cannot be confirmed. The system efficiency in the K-band is slightly higher in Ks, but overall comparable to figure 5.2. The new detector appears to show similar efficiency in the K-band as the old one.

The system efficiency measurements for the 150 lines/mm Ks-grating in K band and the zJHK-grating in J band using the new detector are still pending, as no wide slit data has been taken in these configurations so far. Unknown slit losses (typically up to 10% of the incoming flux can be lost) make the data taken so far unsuitable for a system efficiency analysis. The J-band system efficiency with the old detector is shown in figure 5.4. This detector was known to deliver only a very low QE in the J-band of  $\sim 20\%$ .

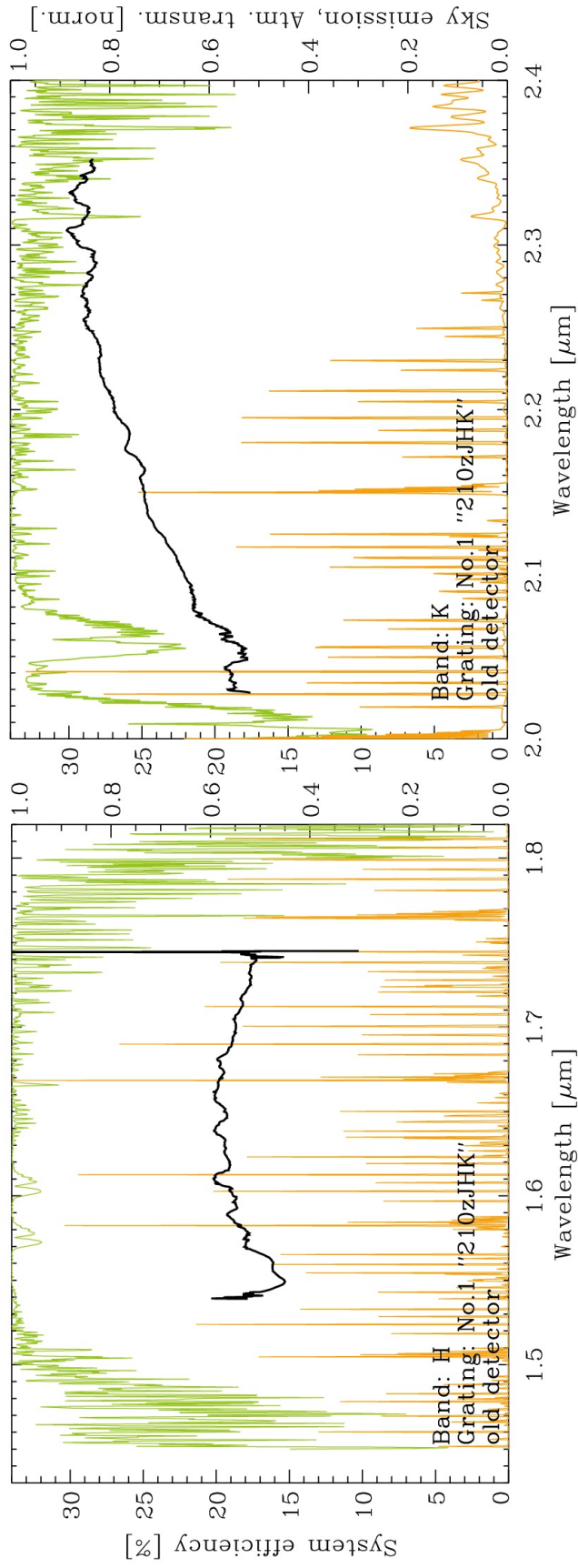


Figure 5.1.: System efficiency in H- (left) and K-band (right) with grating number 1 and H (left) and K (right) filter, old detector. Measured curve in black. Atmospheric transmission (normalized) and sky emission (normalized to strongest OH line in band) are plotted in the background for reference.

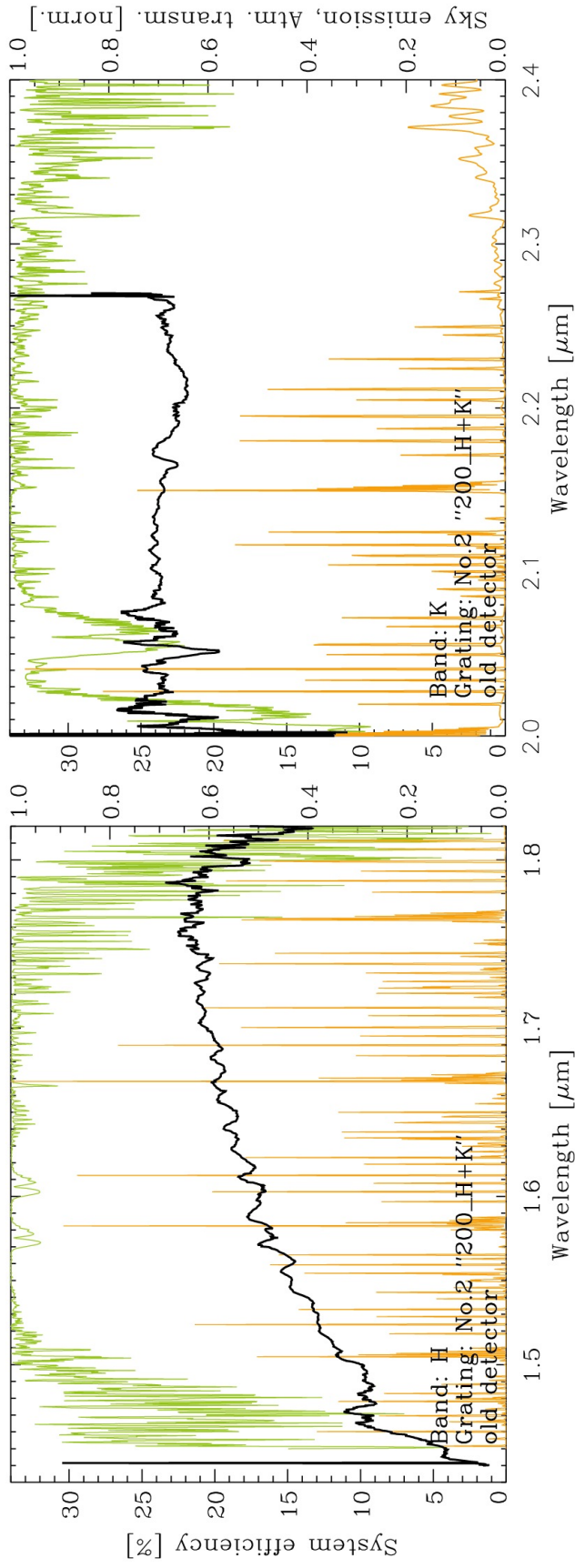


Figure 5.2.: System efficiency in H- (left) and K-band (right) with grating number 2 and H+K filter, old detector. Measured curve in black. Atmospheric transmission (normalized) and sky emission (normalized to strongest OH line in band) are plotted in the background for reference.

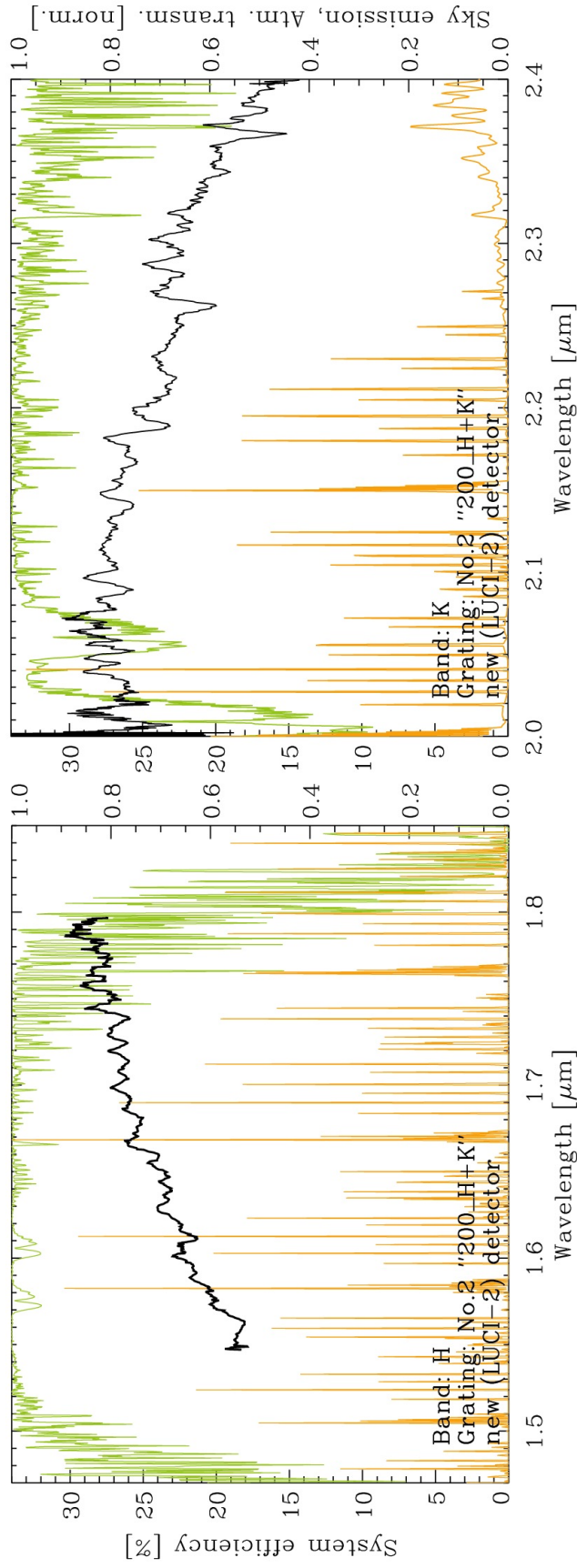


Figure 5.3.: System efficiency in H- (left) and K-band (right) with grating number 2 and H+K filter, new detector. Measured curve in black. Atmospheric transmission (normalized) and sky emission (normalized to strongest OH line in band) are plotted in the background for reference.

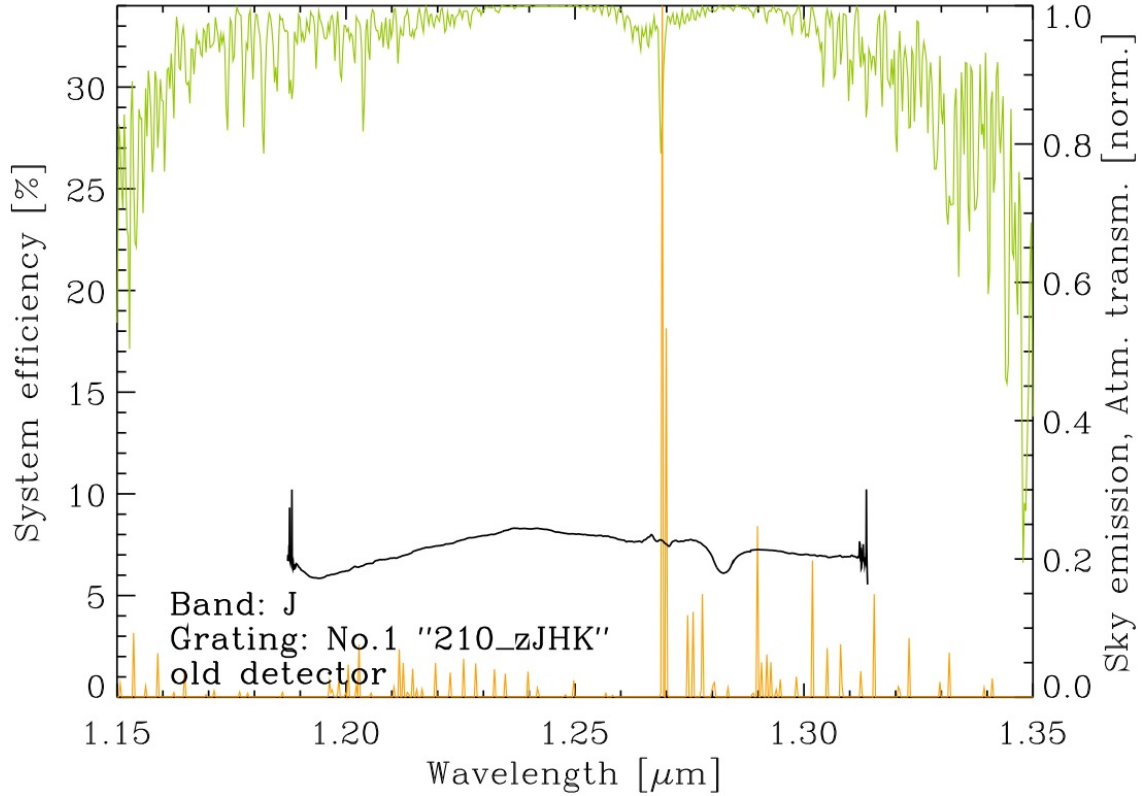


Figure 5.4.: System efficiency in J-band with grating number 1 and J filter, old detector.

## 5.2. Deep faint object spectroscopy

An important observing mode is long-time integration of faint objects, especially in combination with multi object masks. Long integrations on faint objects do not test one particular component of the system but rather long time functionality and stability of the system as a whole, including the telescope.

### 5.2.1. Observations and data reduction

The massive  $11.3 \times 10^{10} M_{\odot}$  disk galaxy Q2343-BX610 at  $z=2.21$  was chosen as the observation target for this test. BX-610 is fairly large in diameter ( $H\alpha$  detected over  $2''.4$ ) It has been observed before with SINFONI and is also one of the targets in the study in Part II of this work. It has a K-band magnitude of 19.2mag  $K_{s,Vega}$ , an  $H\alpha$  flux of  $2.61 \times 10^{-16} \text{erg/s/cm}^2$ , and an  $H\alpha$  equivalent-width of  $268 \pm 30 \text{\AA}$  as measured from SINFONI observations.

Observations were carried out during Lucifer commissioning time over 12 nights in October and November 2009.

Reduction was done in the standard manner for near-infrared longslit spectroscopy: A master dark frame was created from at least three dark frames by averaging for each observing night. Likewise a master flat for flat-fielding was created for each night. We found that flat-fielding can as well just be omitted without any negative impact on the data product (this would of course not apply to a continuum source). Cosmic rays were removed in *iraf* after dark subtraction and flat-fielding. The data were wavelength calibrated using the OH lines. This produced far better results, i.e. less residual OH contamination in the sky-subtracted image than a calibration based on the ArKr arc-lamps. We derived the wavelength solution for each frame by fitting the OH lines present in the spectrum and comparing with an OH line list. The position of the OH lines were traced and fit in slit direction in each frame to correct for spectral curvature in slit direction. Sky subtraction was carried out by pairwise frame subtraction (i.e. A-B) after the frames had been rectified and re-sampled to a common wavelength grid. The science object was observed in each frame and was nodded along the slit so that in each pair one image served as the sky-frame for the other one. Standard stars were observed for flux calibration before and after each observing block and were reduced like the science frames. Registration and average stacking of the positive flux images was done after flux calibration using *DPUSER* and *QfitsView*; both are software packages developed at MPE. A simple averaging of the individual pointings per OB was sufficient to create the master file for each OB since the position of the object in spatial direction was already ensured to be the same by cropping the individual pointing frames and the data were already on the same wavelength grid in spectral direction. To stack different OBs from different nights, the object's position was determined with a centroid fit and the frames were spatially shifted accordingly. A 1D spectrum was extracted from the 2D longslit spectrum with IRAFs 'apall' routine to measure the emission line flux. A simple additive collapse in spatial direction of the 2D spectrum lines containing the object was done for comparison. The  $H\alpha$  and [NII] emission line flux was measured by fitting a gaussian to the spectrum in a free parameter fit, i.e. not constraining the width of the emission line.

### 5.2.2. Results

Figure 5.5 shows the obtained spectrum around the  $H\alpha$  line at  $2.107\mu\text{m}$ . The total integration time for this spectrum is 180min. The LUCIFER data set is shown in black, the corresponding SINFONI dataset in green (see next section). We infer a total  $H\alpha$  flux of  $2.39 \times 10^{-16}\text{erg/s/cm}^2$ . The signal to noise (S/N) in the  $H\alpha$  line is  $\sim 18.5$ . The red dotted lines mark the wavelengths of strong atmospheric OH lines. Their residuals are clearly visible in the LUCIFER spectrum.

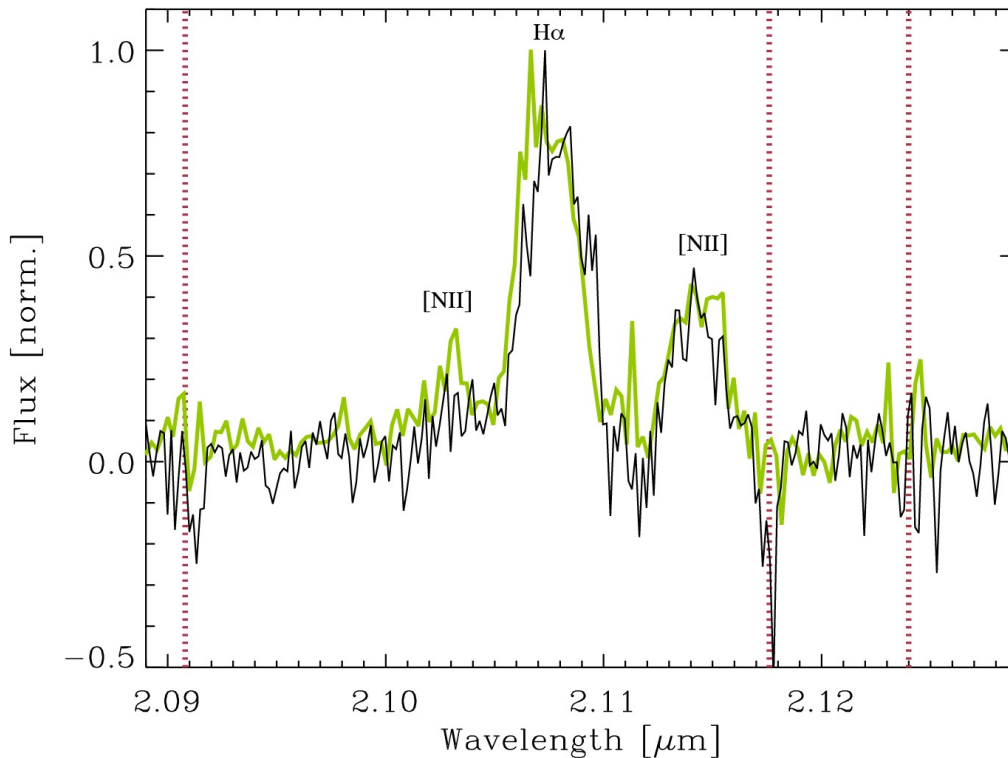


Figure 5.5.: Part of the reduced BX610 1D spectrum taken with LUCIFER (black) and a SINFONI pseudo-longslit spectrum (green) for comparison. OH line wavelength denoted in red.

### Comparison to SINFONI IFU observations

The target BX610 has been observed by our group with SINFONI as part of the SINS survey (see part II of this thesis). Since the instrumental characteristics and performance of SINFONI are very well known, we here compare with the results from the LUCIFER observations. The SINFONI OH-line removal is much more advanced than the relatively simple approach taken in the manual LUCIFER reduction used for the LUCIFER BX610 data set where the dark-subtracted and flat-fielded frame is just wavelength fit and re-sampled (see 7.4.1 for the SINFONI OH removal steps). The OH line removal routines used in the SINFONI pipeline produce significantly lower residuals. As SINFONI is an integral field spectrometer, it does not suffer from flux-calibration errors due to slit losses. This is not the case for LUCIFER being a classical slit-spectrometer. Therefore we do not directly compare the inferred fluxes but compare the signal-to-noise ratio of the two instruments.

### Measured Signal-to-Noise

We use a data set of 180 minutes for both SINFONI and LUCIFER to derive the S/N. The signal-to-noise of SINFONI in the H $\alpha$  line is  $\sim 24.5$ , i.e. it is higher by a factor 1.26

compared to the H $\alpha$  S/N in LUCIFER which was measured to be  $\sim 18.5$ . Taking into account the spectral resolution element of LUCIFER (3 pixel) and SINFONI (2 pixel) this changes the equivalent S/N of LUCIFER to  $18.5\sqrt{3}=32$  and S/N SINFONI to  $24.5\sqrt{2}=35$ , i.e. we measure a factor 1.1 higher S/N in SINFONI. To assess if this is due to a loss in signal, a higher noise or maybe both, we now compare the theoretical signal and noise from known and measured system parameters.

### Theoretical signal and noise comparison

The **signal** depends on the amount of incoming photons and thus scales with the system efficiency and the collecting area of the telescope. The system efficiency for LUCIFER is shown in figure 5.1 and is  $\sim 22\%$  at the H $\alpha$  wavelength of BX610 at  $2.107\mu\text{m}$ , the system efficiency for SINFONI (see figure 5.8) is 25%. The primary mirror of the LBT has a diameter of 8.4m, the VLT of 8m. We therefore infer a LUCIFER signal  $\propto 22\% \cdot 8.4^2 = 15.5$  and a SINFONI signal  $\propto 25\% \cdot 8^2 = 16$  and as such one expects a theoretical ratio of the two instrument signals of  $\text{Signal}[\text{SINFONI}/\text{LUCIFER}] = 1.03$

Several sources of **noise** contribute to the system noise. Shot noise (associated with the source photons, sky photons, and the dark current of the detector and instrument) and the read-out noise of the detector.

$$\text{Noise} = \sqrt{N_{\text{pixel}}} \cdot \sqrt{\text{RON}^2 + (\text{Sky}/\text{pixel})^2 + (\text{Dark}/\text{pixel})^2} \quad (5.1)$$

Table 5.2 lists the different sources of noise and their levels.

Table 5.2.: Noise sources and levels per detector pixel for LUCIFER and SINFONI

Noise source	LUCIFER <sup>(a)</sup>	SINFONI
Read noise	$6e^-$	$7e^-$
Dark current detector	$0.06e^-/\text{s}/\text{pixel}$	$0.15e^-/\text{s}/\text{pixel}$
Total instrument dark in 600s	$\sim 200e^-$	$\sim 50e^-$
Sky between OH (blue K band)	$1250e^-$	$300e^-$

<sup>(a)</sup>The BX610 data were taken with the old detector.

We compare the noise per spectral resolution element in a  $0.75''$  box, i.e.  $3 \times 3$  pixel = 9 pixel for LUCIFER and  $2 \text{ pixel} \times 6 \text{ pixel} \times 3$  slitlets = 36 pixel for SINFONI.

LUCIFER noise:  $\sqrt{9} \cdot \sqrt{6^2 + 1250 + 200} = 116e^-$ , SINFONI noise:  $\sqrt{9} \cdot \sqrt{7^2 + 300 + 50} = 120e^-$ . And thus  $\text{Noise}[\text{SINFONI}/\text{LUCIFER}] = 1.04$

The higher background in LUCIFER is partially compensated by the higher read-noise introduced by four times as many pixel in SINFONI for the same resolution element. To check, comparing the sky contribution (slitwidth·pixelsize·efficiency·mirror size·dispersion)

### 5.3. Performance of the MOS unit hardware

---

yields :

$$\text{Sky} \frac{\text{SINFONI}}{\text{LUCIFER}} = \frac{0.25 \cdot 0.125 \cdot 25\% \cdot 8^2 \cdot 0.00025}{0.75 \cdot 0.125 \cdot 22\% \cdot 8.4^2 \cdot 0.000164} = \frac{1}{3.8}$$

which is in good agreement with the factor 4.2 found in the background shown in table 5.2.

The theoretical **S/N** of SINFONI compared to LUCIFER is  $1.03/1.04 = 0.99$ ,

#### **Conclusion**

1. the measured S/N of the SINFONI observations for the same spectral resolution element is only  $\sim 10\%$  better than the one of LUCI
2. the lower transmission (-12%) of LUCIFER is compensated by the bigger telescope area (+10%)
3. the slightly higher background (+10%) per detector pixel in LUCIFER is partially compensated by the higher read-noise contribution in SINFONI when comparing equivalent sky pixels.

Therefore, without additional losses, the two systems (i.e. including telescope) should have almost equal sensitivity.

Consequently, the measured lower S/N in LUCIFER is likely due to slit-losses, i.e. a loss in signal.

#### **Check for lower signal in LUCIFER**

If our conclusions are correct, we should see a  $\sim 10\%$  lower signal in the measured LUCIFER source signal measured in electrons on the detector. We check with a 60 minute stacked data set of SINFONI and LUCIFER. Extracting the flux over the same area on sky, we measure a total flux of  $25.9 \text{ e}^-/\text{s}$  for LUCIFER and  $29.5 \text{ e}^-/\text{s}$  for SINFONI, i.e. a 13% higher flux in SINFONI. This is good agreement with the expected 10% higher signal in SINFONI from our analysis of the 180 minutes data set given above.

### **5.3. Performance of the MOS unit hardware**

#### **5.3.1. General performance**

The LUCIFER instrument is in regular science operations since end of 2009. The MOS unit is offered for science users since beginning of 2010. Over 4500 mask exchanges

have been run so far during commissioning, test and science nights. The wear of the non lubricated cryogenic gears and ball screws has been found higher than expected, which, in case of the grabber, could not just be cleaned up but required a complete exchange of the drive mechanism twice.

The typical failure rate on the level of *individual/atomic* mechanical movements is only of the order 0.1%, but since a mask exchange (the observation relevant movement-collection) consists of several movements, the failure rate on the operations level increases to overall about 1%.

Most of the occasionally occurring errors so far could be corrected using the built-in recovery functions. In these cases the science observation preparation (acquisition time) typically increased by several (up to 30) minutes or single science frames were lost, but observations could still be carried on during the night.

Still, we have encountered a stop of science observations once every two partner observing blocks, requiring a manual debug resulting in a 30–150 min loss in observing time.

A very few times, however, error recovery required interventions on the hardware engineering level, i.e. recovering the unit or repairing the electronics during daytime or even warming up the instrument. This has led to loss of complete science nights (repair during daytime) or unavailability of the instruments (if a warm-cold cycle of the instrument was needed for repair) of typically 2-3 weeks. These failures subsequently lead to hardware upgrades during three scheduled maintenance runs. These upgrades enhanced the automatic-motion-correction capabilities and reliability of the unit by almost a factor 2.

#### **5.3.2. Encountered, observation-stopping function errors of the MOS**

We have encountered several errors that led to a stop in night time observations and required manual recovery intervention. From most of these errors we could recover by using the engineering interface remotely. Others required repair on site and led to unit upgrades.

##### **Mask selection malfunction**

The mask selection drive failed several times, often resulting in the motion to only turn clock- but not counterclockwise. While an auto-correcting sequence was successfully developed and applied as a software update, the underlying hardware error was not traced down until recently. Communication signal levels in the electronics were noisy,

### 5.3. Performance of the MOS unit hardware

---

resulting in erratic motions. The electronics rack is now upgraded so that this error can no longer occur.

#### **Mask (un-)locking error**

The mask retainer drive limit switch has several times not correctly indicated the limit position. Likewise the open position switches of some retainer arms have been unresponsive several times. Both errors could be fixed in software, the affected switches have been replaced during annual maintenance. Still, their sporadic appearance has led to observation stops with subsequent manual recovery.

#### **Mask grabber malfunction**

The mask grabber drives utilizes a ball screw that is comparably small and thus rather sensitive for abrasion and accumulation of dirt. We have meanwhile replaced the drive screw twice during annual maintenance runs. A permanent fix is not yet identified as the available space in the grabber head is rather tight. A soonish malfunction can be estimated by monitoring the number of steps the grabber needs to open or close. We have implemented an auto correction based on back-and-forth motions, however, if the unit gets stuck when too much dirt has accumulated due to abrasion, the unit needs to be replaced, requiring a warm up of the cryostat.

#### **Limit switch malfunction**

Single limit switches have shown sporadic errors. As these limit switches are used to calibrate motions, they cannot be simply ignored. A recovery always requires a trained person to debug the unit manually on the engineering level as has happened sporadically in the past.

#### **“Disconnect error”**

The “disconnect error” let the unit sporadically disconnect from the instrument server. This caused timeouts propagating to the user GUI level aborting ongoing observations. The two causes have now been identified and corrected. One type of disconnect error was caused by a bug in the firmware of the motion controller leading to a reset once a certain number of steps was commanded that cause a buffer overflow in the firmware. The other one was an internal software timeout due to a communications error.

### 5.3.3. Cabinet Transfer

The cabinet transfer using the two dedicated auxiliary cryostats has shown to be comparably labour-intensive and blocking significant telescope daytime on the days of a cabinet exchange. Currently there exists no alternative method to exchange used and new masks, however, it could be beneficial to investigate alternatives, especially those that would feature an exchange mechanism that can be manipulated from outside or simply rely on manual operation using vacuum feed-throughs.

#### **cabinet (un-)locking error**

The cabinet unlock mechanism has failed to correctly operate, i.e. lock or unlock the cabinet, several times on the first attempt. We have implemented auto-correcting motions that are retrying the movement. So far, this has proven to be reliable. No stop of mountain operations has resulted from this error so far.

#### **Cabinet transfer failure**

On 6 March 2012, a cabinet could not be transferred from the LUCIFER cryostat to the attached auxiliary cryostat. Error recovery showed that the draw bar of the cabinet itself must have warped and hit the bearing of the worm gear inside the auxiliary cryostat, preventing it from moving on into the auxiliary cryostat. As the cabinet could be moved back into LUCIFER but not be extracted, the LUCIFER cryostat had to be warmed up to remove the cabinet. This rendered the system inoperable for 3 weeks, resulting in science time loss for two LBT consortium partners. The cause of the error has meanwhile been identified: the fixation of the draw bar to the mask cabinet is weak and already small shearing forces on the draw bar's far end can misalign the draw bar. Currently, all cabinets are outfitted with a stronger fixation between draw bar and cabinet magazine base.

## 5.4. Lucifer compared to other NIR MOS spectrographs

LUCIFER is one of four near-infrared multi object spectrographs on 8–10m class telescopes to date. The other three comparable instruments are 'MOIRCS' at the Subaru Telescope, 'MOSFIRE' at Keck, both stationed on Mauna Kea, Hawaii, and FLAMINGOS-2 at GEMINI-South. We compare them to LUCIFER in the following. We also compare

## 5.4. Lucifer compared to other NIR MOS spectrographs

---

with two integral field unit instruments, SINFONI at VLT and the upcoming KMOS instrument at the VLT.

### 5.4.1. MOIRCS

MOIRCS (“Multi-Object Infrared Camera and Spectrograph”, Ichikawa et al. 2006; Suzuki et al. 2008) is the NIR multi-object spectrometer and imager at the 8.2m Subaru telescope on Mauna Kea Hawaii, developed by the University of Tohoku and the Subaru National Observatory of Japan. It provides wide field imaging and spectroscopy in z,J,H, and K band on a  $7(6)\times 4$  arcmin<sup>2</sup> FOV at low ( $\sim 500$ ) and intermediate ( $\sim 1300$ ) resolution. Higher resolution modes ( $R\sim 3000$ ) using volume phase holographic gratings are in commissioning. The instrument utilizes two Hawaii-2 focal plane arrays to record the FOV at a pixel scale of  $0.12''$ . The detectors are the same ‘old’ 2k Hawaii-2 arrays as currently in use in LUCIFER. They show  $15e^-$  read noise and  $0.1 e^-/s/pixel$  dark current, which is a little higher than the LUCIFER detectors.

The system efficiency is shown in figure 5.6. While it is roughly comparable to the current LUCIFER, albeit a little lower, note however, that these efficiencies are for the low and intermediate resolutions which make OH avoidance challenging to impossible. The low efficiency of the VPH-gratings for higher spectral resolutions significantly reduces the system efficiency to  $\sim 10\%$  (calculated from the published VPH efficiencies based on figure 5.6), making the instrument less competitive in this observing mode.

MOIRCS consists of two cryostats. The main cryostat houses the instrument optics and detector, the second smaller one houses the slit mask storage unit. A linear robotic arm grabs masks from the turret and transfers them to the focal plane. The cycle time for a mask exchange during observation at night is 25 min, 4-5 times longer than for the same operation in LUCIFER or MOSFIRE (see below). To exchange the MOS slit masks, the smaller cryostat is warmed up and the masks are replaced by manually extracting and inserting masks. The masks are located in a mask turret, housing six long slit masks and up to 9 user laser-cut MOS masks. An exchange of old and new masks in the mask turret takes approximately two days including warm-cold cycling the mask turret cryostat.

The IFU upgrade “nuMOIRCS” is currently being developed. At the current design stage, it features two IFUs with a FOV of  $3\times 3$ arcsec<sup>2</sup> each freely positionable in the imaging FOV of  $7\times 4$ arcmin<sup>2</sup> by robotic arms (similar to ‘KMOS’) and will feed two pseudo longslit into the existing spectrometer.

MOIRCS is currently in limited operation following a major glycol leak on the Subaru telescope which rendered the guiding system unusable. It is expected that MOIRCS will become fully operational again towards the end of 2012.

Table 5.3.: Near-infrared cryogenic multi-object spectrometer in operation

Name	Telescope	FOV [arcmin <sup>2</sup> ] Imaging/ Spectro.	Platescale [arcsec/ pixel]	Wavelength- range <sup>(a)</sup> ( NIR bands/ grsting(s) )	Nyquist- slit width [arcsec]	Slit limited resolution @ Nyquist slit	MOS type <sup>(e)</sup> / exchange time for new 'mask'	Mask number
LUCIFER	LBT	4×4	0.12	z,J,H,K,	0.25	~10000 (J,H,K)	laser cut	6 (LS, fixed)
		4×3	0.25	z,H+K Ks	0.5 0.5	~4000 (J,H,K) ~2000 (H+K)	masks / 5 min.	23 (user)
MOSFIRE	Keck	6×6 <sup>(b)</sup>	0.18	Y,J,H,K	0.48	~4800	config.	1 (config)
		6×4					slit unit 5 min.	
MOIRCS	Subaru	7×4	0.12	z,J,H,K,	0.5	~500 (J,H,K)	laser cut	6 (LS, fixed)
		6×4 <sup>(d)</sup>					masks / 25 min.	15 (user)
FLAMINGOS-2	GEMINI South	6(circ.)	0.18	J,H,K,	0.36	~1200 (JH,HK)	MOS	6 (LS, fixed)
		6(4)×2 <sup>(c)</sup>		J+H, H+K		~3000 (J,H,K)	Masks / nn. min.	9 (user)
SINFONI	VLT	8''×8''	0.12×0.25	J,H,K	-	~4000 (J,H,K)	1 IFU	(32×32 spaxel)
		3''×3''	0.05×0.1	H+K		~2000 (H+K)		
		0.8''×0.8''	0.12×0.25					
KMOS (in 2013)	VLT	2.8''×2.8''	0.2×0.2	iZ,YJ,H,K	-	~3400 (J,H,K)	24 IFUs	(14×14 spaxel each)
		in 6'×6'					6''closest	

<sup>(a)</sup> observing bands: Z~0.85-1.05 $\mu$ m, Y~0.96-1.1 $\mu$ m, J~1.12-1.33 $\mu$ m, H~1.47-1.80 $\mu$ m, K~1.93-2.45 $\mu$ m

<sup>(b)</sup> some vignetting in the corners

<sup>(c)</sup> 4×2 for full spectral band coverage

<sup>(d)</sup> no slits in corner, placement limited by an overlaid 6'' diameter circle

<sup>(e)</sup> Cryogenic MOS; non-cryogenic NIR MOS (e.g. FMOS) exist, but are not usable for  $\lambda \gtrsim 2.1\mu$ m due to instrument thermal radiation.

<sup>(f)</sup> low-efficiency (~15%) volume phase holographic (VPH) gratings in commissioning

## 5.4. Lucifer compared to other NIR MOS spectrographs

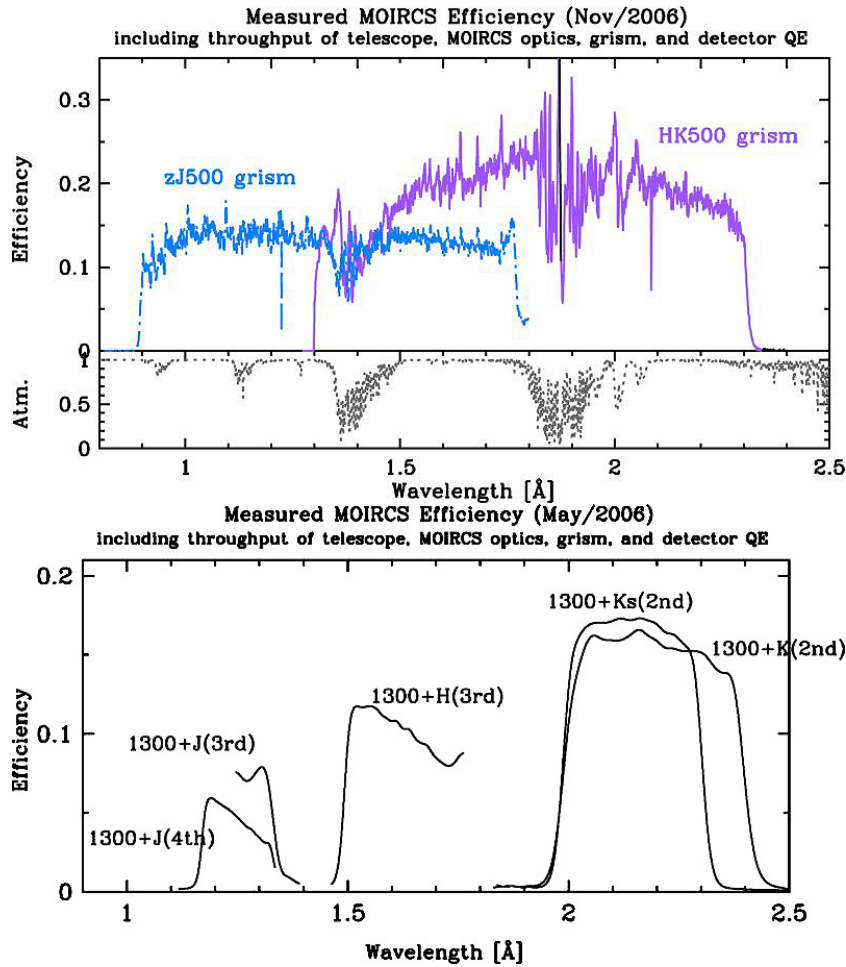


Figure 5.6.: Measured system efficiency for MOIRCS R $\sim$ 500 (upper panel) and R $\sim$ 1300 (lower panel) spectroscopic observing modes (taken from [http://www.naoj.org/Observing/Instruments/MOIRCS/spec\\_sensitivity.html](http://www.naoj.org/Observing/Instruments/MOIRCS/spec_sensitivity.html), 25 May 2012)

### 5.4.2. MOSFIRE

MOSFIRE (“Multi-Object Spectrometer for Infra-Red Exploration”, McLean et al. 2010) is the NIR multi-object spectrometer and imager at the Keck observatory on Mauna Kea Hawaii. It is a joint development of UCLA, Caltech, UCSC and the W.M. Keck observatory. The instrument covers the Y, J, H and K band. The imaging FOV is  $6 \times 4 \text{ arcmin}^2$ , which shows some vignetting in the field corners (collimator free aperture circle  $r=3.4''$ ). The unvignetted usable spectroscopic MOS FOV is  $6 \times \sim 4 \text{ arcmin}^2$ , which is  $\sim 2$  times the area of the LUCIFER MOS FOV ( $4 \times \sim 3 \text{ arcmin}^2$ ).

MOSFIRE does not use cut masks for multi-object spectroscopy but features a unique cryogenic configurable slit unit (dubbed ‘CSU’) developed by the Swiss Centre for Micro-

Electronics. This unit synthesizes a multi-slit mask by moving 46 pairs of metal rods with blackened knife-edges at their ends and stacked adjacent to each other in the FOV to create slits in the FOV. The maximum number of MOS slits is thus 46, each of which are freely positionable in the FOV. As each side of a slit is one knife-edge end of one of the moving rod, and the slits are formed by driving the knife-edges against each other, the slit-size can be chose arbitrarily. Slit height equals the rod height, i.e. 7.3". Long-slits can be created by placing two or more short slits adjacent to each other as the rods are tightly stacked. The design limits the slit geometry to straight slits tilted by 4°. Slits can be positioned anywhere in the field like the laser cut slits in LUCIFER with -like in LUCIFER- the limitation of reduced wavelength coverage when placed near the FOV edges. The time it takes to configure a FOV with slits, i.e. 'exchange a mask' in LUCIFER term, is about 5 minutes, which is comparable to a mask exchange in LUCIFER. Obviously the design has the advantage that masks can be changed during the night according to the field on sky, e.g. position mismatches of reference stars due to proper motion can be compensated. Further, one can adapt to the seeing more easily by narrowing or widening the slits "on the fly". Slits can be first used for alignment and then repositioned for the objects observed. Also, an observing scheme where e.g. one would integrate longer on a few chosen targets than on others by re-configuring only a part of the mask during the observation is easier than using dedicated pre-fabricated masks whose number is limited.

The mechanical construction of the CSU is very complex and likely rather challenging to maintain, extrapolating from the experiences we have gathered from cryogenic precision mechanics with our MOS. No performance data has been published on the CSU yet. Like with the LUCIFER MOS, the MOSFIRE team has implemented various self-debug schemes to facilitate using the unit.

MOSFIRE uses a single static camera and likewise diffraction is done using a single grating in different orders, similar as LUCIFER uses grating no.1. Using a new Hawaii-2 RG array, MOSFIRE already benefits from the higher quantum efficiency of these detectors which is clearly reflected in the theoretical system efficiency spectrum shown in figure 5.7. The detector properties of the Hawaii-2 RG in MOSFIRE are a read noise of  $3.7e^-$  (fowler 32 readout) and a dark current  $<0.01e^-/s/pixel$ . This is comparable with the current LUCIFER-2 detector in use, which is not of the RG type, having a dark current of  $<0.04^-/s/pixel$  and  $7.6e^-$  read noise in MER. The quantum efficiency of the detector is reportedly high with 0.83 at  $1\mu m$  and 0.88 at  $2\mu m$ . To compare, the specification data (Teledyne data sheet) of the first LUCIFER Hawaii-2 RG are very similar to the MOSFIRE RG array: QE 0.87 and 0.82 at 1 and  $2\mu m$ , read out noise is  $3.1^-$  and the dark current was measured as  $<0.01e^-/s/pixel$ .

The instrument recently had its first light on April 4th 2012 and is currently in the commissioning phase. It will likely be offered for science use to the Keck community from later 2012B on.

## 5.4. Lucifer compared to other NIR MOS spectrographs

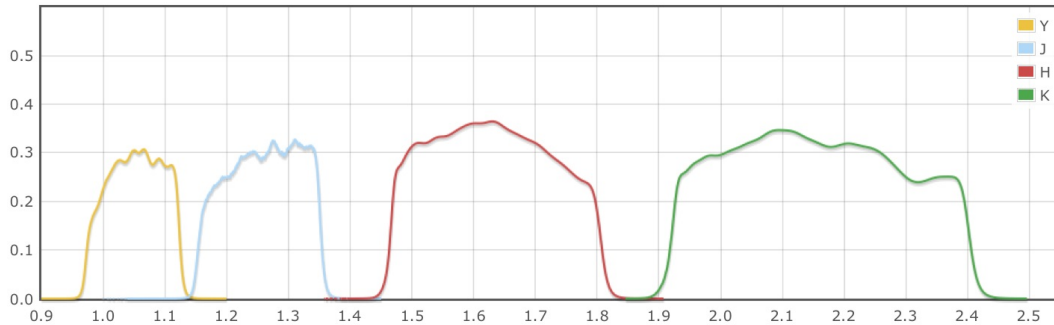


Figure 5.7.: Theoretical system efficiency calculation including sky, slit, optics, and detector for MOSFIRE at Keck. Values taken from the MOSFIRE preliminary ETC webpage Version 14 March 2012 ([http://www.astro.caltech.edu/~njk/etc/mosfire\\_etc.html](http://www.astro.caltech.edu/~njk/etc/mosfire_etc.html))

### 5.4.3. FLAMINGOS-2

FLAMINGOS-2 is the “Facility Near-Infrared Wide-field Imager & Multi-Object Spectrograph for Gemini” (Eikenberry et al. 2004) designed by the University of Florida and installed on GEMINI-South. It has a circular  $\sim 6'$  FOV with a spectroscopic MOS FOV of  $\sim 4 \times 2'$ . It features spectral resolutions of  $\sim 3000$  in J,H, or K and  $\sim 1300$  in J+H or H+K band coverage for a  $0.36''$  slit. The detector is a Hawaii-2 array showing slightly higher dark current ( $0.5^-/s$ ) and comparable read noise ( $\sim 6e^-$ ) compared to the other NIR MOS spectrographs. The published theoretical system efficiency curves do not include the atmosphere, telescope and detector. Thus a comparison to the other instruments is not sensible. On-sky performance values were not available at the time of writing.

Like MOIRCS a dedicated Mask-Cryostat in front of the main instrument hoses a wheel with 6 long-slits and 9 places for user MOS masks. As masks are exchanged during observations by simply turning the mask-wheel, the mask exchange time is only 1–2 minutes. A mask exchange of old and new laser cut MOS masks requires warming up the front cryostat and takes  $\sim 1$  daytime period, i.e. masks can be exchanged between two observing nights.

Like LUCIFER it can be combined with a wide-field AO system in the future to provide imaging and MOS spectroscopy over a  $2 \times 2$  ( $2 \times 1$ ) arcmin<sup>2</sup> AO corrected FOV (LUCIFER will feature a  $4 \times 4$  ( $4 \times 3$ ) arcmin<sup>2</sup> AO corrected FOV for imaging and MOS spectroscopy).

FLAMINGOS-2 was brought to GEMINI in 2009 but was de-mounted after first tests indicated several issues which prevented reliable science operations. It subsequently underwent major rework and was installed again at the telescope in December 2011. It currently is in commissioning on sky and is planned to be offered from 2012-B on.

#### 5.4.4. SINFONI

SINFONI (SINgle Faint Object Near-IR Investigation) is the adaptive optics assisted integral field spectrometer at the Very Large Telescope (Eisenhauer et al. 2003a; Bonnet et al. 2004) which was used in the scientific study in the second part of this thesis and is described in detail in section 7.1, page 133. Being an integral-field spectrometer, data taken with SINFONI do not suffer from slit-losses. We compare with SINFONI as it is used in the second part of this thesis and is the ‘workhorse’ of our group. It was also used in the faint object performance analysis of LUCIFER in section 5.2. SINFONI utilizes the same Hawaii-2 detector as LUCIFER with comparable noise characteristics of  $7e^-$  read noise and  $0.15e^-/s$  dark current. We show the system efficiency for comparison in figure 5.8. The efficiency in J, H, and K-band is higher by 5–10% than for LUCIFER. This is partly because for each band, SINFONI uses a different optimized grating. Also, the comparably low efficiency of the LUCI-1 interim detector in H and K plays a role. Comparing with the old LUCI, detector, the farer K-band efficiency (cf. figure 5.1) was comparable to SINFONI. The lower SINFONI efficiency in the blue part of the J-band is due to the SINFONI detector being rather insensitive in J-band towards lower wavelengths.

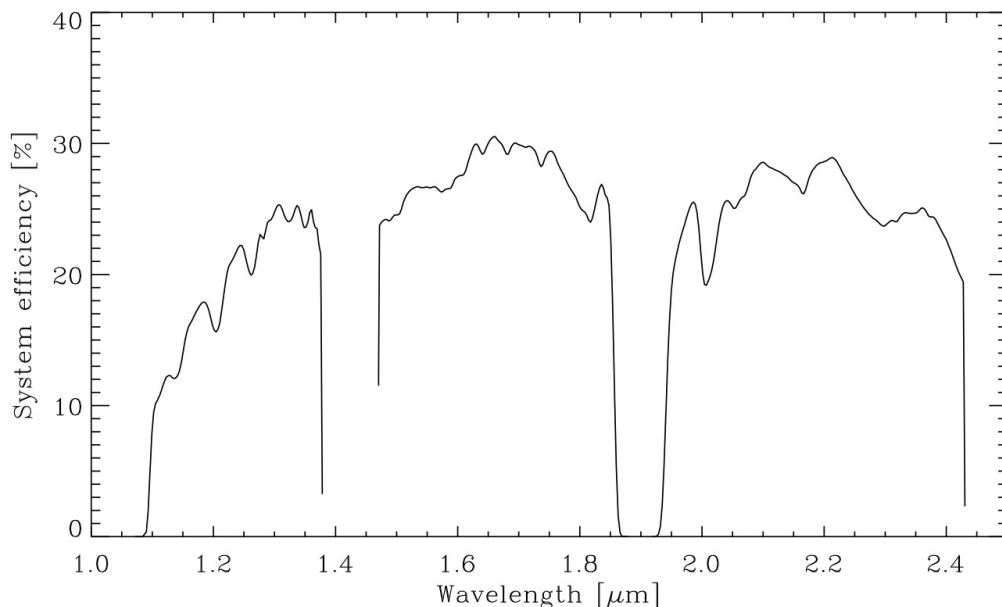


Figure 5.8.: Measured system efficiency for SINFONI at VLT. Data taken from the SINFONI exposure time calculator provided by ESO as of 10 June 2012 (<http://www.eso.org/observing/etc/>)

### 5.4.5. KMOS

KMOS (Sharples et al. 2006, 2010) is a new 2nd generation cryogenic near infrared multi-object IFU instrument, planned for installation at the VLT in 2013. It is built by a consortium of German and British institutes, including our group, together with ESO. It will feature 24 IFUs, each of which has 14x14 spatial elements with a 2.8'' FOV that can be positioned anywhere in the 7.2' diameter unvignetted field of the VLT Nasmyth focus. Closest approach of  $\gtrsim 2$  IFUs will be 6'' and  $\gtrsim 3$  IFUs can be clustered within a field of one square arcminute. The 24 IFUs are fed into three identical spectrographs with a resolution of  $R \sim 3500$  in i, Z, Y, J, H, and K band. Each spectrometer is equipped with one 2kx2k Hawaii-2 RG detector array. The IFUs are positioned in the field using cryogenic robotic arms with pickoff mirrors located at their tips. The efficiency of KMOS will be >20% in iZ, >20% in YJ, >30% in H, and >30% in K-band.

KMOS will combine the multiplexing capabilities of MOS instruments with the benefits of IFU instruments, e.g. no slit losses and full spatial information of the object. While the instrument will be featuring seeing-limited observations only, it is fair to say, that it will likely be a major game changer once operational on sky.

## 5.5. Lessons learnt

### 5.5.1. The LUCIFER MOS based high-z galaxy survey project

The ongoing high-z galaxy survey with the LUCIFER/MOS is a follow up of our SINS IFU-based survey of high redshift galaxies at  $z \sim 1.5-3$ , which the second part of this thesis is a project of. The SINS survey is described in detail in Part II, section 6.3.2.

The motivation is now to spectroscopically sample the high-redshift universe in the NIR which is only possible with multi-object capable spectrographs given the long integration times of several hours of these targets. This study aims at filling the gap between statistical population studies based on very large samples such as deep/wide photometric surveys and detailed case studies of smaller numbers of individual galaxies, e.g. from integral field spectroscopy. Robust measurements are needed of stellar mass, age, star formation rate, gas-phase metallicity and ionization state, dust obscuration, sizes, and morphologies, as well as accurate redshift determinations for sizable and complete samples of  $z \sim 1 - 3$  galaxies. High angular resolution near-IR imaging will constrain the structural parameters and distribution of the bulk of stellar mass from the rest-frame optical morphologies. For applications to  $z > 4$  studies, LUCIFER imaging and spectroscopy will probe the rest-frame UV properties of the most distant galaxy populations, in a manner analogous to what optical surveys are carrying out at  $z \sim 1-4$ .

### Pilot study

The pilot study aims to observe a large sample of mass-selected galaxies at  $z > 1$  with the science goal to

- to calculate dust/SFRs/gas fractions by observing  $H\alpha$ ,  $H\beta$ , and the continuum,
- constrain metallicity and line excitation mechanisms by measurement of all four BPT diagnostic lines ( $H\alpha$ ,  $H\beta$ , [NII]5838, [OIII]5007),
- to infer electron densities from stacked spectra for [SII] and [OI]
- to look at feedback effects via stacked spectra for broad emission line components.

For this study, fields visible from the LBT with a high density of known spectroscopic ( $z > 1$ ) redshifts need to be considered: GOODS-N, COSMOS, AEGIS, Lockmann Hole, Q2343, UDS/VVDS. By far best field for our study is GOODS-North, since it features the highest density of available spectroscopy for distant galaxies and is readily accessible for longer observing periods for the LBT site and features available multi-wavelength broad band imaging. Also, one of the ongoing Herschel/PACS survey fields of our group is located in GOODS-N, thus providing possible synergies between the projects.

The primary selection criteria for targets are:

- Galaxies at  $1 < z < 3$  with known  $z_{\text{spec}}$  to check emission lines for atmospheric OH-line avoidance
- Galaxies who have all four BPT lines ( $H\alpha$ ,  $H\beta$ , [NII]5838, [OIII]5007) visible between OH lines have high priority, or  $H\alpha$  + [NII] otherwise
- the sub-field has to have a high surface density for MOS

### Status to date

To date, May 2012, 10 observation runs with each 2-3 nights of observation have been carried out over the last 2.5 years. During this time we were able to complete spectroscopic observations of 9 masks in H- and K-band each. We have attempted to observe 157 objects, selected according to the criteria given above, in the GOODS-North field and the Q2343 field (also used in the second part of this thesis). For 101 objects, spectroscopic redshift were available, for 49 only photometric redshifts. In addition, we put in 7 “filler” objects of unknown redshift.

Of the 157 objects, 95 objects (60%) have been detected in at least one emission line, with a higher rate of positive detections for the targets with spectroscopic redshifts (70%)

## 5.5. Lessons learnt

---

than for photometric redshifts (30% positive detections). One of the filler objects was detected. The reasons for the non-detections are likely intrinsic faintness of the object but also wrong redshift, that place the emission lines in other observing bands or entirely onto OH lines. This is supported by the relative higher fraction of positive detections based on spectroscopic redshifts.

Either one or both  $H\alpha$  and  $[\text{NII}]\lambda 6584$  lines were detected in 85 objects (89% of the detected sources) of which 33 objects have robust detections in both lines (34% of all detected objects). Thus we can derive metallicity (limit-) values for 89% of the detected sources (48% of all attempted) and robust values for 34%. All four BPT lines however were only robustly detected in 7 of the detected sources, including limits due to limits in either  $[\text{OIII}]\lambda 5007$ ,  $[\text{NII}]\lambda 6584$  or  $H\beta$  the number of BPT object rises to 36 (37% of the detections). 36% of the metallicity limits are due to OH line contamination, for the rest the  $[\text{NII}]$  line was too weak to detect. In turn, OH lines were responsible for 27% of the limits of the BPT data points.

Despite the selection for OH line avoidance, 49 (=51%) of the detected objects still show contamination of one (33 objects) or more (17 objects) emission lines with a nearby OH line.

One target, which our group had already observed in the sub-mm wavelength regime using the IRAM interferometer on the Plateau de Bure, we have observed in pseudo-IFU mode, synthesizing a 3D IFU data cube by doing adjacent long-slit observations. This mode has proven to be very successful, albeit a significant overhead due to the eight individual longslit pointings. The positive result however shows the possible high accuracy of the instrument-telescope system under good weather and observing conditions. Currently we apply this scheme to a MOS masks where we will “slit-scan” seven objects simultaneously. If successful, this technique could mitigate the significant overhead in the single-object “longslit-scan-IFU-mode”.

The data analysis is currently ongoing and will be presented in two upcoming papers (Kurk et al. in prep.; Loose et al. in prep.).

### 5.5.2. Lessons learnt during observation

#### Observing time loss

From February 2009 till March 2012 the german LBTB consortium had a total of 1097h of observation time, of which our share was 37% or 142.3h. In the following, we list the fraction of the total 1097h observing time lost due to various reasons:

- telescope errors: 3.1%
- instrument errors: 5.0%
- weather loss: 46.4%

While observing conditions are often excellent with regular seeing values of  $\lesssim 0.6''$  during clear nights, the number of closed-dome nights is very significant mostly due to high winds or longer periods of rain and snow.

### **Complications on the operations level**

During operations it has shown that the instrument is fairly complex to handle and requires skillful observers and good preparation. The current software GUIs and scripting engine still needs to be improved in terms of usability. Especially doing quick on-the-fly changes during the night have been prone to operating errors. Incorrect scripts have led to numerous wrong instrument setups and/or telescope setups and subsequent loss of observation time. While a script-structure checking tool is available, a semi automatic semantic checker is not yet available. Also operations cannot be automated yet. However, an observation planning tool that allows for queuing, pausing and skipping scripts is currently under development. Recovering from instrument errors required instrument team personnel to be present remotely for a greater fraction of instrument errors, especially during the early operation phases. The telescope performance and operations efficiency is constantly increasing, however, compared to e.g. the VLT, the LBT still needs to improve on operational level.

## **5.6. Summary and Outlook**

Near infrared MOS spectroscopy of faint sources is now routinely done, it remains - however- challenging. In the following, we give a summary of the current state and an outlook to the next steps in instrument operations.

### **5.6.1. Summary**

#### **Overall good instrument performance**

The system efficiency is comparable to or even exceeds other competing NIR (multi object) spectrometers, the two camera design means no tradeoff between imaging and

## 5.6. Summary and Outlook

---

spectroscopy, the different gratings optimize efficiency and offer useful resolutions in seeing and -in the future- diffraction limited observations. The FOV is a little smaller than for competing instruments. The reliability of the unit is good with occasional errors, which, however, after various upgrades, have not lead to major time loss in recent times as compared to the first months on sky. The versatility afforded by the diverse operation modes makes LUCIFER a very competitive instrument, especially with the upcoming adaptive optics assisted observation modes.

### **Limiting factor: instrument complexity**

The LUCIFER MOS imager and spectrograph is a very complex interplay of various units. The compact design and design-changes late in the project have led to complications that caused some designs, especially of the MOS unit, to be very complex and susceptible to errors. Various hardware simplifications and descoping of functionality were introduced in the last years, however, some designs cannot be changed with the unit now completed. Small errors in these units can still potentially cause downtime of up to several days. Also, some recovery still requires deep knowledge of the various sub-units and their interplay. The mask cabinet exchange mechanism with auxiliary cryostats is very complex and labor-intensive in terms of on-site operations.

### **Limiting factor: observation- and facility efficiency, weather**

On-site operations have greatly improved over the last two years, however, a significant time loss can still be attributed to observation and facility errors. The complexity of the instrument is quite demanding and well prepared observation scripts -and observers- are mandatory. A more user friendly GUI could increase efficiency especially if on-the-fly changes to the instrument and telescope configuration are needed. The telescope performance and operations efficiency is constantly increasing, however, compared to e.g. the VLT, the LBT still needs to improve on operational level. The introduction of service-mode observations should be discussed given the system (telescope and instrument) complexity.

Another important limiting factor is the weather on site. While observing conditions are often excellent with regular seeing values of  $\lesssim 0.6''$  during clear nights, the number of closed-dome nights is still very significant mostly due to high winds or longer periods of rain and snow;  $\sim 45\%$  of observation time in the last 2.5 years were lost due to bad weather.

**Static masks are not limiting the science - when cut and handled right**

The static user cut MOS masks have proven to be very reliable. Mask exchange times of  $\lesssim 5$  minutes are only of small fraction of the overall acquisition and setup time prior to an observation block. Currently the turnaround time for new masks from design to availability in the instrument is  $\sim 1$  month. This time should be reduced as it could potentially lead to situations where -given good observing conditions and good efficiency- science programs could run 'out of masks' if pre-imaging / results from the last run are needed for mask design for the next run.

**5.6.2. Outlook to future use, science project planning and upgrades****Two LUCIFERs significantly raising efficiency**

From 2013 on both LUCIFER instruments will be mounted to the telescope. This provides an immense boost in efficiency and versatility as the instruments can be used together or independently (limited to roughly the same field on sky) in imaging or spectroscopy - each one with or without adaptive optics.

**Efficiency boost by Hawaii-2 RG detector very soon**

The new Hawaii-2 RG detectors in LUCIFER 1 and 2 have significantly higher quantum efficiencies, which raise the overall system efficiency by likely 40–60%, i.e. total efficiency up to 35–40%. The first RG detector has now arrived at the test lab and features a quantum efficiency of 0.87 and 0.82 at 1 and  $2\mu\text{m}$ , a read-out noise of  $3.1e^-$  and a dark current  $< 0.01e^-/\text{s/pixel}$ . These values are very competitive and will get LUCIFER on par with the system efficiency of MOSFIRE.

**Configurable slit upgrade - possible, but detailed benefit check needed**

Given the versatility of a configurable slit unit as discussed above and given the complexity of the current MOS mask unit, a change to a configurable slit unit should be evaluated. However, the MOSFIRE slit unit design can likely not be adapted as the mechanical dimensions of the LUCIFER focal plane alone are 2 times smaller and the cryo-mechanics of the MOSFIRE CSU could not be adapted. First ideas of alternative designs have been discussed, but a mechanism with significantly higher reliability than the current design

## 5.6. Summary and Outlook

---

and with a simpler design than the MOSFIRE CSU needs yet to be designed. The available free space envelope in the instrument is likely sufficient to retrofit LUCIFER with a configurable slit unit *along with* the current unit. Given the significant costs and time for a new MOS-unit design, a detailed benefit check is needed.

### **IFU upgrade - powerful and possible**

The available space envelope in the lower part of the LUCIFER cryostat is spacious enough to potentially house an IFU along the current MOS unit. Such an IFU would -similar to the 'nuMOIRCS' design- be deployed into the beam from the side and generate an f-ratio matched pseudo long slit output in the focal plane using e.g. fibers with a lenslet array. The output slit ideally would consist of 2048 square spaxel slit, 150mm long, resulting in a full J, H or K band coverage at  $R \sim 4000$ . The on sky resolution element could be 100 or 50mas (= 60 or  $30\mu\text{m}$  in the focal plane) resulting in a FOV of  $32 \times 64$  spaxel =  $3.2'' \times 6.4''$  at 100mas resolution or  $1.6'' \times 3.2''$  at 50mas. The FOV could be divided into two arms which could position their field inside the  $4' \times 4'$  instrument FOV. From the scientific point of view this could be an interesting NIR complement to the IRAM interferometer both being located on the northern hemisphere.

### **Choose your science well!**

Operations have shown that a good preparation is key to successful NIR MOS observations. Extra care needs to be taken to match the used slit width to the prevailing conditions but at the same time paying attention to the change in spectral resolution and thus efficiency of OH line avoidance. High-z objects need to be chosen entirely on spectroscopically confirmed redshifts as the fraction of successful photometric redshift selected objects is comparably low. The high fraction of lost nights due to weather demand that operating errors are minimized and observers are readily prepared for the observations.

### **Laser and NGS adaptive optics**

LUCIFER will greatly benefit from the upcoming adaptive optics capabilities of the LBT. In the first stage imaging of a  $30'' \times 30''$  FOV will be commissioned, spectroscopy thereafter. The ARGOS GLAO system will be most beneficial for MOS spectroscopy as the AO correction will be on the full FOV, enabling the choice of small slits and thus good OH avoidance at  $R \sim 4000$  while still covering the full H or K band on the detector.

To close the first part, we present the first -preliminary- LUCIFER data which already at this very early stage show the impressive capabilities of this new instrument and give a hunch on what will be possible in terms of scientific analysis and discovery in the very near future - skillful operation and good weather provided.

In figure 5.9 we show a  $[\text{NII}]\lambda 6584/\text{H}\alpha$  vs.  $[\text{OIII}]\lambda 5007/\text{H}\beta$  line diagnostics diagram ('BPT diagram, see 9.2.2) with LUCIFER (green) and SINFONI (blue) galaxies plotted as star shapes and the local galaxy population from the SDSS as grey points in the background. See caption for details.

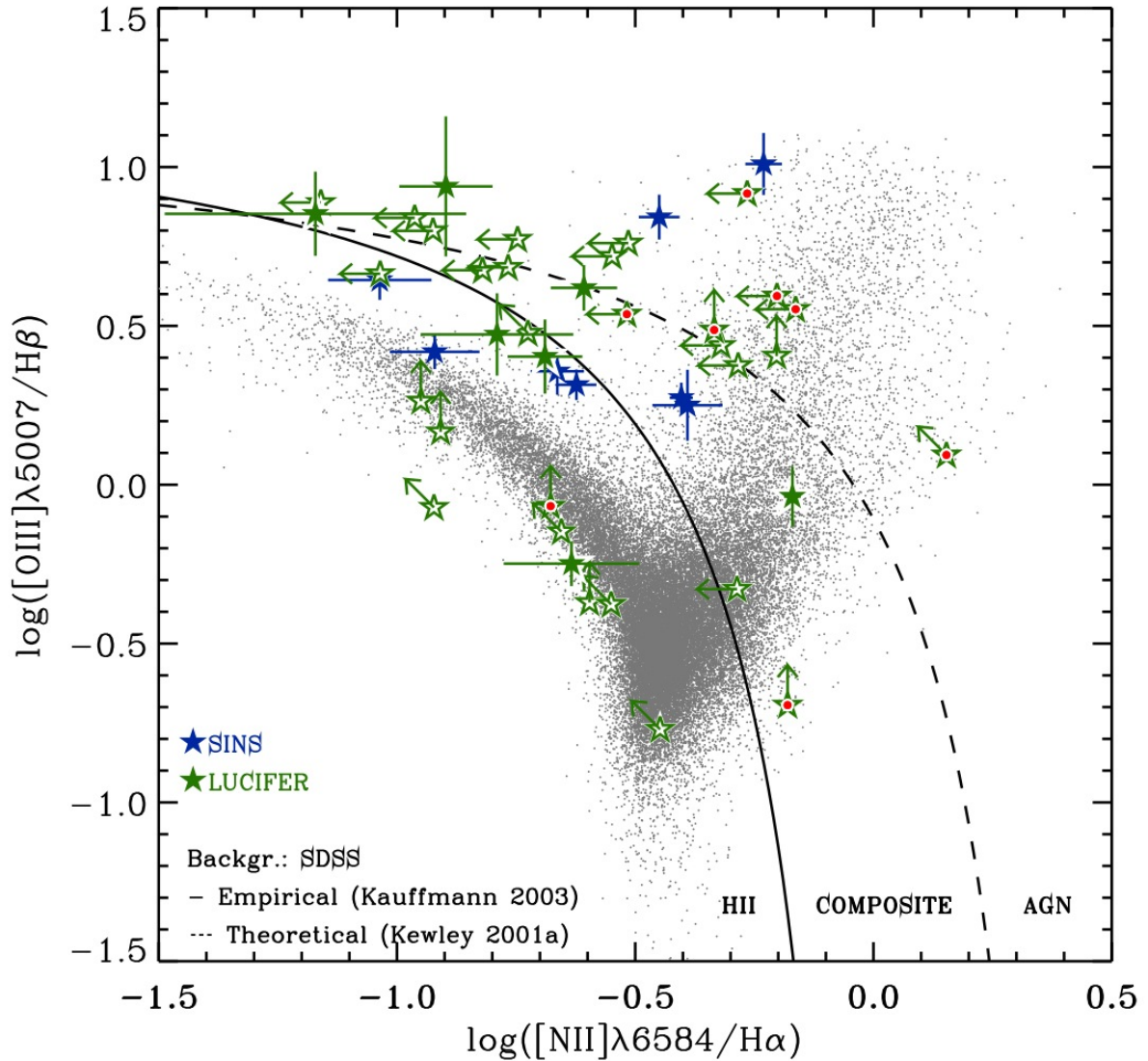


Figure 5.9.:  $[\text{NII}]\lambda 6584/\text{H}\alpha$  vs.  $[\text{OIII}]\lambda 5007/\text{H}\beta$  'BPT' diagram showing integrated values. Background: local galaxy population from the SDSS. Star-forming galaxies and HII-regions are located on the left branch with decreasing gas-phase oxygen abundances towards lower  $[\text{NII}]/\text{H}\alpha$  and higher  $[\text{OIII}]/\text{H}\beta$  ratios. Galaxies with shocks and AGN dominating the gas excitation are located on the right branch. The blue 'star' data points show the source-integrated measurements from the SINS galaxies in this work. The green 'stars' are preliminary LUCIFER data (open stars being limit). Red dots indicate objects where one or more lines show considerable OH contamination. Like the galaxies analyzed in this work, the LUCIFER galaxies tend to be offset towards the region between the star-forming and AGN branches, suggesting that various excitation mechanisms contribute in different proportions to the global line emission or, possibly, different physical conditions are prevailing in non-AGN actively star-forming galaxies.

## **Part II.**

# **Massive star-forming galaxies at high-redshift: a study of spectrally- and spatially-resolved line excitation, metallicity and extinction**



## Chapter 6.

### The universe at $z \sim 1-3$

#### 6.1. Galaxy formation and evolution over cosmic time

Over the past two decades, progress in the field of observational cosmology has been spectacular. In particular, the results from measurements of the cosmic microwave background with the Wilkinson Microwave Anisotropy Probe (WMAP) have been a significant step toward the adoption of a concordance cosmology with impressively accurate determinations of many of the relevant cosmological parameters (Larson et al. 2011; Komatsu et al. 2011; and references therein). This now “standard model” provides the backbone for studies of galaxy formation and evolution. It includes a fairly mature view of the hierarchical structure formation in the cold dark matter (CDM) paradigm, under the sole influence of gravity (e.g., White et al. 1978; Blumenthal et al. 1984; Davis et al. 1985; Springel et al. 2006).

The same is not true for our understanding of the formation and evolution of galaxies. In the framework of the  $\Lambda$ -CDM paradigm, galaxies form as baryons cool and condense at the center of dark matter halos, and subsequently grow through further gas infall and merger events. However, the evolution of the baryonic component does not follow simply the hierarchical merging of dark matter structures. It is a highly non-linear problem, which is largely driven by the complex and competing processes of cooling, angular momentum loss and exchange, and feedback from star formation and active galactic nuclei (AGN). Phenomenological (or “semi-analytical”) models and numerical simulations (based on N-body and/or hydrodynamical codes) have been developed to describe the formation and evolution of galaxies in a cosmological context (see reviews by Bertschinger 1998 and Baugh 2006). Although these approaches are very powerful, they rely heavily on simple parameterizations of the physical mechanisms that likely drive galaxy evolution. A major challenge is the tremendous dynamic range required — from the sub-parsec scales of molecular cloud cores to the mega-parsec scales of the relevant environment around galaxies, and from densities of  $n \sim 10^{-6}$  to at least  $\sim 10^3 \text{ cm}^{-3}$ . The sub-parsec scales on which relevant processes occur still remain currently inaccessible, and recipes

for the implementation of the “sub-grid physics” are needed. Consequently, current state-of-the-art modeling of galaxy formation and evolution relies on observations to not only provide the tests of such models, but the input as well.

The rapid multiplication of deep, wide-area multi-wavelength surveys and optical spectroscopic campaigns over the last fifteen years has yielded impressively large samples of galaxies at redshift  $z \gtrsim 1$  that are available for study as a function of lookback time. We now have a fairly robust outline of the global evolution of the cosmic stellar mass and luminosity density, star formation history, and nuclear activity. Roughly half of the stellar mass in galaxies (and  $> 90\%$  in massive  $\gtrsim 10^{11} M_{\odot}$  galaxies) was assembled by redshift  $z \sim 1$ , i.e., during the first six billion years after the Big Bang. The peak of star formation (Figure 6.1), major mergers, and quasar activity indicative of the growth of super-massive black holes occurred around  $z \sim 1 - 2$  (e.g., Fan et al. 2001; Chapman et al. 2005; Hopkins & Beacom 2006; Rudnick et al. 2003, 2006; Grazian et al. 2007; Perez-Gonzalez et al. 2008; Le Borgne et al. 2009; Gruppioni et al. 2010 ). The epochs around  $z \sim 1 - 2$  also appear to correspond to a crucial transition with the emergence of the bimodality in galaxy colors and the Hubble sequence of galaxies as observed in the present-day universe, characterized by mostly red spheroidal systems with little on-going star formation and a blue population of spiral and irregular galaxies actively forming stars (e.g., Bell et al. 2004; van den Bergh et al. 1996, 2001; Lilly et al. 1998; Stanford et al. 2004; Ravindranath et al. 2004; Papovich et al. 2005; Kriek et al. 2008, 2009; Williams et al. 2009). These surveys have set the stage for detailed spatially-resolved studies of individual galaxies, essential to address the issue of *how* galaxies acquired their mass and were shaped into the present-day population.

In particular, the internal motions, the structure, and the distribution of stars, metals, dust, and gas within galaxies provide crucial constraints on the physical processes at play, their relative importance, and their timescales. These properties can now be mapped for distant galaxies thanks to significant progress in instrumentation. By revealing better the internal workings such studies have led to major advances in our understanding of how galaxies formed and evolved in the early universe.

## 6.2. Recent developments and the emerging picture

For some time, the star formation and stellar mass growth of massive galaxies at early cosmic epochs had been widely attributed to violent major merger events between galaxies (i.e., with progenitor mass ratio  $\gtrsim 1 : 3$ ).

Recently, our picture has been shifting towards one in which a substantial fraction — if not the majority — of  $z \sim 1 - 3$  star-forming galaxies appears to be continuously fed by gas promoting and maintaining star formation rather than being occasionally bursting

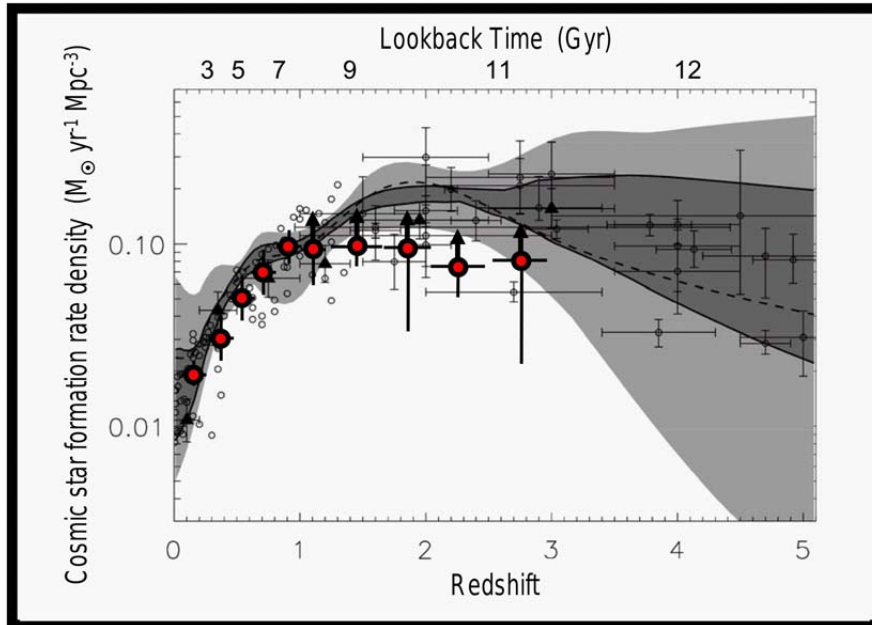


Figure 6.1.: A recent version of the variation of cosmic star formation rate density as a function of redshift, or lookback time (taken from Le Borgne et al. 2009, Fig. 8). The data points are a compilation of selected observational results (including earlier data from Hopkins & Beacom 2006) and the grey-shaded areas show regions covered by a range of models of the galaxy luminosity function to reproduce observed number counts in the mid- and far-IR regimes. The large red-filled circles are derived from the most recent and direct calorimetric measurements of the star formation rates from observations with the PACS instrument on-board the Herschel satellite (from Grupioni et al. 2010). The broad peak around  $z \sim 1 - 3$  indicates the epochs of most active cosmic star formation activity, when massive galaxies were undergoing rapid growth in their stellar mass (e.g., Rudnick et al. 2003, 2006; Pérez-González et al. 2009).

as a result of a (major) merger. Spatially-resolved mapping of the gas kinematics, now possible at  $z \gtrsim 1$ , have provided some of the most convincing evidence for the existence of many large rotating *disks* among the bulk of the massive star-forming population, without any sign of on-going merger (e.g., Förster Schreiber et al. 2006, 2009; Genzel et al. 2006, 2008; Shapiro et al. 2008; Cresci et al. 2009; Épinat et al. 2009; Jones et al. 2010; Gnerucci et al. 2010; Wisnioski et al. 2011). In parallel, multiwavelength galaxy surveys have shown that the SFR correlates tightly with stellar mass  $M_*$  (with small scatter  $\sim 0.3$  dex in logarithmic units), and that the  $\text{SFR}(M_*)$  relation steadily declines from  $z \sim 2.5$  to  $z \sim 0$  (Daddi et al. 2007; Elbaz et al. 2007; Noeske et al. 2007). The tightness of this relationship, dubbed the “main-sequence” of star-forming

## 6.2. Recent developments and the emerging picture

---

galaxies, is difficult to reconcile with a (gas-rich) major merger dominated scenario in which galaxies undergo large and brief variations in their star formation rates. Most recently, the dominance of large structurally disk-like galaxies on the “main sequence” and the scarcity of major-merger driven systems at  $z \sim 1-3$  have been set on a robust statistical footing (e.g. Wuyts et al. 2011, Rodighiero et al. 2011). Observations of (sub-)millimeter CO line emission in non-major merging “main-sequence” galaxies at  $z \sim 1-3$  uncovered large molecular gas reservoirs implying gas-to-total baryonic mass fractions of  $\sim 20-80\%$ , providing further evidence in support of efficient but fairly smooth gas accretion mechanisms (Tacconi et al. 2010; Daddi et al. 2010; Genzel et al. 2011).

The detailed properties of high redshift galaxy disks, which can now be measured on physical scales as small as just a few kiloparsecs (see Section 6.3), have revealed important clues on their formation and evolution. The ionized gas kinematics and morphologies indicate that high-redshift disks follow a similar size-velocity relation as  $z \sim 0$  late-type spiral galaxies, and the specific angular momenta of their baryons are inferred to be comparable to those of their dark matter halos (e.g., Förster Schreiber et al. 2006; Bouché et al. 2007). The results also suggest little net transfer of angular momentum between the disk’s baryons and the parent dark matter halo upon collapse of the baryons from the virial radius to the disk scale length of a few kiloparsecs. High-redshift disks appear to be generally characterized by high intrinsic local gas velocity dispersions of  $\sigma_0 \sim 30-90 \text{ km s}^{-1}$  and low ratios of circular velocity to intrinsic velocity dispersion  $v_c/\sigma_0 \sim 2-6$  (e.g., Genzel et al. 2006, 2008, 2011; Förster Schreiber et al. 2006, 2009; Cresci et al. 2009; Wright et al. 2009; Épinat et al. 2009; Jones et al. 2010; Wisnioski et al. 2011). These properties imply that the disks are geometrically thick, as inferred from the morphologies of distant edge-on disk-like systems (e.g., Elmegreen et al. 2005c). Furthermore, high-redshift disks can exhibit prominently clumpy and irregular morphologies, despite their ordered rotation-dominated gas kinematics. Large kpc-sized clumps are observed in the ionized gas distribution tracing star formation, in the stellar populations seen in rest-UV and rest-optical continuum light, and in the molecular gas and dust content; their inferred masses are in the range  $\sim 10^7-10^{9.5} M_\odot$ , typically a few percent and up to as much as  $\sim 20\%$  of the host galaxy’s total mass (e.g., Elmegreen et al. 2009; Tacconi et al. 2010; Genzel et al. 2008, 2011; Jones et al. 2010; Förster Schreiber et al. 2011b; Swinbank et al. 2011; Guo et al. 2011, Wisnioski et al. 2011).

This new empirical evidence on the nature of massive star-forming galaxies and the properties of disks at  $z \sim 1-3$  matches remarkably well with state-of-the-art cosmological simulations. In these simulations, massive galaxies acquire a large fraction of their baryonic mass via steady, narrow, fairly smooth cold streams or rapid series of minor mergers (e.g., Binney 2004; Kereš et al. 2005; Dekel & Birnboim 2006; Dekel et al. 2009; Agertz et al. 2009; Ceverino et al. 2010). The cold streams are able to penetrate effectively through the shock-heated media of massive dark matter halos and, along with minor merger events, can sustain elevated star formation rates over much longer timescales

than violent dissipative major mergers. Under these conditions, the net angular momentum is largely preserved as matter is accreted, early disks can survive and be continuously replenished with fresh gas, and internal dynamical processes can largely drive their early evolution. Both theoretical arguments and numerical simulations of gas-rich turbulent disks indicate that massive kpc-sized clumps can form in-situ through gravitational instabilities (e.g., Noguchi 1999; Immeli et al. 2004a, 2004b; Bournaud et al. 2007; Elmegreen et al. 2008; Dekel et al. 2009; Agertz et al. 2009; Ceverino et al. 2010, 2012; Genel et al. 2012). The predicted clump sizes and masses are comparable to those inferred from the observations (e.g., Genzel et al. 2008, 2011; Bournaud et al. 2008; Elmegreen et al. 2009; Jones et al. 2010). The first measurements of the Toomre  $Q$  parameter (Toomre 1964) in several  $z \sim 2$  clumpy disks indicate  $Q < 1$ , with clumps located in regions of minimum  $Q$ , providing further empirical support for clump formation via disk instabilities (Jones et al. 2010; Genzel et al. 2011; Aumer et al. 2010; Genel et al. 2012).

According to these theoretical arguments and numerical simulations, the massive clumps could migrate towards the gravitational center as a result of their mutual interactions and of dynamical friction against the host disk, and coalesce into a young bulge on timescales of  $\lesssim 1$  Gyr. Clumps may also contribute to the redistribution of mass and angular momentum and to the growth of the disk by losing part or most of their mass through vigorous stellar feedback and/or strong tidal torques, depending on the importance of these disruptive effects. This “clump-driven” scenario has gained popularity over the past few years as an important path for the early formation phases of the spheroidal and disk components of present-day massive galaxies although its importance is still debated (e.g. Bournaud et al. 2007; Murray et al. 2010; Krumholz et al. 2010; Genel et al. 2012; Genzel et al. 2011; Guo et al. 2011; Hopkins et al. 2011; Wuyts et al. 2012; Newman et al. 2012). The large velocity dispersions and gas mass fractions make high-redshift disks very different from their present-day counterparts, which have typically  $v_c/\sigma_0 \sim 10 - 20$  and molecular gas mass fractions of  $\lesssim 10\%$  (e.g., Dib et al. 2006; Épinat et al. 2010; Leroy et al. 2005). The high gas mass fractions and low  $v_d/\sigma_0$  ratios observed in  $z \gtrsim 1$  disks naturally lead to the formation of larger self-gravitating, star-forming complexes than in the less gas-rich, dynamically cold, and geometrically thin  $z \sim 0$  disks (e.g., Escala & Larson 2008; Elmegreen et al. 2009b; Genzel et al. 2011). In addition, the presence of a massive stabilizing stellar disk and/or bulge in local mature disk galaxies also leads to smaller lower-mass star-forming complexes, or even to the suppression of their formation (e.g., Bournaud et al. 2007; Dekel et al. 2009; Ceverino et al. 2010).

### 6.3. Spatially- and spectrally-resolved studies

Results from spatially- and spectrally-resolved observations at near-IR wavelengths ( $\lambda = 1 - 2.5 \mu\text{m}$ ) have made a significant contribution to the emerging picture summarized in Section 6.2. While much remains to be learned, this highlights the great potential of such resolved in-situ investigations in elucidating the role of, and the interplay between the various processes that drive galaxy evolution at  $z \sim 1 - 3$ . Such studies have now become possible thanks to major instrumental advances. The “SINS” survey, the backdrop for the work presented in the second part of this thesis work, has been ground-breaking in exploiting these new opportunities, as outlined in this section.

#### 6.3.1. Near-IR integral field spectroscopy

The advent of sensitive near-IR integral field spectrographs on 8 – 10 m-class ground-based telescopes has opened new avenues in the study of distant galaxies. Integral field spectroscopy provides simultaneously the full spectral information across the entire field of view, providing a full two-dimensional mapping of the kinematics, star formation, and physical conditions across galaxies. Compared to slit spectroscopy, integral field spectroscopy does not suffer from the biases resulting from slit losses, slit alignment, or uncertainties in the slit positioning. Observations in the near-IR allow one to measure the *rest-frame optical* emission from objects at  $z \sim 1 - 4$ , where the effects of dust attenuation are less severe and the contribution from hot young stars less important than at rest-UV wavelengths. The rest-frame optical regime contains numerous key diagnostic spectral features that are well-understood physically and have been extensively studied from large samples of galaxies in the local universe, enabling consistent comparisons between distant and present-day galaxies. The strongest emission lines include notably the Balmer H recombination lines of  $H\alpha$  and  $H\beta$ , and forbidden transitions of singly- and doubly-ionized N, O, and S ([NII]  $\lambda\lambda 6548, 6584\text{\AA}$ , [OIII]  $\lambda\lambda 4959, 5007\text{\AA}$ , [OII]  $\lambda\lambda 3726, 3729\text{\AA}$ , [SII]  $\lambda\lambda 6716, 6731\text{\AA}$ ; Osterbrock 1989 gives an extensive review). These nebular emission lines provide measures of the intensity and hardness of the ionizing radiation field, produced by hot young massive stars or an AGN. Their relative intensities can be used to constrain the amount of attenuation by interstellar dust (“extinction”), the main sources of line excitation (via photoionization and shocks), the chemical composition, the ionization parameter and the electron density of the nebular gas. The emission line widths, centroids, and spectral profiles contain information on the ionized gas kinematics.

Table 6.1 lists the relevant set of rest-frame optical emission lines along with the near-IR band into which they are shifted for  $z \sim 2$  sources. Key diagnostic ratios based on these strong lines are listed in table 6.2.

Line	$\lambda_{\text{rest}}$ [Å]	NIR observation band for $z \sim 2$ sources
[OII]	3726, 3729	J
H $\beta$	4861	H
[OIII]	4959, 5007	H
[NII]	6548, 6584	K
H $\alpha$	6563	K
[SII]	6716, 6731	K

Table 6.1.: The strongest nebular rest-frame optical emission lines most relevant for the study of high-redshift galaxies and the near-infrared atmospheric transmission band where they can be observed for  $z \sim 2$  sources.

Line ratio	Main dependence on property
[NII]6584 / H $\alpha$	Metallicity, ionization parameter <sup>a</sup>
[OIII]5007 / [OII]3727	Metallicity, ionization parameter
[OIII]5007 / H $\beta$	Ionization parameter
[NII]6584 / [OII]3727	Metallicity
[SII]6716, 6731 / H $\alpha$	Hardness of ionization spectrum
[SII]6716/6731	Electron density
[OII]3729/3726	Electron density
H $\alpha$ / H $\beta$	Nebular extinction

<sup>a</sup> This parameter quantifies the number of hydrogen ionizing photons impinging on the gas per H atom and per unit of time. For the classical Strömgren sphere representation consisting of a shell with uniform gas density and radius  $R$  around a central point-like source,  $U \equiv Q / (4 \pi R^2 n_{\text{H}} c)$ , where  $Q$  is the H ionization rate of the source,  $n_{\text{H}}$  is the H density ( $\approx n_{\text{e}}$  in fully ionized nebulae), and  $c$  is the speed of light.

Table 6.2.: Commonly used strong line diagnostics of the physical conditions of ionized gas and nebular extinction

### 6.3. Spatially- and spectrally-resolved studies

---

Cosmological surface brightness dimming, which scales in intensity as  $I(z)/I(z=0) \propto (1+z)^4$ , implies that distant galaxies are faint even if they are intrinsically luminous. For instance, main-sequence  $z \sim 2$  star-forming galaxies with stellar masses  $M_* > 10^{10} M_\odot$  and intrinsic star formation rates from  $\sim 10$  up to several times  $100 M_\odot \text{ yr}^{-1}$  have observed H $\alpha$  emission line fluxes between a few  $10^{-17}$  and a few  $10^{-16} \text{ erg s}^{-1} \text{ cm}^{-2}$  only (Erb et al. 2006; Förster Schreiber et al. 2009; Mancini et al. 2011). With such low flux levels, high-redshift galaxies only became routinely accessible with the newest generation of high-throughput near-IR integral field spectrographs equipped with more sensitive detectors, and with the increased light-collecting power of 8 – 10 m-class telescopes.

Large cosmological distances also imply small apparent angular sizes; for  $z \sim 1 - 3$ ,  $1''$  corresponds roughly to 8 kpc. Thus, observations of distant galaxies further benefit from the higher resolving power afforded by large telescopes and, even more, by the technique of adaptive optics (AO). AO systems were devised to correct for the blurring effects of atmospheric turbulence, which limits the effective angular resolution and prevents reaching the diffraction limit of large ground-based telescopes (for an 8-m telescope, the diffraction limit is  $\approx 60 \text{ mas}$  at  $\lambda \approx 2 \mu\text{m}$ ). In practice, due to the trade-off between surface brightness sensitivity (driving the choice of instrumental pixel scale) and resolution, AO-assisted near-IR integral field spectroscopic observations of faint high-redshift galaxies reach  $0''.1 - 0''.15$ , or  $\sim 1 \text{ kpc}$  at  $z = 2$ . This resolution represents an improvement by a factor of  $\sim 4 - 5$  over what is achieved under good seeing conditions in the near-IR of  $\sim 0''.5$ .

#### 6.3.2. The SINS survey

The “SINS” survey is a major survey of high-redshift galaxies based on near-IR integral field spectroscopy, carried out with the SINFONI instrument at the Very Large Telescope (VLT) of the European Southern Observatory (ESO). SINFONI consists of the near-IR integral field spectrograph “SPIFFI” built by MPE and the AO module “MACAO” developed by ESO (Bonnet et al. 2003; Eisenhauer et al. 2004). The main goals of SINS are to investigate in detail the mass assembly, star formation, and feedback processes in young galaxies through full two-dimensional spatially-resolved mapping of the kinematics, the distribution of star formation, and the physical conditions of the interstellar medium. Initiated in 2004, SINS has collected SINFONI data of 80 massive star-forming galaxies in the redshift range  $1.5 \lesssim z \lesssim 3$ , the epoch of peak cosmic star formation rate density (see Förster Schreiber et al. 2009, hereafter FS09). First carried out as a key program part of the MPE Guaranteed Time Observations at the VLT in return for the development of SPIFFI, it is continuing through several Open Time programs to expand the sample as well as the set of spectral diagnostics mapped on scales of 1 – 5 kpc. The largest subset of SINS consists of 62  $1.3 < z < 2.7$  objects drawn from parent samples selected on the basis of their rest-optical or rest-UV magnitudes and/or colors and for

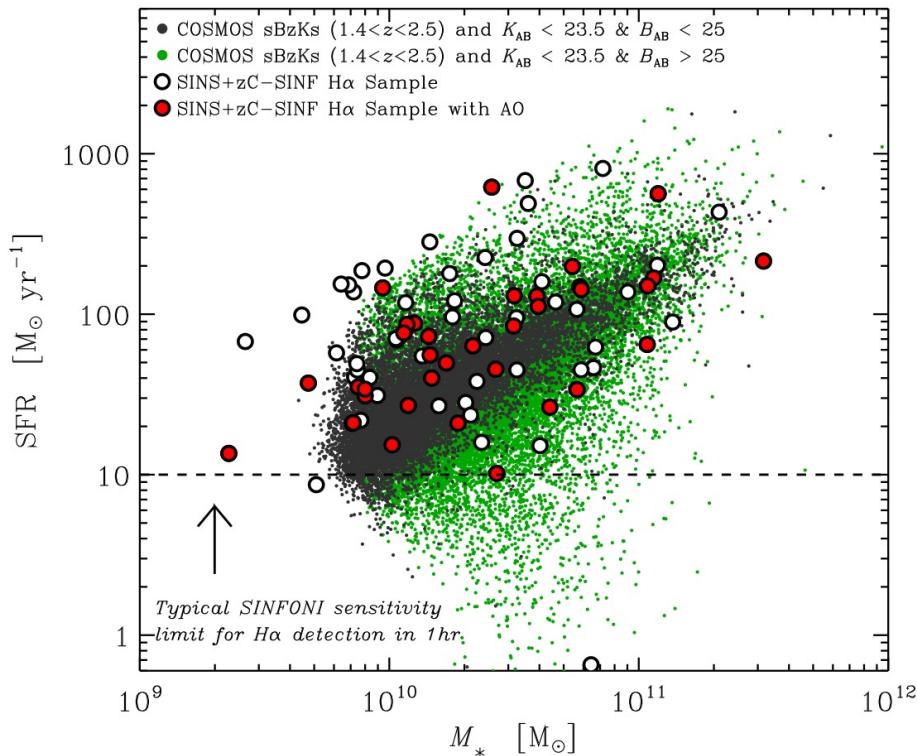


Figure 6.2.: Distribution of the SINS and zC-SINF  $H\alpha$  samples in the stellar mass ( $M_*$ ) versus star formation rate (SFR) plane (based on data presented by Förster Schreiber et al. 2009 and Mancini et al. 2011). The large white-filled circles correspond to galaxies observed with SINFONI in seeing-limited mode with typical angular resolution of  $\text{FWHM} \approx 0''.6$  (or  $\approx 5$  kpc at  $z \sim 2$ ). Red-filled symbols correspond to the subset of the targets followed-up with adaptive optics, with a resolution of  $\approx 0''.15 - 0''.2$  (or  $\approx 1.3 - 1.7$  kpc). The SINS and zC-SINF  $H\alpha$  samples are compared to the distribution of the more general population of massive  $z \sim 2$  galaxies in the COSMOS survey field down to the same  $K$ -band magnitude as the faintest SINS/zC-SINF objects with  $B$ -band magnitude brighter or fainter than 25 mag (small grey and green dots, respectively; from Mancini et al. 2011). The SINS and zC-SINF  $H\alpha$  samples probe the bulk of the massive star-forming populations at  $z \sim 2$  over roughly two orders of magnitude in  $M_*$  and SFR, with some bias towards the most actively star-forming galaxies (especially at lower masses) resulting from the selection of targets with an accurate redshift from optical spectroscopy and preferentially with  $\text{SFR} \gtrsim 10 M_\odot \text{yr}^{-1}$  to help ensure detection of the targeted  $H\alpha$  line emission.

which the Balmer recombination line of  $H\alpha$  was targeted (hereafter the “SINS  $H\alpha$  sample”). An additional set of 30 similar galaxies were observed as part of an on-going ESO Large Program to expand on the SINS survey, the “zC-SINF  $H\alpha$ ” sample (Mancini et al.

### 6.3. Spatially- and spectrally-resolved studies

---

2011). In total, 110  $z \sim 1.5 - 3$  galaxies have been observed with the full SINS/zC-SINF survey, probing the bulk of the massive star-forming population over roughly two orders of magnitude in stellar mass and in star formation rate ( $M_\star \sim (0.3 - 30) \times 10^{10} M_\odot$  and  $\text{SFR} \sim 10 - 1000 M_\odot \text{yr}^{-1}$ ; see Figure 6.2). All galaxies were observed in seeing-limited mode with a typical resolution of  $\approx 0''.6$  (or  $\approx 5$  kpc at  $z = 2$ ) and 35 targets are followed-up with AO and a resolution of  $0''.15 - 0''.2$  (or  $\approx 1.5$  kpc).

SINS was the first, and is the largest near-IR integral field spectroscopic survey carried out at  $z \gtrsim 1$  to date. Similar studies of  $z \sim 1-3$  star-forming galaxies by other groups have been carried out or are ongoing — albeit mostly for smaller samples — using SINFONI or other near-IR integral field spectrometers such as OSIRIS at the Keck II telescope and NIFS at the Gemini North telescope. To list a few, the OSIRIS samples of Law et al. (2007; 2009) and Wright et al. (2007; 2009) span a very similar redshift range as SINS, the MASSIV and WiggleZ surveys focus on galaxies at  $z \sim 1 - 1.5$  (Épinat et al. 2009; Queyrel et al. 2009; Wisnioski et al. 2011; Queyrel et al. 2012; Contini et al. 2012), the AMAZE and LSD programs target  $z \sim 3$  rest-frame UV-selected samples (Maiolino et al. 2008; Mannucci et al. 2009; Gnerucci et al. 2011), and several strongly-lensed  $z \sim 1 - 3$  objects have been studied by Stark et al. (2008) and Jones et al. (2010).

One of the key outcome of SINS pertains to the kinematic diversity of massive star-forming galaxies at  $z \sim 2$ . About 1/3 of the galaxies are rotation-dominated turbulent disks, another 1/3 comprises major mergers with disturbed kinematics, and the remaining 1/3 are typically compact systems with velocity dispersion-dominated kinematics (Förster Schreiber et al. 2006, 2009; Shapiro et al. 2008; see Figure 6.3). Among the larger more luminous systems, disks account for  $\sim 2/3$  while major mergers represent a minority. The most recent AO-assisted observations from SINS/zC-SINF, reaching  $\sim 1$ -2kpc resolution, now reveal ordered disk-like kinematics in many of the compact objects that appeared dispersion-dominated in seeing-limited data, and show others to be more consistent with mergers Newman et al. (2012, in preparation). Concurring results on the kinematic mix at  $z \sim 1 - 3$  have been found by other groups (e.g., Épinat et al. 2009; Gnerucci et al. 2010; Law et al. 2009; Jones et al. 2010; Wisnioski et al. 2011). As noted in Section 6.2, a significant implication of these results is that major mergers appear not to dominate and smoother mass accretion modes must play an important role in the assembly of galaxies at  $z \sim 2$ . The results from the SINS survey have been significant in constraining the angular momentum of early disks and the Tully-Fisher relation at  $z \sim 2$ , in revealing the dynamical state and (often clumpy) spatial distribution of star formation, and in supporting the role of internal dynamical processes in the evolution of early disks (Förster Schreiber et al. 2006, 2009; Genzel et al. 2006, 2008, 2011; Bouché et al. 2007; Cresci et al. 2009). While this area of research is still in its infancy, it is clear from the results so far that there is much to be gained from detailed in-situ studies of galaxy formation and evolution as now possible with near-IR integral field spectroscopy.

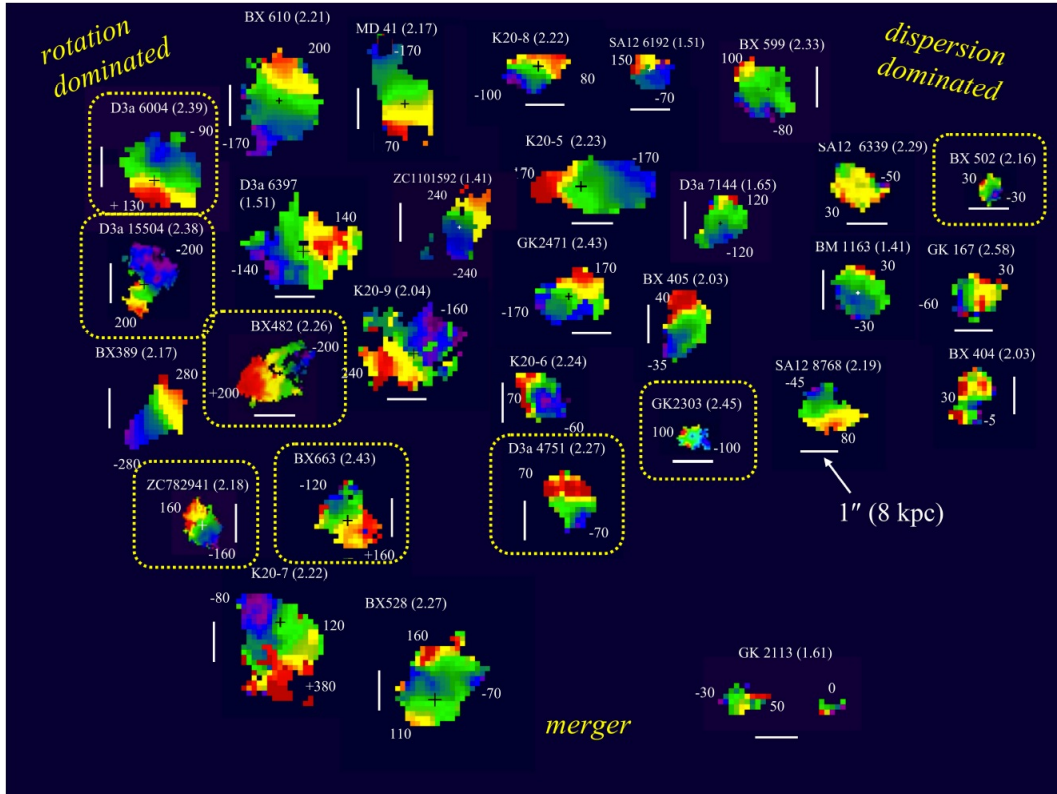


Figure 6.3.: Overview of the velocity fields of massive star-forming galaxies from the SINS  $H\alpha$  sample (taken from Förster Schreiber et al. 2009, Fig. 17). The velocity fields are derived from the  $H\alpha$  line emission (with the exception of K20-ID5, which was obtained from the  $[O\ III] \lambda 5007$  line). The color coding is such that blue to red colors correspond to the blueshifted to redshifted line emission with respect to the systemic velocity. The minimum and maximum relative velocities are labeled for each galaxy (in  $\text{km s}^{-1}$ ). All sources are shown on the same angular scale; the white bars correspond to  $1''$ , or about 8 kpc at  $z = 2$ . Galaxies observed with the aid of adaptive optics are indicated by the yellow rounded rectangles. The galaxies are sorted from left to right according to whether their kinematics are rotation-dominated or dispersion-dominated, and from top to bottom according to whether they are disk-like or merger-like as quantified by kinemetry (Shapiro et al. 2008). The 30 galaxies plotted form a subset of the original SINS sample of 62 rest-UV/optically-selected galaxies, for which the  $H\alpha$  line emission was targeted to map their internal ionized gas motions. For this full  $H\alpha$  sample, as well as the subset shown, roughly 1/3 of the sources have rotation-dominated kinematics, another 1/3 have dispersion-dominated kinematics, and the remaining 1/3 exhibit more disturbed kinematics indicative of major mergers.

## 6.4. Motivation for this work

In addition to the kinematics and star formation properties, information on the heavy element abundances, the relative role of AGN and star formation, and the distribution of dust extinction within galaxies is essential to our understanding of the early evolution of galaxies. This work exploits the additional information on the physical conditions of  $z \sim 2$  star-forming galaxies obtained as part of the SINS survey through observations of [OIII] and  $H\beta$  complementing the  $H\alpha$  and [NII] data sets. The faintness of these lines and the requirement that all, or a significant subset of them should be observable between the bright night sky OH lines in the near-IR atmospheric windows (see 7.4.1 and appendix A) make such studies very challenging. The SINS survey allowed us to cull a sizeable amount of suitable targets for a first exploration of spatially-resolved metallicities, extinction and excitation in massive  $z \sim 2$  star-forming galaxies. The key open issues can be summarized as follows.

### Heavy-element abundances of galaxies

The chemical evolution of galaxies reflects the interplay between the star formation history, the gas accretion history, and the expulsion of material outside of galaxies through galactic-scale outflows. The zero-point and slope of the relationships between galaxy mass, luminosity, and metallicity result from the combination of these effects and can be used to explore their relative role as a function of lookback time. The local relationships have been extensively studied but samples with abundance determinations at higher redshift are still scarce. The studies at  $z \sim 1 - 3$  published so far rely on small numbers of galaxies showing a large scatter in measurements, or on average spectra of galaxies binned in terms of galaxy parameters such as stellar mass (e.g., Erb et al. 2006; Liu et al. 2008; Maiolino et al. 2008; Queyrel et al. 2009, 2012; Mannucci et al. 2009). The interpretation of the results is also complicated by the use of different indicators of nebular abundances, and by limitations associated with the selection of galaxy samples and flux sensitivity of the data sets. A further complication stems from recent suggestions that the mass-metallicity relation is a projection of a more fundamental plane between stellar mass, metallicity, and star formation rate, possibly forcing a revision of the interpretation in terms of redshift evolution (Maiolino et al 2008; Mannucci et al. 2009).

### Spatial variations in nebular abundances of galaxies

Even fewer empirical constraints have been published on the spatial variations of nebular abundances within galaxies. Metallicity gradients give more direct insights into the internal redistribution of metals, and additional constraints on the exchange of material between a galaxy and its environment. For disk galaxies in particular, the distribution of heavy element abundances as a function of galactocentric radius and its evolution over cosmic time provide powerful constraints on models of disk formation and evolu-

tion. Sophisticated models are successful at reproducing the (negative) radial metallicity gradients in present-day spiral galaxies but diverge in terms of the evolution with time; some models predict a steepening of gradients with decreasing redshift (e.g., Chiappini et al. 1997, 2001) and others predict instead a flattening (e.g., Prantzos & Boissier 2000; Fu et al. 2009). The scarcity of empirical constraints at high redshift currently severely hampers progress. The few available measurements reported at  $z \sim 1 - 3$  also show diverse results. For two strongly-lensed disks at  $z = 1.5$  and  $z = 2$ , the derived radial metallicity gradient is steeper than for local late- or early-type galaxies, consistent with expectations for the “inside-out” scenario for the formation of disks (Jones et al. 2010; Yuan et al. 2011). Another non-lensed galaxy at  $z = 2.2$  obtained early in the SINS survey also shows a negative gradient (Förster Schreiber et al. 2006; Genzel et al. 2008). On the other hand, more complex spatial variations or even inverted gradients were inferred for three isolated non-lensed rest-UV-selected “Lyman-break galaxies” at  $z \sim 3$ , interpreted as a signpost of “cold flow” accretion bringing primordial gas to the galaxies’ central regions (Cresci et al. 2010). Similarly positive metallicity gradients were reported in several  $z \sim 1.2$  massive star-forming galaxies by Queyrel et al. 2012. Here, the significant fraction of interacting/merging systems among those suggest the interactions are responsible for bringing metal-poor gas in the central regions, thereby flattening or inverting the metallicity gradients.

### **Line excitation, and the role of AGN and shocks**

First and foremost, the interpretation of the rest-frame optical line spectrum of distant galaxies needs to account for the possible contribution of AGN and/or shocks in addition to photoionization by young stars in HII regions. In particular, AGN contamination has been invoked to account for the reported offset towards higher excitation of high-redshift galaxies compared to the sequence of local HII regions and purely star-forming galaxies in the classical  $[\text{OIII}] \lambda 5007 / \text{H}\beta$  versus  $[\text{NII}] \lambda 6584 / \text{H}\alpha$  diagnostic diagram introduced by Baldwin, Phillips, & Terlevich (1981). Although other factors can also cause the observed offset (including shock activity, increased interstellar gas pressures and/or ionization parameter; e.g., Liu et al. 2008; Brinchmann, Pettini, & Charlot 2008), an AGN contribution certainly is of concern at  $z \sim 1 - 3$  where the peak in cosmic star formation density is accompanied with that in AGN activity. The combination of several diagnostic lines are necessary to disentangle the effects of AGN or shocks from those of nebular abundances. Even so, weak AGN can be difficult to identify in integrated line ratios and spatially-resolved data can help uncovering them as demonstrated by the case study of a  $z = 1.6$  galaxy by Wright et al. (2009).

### **Interstellar dust extinction**

The presence of dust within galaxies can dramatically alter their observed properties by obscuring the background light, and accurate corrections are essential to recover the intrinsic properties of galaxies. At high redshift, estimates of the dust extinction have been most commonly derived from the rest-UV/optical colors of galaxies through evolutionary synthesis modeling of their broad-band spectral energy distributions (SEDs) or from measurements of the UV spectral slope. In both cases, the derived reddening applies to the stellar population that dominates the underlying continuum emission and is degenerate with other galaxy parameters such as the stellar age and star formation history. As alternative and independent method to determine the extinction, hydrogen recombination lines provide excellent diagnostics for extinction estimates because their intrinsic emissivities are well determined theoretically (e.g., Hummer & Storey 1987). The “Balmer decrement”, i.e. the ratio of  $H\beta/H\alpha$ , has been extensively used in studies of local galaxies and is accessible through near-IR observations for sources at  $1.3 \lesssim z \lesssim 2.7$ . It is unclear whether the extinction as derived towards the bulk of stellar populations is applicable for the HII regions as well, for instance to derive intrinsic instantaneous star formation rates from extinction-corrected  $H\alpha$  line fluxes. Indeed, there is evidence in local star-forming galaxies that the visual nebular extinction might be on average roughly twice higher than that towards the stars (e.g., Calzetti et al. 2000; Mayya et al. 2004; Cid-Fernandes et al. 2005). At  $z \sim 2$ , indirect evidence has led to contradictory claims (e.g., Erb et al. 2006c; Förster Schreiber et al. 2009; Reddy et al. 2010; Mancini et al. 2011). Only few direct measurements of the Balmer decrement exist at high redshift; the results appear to support extra attenuation towards the HII regions but the very limited samples and large uncertainties hamper conclusive results (Yoshikawa et al. 2010; Onodera et al. 2010).

#### **6.4.1. Overview of Part II of this thesis**

The present study is based on the SINS survey. It uses the full set of primary observations targeting the wavelength range around the  $H\alpha$  emission line (the primary kinematics and star formation tracer) and neighboring [NII] lines. The analysis further includes the subset of galaxies for which additional SINFONI observations were taken in other near-IR bands, providing measurements of  $H\beta$ , and [OIII] emission lines. With this set of emission lines, the dominant line excitation mechanism, gas-phase oxygen abundance, and interstellar dust extinction are examined. Based on a larger and less biased galaxy sample, the results from this work constitute a substantial improvement over previous studies.

The second part of this thesis is organized as follows. Chapter 7 presents the sample of galaxies considered in this work and the SINFONI observations. We also describe the

data reduction procedure and the method employed for measuring the emission lines of interest. Chapter 8 presents in detail the data sets obtained and describes the morphologies and kinematics of the observed sources. The main results are presented in the two subsequent Chapters. Diagnostic line ratios are analyzed to constrain the line excitation mechanism and the gas-phase abundances of the galaxies in Chapter 9. The dust extinction towards the star-forming regions is derived in Chapter 10 and compared to the extinction towards the bulk of stars dominating the continuum emission. Chapter 11 summarizes the main conclusions from this work, and gives a brief outlook for future studies. Throughout, a “concordance” cosmology with  $H_0 = 70 h_{70} \text{ km s}^{-1} \text{ Mpc}^{-1}$ ,  $\Omega_m = 0.3$ , and  $\Omega_\Lambda = 0.7$  is assumed. For this cosmology,  $1''$  corresponds to 8.4 kpc at  $z = 2$ .

#### 6.4. Motivation for this work

---

## **Chapter 7.**

# **Observations, sample selection and data reduction**

In this chapter, the observations used for the analysis of the line excitation, metallicity and extinction are described. The data were obtained with SINFONI, the near-infrared integral field spectrometer at the ESO VLT. Integral field spectroscopy (IFS) is the most efficient way to fully map astronomical sources along two spatial and the spectral dimension simultaneously. Spatial- or spectral-scanning techniques (e.g. Scanning Fabry-Perot, Imaging Fourier Transform spectroscopy) are inefficient in this case since they would require many times the already several hour long exposure times needed by IFS, dictated by the faintness of high- $z$  galaxies.

This technique and SINFONI are briefly outlined in the first section. In the second section the selection of galaxies studied in this thesis is presented. The data sets obtained are listed thereafter. The next section presents the steps applied during data reduction. We also discuss the topic of OH lines airglow as a major source of background radiation in the NIR, their origin, removal and obstacles in some detail. In the last section we describe how the emission line flux was measured, how 2D emission line maps were created and how the line ratio maps were derived.

### **7.1. Integral-field spectroscopic observations with SINFONI**

All observations were carried out using the integral field spectrometer SINFONI (Eisenhauer et al. 2003a; Bonnet et al. 2004), which is mounted on the Cassegrain focus of the Very Large Telescope Unit Telescope 4. Integral field spectroscopy, first introduced by Courtès (1982), produces a spectrum for each spatial element in a two dimensional spatial field. This results in a data cube where two axes span the spatial image and the third axis opens the spectral dimension. Integral field spectroscopy has the following main advantages over classical long-slit spectroscopy:

## 7.1. Integral-field spectroscopic observations with SINFONI

---

1. No slit losses of observed flux if the object fits in the FOV of the integral field unit and the object is completely sampled. This implies high observing efficiency.
2. No need for separate pointings across an extended object to get spectral coverage over the whole source.
3. Target acquisition is facilitated since the object does not need to be positioned exactly on a slit.
4. Seeing variations have less impact on the total observed flux of objects during the observations.

With IFS, all the data are taken simultaneously, without requiring spatial- or spectral-scanning. To achieve this, the spatial 2D plane is divided into spatial samples / elements in the first part of the instrument, the integral field unit (IFU), and each sample / element is then dispersed in the second instrument part, the spectrometer. All the spectra –each of which represent the spectrum for a specific part of the 2D spatial plane– are then projected on the detector. The reconstruction of the  $x$ - $y$ - $\lambda$  data cube is done in the data reduction steps afterwards. There exist three main techniques to sample the focal plane: **Lenslets** can be used to produce an image of the telescope pupil for every spatial sample (e.g. Courtès 1982, Afanasiev et al. 1990, Bacon et al. 2001). The pupil images are smaller than the extent of each spatial sample and can thus be dispersed to produce the respective spectra. To minimize spectral overlap, i.e. to increase the spectral coverage, the dispersion direction can be tilted with respect to the sample grid. Because the detector is shared by several spectra in spectral direction (i.e. several adjacent spectra per detector row), the spectral coverage is more restricted than with other techniques given the same spectral resolution. Instruments using this technique are, for example, SAURON at the William-Herschel Telescope and OSIRIS at Keck.

A second technique utilizes a **combination of lenslets and fibers**: A lenslet array is used to couple the individual spatial samples of the focal plane to individual fibers (e.g. Allington-Smith et al. 2002). Each fiber represents one  $x,y$  pixel in the final 3D data cube. For the output to the spectrograph the fibers are rearranged in a way such that they form a pseudo-longslit, which is then dispersed. Usually a second ‘longslit’ lenslet array is used to couple the light out of the fibers. By dispersing a pseudo-longslit, no spectra can overlap; the spectral range is thus larger and the detector area can be almost fully utilized.

**Image slicers** are the third technique and offer the highest performance in terms of throughput (e.g. Weitzel et al. 1996; Thatte et al. 1997; Content 1997; Dubbeldam et al. 2000). The image slicer consists of two stacks of thin mirrors. The mirrors in the first stack slice the focal plane into  $n$  image slices parallel to one direction (hereafter ‘ $y$ ’) and of equal width along the other direction (hereafter ‘ $x$ ’), the so-called slitlets. The width of one slicing mirror therefore is analogous to the slitwidth in a longslit spectrometer. The optical surfaces of the slitlet mirrors are slightly tilted with respect to each other, each

one reflecting its image slitlet to a corresponding mirror in the second stack. The second stack then rearranges all  $n$  slitlets into a pseudo-longslit which is dispersed in the spectrometer. On the detector, one  $y$ - $\lambda$  plane is projected for each  $x$ -value slitlet. Depending on the geometry of the slicer, the individual  $y$ - $\lambda$  slitlet spectra are more or less spectrally aligned and arranged adjacent to each other. SINFONI at the VLT is an example of an IFU based on an image slicer.

## SINFONI

SINFONI (SINgle Faint Object Near-IR Investigation) is the AO-assisted integral field spectrometer at the VLT (Eisenhauer et al. 2003a; Bonnet et al. 2004). It consists of the adaptive optics module MACAO (Multiple Application Curvature Adaptive Optics, built by ESO) which feeds the near-infrared integral field spectrograph SPIFFI (SPectrograph for Infrared Faint Field Imaging, built by the IR/sub-mm group at MPE). SPIFFI's image slicer divides the FOV into 32 slitlets. Each slitlet is imaged onto 64 pixels of the  $2k \times 2k$  HAWAII-2 detector, thus obtaining 2048 spectra simultaneously. Three pre-optics define the FOV and thus the size of the slices on sky. Along the spatial dimensions, the pixels (or 'spaxels') are rectangular in a FOV of  $8'' \times 8''$ ,  $3'' \times 3''$  or  $0.8'' \times 0.8''$  (depending on the pre-optics). The corresponding angular sizes are  $125\text{mas} \times 250\text{mas}$ ,  $50\text{mas} \times 100\text{mas}$  and  $12.5\text{mas} \times 25\text{mas}$  respectively. SPIFFI features 4 gratings to take spectra in J, H, K, or H+K band at a spectral resolution  $R := \lambda/\Delta\lambda \sim 2000$  in J to  $\sim 4000$  in K and  $\sim 1500$  in H+K. Typical limiting magnitudes (signal-to-noise (S/N) = 10, 1h integration) are around 17-18mag in J, H and K. The largest pixel scale is intended for seeing-limited operations where the AO module does not correct the wavefront. The two other pixel scales allow to sample the AO-corrected spatial PSF, with the smallest scale designed to Nyquist sample the diffraction limit of the 8m VLT unit telescope. The AO module can use either a natural guide star or an artificial laser guide star provided by the sodium laser PARSEC (Rabien et al. 2003) to analyze and correct the tip/tilt component and the higher order wavefront distortions of the incoming light. The laser guide star can further be used without a Tip-Tilt star providing seeing-enhanced observations. See Appendix C for an overview of the workings of an AO system.

## 7.2. Sample Selection for this study

### 7.2.1. General constraints and strategy for target selection

All galaxies in this study are drawn from the sample of  $z \sim 1$ – $3$  star-forming galaxies observed in the SINS Survey. All SINS targets detected in Ha and [NII] line emission were included in the analysis of the source-integrated metallicities (based on the [NII]/Ha line ratio). For the study of line excitation and dust extinction relying on the additional emission lines of [OIII] and H $\beta$ , the subset of the best targets was selected in terms of scientific feasibility and impact as well as practical observation considerations. These

## 7.2. Sample Selection for this study

---

targets are among the brighter objects in the SINS sample, enabling us to observe the relatively weak  $H\beta$  and [OIII] in comparatively short exposure times. The resulting 12 targets present a rough exemplary sample of the galaxies in the SINS survey. They span the range in stellar mass from  $0.77 - 31.6 \times 10^{10} M_{\odot}$ , and star formation rate from 16 to  $560 M_{\odot}/\text{yr}$ . They include various kinematic types: rotation and dispersion dominated objects as well as merging systems. For all the targets the  $H\alpha$  and [NII] data had already been taken during various previous SINFONI observing runs. The most stringent criterion considered in selecting targets for the [OIII] and H $\beta$  follow-up observations was that these lines should be shifted at wavelengths away from bright night sky lines.

The data analysis technique requires the detection of four rather faint near-infrared emission lines for each target. For ground-based observations the near-infrared regime is divided into three atmospheric windows, the J ( $1.1-1.35\mu\text{m}$ ), the H ( $1.5-1.8\mu\text{m}$ ) and the K band ( $2.0-2.4\mu\text{m}$ ). Especially in the H and K band, several dozens of spectrally densely packed narrow atmospheric OH radical emission lines contaminate the observed spectra. Their intensities are highly variable in time and are strong enough to outshine the emission lines of faint high- $z$  objects by up to several orders of magnitude - and have thus to be avoided. Targets were only suited for this study if their four emission lines under study were within the J, H or K band and, ideally, all between the OH lines therein. Hence for successful selection of targets, it was mandatory to know their spectroscopic redshifts to calculate the redshifted wavelengths of the emission lines. Galaxies observed as part of SINS all had a redshift from optical spectroscopy, confirmed with high accuracy from the  $H\alpha$  observations with SINFONI.

### 7.2.2. The SINS sample

As for the parent SINS sample, our targets include objects with a variety of primary photometric selection criteria. These include the “BM/BX” class based on  $U_rGR$  colors (Adelberger et al. 2003) and star-forming “ $BzK$ ” objects (Daddi et al. 2004)

Table 7.1 lists the selected targets together with their coordinates, redshifts and K-band magnitudes. The redshift is derived by fitting a Gaussian profile to the  $H\alpha$  line emission in the spatially-integrated spectrum determining the central wavelength (see Förster Schreiber et al. 2009). For BM1163 no K-band observations were taken (Erb et al. 2006b). For MD41, no K-band photometry was published by Erb et al. (2006b); the K-band magnitude was measured from publicly available archival imaging obtained with the SOFI instrument at the ESO NTT. In the final sample, BX663, K20-ID5 and D3a-15504 are known to host an AGN based on their optical (rest-UV) spectrum, or near-IR (rest-optical) spectrum from either previous long-slit observations or the SINS SINFONI data. For all three clear signs of AGN activity are identified from the [N II]/ $H\alpha$  line ratio and/or the line widths. D3a-6004 (and potentially D3a-6397) may also host an AGN based on [NII]/ $H\alpha$  maps and radial/aperture profiles (see section 9.3). For K20-ID5, the rest-frame optical emission characteristics were argued by van Dokkum et al. (2005) to be more consistent with starburst-driven shock excitation rather than AGN activity.

Table 7.1.: List of observed targets

Object	Coordinates		$Z_{H\alpha}$	$K_{Vega}$ (mag)	Primary photo- metric selection	Parent survey	References <sup>(a)</sup>
	RA	DEC					
Q1307-BM1163	13:08:18.0	29:23:19.3	1.4104	...	BM	BX/BM NIRSPEC	1,2
Q2343-BX389	23:46:28.8	12:47:33.5	2.1733	20.18	BX	BX/BM NIRSPEC	1,2
Q2346-BX482	23:48:12.9	00:25:46.3	2.2571	...	BX	BX/BM NIRSPEC	1,2
Q2343-BX610	23:46:09.4	12:49:19.2	2.2103	19.21	BX	BX/BM NIRSPEC	1,2
Q1623-BX663	16:26:04.5	26:48:00.2	2.4332	19.92	BX	BX/BM NIRSPEC	1,2
D3a-6004	11:25:03.8	-21:45:32.7	2.3867	19.01	sBzK	Deep3a	4
D3a-6397	11:25:10.5	-21:45:06.1	1.5138	18.56	sBzK	Deep3a	4
D3a-15504	11:24:15.6	-21:39:31.0	2.3826	19.42	sBzK	Deep3a	4
ZC-782941	09:59:55.9	02:06:51.3	2.1814	19.65	sBzK	zCOSMOS	4
K20-ID5	03:32:31.4	-27:46:23.2	2.2243	19.04	sBzK	K20	5,6
K20-ID7	03:32:29.0	-27:46:28.4	2.2241	19.61	sBzK	K20	5,6
SSA22a-MD41	22:17:39.9	00:17:11.0	2.1704	20.42	BX	BX/BM NIRSPEC	1,2,3

<sup>(a)</sup> REFERENCES: (1) Erb et al. 2006b; (2) Steidel et al. 2004; (3) Erb et al. 2003;  
(4) Kong et al. 2006; (5) Daddi et al. 2004a; (6) Mignoli et al. 2005

## 7.2. Sample Selection for this study

Table 7.2 lists general SED-derived properties for the targets, as determined in the SINS survey: the stellar mass,  $M_*$ , the star formation rate, the extinction  $A_{V,SED}$  and the age. The data are taken from Förster Schreiber 2009 and 2011a.

Table 7.2.: General target properties

Object	$M_*$ ( $10^{10}M_{\odot}$ )	SFR $M_{\odot}/\text{yr}$	$A_{V,SED}$ [mag]	Age [Gyr]
BM1163	... <sup>(a)</sup>	... <sup>(a)</sup>	... <sup>(a)</sup>	... <sup>(a)</sup>
BX389	$4.12^{+0.77}_{-2.16}$	$25^{+17}_{-2}$	$1.0^{+0.2}_{-0.2}$	$2.75^{+0.22}_{-0.20}$
BX482	$1.84^{+0.79}_{-0.46}$	$80^{+42}_{-32}$	$0.8^{+0.2}_{-0.2}$	$0.32^{+0.49}_{-0.14}$
BX610	$10.00^{+2.70}_{-0.60}$	$64^{+26}_{-1}$	$0.8^{+0.2}_{-0.2}$	$2.75^{+0.17}_{-0.65}$
BX663	$6.40^{+0.22}_{-2.28}$	$42^{+13}_{-12}$	$0.8^{+0.2}_{-0.2}$	$2.50^{+0.15}_{-0.80}$
D3a-6004	$31.63^{+4.68}_{-1.49}$	$214^{+110}_{-75}$	$1.8^{+0.2}_{-0.2}$	$0.64^{+0.17}_{-0.13}$
D3a-6397	$11.96^{+1.84}_{-0.36}$	$563^{+9}_{-203}$	$2.2^{+0.2}_{-0.2}$	$0.20^{+0.12}_{-0.02}$
D3a-15504	$10.86^{+2.66}_{-0.12}$	$150^{+1}_{-54}$	$1.0^{+0.2}_{-0.2}$	$0.45^{+0.19}_{-0.05}$
ZC782941	$2.99^{+0.07}_{-1.03}$	$215^{+161}_{-1}$	$1.2^{+0.2}_{-0.2}$	$0.14^{+0.02}_{-0.09}$
K20-ID5	$7.18^{+4.16}_{-0.05}$	$809^{+6}_{-326}$	$2.0^{+0.2}_{-0.2}$	$0.11^{+0.21}_{-0.01}$
K20-ID7	$3.95^{+0.10}_{-0.26}$	$112^{+4}_{-2}$	$1.0^{+0.2}_{-0.2}$	$0.51^{+0.13}_{-0.06}$
MD41	$0.77^{+0.10}_{-0.03}$	$185^{+3}_{-70}$	$1.2^{+0.2}_{-0.2}$	$0.05^{+0.03}_{-0.00}$

<sup>(a)</sup> For BM1163, photometry is only available in three optical bands, preventing reliable SED modeling to derive the stellar properties

### 7.3. SINFONI observations

The data were collected during various observing campaigns between July 2004 and March 2010 as part of the SINS survey program. The observing conditions were generally good to excellent, with clear to photometric sky transparency and typical seeing at near-IR wavelengths with a FWHM around  $0.''7$ . Table 7.3 lists all observing runs during which the data of the 12 sources with Ha, [NII], [OIII], and Hb observations were obtained (observing details for other sources with only Ha+[NII] data can be found in FS09). The table also gives the band/grating, pixel scale, observing mode, and the total on-source integration time. For simplicity '125' refers to the largest scale with nominal pixels of  $0.125'' \times 0.250''$  and field of view of  $8'' \times 8''$ , and '50' refers to the intermediate scale with nominal pixels of  $0.05'' \times 0.125''$  and a field of view of  $3.2'' \times 3.2''$ . The total exposure time listed refers to the integration time used in the analysis. For some objects more data were taken, but during data reduction some OBs were found to be of significantly lower quality mostly due to poor observation conditions or persistence being present in the detector and were removed from the final data set.

The data quality and derived data products are discussed and listed in section 8.1 and table 8.1.

#### Observing strategies, dithering

In addition to the science target data, it is mandatory for ground-based NIR observations to take images or spectra of a source-free part of the sky, which are subtracted from the actual science frame(s) during the data reduction to remove the bright 'background' emission (i.e atmospheric OH lines and atmospheric and instrument thermal emission above  $\lambda \geq 2\mu\text{m}$ ). This is exacerbated by the rapid variations in intensity of telluric lines, on timescales as short as a few minutes. For imaging of extragalactic fields where distant galaxies have angular sizes typically smaller than the separation between neighboring objects, this is usually done by randomly dithering short successive exposures within a box of appropriate size. This dithering also avoids sources falling at redundant pixel positions on the detector, efficiently minimizing the impact of bad pixels and other detector/instrumental artifacts. The background level at any detector pixel is estimated from the median over all non-registered frames, which samples mostly areas empty of (detected) sources. For long-slit spectra, nodding (i.e., offsetting the object) along the slit between successive exposures is an easy way to obtain pairs of exposures, which can then be subtracted from each other. The observing strategy for SINFONI is however more complex since various boundary conditions come into play:

### 7.3. SINFONI observations

---

- The FOV of SINFONI is  $8'' \times 8''$  ( $125 \times 250$  mas/pixel) for seeing-limited observations and  $3'' \times 3''$  ( $50 \times 100$  mas/pixel) for AO observations of our faint objects. Moreover, because the source signal is spread over many spatial and spectral pixels, sufficiently long exposures (of  $\sim 5$ - $15$  min typically) are required to ensure background-limited observations and maximize the sensitivity of the resulting data sets. For smaller sources, and depending on the pixel scale/FOV, it is still possible to follow an 'on-source dithering strategy' by placing the object in opposite quadrants or halves of the FOV in successive exposures. For larger sources, the sky needs to be taken 'off-source' away from the target.
- For successful wavefront correction, the natural guide star (or tip-tilt correction star for LGS) should not be more than  $10$ - $15''$  (depending on the selected waveband J,H or K) away from the science target. Under excellent observing conditions a distance of  $\sim 25''$  can still provide some improvement of the image quality in NGS, and up to  $\sim 60''$  for TTS in LGS. Ideally the AO guide star should not be fainter than  $\sim 14$  mag in R-band. During observations for this work, we have successfully used AO guide stars as faint as  $18$  mag still enabling partial wavefront correction.

Following these constraints, and depending on the source and the observing conditions, two strategies were followed for our observations: An efficient 'on-source-dithering' where the object is kept in the FOV for all exposures and an 'offset to sky' scheme with sky background frames taken away from the science target.

The 'on-source dithering' was used in seeing-limited observations where the FOV is larger and thus the science target occupies only roughly a quarter or less of the FOV, making it possible to 'move it around' in the FOV. In this scheme the data were taken in AB cycles allowing pair-wise subtraction between two exposures. Depending on the source geometry, the telescope offsets were usually carried out in a diagonal fashion or left-right shifting by roughly half a field of view. To reduce the number of redundant positions on the detector, the offset positions were jittered by about  $1/10$  of the FOV. The 'offset-to-sky' variant was mainly used in adaptive-optics assisted observations with the small FOV of  $3'' \times 3''$ . In this observation scheme the telescope pointing was alternated between the object ('O') and adjacent sky regions ('S'), free of sources, usually in an 'O-S-O-O-S-O' pattern for each observing block. Like in the on-source scheme every pointing was varied by about  $1/10$  of the FOV, to ensure independent sampling of the sky signal subtracted from each of two object frames that share the same sky frame.

Individual exposure times were usually  $600$  s (in some cases  $300$  s) to optimize the background subtraction and remain in the background-limited regime in the wavelength regions around the emission lines of interest. The total on-source integration times ranged from  $\sim 1$  h to  $10$  h ( $24$  hours in AO), with an average of  $4.5$  h spent per band and pixel scale for each target. The total integration times were driven by the surface brightness of the sources and by the aim of mapping the line emission out to large radii.

Table 7.3.: Overview of the SINFONI observations for our main targets with Ha, [NII], [OIII], and H $\beta$  emission line mapping

Object	Band	Scale [mas]	Mode	$t_{\text{int}}$ [s]	Observing Date(s) [MonthYY]
Q1307-BM1163	J	125	seeing-limited	7200	Mar05
	H	125	seeing-limited	14400	Mar05
Q2343-BX389	H	125	seeing-limited	15900	Jun06, Aug06
	K	125	seeing-limited	14400	Oct05
Q2346-BX482	H	125	seeing-limited	15000	Aug06, Nov06
	K	125	seeing-limited	14400	Nov04, Aug07
	K	50	LGS-AO	31800	Oct07, Jul08, Nov09, Jan10
Q2343-BX610	J	125	seeing-limited	14400	Oct05
	H	125	seeing-limited	30000	Oct05, Nov07
	K	125	seeing-limited	10800	Jun05, Aug05
Q1623-BX663	H	125	seeing-limited	3600	Apr07
	K	125	seeing-limited	26400	Jul04, Apr07
D3a-6004	H	125	seeing-limited	13200	Feb10, Mar10
	K	125	seeing-limited	36000	Mar06, Mar07
	K	50	LGS-AO	7200	Jan10
D3a-6397	J	125	seeing-limited	10800	Apr07
	H	125	seeing-limited	24000	Apr07, Mar08
	H	50	LGS-AO	19200	Feb09, Mar09, Jan10
D3a-15504	H	125	seeing-limited	14400	Apr06
	K	125	seeing-limited	21600	Mar06
	K	50	LGS-AO	67200	Mar06 – Apr10
ZC-782941	H	125	seeing-limited	20400	Dec09, Jan10
	K	125	seeing-limited	7200	Mar07
	K	50	LGS-AO	37800	Apr07
K20-ID5	H	125	seeing-limited	7200	Mar05
	K	125	seeing-limited	9600	Mar05
K20-ID7	H	125	seeing-limited	24000	Jan10, Feb10
	K	125	seeing-limited	31200	Oct05, Nov06
SSA22a-MD41	H	125	seeing-limited	3600	Apr07
	K	125	seeing-limited	25200	Nov04, Jun05

To monitor the seeing and have a measure of the PSF corresponding to the science frames, exposures of the acquisition stars used for the blind offsets to the galaxies were taken. For flux calibration and atmospheric transmission correction late-O, B and G1V to G3V stars were observed with near-IR magnitudes in the range  $\sim 7$ -10 mag. Telluric standard stars were observed every science night, as close in time and airmass as possible to each science target observed. The acquisition and telluric standard stars were always observed using the same band and pixel scale as was used for the science objects.

## 7.4. Data reduction

### 7.4.1. Reduction steps

Reduction of the science data was done using the software package SPRED. This package was developed specifically for the reduction of SPIFFI data (Schreiber et al. 2004; Abuter et al. 2006). Additional routines were developed to minimize the impact of bright OH lines (Davies 2007). By taking into account shifts in wavelength calibration between different exposures as well as the different variations in time of different groups of telluric OH transitions, these procedures vastly improve the quality of the resulting data sets. The data reduction flow is comparable to a standard NIR longslit spectra reduction with the addition of creating a 3D data cube from the individual slitlet spectra created by the IFU image slicing mechanism. The SPRED package consists of various python scripts to prepare calibration frames, create, combine and calibrate 3D data cubes.

Special care has been taken for the removal of atmospheric OH lines, which by far dominate the near-infrared background. The standard technique of subtracting sky spectra or frames from the object spectra is not sufficient, leaving residuals in the data cube that would strongly affect the subsequent analysis needed in this work. See Appendix A for a detailed description of atmospheric OH line emission.

### Calibration file preparation

In a first step the calibration files needed are reduced and generated:

- One or more master **dark frames** are created by combining all dark frames of the same exposure time for one or more nights. Exposure times of dark and science frame need to match because the level of the dark current depends on the exposure time. An *initial* bad pixel mask is generated from the dark frames.
- A **flatfield** image is created for each observing night individually. The flat field is to

compensate for deviations from an uniform field illumination induced by the optical train and to correct for sensitivity variations among individual detector pixels. In SINFONI, slitlets 1, 16 and 17 in particular suffer from partial vignetting due to the design of the image slicer, which needs to be corrected for.

- By combining the flat and dark frames and thresholding a final **bad pixel mask** is derived to identify hot or cold pixel which are defective, permanently giving a maximum or no signal.
- Using existing distortion map and arc lamp data, an initial **wavelength solution** is generated. The wavelength solution is basically a wavelength map for the detector x-y image coordinates. It is needed for rectifying the spectral curvature and for correcting the spectral alignment of the individual slitlets, which are not in mutual alignment in wavelength space when projected on the detector due to the very construction of the IFU image slicing mechanism itself.
- A **2D-to-3D lookup table** is calculated which gives the correspondence between 2D spatial detector pixel coordinates to 3D x-y- $\lambda$  coordinates in the final 3D data cube.

### **Basic reduction steps**

Next, the wavelength solution is refined using sky emission lines to correct for small shifts and flexure. After this, removal of cosmic rays follows. This step is carried out on the raw science frames using the L.A.Cosmic removal algorithm developed and described by van Dokkum (2001). It uses a Laplacian edge detection algorithm to identify cosmic rays of arbitrary shapes and sizes by the sharpness of their edges. This method is better suited than algorithms involving median filtering since those tend to fail when the PSF is smaller than the filter or cosmic rays affect more than half the filter area (van Dokkum 2001). The calibrations files created in the steps above are then used to process the raw science frames and extract the data cubes.

### **Intermediate 3D-data-cube**

Since the subsequent steps and scripts operate on 3D data cubes, the raw 2D science frames are converted into 3D cubes using the wavelength calibration files and lookup tables. The result is a raw science cube, that is wavelength calibrated, dark subtracted, divided by the flat field and corrected for atmospheric dispersion but still contains all OH lines, and thermal background. Each two cubes that have been taken successively on sky as A-B pairs are then used in the OH line removal process (see section 7.4.1 for a detailed

description of the OH line treatment and removal), which creates a sky-subtracted cube from the raw cube. The sky-subtracted cubes are then fed into a refined background subtraction routine. The background to be subtracted is derived for each slitlet individually using a linear fit along the spatial direction to remove residual features.

After all frames have been processed, the science cubes of one observing block are usually combined for a first evaluation of the data quality. This is done since the S/N for our faint high- $z$  sources in individual 600s exposure cubes is relatively low and often the sources cannot be detected in individual exposures, except for the brightest ones or when the continuum level is high. Spatial alignment of the single-exposure cubes is done according to the dither offsets sequence used for the observations because the targets are too faint to determine their position in individual exposures from centroid fitting or cross-correlation. The small offsets applied within an OB for dithering or offsets-to-sky are very accurate at the VLT, as they are performed relative to the telescope active optics guide star.

To combine all OB cubes, the relative offsets between them (often taken on different nights) are determined in three manners: based on the measured position of the acquisition star observed for each OB and the known offsets that were applied to go on target, by measuring the centroid position of the sources in the individual combined OB-cubes provided the source is sufficiently bright and compact, or from the relative offsets between OBs if they are taken successively without reacquisition in between. In this work all targets had their OB cubes registered by measuring the centroid position of the source as this was found to yield the best registration.

At this point a sky-subtracted master science cube has been produced. This cube is still not flux-calibrated, which is done in the next step.

### **Flux calibration and atmospheric correction**

Flux calibration and correction for atmospheric transmission is done on the individual single-exposure science cubes on a night-by-night basis. The data of the telluric standard stars and the acquisition stars are reduced in a similar way as the science data. The standard star spectrum is extracted from the data cube and further processed as follows.

Firstly, an atmospheric template is generated from the standard star spectrum by removing intrinsic stellar absorption lines and a calculated blackbody spectrum. The star spectrum is divided by a model atmosphere spectrum generated using the `atran` software package (Lord et al. 1992) for the corresponding spectral resolution, airmass and atmospheric water vapor content for the telluric star's data. After absorption line cor-

rection, the star spectrum is again multiplied by the model atmosphere. These tasks are done in IRAF. For late O and B stars the only significant features that need to be removed are the H lines of the Brackett series (e.g. Br $\gamma$  at 2.166 $\mu$ m in the K band). For G stars, a solar template matched to the filter and pixel scale of the observation is used as diverse lines need to be removed. The spectrum is then divided by a black body spectrum corresponding to the star's temperature, and normalized to peak transmission of unity.

The next step is the flux calibration: the standard star is used to calculate the flux in physical units per ADU (i.e detector counts, 'analog-to-digital unit'). The synthetic broad band magnitude is calculated from the telluric standard star spectrum in ADU. The photometric zero point is then derived by comparing with the star's magnitude in physical units.

### **Final 3D-data cube**

In the next step, the individual sky-subtracted cubes are first corrected for atmospheric transmission using the atmospheric template created as described above. These new cubes are then flux-calibrated using the nightly conversion factor derived from the analysis of the standard star flux.

The final step is the combination of all flux- and transmission-calibrated science cubes of a given target by averaging with sigma-clipping (i.e., iteratively removing data points deviating from the mean, typically clipping at the  $2.5\sigma$  level). This step also generates a 'sigma cube', which contains the standard deviation of the values for a given pixel in the 3D data cube across all cubes combined. To ensure the statistics (e.g. the sigma cube) are calculated correctly, the individual calibrated frames from all OBs are combined, rather than combining each OB into an OB-cube and then combining the OB-averaged cubes.

### **PSF determination**

Determination the PSF is necessary in order to determine the spatial resolution of cubes in different bands if they are to be combined for a spatial analysis. The effective PSF of a science cube is determined from the acquisition stars observed immediately before or after the science object. For this, a broad-band image of the acquisition stars is created by averaging together all wavelength channels of the reduced cube of the PSF-star using sigma-clipping to exclude the strongest residuals due to night sky lines. When a science data cube is a combination of several OBs, the PSF for the combined cube is measured from the shifted and coaveraged PSF cubes of the individual OBs. For the purpose of characterizing the angular resolution of the data, the effective PSF shape is

well approximated by a Gaussian for both seeing-limited and AO-assisted SINFONI data (e.g. Förster Schreiber et al. 2009).

### **OH line removal**

As mentioned above, the dominant source of background radiation in the near-IR is the OH airglow emission. Appendix A gives a more detailed description of the telluric OH lines. Here we describe the steps in the reduction, which allow us to minimize the impact of bright OH lines on the data by reducing their residuals left after simple 'on-off' image subtraction.

In general, if a faint object's emission line comes to fall directly onto a bright OH line, no recovery is possible (the case of broad emission lines can be an exception in this respect). For all other cases, the standard technique for OH-line removal is the subtraction of a 'sky' spectrum, taken from a blank piece of sky, from the 'object' spectrum. For longslit and even multi-object spectroscopy there is always a part of blank sky in the slit that can be taken as the sky spectrum, so this can be done simultaneously. For integral field spectroscopy this is also possible if the object is sufficiently small compared to the FOV. Otherwise this then requires taking separate sky and object frames which need to have the same exposure time in an object-sky-object pattern.

For the subtraction of sky and object frames one property of the OH emission becomes particularly important: the absolute and relative intensity is temporally variable on timescales of the order of a few minutes. Since typical exposure times for the high redshift sources in this work are around 10 minutes, the standard object minus sky technique is generally not sufficient to eliminate all OH contamination. In addition, as an effect of instrument flexure while tracking, the wavelength calibration of the actual science data frame and the wavelength calibration frame (taken with an arc lamp usually at daytime) can differ (up to 1/2 pixel for SINFONI), leading to asymmetric, 'P-Cygni'-type, residual profiles.

To tackle these effects the wavelength calibration and sky subtraction used in this work were optimized using the method developed by R. Davies (2007a). This method has been integrated into our data reduction pipeline. The science frames are first interpolated to a common wavelength grid with an accuracy better than 1/30 of a pixel. The wavelength information needed for this step is derived from the night sky lines from the raw science frames. The sky subtraction is then improved by separately scaling the flux of each transition group of OH lines. This reduces the residuals around the emission lines under study.

From the analysis point of view, even if the OH line is very close or overlaps with the blue or red wing of an astronomical emission line the information can be recovered by fitting

the emission line using the remaining uncontaminated portion of the line profile. This, however, requires the resolution of the spectrograph to be sufficiently high, i.e.  $R \approx 4000$ , and that residuals have been minimized as described above. Especially in such cases, the use of integral field spectroscopy often makes it possible to still analyze a part of the object, namely those regions which are blue- or redshifted out of the contaminating OH line.

Despite all sophisticated OH line removal schemes and algorithms, good OH line avoidance in the first place has been done when selecting the objects, so that all emission lines of interest simultaneously come to fall in the free spectral range between *bright* OH lines. For all SINS galaxies, the  $H\alpha$  line had been observed previously. The spectroscopic redshift from  $H\alpha$  ( $z_{sp} = (\lambda_{H\alpha}[\text{nm}]/656.46) - 1$ ) was used to calculate the expected wavelengths of the [OIII] and Hb lines of interest, in order to optimize our target selection for OH line avoidance. However, despite the stringent selection criteria, for some objects one or two emission lines were contaminated by *weaker* OH lines on their blue or red side hampering a full spatial analysis.

## 7.5. Emission line measurements

The source-integrated emission line fluxes and the line maps used to create line excitation, metallicity and extinction maps were extracted from the final science data cubes using line profile fitting. Fits to the spectrum of individual spaxels lead to maps. Fits to the spectrum summed over all spaxels within larger apertures were used to derive source-integrated properties or radial/axis profiles

### 7.5.1. Emission line fit

To fit the emission lines the code LINEFIT was used which has been developed by the MPE IR Workgroup specifically for the scientific exploitation of SINFONI IFS data (Davies 2011).

Before starting the actual fit, a 3 pixel wide median filter was applied to the data cubes to slightly increase the signal-to-noise (S/N). The fit is then carried out on the spectrum of each spatial pixel. LINEFIT returns a 2D map of the object with the derived flux value as the intensity for every spatial pixel. At the same time, error and S/N maps as well as velocity and dispersion maps and their corresponding error maps are created.

By default the fitting routine assumes a single Gaussian line profile. This makes the fit routine sensitive to the dominant emission line component. A possible low-amplitude

## 7.5. Emission line measurements

---

broad line component is ignored (such a component occurs naturally in some galaxies e.g. as a result of outflowing ionized gas (e.g. Genzel et al. 2011, Newman et al. 2012) or can be introduced by beam smearing at larger radii of a central high velocity dispersion source). LINEFIT uses weighted fits (uniform, gaussian or poisson weighting), which results in more robust measurements of the line flux, width and central wavelength for data where the noise level varies strongly as a function of wavelength. The weighting is done based on the corresponding noise spectrum (derived from the 'sigma' cubes described in section 7.4.1). To take the spectral resolution into account, LINEFIT convolves the assumed intrinsic emission line profile of the source with a line profile template (i.e. the spectral PSF) representing the effective resolution of the instrument. In the fitting process, a continuum component is subtracted. This component is derived by fitting first-order polynomials to the adjacent line-free spectral intervals. This procedure is generally satisfactory for subtracting the continuum at the wavelength of the emission line of interest, but it often results in a rather noisy continuum map. For our faint objects, a S/N improvement for continuum maps was obtained by taking an average of OH and emission line free spectral channels, iteratively varying the threshold to exclude spectral channels based on the noise cube to optimize the S/N for the continuum map

In extracting the maps of the emission line fluxes and kinematics, the line fitting was carried out with the amplitude, centroid, and width as free parameters in order to compare the kinematics in different emission lines.

Computing measurement uncertainties is complicated by complex noise properties, which make an analytical error propagation rather difficult. An empirical approach based on Monte Carlo simulations was found to lead to realistic estimates of the formal uncertainties on all fitted parameters (e.g., FS09; Davies et al. 2011). For the simulations it is assumed the noise behavior is Gaussian for a given wavelength channel and a given aperture size but is not across wavelengths and as a function of aperture size. This assumption was verified using actual data, analyzing the pixel-to-pixel rms and the distribution of counts measured in non-overlapping apertures over a range of aperture size that are randomly placed in regions lacking source emission in the reduced data cubes. The analysis provides the average pixel-to-pixel rms noise at each wavelength over the effective FOV and the appropriate scaling as a function of aperture size (most relevant for the integrated spectra as described in the next section), which is then used as input noise spectrum in the line fitting.

### 7.5.2. Spatially-integrated line fluxes

To derive the global emission line properties of an object, a spatially-integrated spectrum of the source was extracted from the data cube and fit in the same manner as described in the previous section. The spectra were extracted in elliptical apertures spatially cen-

tered on the location of peak line emission as derived from a centroid fit to the  $H\alpha$  line maps. The position angle of the major axis was taken from the velocity field following the direction of the strongest gradient. The eccentricity was taken from calculations in Cresci et al. (2009). More sophisticated apertures e.g., following isophotal contours, were not used as noise grows significantly near the edge of galaxies, which complicates a detailed contour definition. To exclude an artificial broadening of the spatially-integrated line profile due to the velocity field of the galaxy, the individual spectra of all pixels were spectrally shifted to the systemic velocity based on the derived velocity map from  $H\alpha$ . As we will see in section 8.2, the kinematics of [NII], [OIII], and  $H\beta$  are consistent with those of  $H\alpha$  in all cases where we can extract them reliably, justifying the use of the velocity field from the higher S/N  $H\alpha$  emission as common reference. Fluxes were extracted for elliptical apertures with increasing major axis radii from 1 to  $\sim 13$  pixels, and plotted for a flux curve-of-growth analysis. The curve-of-growth of our objects typically flattens at large radii or slightly increases further. However, towards the edges of the FOV, noise levels increase or residual systematics get stronger. The further increase of the flux may be due to artifacts rather than intrinsic emission from the observed object. Therefore the first aperture containing  $\gtrsim 90\%$  of the total flux measured was taken as the aperture for total flux extraction. Typical 90% radii are  $1.0''$ – $1.25''$  for seeing-limited and  $0.5''$ – $0.75''$  for adaptive optics assisted observations. This conservative choice implies that the total line fluxes and size estimates may be slightly underestimated.

For the data used to calculate line ratios, the same extraction aperture radius was taken for all emission lines if the line emission was detected over the full aperture for the relevant lines. In some cases, not all four lines could be detected over the whole galaxy (as defined by the  $H\alpha$  map) or were in part affected by an OH line nearby. In these cases, either sub-regions were used to derive fluxes only for regions where the lines were unaffected by OH contamination or the cubes were masked by a  $3\sigma$  detection mask from the weakest line before the extraction algorithm was used on the data cube.

For lines that were undetected over the entire galaxy, a  $3\sigma$  upper limit was derived. The limit is based on the noise spectrum for the wavelengths corresponding to the line of interest based on the  $H\alpha$ -derived redshift, assuming the same line width as  $H\alpha$ , and within the same aperture as used for the  $H\alpha$  line measurements.

Weighting and derivation of the formal uncertainties of the best-fit fluxes, relative velocities and redshift, and velocity widths were based on an input noise spectrum calculated for the aperture size over which the spectra were spatially-integrated. This was done according to the empirically derived noise model described in Förster Schreiber et al. (2009; Appendix C) which accounts for the fact that the effective noise properties in the reduced SINFONI data cubes are not purely Gaussian due, notably, to a contribution from correlated noise introduced by the data reduction procedure.

The uncertainties from the absolute flux calibration are estimated to be  $\sim 10\%$  and those from the wavelength calibration  $\lesssim 5\%$ . Other sources of uncertainties include contin-

uum placement and the wavelength intervals used for line and continuum fits. The latter effects were estimated for a subset of the sources by slightly varying the line and continuum intervals. With the results from the curve of growth analysis, the results suggest that the systematics typically amount to 20%-30% for most sources and up to  $\sim 50\%$  for sources with low S/N.

### 7.5.3. Inter-band alignment of emission line and ratio maps

The analysis presented in this work involves ratios of emission lines observed separately in different bands. For instance, one of the methods presented is a pixel-by-pixel BPT analysis where for each spatial pixel of the object under study the ratio values  $[\text{OIII}]/\text{H}\beta$  and  $[\text{NII}]/\text{H}\alpha$  are derived and plotted in the BPT diagram. This analysis requires the line ratio maps originating from two different observing bands to be properly spatially aligned. While the image scale itself does not differ between the two bands, the absolute spatial position of the object in the data cube is generally not the same.

Similar to spatial registration of single-OB cubes when stacking them to the master all-OB-cube the straightforward approach of relying on the telescope pointing is usually not correct. A simple centroid measurement on e.g., the comparably bright  $\text{H}\alpha$  line as is done when generating offsets for cube-stacking does not necessarily provide the position needed for correct spatial inter-band alignment either. This is mainly because

- the objects morphology can be different for different emission lines,
- the morphology is roughly the same but the regions for line emission do not match within the morphology,
- one or more lines are undetected or too faint to give a reasonably accurate position fit.

Therefore it is necessary to choose a suitable alignment method on a case-by-case basis. The following steps were used to determine the best alignment method in this work:

1. In the first step we check for the **continuum emission** of the source. All cube spectral planes are stacked to create a broad-band image of the source. If a bright continuum is visible in both bands, its position is fit with a centroid that is used for registration between the data of different bands.
2. If there is no bright continuum detected that can be fit, the second step is to compare the **morphology** of the  $\text{H}\beta$  and  $[\text{OIII}]$  line emission with the  $\text{H}\alpha$  emission morphology.

- *no resemblance*: If a bright compact object (star, other galaxy, possibly with AGN) is nearby, this position is fit and the cubes are aligned. If no helper object is present the telescope offset is used.
  - *partial resemblance*: Either  $H\beta$  or [OIII] whose morphology matches best the  $H\alpha$  morphology is used. If a centroid cannot be fit over the whole source, because of e.g. low surface brightness or a nearby OH-line contaminating one side of the emission line, the centroid fit is done on the part of the galaxy that has the highest brightness in the  $H\beta$  or [OIII] line.
  - *resembling morphology*: First it is checked if the  $H\beta$  and [OIII] line emission peak is (roughly) at the same position within the object. If yes, the positions are fit, averaged and the two observing band cubes are aligned with the derived offsets. If the position of peak emission of  $H\beta$  and [OIII] actually differs (and this offset is not due to errors in the reduction process or partial line contamination by an OH line that makes the red or blue side of an emission line inaccessible) it is better to rely on the telescope offset than on a wrong centroid fit. If OH contamination is present in one line, the uncontaminated is used.
3. In the case that an object is not detected in one or more lines and an upper limit for the integrated line emission is calculated, the **telescope pointing** information in the fits header is used.

### Effects of misalignment

Spatial misalignment between data sets from two different observation band or cubes can have different effects depending on the derived quantity. This work investigates either two line ratios from two different cubes, which are plotted in relation to each other (the BPT diagram of  $[NII]/H\alpha$  and  $[OIII]/H\beta$ ) or one line ratio where the two lines originate from two separate wavebands and data cubes (the Balmer decrement  $H\alpha/H\beta$ ). Since the pairs  $H\alpha$ , [NII] and [OIII],  $H\beta$  are each observed in a given band, and since, at the resolution of our data and for our objects, spatial variations in the line ratios are generally modest, small misalignment error for the BPT analysis does not result in large changes in the  $[OIII]/H\beta$  vs  $[NII]/H\alpha$  plane. For the Balmer decrement, which combines  $H\alpha$  and  $H\beta$  observed in different bands, experimentation shows misalignment has more important consequences, so extra care has been taken in interband alignment.

Generally the error due to misalignment gets stronger, as the spatial resolution of the analysis increases, i.e. a pixel-to-pixel analysis is much more affected than a spatially-integrated measurement. For the pixel-to-pixel analysis the outer disk regions are espe-

## 7.5. Emission line measurements

---

cially sensitive to misalignment as the signal-to-noise is intrinsically lower than towards the center with higher emission line fluxes. Thus in turn the presence of ‘unphysical values’, i.e. unreasonably high extinction values or unphysical ratios of  $H\beta/H\alpha$  larger than the theoretical intrinsic ratio for case B recombination appropriate for ionized nebulae (1/2.8), can be an indication of misalignment. Misalignment effects in the BPT diagram may be more subtle to identify, but the stronger effects would place measured line ratios well away from the regions occupied by a range of astronomical sources at low and high redshift. As a consistency check, brighter pixels with robust S/N should occupy the same regions as integrated measurements.

In addition to the spatial registration, large PSF differences would affect the comparisons between emission line properties and distribution between different bands. As reported in Tables 8.1 and 8.2 in the next Chapter, the PSF FWHMs in the different bands for all multi-line targets except for two (BX663 and K20-ID5) agree on average within 30% or better (the ratio of their FWHMs range from 0.9 to 1.3). These differences are equal to or smaller than the combined uncertainty ( $\approx 30\%$ ) of the resolution of the data sets, estimated based on the variations in FWHM of the PSF star’s data associated with individual OBs. For BX663, the H- and K-band PSFs differ by a factor of 1.6. However, it turned out that one of the lines targeted in the H-band ( $H\beta$ ) is unfortunately still heavily affected by an OH airglow line. This prevents including BX663 in the line excitation and nebular extinction analysis, so that neglecting the PSF mismatch is of no consequence. For K20-ID5, the H- and K-band PSFs differ by a factor of 1.4. This galaxy is excluded from the analysis of nebular extinction (in part because of AGN contribution complicating the  $H\alpha$  and  $H\beta$  line fits) but is considered for the line excitation analysis. The uncertainty introduced by neglecting the PSF differences are estimated to be a factor of  $\sim 1.5$  at most, or  $\sim 0.18$  dex in logarithmic units, between the  $[NII]/H\alpha$  and  $[OIII]/H\beta$  ratios. Given the location of BX663 in the AGN regime of the BPT diagram (Figure 9.2), well away from the “star-forming” and “composite” regions, neglecting the effects of PSF differences has little consequence on the analysis presented in Chapter 9. These effects are more important for the comparison between maps (see Figure 8.10) but smoothing the K-band data ( $H\alpha$  and  $[NII]$ ) to match the resolution of the H-band data ( $[OIII]$ ;  $H\beta$  undetected) would not alter the qualitative differences seen between the  $H\alpha$  and  $[NII]$  morphologies and kinematics and those of  $[OIII]$ .

# Chapter 8.

## The SINS multi-line data sets

In this chapter, the data sets obtained are described in detail. We start out with a general overview and description of data products. In the second section, we investigate the objects morphologies and kinematics, and compare the results from different emission lines.

### 8.1. Overview and data quality

Tables 8.1 and 8.2 list for each target the resolution of the data in each observation band, and the kind of data product and physical properties that could be derived separately for spatially-integrated and spatially-resolved results.

The data quality is given as the FWHM of the PSF in the observed band. It was measured using the PSF of the acquisition stars used for telescope and instrument setup in each observing block.

The next four columns list the best data product that could be derived for each emission line. 'Map' denotes that a full spatially-resolved emission line map could be extracted from the SINFONI cube. If only a source-integrated value could be obtained for a given emission line this is denoted by 'Aperture'. For the cases where a line could not be detected 'limit' is stated in the table. For all three cases, if the spectrum was contaminated by a nearby OH line, this is indicated by an additional '(OH)'. Since integral field spectroscopy also resolves an object spectrally (e.g., the approaching and receding sides for a rotating system), a nearby OH line usually affected only one part of the target. In these cases, some regions of the object could still be analyzed. This is noted by 'partial'. For integrated ('Aperture') values, apertures smaller than the whole target could in some cases be used for analysis.

The last two columns list the derived quantities. For integrated properties these are the metallicity indices. 'N2' or 'O3N2' (the N2 index is defined as  $\log([\text{NII}]6584/\text{H}\alpha)$ , and the O3N2 index as  $\log([\text{OIII}]5007/\text{H}\beta)/([\text{NII}]6584/\text{H}\alpha)$ ; Pettini & Pagel 2004), the

## 8.1. Overview and data quality

---

position in the  $[\text{NII}]/\text{H}\alpha$  vs  $[\text{OIII}]/\text{H}\beta$  'BPT' diagram and/or an overall extinction value ' $A_V$ '. For targets where emission line maps could be produced the derived quantities are spatially-resolved. 'full p2p' denotes that for the whole target an analysis was possible on a pixel-to-pixel basis. 'region' is stated when either a sub-region could be analyzed in a pixel-to-pixel map or single aperture. For targets where high resolution AO observations were carried out, it is noted whether these data could be used, or had too low S/N for analysis.

Table 8.1.: Overview over the data quality, derived data products and quantities

Object	PSF FWHM [arcsec]	H $\alpha$	[NII]	H $\beta$	[OIII]	Derived quantities integrated	Derived quantities spatially resolved
Q1307-BM1163	J 0.77 H 0.61	Map	Map	Map	Map	N2, O3N2, BPT	- PSF $\approx$ source size
Q2343-BX389	H 0.50 K 0.54	Map	partial Map(OH)	partial Map(OH)	Map	N2, O3N2, BPT $A_V$	-
Q2346-BX482	H 0.61 K 0.50 K 0.17 (AO)	Map	Map (low S/N)	Limit (OH)	Map	N2	-
Q2346-BX610	J 0.60 H 0.57 K 0.39	Map	Map	partial Map(OH)	partial Map(OH)	N2, O3N2, BPT $A_V$	Metallicity map partial $A_V$ map
Q1623-BX663	H 0.63 K 0.39	Aperture	Aperture	Limit	Aperture	N2	-
D3a-6004	H 0.68 K 0.53 K 0.17 (AO)	Map	Map	Aperture (low surface brightness)	Aperture (low surface brightness)	N2, O3N2, BPT	Metallicity map

Table 8.2.: Overview over the data quality, derived data products and quantities; cont.

Object	PSF FWHM [arcsec]	H $\alpha$	[NII]	H $\beta$	[OIII]	integrated	derived quantities spatially resolved
D3a-6397	J 0.77 H 0.77 H 0.17 (AO)	Map	Map	Limit (low S/N)	Limit (low S/N) (OH)	N2	Metallicity map
D3a-15504	H 0.61 K 0.52 K 0.16 (AO)	Map	Map	Map	Map	N2, O3N2, BPT A <sub>V</sub>	BPT Metallicity map
ZC-782941	H 0.64 K 0.57 K 0.17 (AO)	Map	Map	Map	Map	N2, O3N2, BPT A <sub>V</sub>	BPT Metallicity map AO metallicity map
K20-ID5	H 0.71 K 0.51	Map	partial Map	partial Map (low S/N)	Map	N2, O3N2, BPT	-
K20-ID7	H 0.66 K 0.50	Map	Map	partial Map (low S/N)	partial Map	N2, O3N2 A <sub>V</sub>	Metallicity gradient
SSA22a-MD41	H 0.43 K 0.44	Map	Map	Map	Map	N2, O3N2, BPT A <sub>V</sub>	-

## 8.2. Morphologies and kinematics from the different emission lines

The morphology, i.e. the spatial distribution of light in a certain wavelength or wavelength range emitted from an object, and the kinematics (or internal motions) reveal important information on the nature of a source. In what follows, the morphology and kinematics of the main targets for multi-line analysis are inspected in each emission line. The goals are to compare the spatial distribution and kinematics inferred from different emission lines, to look for features that might reveal additional information about the objects (e.g., evidence for the presence of a previously unidentified AGN), and to identify regions of interest or most suitable for the quantitative analysis presented in Chapters 9 and 10. For each galaxy, a summary of their main properties from previous studies of their SEDs and detailed  $H\alpha$  kinematics (e.g., Erb et al. 2006b; Genzel et al. 2006, 2008, 2011; FS et al. 2006, 2009, 2011a,b; Shapiro et al. 2008; Cresci et al. 2009) is also given to place the results of our new data in context.

Figures 8.1 to 8.11 show the morphology, velocity field and velocity dispersion map for the different emission lines for which maps could be extracted. All sources are shown on the same angular scale. A S/N cut of 3 on the line flux was applied in masking the maps. The maps are arranged in the same pattern for each source: in the top row the line maps for the  $H\alpha$ ,  $[\text{NII}]\lambda 6583$ ,  $H\beta$  and  $[\text{OIII}]\lambda 5007$  emission line are shown. In the middle row the corresponding velocity maps are presented. The bottom row shows the velocity dispersion map for each emission line.

Generally, the line maps show the distribution of line flux throughout the galaxy. In some cases, a nearby or partly overlapping OH line was present. As a consequence parts of the galaxy are missing because, due to the velocity shift across the object, the emission line is then shifted completely into the OH line for the corresponding side of the galaxy and could not be fit. For some of the galaxies multiple peaks can be observed especially in the brighter  $H\alpha$  line maps. These are indications for clumps in the galaxy or a possible merger. Information from the kinematics then helps in discerning the two scenarios. The colors in the line map are scaled to maximize for the best visibility of morphological features for each source. The contours overlaid follow the  $H\alpha$  line map to guide the eye for comparing the line maps.

In the velocity map the color coding is such that blue to red colors correspond to the blueshifted to redshifted line emission with respect to the systemic velocity. The scaling is maximized in each plot. The minimum and maximum relative velocities are labeled for each galaxy (in km/s). In the case of a rotating disk an ordered rotation pattern resembling the classical “spider-diagram” can be observed. In contrast, irregular or perturbed velocity fields are indicative of mergers. The velocity dispersion map is likewise scaled to maximum values. The velocity dispersion is a measure of the intrinsic local random motions of the gas along with any velocity gradient that is unresolved in indi-

## 8.2. Morphologies and kinematics from the different emission lines

---

vidual spatial resolution elements. For a pure rotating thin disk, the velocity dispersion map is characterized by an axisymmetric distribution, peaking at the dynamical center due to beam-smearing of the steep inner velocity gradient. The degree of asymmetry in the velocity and velocity dispersion maps is a measure of the object being more disk- or merger-like (Shapiro et al. 2008). The higher the asymmetry the more merger-like an object is. A low asymmetry is indicative for a more disk-like system.

**General findings:** Overall, the emission line and kinematic maps for the different emission lines of our targets are in good agreement. For most sources, the main emission peak in the individual line maps is found at the same location inside the source boundaries. Some notable exceptions exist for a couple of sources, where especially [OIII] was significantly offset from the  $H\alpha$  emission or additional emission peaks not reflected in other line maps were observed.

**MD41:** SSA22-MD41 at  $z=2.172$  is, with  $H\alpha$  detected over a projected diameter of  $2''.9$  (24 kpc), one of the larger sources of the SINS sample. We could derive emission line maps and their corresponding velocity and velocity dispersion maps for all four BPT lines over large parts of the galaxy. MD41 has been studied in detail in previous papers by our group in terms of  $H\alpha$  emission, kinematics and morphology. While the seeing-limited data in figure 8.1 shows more of a tadpole shape, high resolution HST imaging, taken in i- (ACS  $i_{814}$ ) and H-band (NIC2  $H_{160}$ ), shows rich substructure with several bright clumps with a typical size of  $\sim 1$  kpc. The SINFONI seeing-limited line maps show that  $H\alpha$  and [OIII] have their emission peak located in the same area, towards the south-west. [NII] peaks a little offset to the north-east, coinciding more closely with the kinematic center. However, [NII] is very faint compared to  $H\alpha$ , its emission is robustly detected towards the blue side but only barely detected (S/N just above the S/N=3 cutoff) towards the red side of the galaxy. For  $H\beta$  the red side of the map is truncated as an OH line is located close to the red side of the  $H\beta$  emission line. The peak offset of the  $H\beta$  emission in the map (similar to the [NII] peak offset) might therefore be not a robust depiction of the actual  $H\beta$  distribution. Over the regions where relative velocities and velocity dispersions can be compared, there is overall good agreement among the results from all four lines. The velocity fields are consistent with a large rotating disk with a smooth and monotonic velocity gradient. In our SINS sample, MD41 is among those with lowest stellar mass,  $0.77 \times 10^{10} M_{\odot}$ . It is a young system with an inferred stellar age of 50 Myr from SED modeling. It has a moderate extinction derived from the SED modeling ( $A_{V,SED} = 1.2$  mag), and has one of the lowest nebular extinction among the subset of galaxies for which we could calculate a reliable Balmer decrement ( $A_{V,neb} \approx 1.8$  mag; Chapter 10). The SFR was calculated as  $185 M_{\odot}/\text{yr}$ .

**BX482:** For BX482 at  $z=2.257$  all lines have been detected but only  $H\alpha$ , [NII], and [OIII] could be mapped at least for a part of the object as  $H\beta$  suffers from heavy OH line contamination. A higher resolution AO data set for  $H\alpha$  and [NII] had been taken previously but was too shallow in [NII], preventing a robust AO-resolution metallicity analysis.

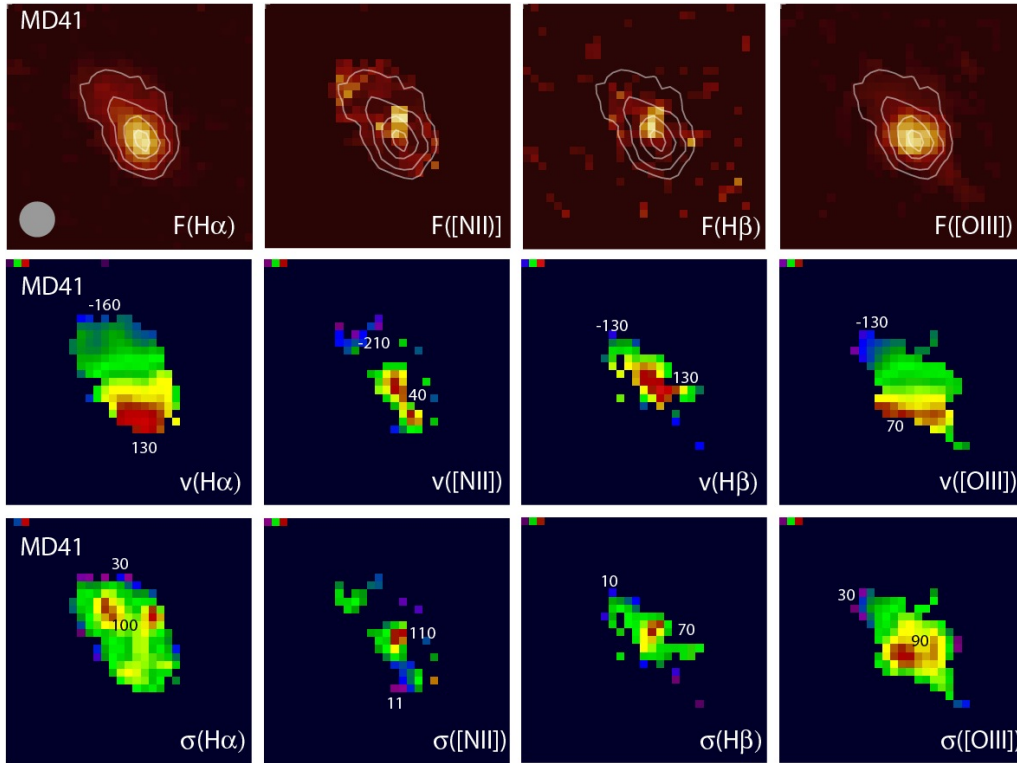


Figure 8.1.: Line-, velocity- and dispersion maps of emission lines for MD41

$H\alpha$ ,  $[\text{NII}]\lambda 6584$ ,  $H\beta$  and  $[\text{OIII}]\lambda 5007$  emission line flux and their respective velocity and velocity dispersion maps are shown. Maps are generated from pixel-to-pixel emission line fitting (see 7.5). The  $H\alpha$  flux morphology is overlaid as intensity contours. The intensity scale is normalized to the maximum value in each line flux map. For the velocity and dispersion maps, the color coding scales linearly with the values, and is such that blue to red colors correspond to the blueshifted to redshifted line emission with respect to the systemic velocity.

The system has been studied in detail previously in terms of morphology and kinematics (e.g. Genzel et al. 2008). BX482 is a system that has an actively star-forming and presumably gas-rich clumpy ring with a regular, disk-like velocity field. The  $H\alpha$  flux is fairly asymmetric, so is  $[\text{OIII}]$ .  $[\text{OIII}]$  shows a brighter feature towards the south-west from the  $H\alpha$  peak, where  $H\alpha$  is of comparably lower brightness. High resolution  $H\alpha$  data obtained with SINFONI LGS-AO and HST NIC2  $H_{160}$  reveal however a clump at this position. The  $[\text{NII}]$  line has a very low surface brightness and is only reliably detected in the location for the brightest  $H\alpha$  peak to the east. The  $H\beta$  line is heavily contaminated by a nearby OH line. Therefore the pixelwise-emission line fit could not be done. The velocity field match taking the limitations for  $[\text{NII}]$  into account. Similarly to MD41, BX482 is one of the

## 8.2. Morphologies and kinematics from the different emission lines

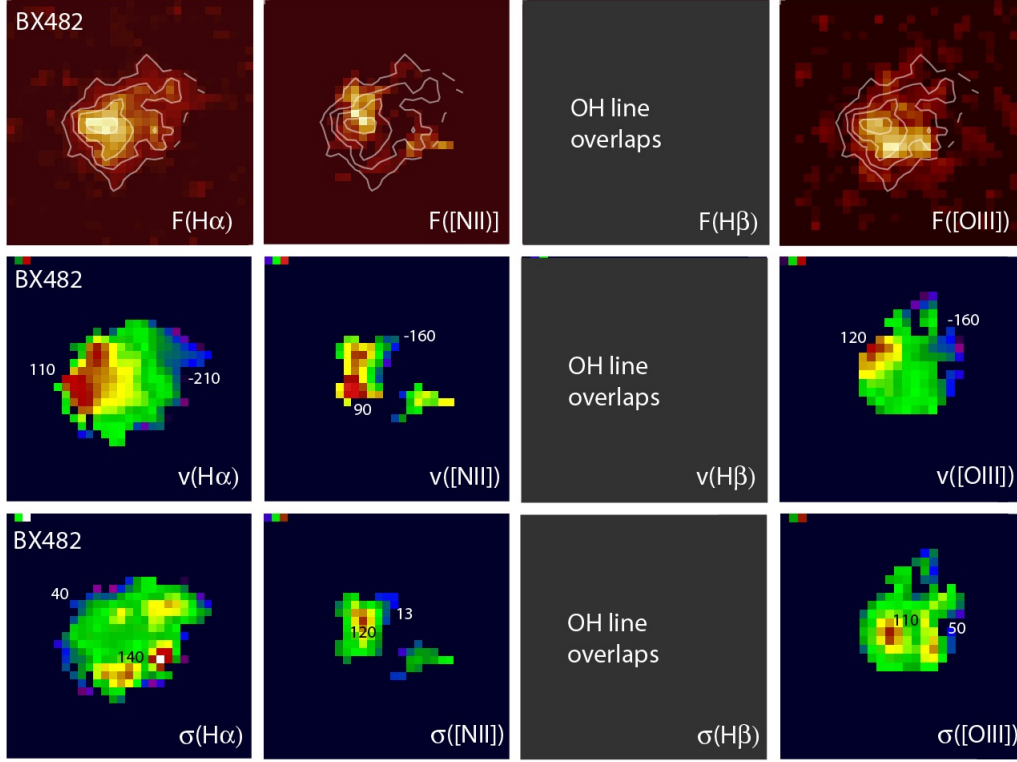


Figure 8.2.: Line-, velocity- and dispersion maps of emission lines for BX482

largest disks among the SINS sample but with rather low stellar mass ( $1.84 \times 10^{10} M_{\odot}$ ), young stellar age (320 Myr), modest extinction ( $A_{V,SED} = 0.8$  mag) and  $SFR = 80 M_{\odot}/yr$  as inferred from SED modeling.

**BM1163:** This  $z=1.41$  object is compact, with an apparent size of the order of the measured PSF. It has a small velocity gradient and a comparably large observed line width, making it a dispersion-dominated object based on the available seeing-limited data. For BM1163 there exists no SED modeling, for lack of photometric data covering a sufficiently large wavelength range. It is the brightest objects in our sample with an  $H\alpha$  flux of  $6.42 \times 10^{16} \text{erg/s/cm}^2$ . Despite its brightness and all lines being detected with high signal-to-noise, it is small and we can derive only spatially-integrated quantities because this source is only marginally resolved in our data.

**BX389:** For BX389 at  $z=2.173$  only  $H\alpha$  and [OIII] could be resolved with a sufficiently high S/N and maps were derived. [NII] largely overlaps with an OH line and has a rather low S/N hampering reliable extraction over most of the object. For  $H\beta$ , the red side of the emission line partly overlaps with OH emission, it is thus detected only for the south eastern, blueshifted part of the galaxy. For these two lines, only aperture values and source-integrated measurements were extracted from the data. Comparing

the  $H\alpha$  and [OIII] line map in figure 8.3, the morphology matches for the north-western and south-eastern knots but [OIII] features a third bright compact structure towards the south-west, where the  $H\alpha$  map only shows a comparably faint extension. The velocity fields are regular and steepest along the  $H\alpha$  morphological major axis with a gradient of  $v_{obs} \sim 500\text{km/s}$ , among the largest observed gradients of our SINS sample. BX389 is also one of the more edge-on systems in the SINS survey. For the extending structure to the south west, the velocity does not appear to be different from the main part next to it. Thus a physical association between the two seems likely. Higher resolution HST NIC2 H-band imaging resolves well the main disk and a small faint source at the position of this southern extension, with a projected distance of 5kpc. The companion is possibly an ongoing minor merger. This is especially interesting in terms of metallicity differences between the two components, given their different [OIII]/ $H\alpha$  ratio (see section 9.3). SED modeling implies a mature stellar population with 2.75 Gyr, a star formation rate of  $\sim 25 M_{\odot}/\text{yr}$ , a stellar mass of  $4 \times 10^{10} M_{\odot}$  (close to the median of the SINS  $H\alpha$  sample), and a moderate extinction ( $A_{V,SED} = 1.0$  mag) comparable to the  $\sim 0.8$  mag derived from the Balmer decrement (Chapter 10).

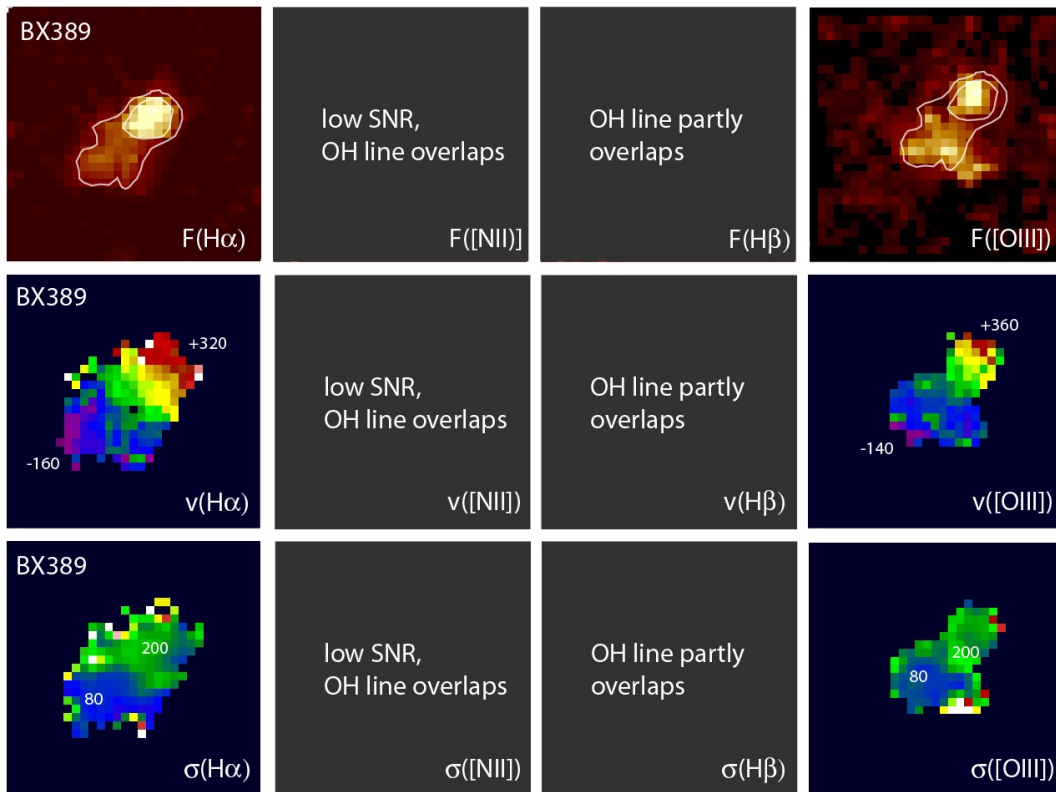


Figure 8.3.: Flux- and kinematic maps of emission lines for BX389

## 8.2. Morphologies and kinematics from the different emission lines

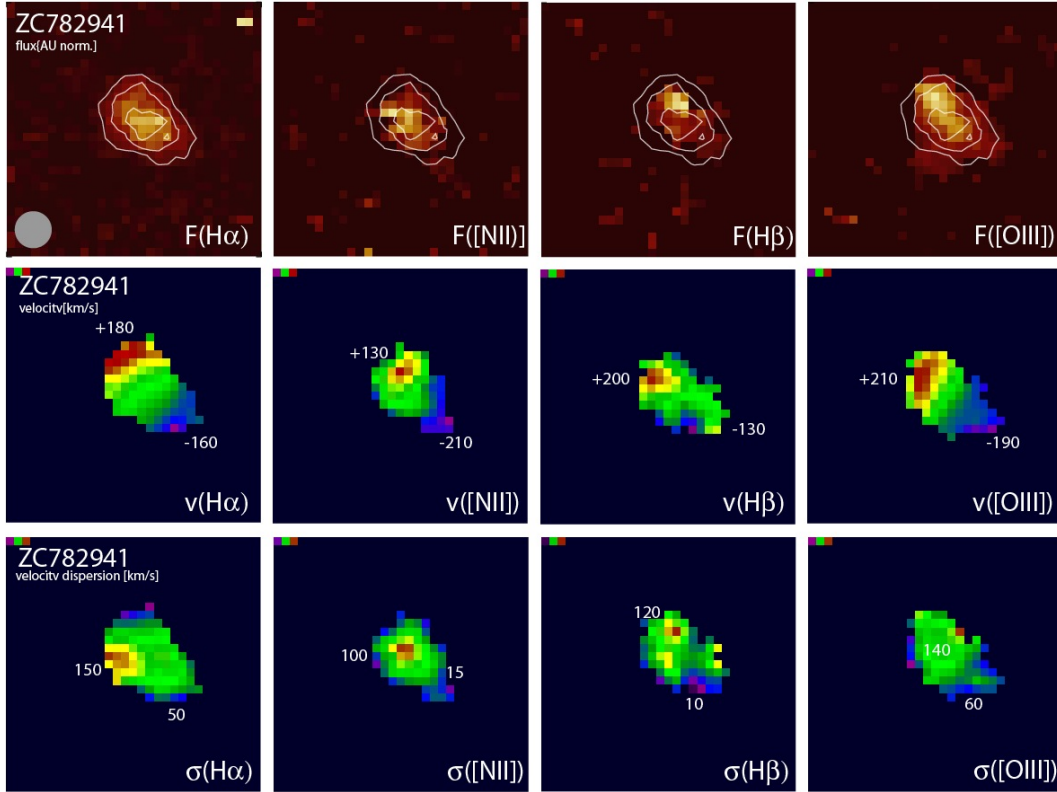


Figure 8.4.: Line-, velocity- and dispersion maps of emission lines for ZC782941

**ZC782941:** For this  $z=2.18$  galaxy all four lines could be mapped out making a full spatially-resolved analysis possible. The overall shape of the object in all four lines is in good agreement. However taking a more detailed look at the spatial distribution of light in each line, [OIII] and H $\beta$  show more flux towards the northeastern side, with their flux peaks offset from H $\alpha$  and [NII]. The high resolution AO map of ZC782941 reveals a more asymmetric light distribution in H $\alpha$  and [NII] (cf. Genzel et al. 2008; 2011 and figure 8.5). The asymmetry is mainly caused by a compact source north-east of the main body the galaxy, which is not resolved in the seeing-limited data set in figure 8.4 but in the adaptive optics data set (figure 8.5) as well as in ACS i-band imaging available for this galaxy. This source could be a bright disk clump at the edge of the system or a second, lower mass galaxy interacting with the main galaxy, a minor merger. The overall velocity field is consistent with a large disk galaxy, while on kpc-scales deviations from pure rotation are visible and the north-eastern part appears more disturbed. The [NII] line emission in the AO data set does not follow H $\alpha$  fully and is comparably weak and does not have an as high S/N as the H $\alpha$  line throughout the whole galaxy. Interestingly there seems to be slightly higher [NII] emission *between* the main part and the NE H $\alpha$  peak which we will analyze further in section 9.3. The SED modeling indicate a similar stellar mass as the median of the SINS sample ( $\approx 3 \times 10^{10} M_{\odot}$ ), and imply a fairly young, actively star-forming, and moderately obscured population dominates the SED (stellar age of  $\sim 140$  Myr, star formation rate of  $210 M_{\odot}/\text{yr}$ , and  $A_{V, \text{SED}} = 1.2$  mag).

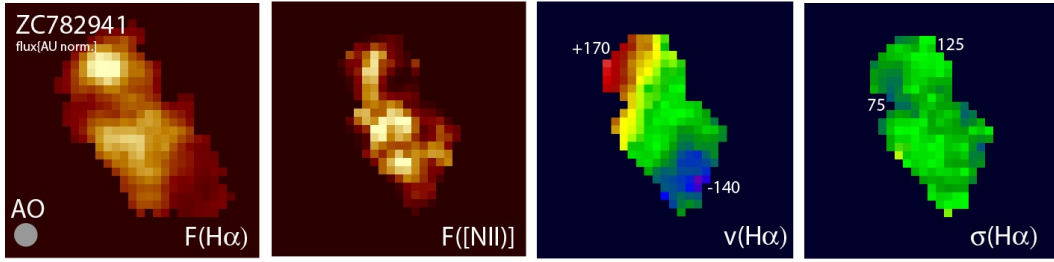


Figure 8.5.: Line maps of emission lines for ZC782941, AO data set

**K20-ID7:** ID7 at  $z=2.23$  could be mapped fully in  $H\alpha$  and [NII], in [OIII] mostly for the brighter north-western part.  $H\beta$  has too low surface brightness for mapping. All three line maps peak at the same spatial location to the north-west. The velocity fields and dispersion maps are fairly asymmetric and disturbed. From its morphology ID7 looks more like a single object; the irregular velocity fields are probably the result of a later-stage merger event. The properties derived from SED modeling indicate a stellar mass of  $\approx 4 \times 10^{10} M_{\odot}$ , again close to the median of the SINS Ha sample, moderate  $A_{V,SED} = 1$  mag, a star formation rate of  $110 M_{\odot}/\text{yr}$ , and an intermediate stellar age of  $\sim 500$  Myr.

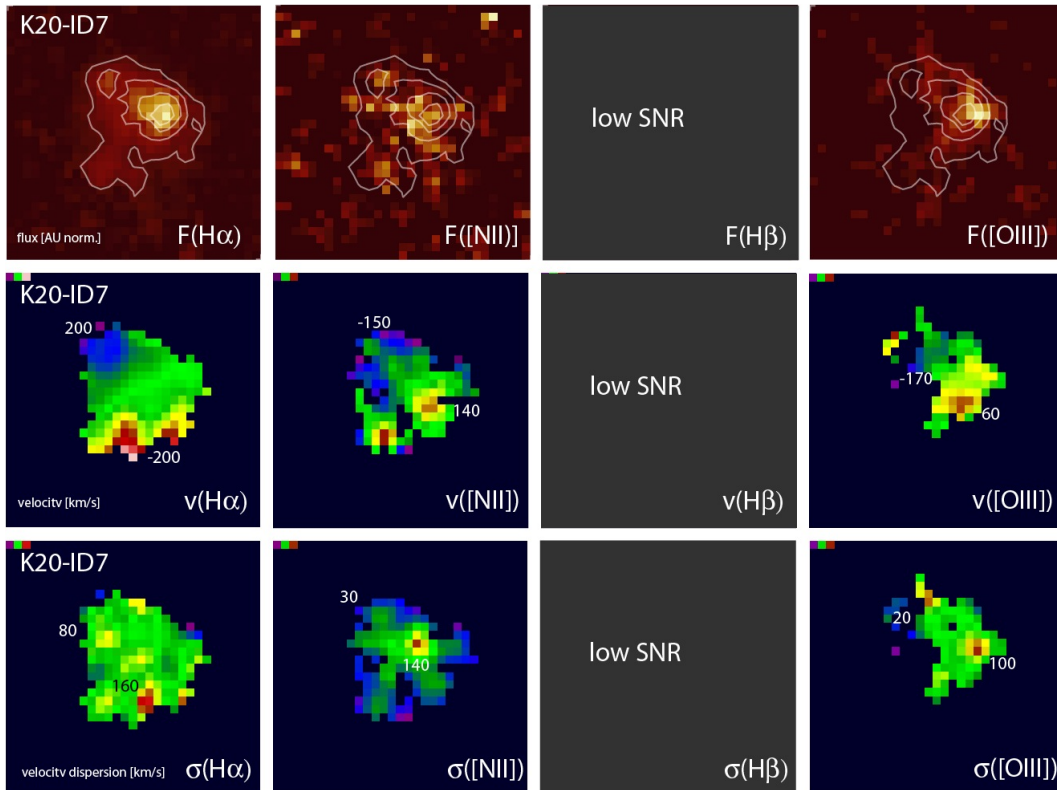


Figure 8.6.: Line-, velocity- and dispersion maps of emission lines for ID7

## 8.2. Morphologies and kinematics from the different emission lines

**D3a-6004:** D3a-6004 is a  $z=2.39$  large disk galaxy. Both  $H\alpha$  and [NII] lines could be mapped. [NII] is faint but was still detected with a  $S/N \gtrsim 3$  over most of the galaxy.  $H\beta$  and [OIII] are of comparably low surface brightness and could only be robustly measured over a small region on the western side, corresponding to the location of the peaks in  $H\alpha$  and [OIII]. The regions of brighter  $H\beta$  emission still roughly follow the location of the bright  $H\alpha$  emission. Our 2h K-band AO data set has low [NII] surface brightness preventing a high resolution spatial analysis. The  $H\alpha$  and [OIII] emission peaks in the outer disk towards the west, well offset from the center. The velocity maps in  $H\alpha$  and [NII] show the well known spider-diagram pattern of an ordered rotation as in a large disk galaxy. The  $H\alpha$  kinematics can be fitted by a disk or possibly ring around a massive spatially concentrated central bulge, which is clearly detected in both the H- and K-band continuum. The  $H\alpha$  morphology might favor a scenario where a star-forming ring or several bright star-forming clumps are present at large radii. The diameter of the central continuum region as measured from the AO data set is  $\sim 0.35''$  ( $\sim 2.8$  kpc) while the disk (or ring) radius is about 6.9 kpc. Although optical spectroscopy shows no sign of AGN activity, the higher [NII]/ $H\alpha$  values in the compact central region suggests a possible AGN (see the metallicity map in figure 9.15). The overall comparably high [NII]/ $H\alpha$  ratio and a stellar age of 640 Myr suggest that D3a-6004 is a fairly evolved system. Its stellar mass is the largest among our sample ( $31.6 \times 10^{10} M_{\odot}$ ), it is actively forming stars at a rate of  $\sim 210 M_{\odot}/\text{yr}$ , and it has  $A_{V,SED} = 1.8$  mag from the SED modeling.

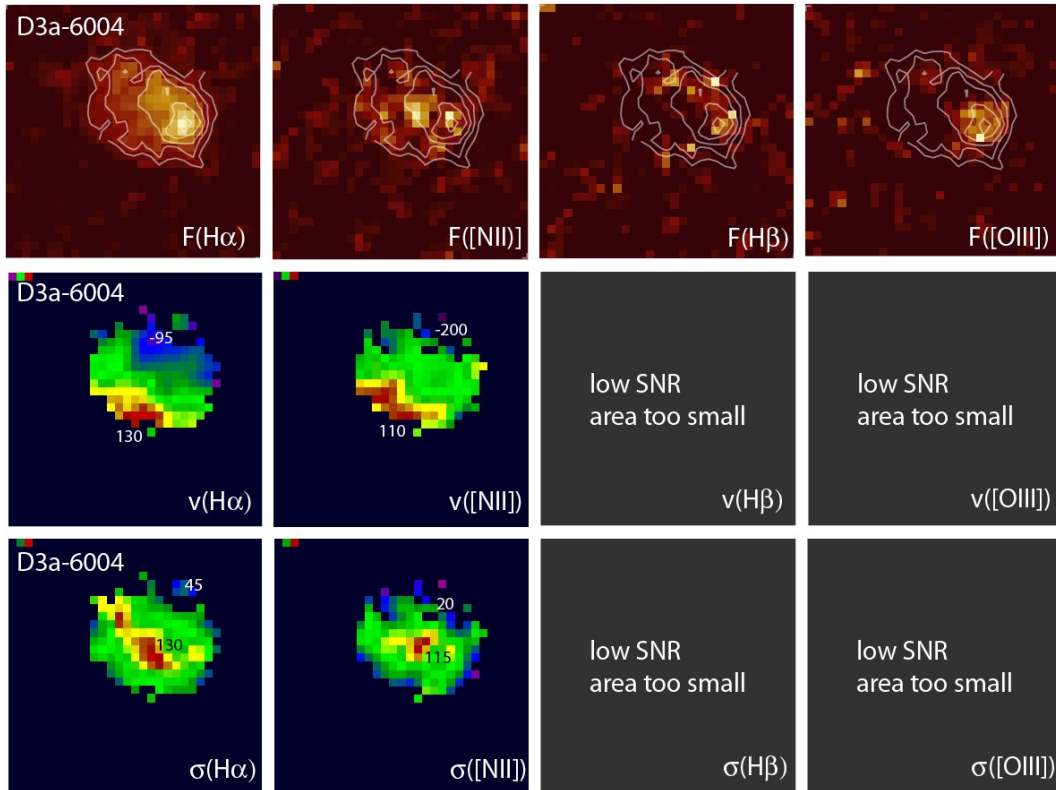


Figure 8.7.: Line-, velocity- and dispersion maps of emission lines for D3a-6004

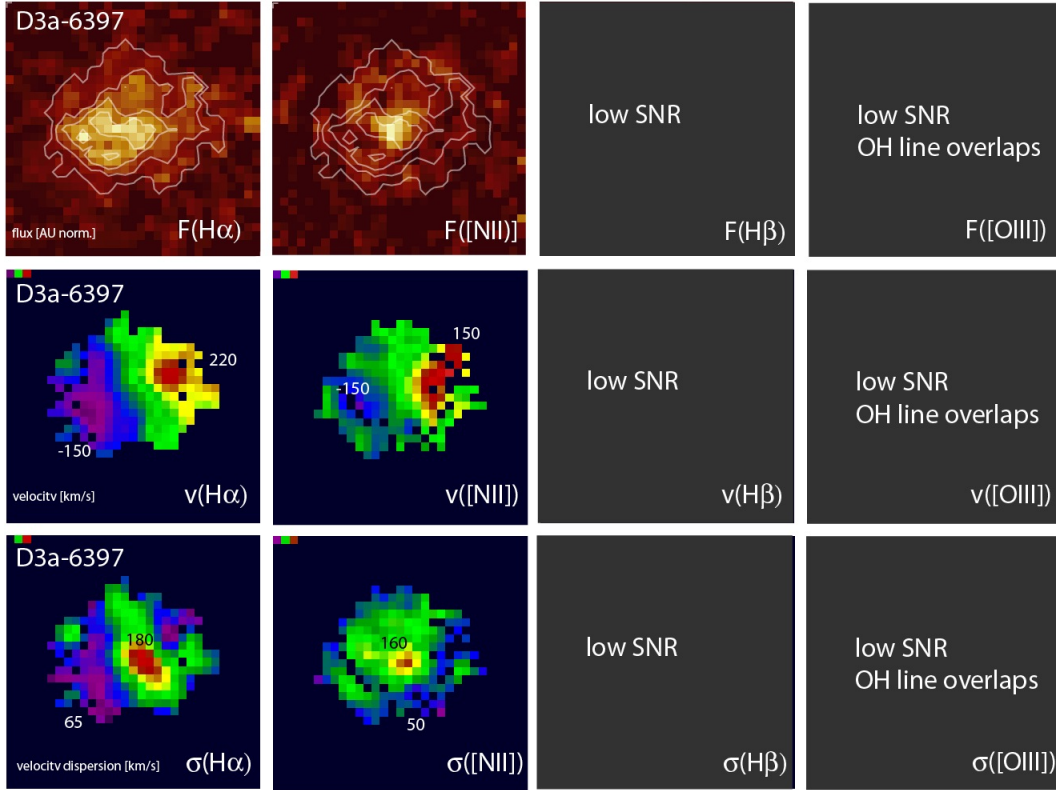


Figure 8.8.: Line-, velocity- and dispersion maps of emission lines for D3a6397

**D3a-6397:** For the redshift  $z=1.51$  object D3a-6397, H $\alpha$  and [NII] could be mapped over the entire galaxy, making a spatially-resolved metallicity map possible. The [OIII] and H $\beta$  line have too low surface brightness to be mapped. [OIII] is furthermore contaminated by OH airglow emission. In the AO H-band data set, the S/N of Ha and [NII] is too low for reliable maps extraction (because of the low surface brightness of this large extended disk system). However, we detect a continuum-bright spatially-concentrated region at the center, with a diameter of 0.38" (or 3.21 kpc). Like D3a-6004, this galaxy shows a bright very concentrated [NII] peak in the center. There is maybe a trend of a dip in [NII] flux about half way between the center and the outer radii where line emission is detected in our data, which is more clearly seen in the resulting metallicity map. However, the S/N for the [NII] line is also low  $\sim 3$  in this area. From the kinematic aspect, the velocity and dispersion maps of D3a-6397 clearly show all features of disk rotation. The SED modeling yields an intrinsic star formation rate of this disk galaxy of  $560^{+9}_{-200} M_{\odot}/\text{yr}$ , which is the second highest SFR in the whole SINS sample. If D3a-6397 is hosting an AGN, as the spatially concentrated high [NII]/H $\alpha$  ratio tentatively supports (see figure 9.16), this high SFR could in part be driven by non-stellar emission. This galaxy is also at the high stellar mass end of the SINS Ha sample ( $12 \times 10^{10} M_{\odot}$ ), with a fairly young and fairly obscured dominant stellar population (age of  $\sim 200$  Myr,  $A_{V,SED} = 2.2$  mag).

## 8.2. Morphologies and kinematics from the different emission lines

**BX610:** For the  $z=2.21$  galaxy BX610, all four lines could be detected with high signal-to-noise ratio. The  $H\alpha$  and [NII] line maps cover the whole object, both  $H\beta$  and [OIII] line maps are not available for the most northern part of the galaxy as both lines are contaminated by nearby OH line emission on the red side. The [NII] emission peaks slightly to the North of  $H\alpha$ , very close to the center. BX610's kinematics show clearly that this system is a large rotating disk. High resolution NIC2 H-band maps reveal several bright clumps that are not resolved in our seeing-limited data cubes. BX610 is a massive ( $10.0^{+2.7}_{-0.6}10^{10}M_{\odot}$ ), evolved system with an inferred age of 2.75 Gyr, moderate extinction of 0.8 mag, and star formation rate of  $60 M_{\odot}/\text{yr}$ , as derived from SED modeling.

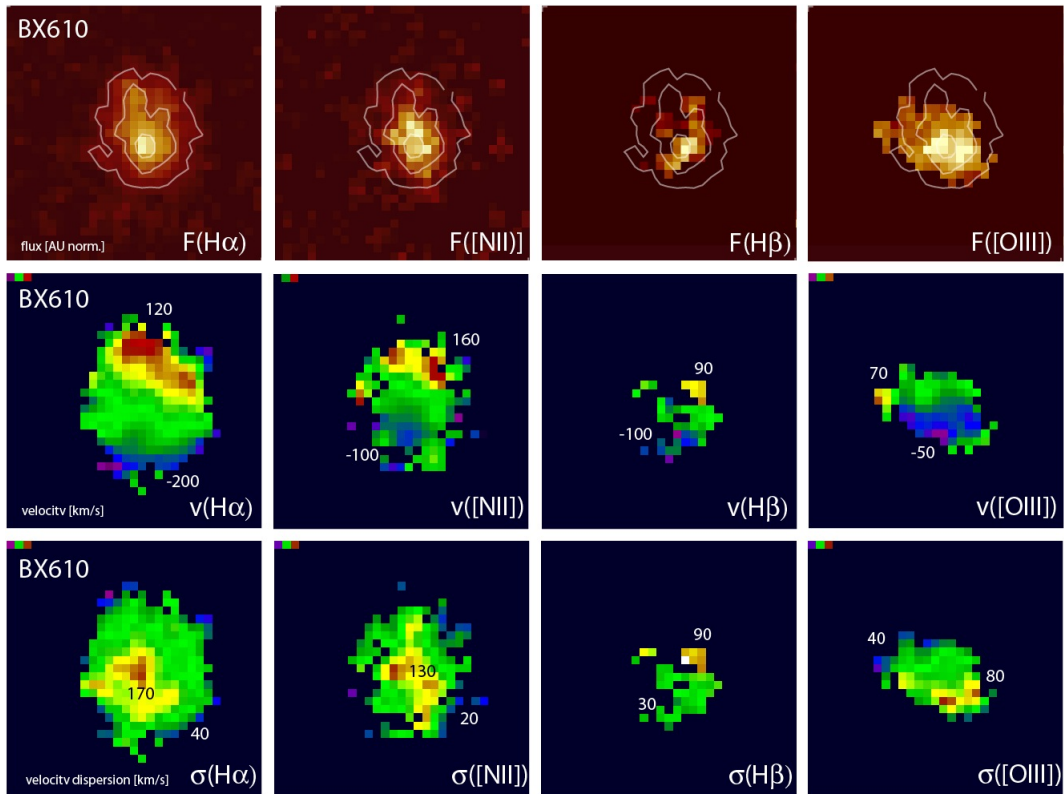


Figure 8.9.: Line-, velocity- and dispersion maps of emission lines for BX610

**BX663:** For BX663 at  $z=2.43$  an  $H\alpha$  and [NII] line flux could be measured in an aperture, for [OIII] and  $H\beta$  only a  $3\sigma$  upper limit could be derived for the line flux. The integrated restframe-UV and restframe-optical spectra show signatures of a Type-2 AGN (Shapley et al. 2004; Erb et al. 2006) further supported by mid-IR SED from Spitzer IRAC and MIPS photometry (Reddy et al. 2010). A broad emission line component is evident in our integrated  $H\alpha$  and [NII] SINFONI spectrum, the signature of the AGN, underneath the narrow component associated with star formation. The SED modeling imply a stellar mass of  $6.4 \times 10^{10} M_{\odot}$ , a mature stellar population with age  $\sim 2.5$  Gyr, and modest extinction and star formation rate ( $A_{V,SED} = 0.8$  mag,  $SFR \approx 40 M_{\odot}/\text{yr}$ )."

**K20-ID5:** The nature of ID5 ( $z=2.22$ ) has been debated in the literature. Although its optical spectrum shows high ionization lines, its soft x-ray luminosity and radio luminosity were found to be consistent with x-ray/radio correlations for pure actively star-forming galaxies (Daddi et al. 2004). The long-slit near-IR spectroscopy presented by van Dokkum et al. (2005) also shows high nebular excitation but over spatially extended regions, which these authors argue would favor shock excitation rather than AGN excitation. Our 2D SINFONI maps and spectra show compact and very broad  $H\alpha$  and [NII] emission. [OIII] is detected over a significantly larger extent in our SINFONI data but this cannot only be due to the larger PSF of the H-band observations ( $\text{FWHM} = 0.71''$  versus  $0.51''$  for the K band; Table 8.2) because the spatial distribution is also different: the brightest [OIII] emission regions are offset to the west of the  $H\alpha$  peak and there is fainter but extended emission seen to the east as well. The integrated line ratios place ID5 in the AGN regime (see section 9.2.2) but contributions from shocks and star formation (mostly at larger radii) cannot be excluded. The overall kinematics (especially from the more extended [OIII] emission in our data) appear to be consistent with disk rotation. From the SED modeling, this system appears to be fairly young and obscured (stellar age  $\sim 115$  Myr,  $A_{V,\text{SED}} = 2.0$  mag), with a stellar mass of  $\approx 7 \times 10^{10} M_{\odot}$ . ID5 has the highest inferred star formation rate among the SINS  $H\alpha$  sample,  $810 M_{\odot}/\text{yr}$ , which, as for D3a6397, could be influenced by the AGN contribution to the broad-band SED.

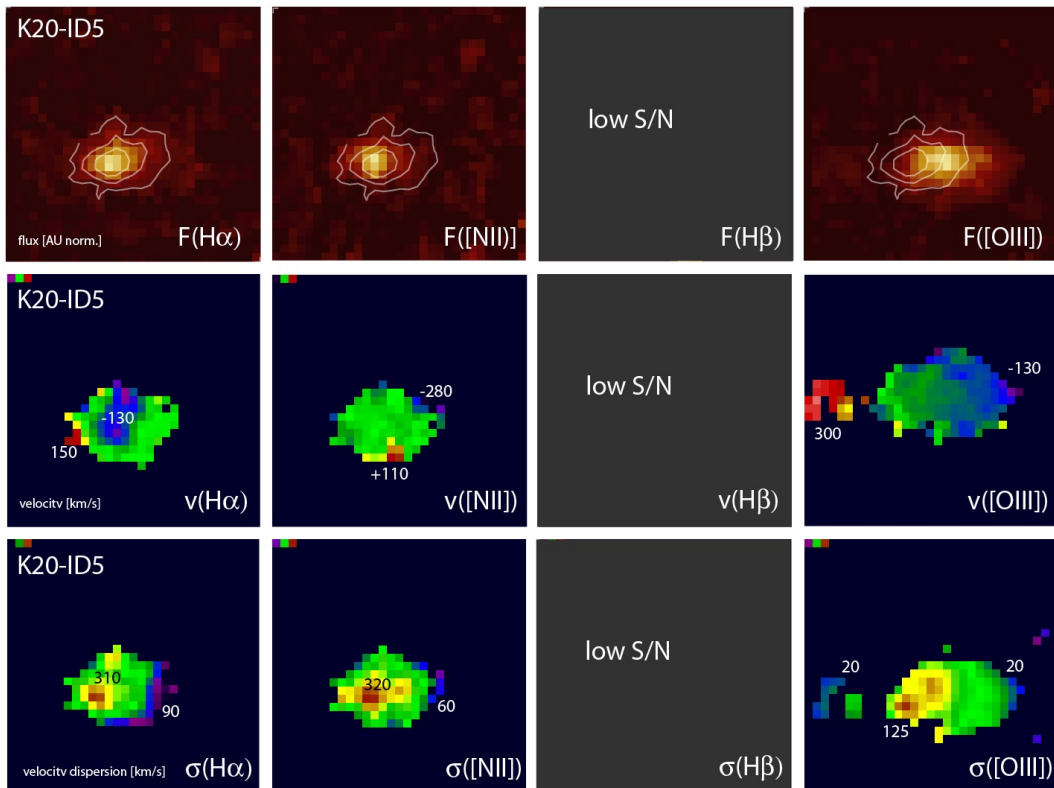


Figure 8.10.: Line-, velocity- and dispersion maps of emission lines for ID5

## 8.2. Morphologies and kinematics from the different emission lines

**D3a-15504** This  $z=2.38$  object is a large massive rotating disk, which hosts an AGN as revealed by detection of characteristic high-excitation lines in its optical (rest-UV) spectrum, and by the rest-optical line ratios and line widths in our SINFONI data (see sections 9.4 and 9.3 and also Genzel et al 2006,2011). The bright  $H\alpha$  and [OIII] emission lines are well detected across the galaxy, and [NII] over most of the same regions. The fainter  $H\beta$  line has lower S/N and is partly affected by an OH line on the blueshifted side of the galaxy. The deep, AO-assisted  $H\alpha$  map obtained for this galaxy shows that the star formation activity in the large disk takes place in several moderately bright clumps superposed on diffuse emission. In contrast to ID5, the contribution from star formation to the integrated emission is more important than that from the AGN, which dominates only in the central part. According to the SED modeling, D3a15504 has a high stellar mass (about  $10^{10}M_{\odot}$ ) and high SFR  $\sim 50 M_{\odot}/\text{yr}$ , but moderately evolved stellar population (age of  $\sim 450$  Myr) and extinction (1 mag).

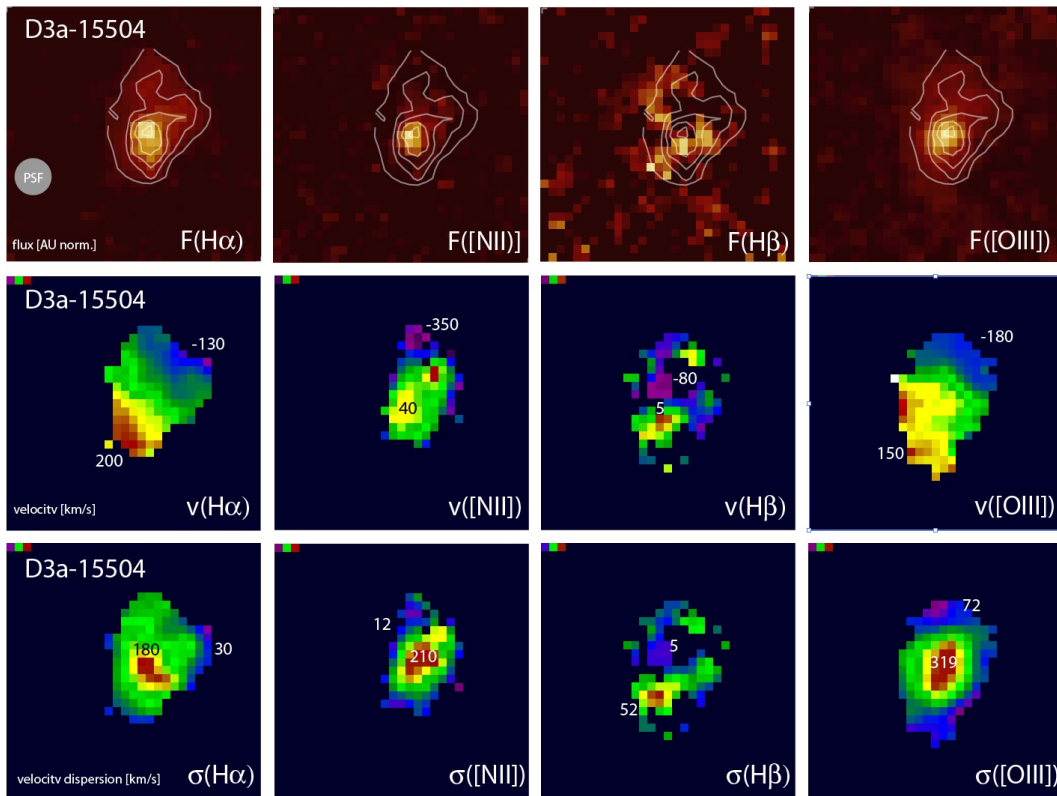


Figure 8.11.: Line-, velocity- and dispersion maps of emission lines for D3a-15504

## Chapter 9.

# Excitation mechanisms and metallicity at high redshift

In this chapter, we analyze the line ratios to determine the dominant excitation mechanism and to constrain the gas-phase abundances. After a general introduction to optical nebular line emission, we start out in the first section with an analysis of source-integrated emission line fluxes and ratios for all sources and apply line excitation diagnostics to determine the dominant excitation mechanism. In the second section, we begin with an overview of metallicity diagnostics, calibrations, and relations. We then use our data to construct relations with global properties (e.g. mass, metallicity and star formation). After this global analysis, we exploit the spatially-resolved information and examine variations within individual galaxies for which high S/N data sets have been obtained. We also assess metallicity gradients and the presence of AGN among our sample of galaxies. We close an analysis of the distribution of individual pixel values in the line excitation diagram for two case studies, illustrating the potential of this detailed approach in gaining insights into the nature of distant galaxies.

### 9.1. Optical nebular line emission

#### 9.1.1. H recombination lines

Hydrogen recombination lines are conspicuous in the emission spectrum of ionized gas, or nebulae in galaxies. The line strengths of H recombination lines can be accurately determined theoretically (e.g., Hummer & Storey 1987). “Case B” recombination is usually assumed (e.g., for HII regions around young stars), i.e., the emitting gas is optically thick in the HI Lyman lines but optically thin in all other lines. The absolute intensity of H recombination lines is proportional to the H ionizing rate. Since the ionizing output from stars is known, these lines provide notably a means of measuring the number of OB stars in star-forming regions and therefore a measure of the current star formation rate (e.g.,

## 9.1. Optical nebular line emission

---

Kennicutt 1998). The intrinsic line emissivities depend on the electron temperature and density ( $T_e$  and  $n_e$ ) of the nebular gas. The variations with  $T_e$  are stronger because the total H recombination coefficient  $\alpha_B \propto T_e^{-0.81}$  but it depends only weakly on  $n_e$  (Hummer & Storey 1987). The relative intrinsic line emissivities depend significantly less on  $T_e$  and  $n_e$ , so that ratios of H recombination lines constitute excellent probes of the (wavelength-dependent) attenuation by interstellar dust (as described in Section 10.1). The  $H\alpha$  and  $H\beta$  lines from the Balmer series are most relevant for this work. Considering typical conditions within star-forming regions, for  $T_e$  between 5000 and 20000 K and a fiducial  $n_e = 10^2 \text{ cm}^{-3}$ , the  $H\alpha/H\beta$  ratio changes from 3.03 to 2.74. For variations in  $n_e$  from  $10^2$  to  $10^6 \text{ cm}^{-3}$  with  $T_e = 10^4 \text{ K}$ , the  $H\alpha/H\beta$  ratio changes from 2.86 to 2.81.

### 9.1.2. Forbidden line emission

Forbidden lines of common heavy elements in different ionization stages are also among the strongest emission lines in astrophysical nebulae (Table 6.1 lists some of the strongest ones in the rest-optical regime). These fine-structure lines arise from levels within a few eV of the ground level and can therefore be excited by collisions with thermal electrons. The density of many types of nebulae is low enough so that the lifetime of forbidden transitions is shorter than the mean time between collisions. Metastable states and higher order transitions with low transition rates are overpopulated in the statistical distribution of excited states and thus forbidden lines dominate the spectrum. Collisional excitation of low-lying energy levels of ions of common heavy elements is a very important source of radiative cooling in astronomical objects. Together with recombination lines, forbidden lines provide useful diagnostics of the electron density and temperature, of the shape of the ionizing radiation field, and of the heavy element abundances. A comprehensive overview can be found in Osterbrock (1989), a brief summary is given here.

Ratios of collisionally-excited lines from the same ion but from transitions with different critical densities are sensitive to the electron density of the nebular gas. In the optical regime, the doublet line ratios  $[\text{OII}] \lambda 3729 / [\text{OII}] \lambda 3726$  and  $[\text{SII}] \lambda 6716 / [\text{SII}] \lambda 6731$  are frequently used to determine the electron density, and are sensitive roughly in the range  $n_e \sim 10^2 - 10^4 \text{ cm}^{-3}$ . Ratios of ionic lines arising from upper levels with different excitation energies are in turn sensitive to the electron temperature. Two commonly used  $T_e$  indicators in the optical regime are  $([\text{OIII}] \lambda 4959 + [\text{OIII}] \lambda 5007) / [\text{OIII}] \lambda 4363$  and  $([\text{NII}] \lambda 6548 + [\text{NII}] \lambda 6584) / [\text{NII}] \lambda 5755$ , with the singlet transitions originating from the upper  $^1S$  level and the doublet transitions from the lower  $^1D$  level. Ratios of lines originating from species with different ionization potentials are sensitive to the spectral slope, or hardness of the ionizing spectrum. For instance, the ionization potentials for  $\text{H}^+$ ,  $\text{N}^+$ , and  $\text{O}^{++}$  are 13.6, 14.5, and 35.1 eV, respectively; consequently, the ratio of the two nearby lines of  $[\text{OIII}] \lambda 5007 / H\beta$  is significantly more sensitive to the hardness of the ionizing radiation field than  $[\text{NII}] \lambda 6584 / H\alpha$ . Clearly, ratios of emission lines from different

elements are also sensitive to the relative abundances of the elements involved; we discuss this aspect further in Section 9.2.3.

## 9.2. Sources as a whole: integrated measurements

Integrated emission line measurements of small sets of high redshift sources have been presented in various works (e.g., Pettini et al. 2001; van Dokkum et al. 2005; Shapley et al. 2005; Erb et al. 2006; Kriek et al. 2007; Liu et al. 2006; Nesvadba et al. 2007; Hayashi et al. 2009; Yoshikawa et al. 2010; Yabe et al. 2011; Queyrel et al. 2009, 2012). Relations which are long known in the local universe, like the mass-metallicity relation, could be extended to intermediate and high redshifts. Most of these studies have presented the analysis of a handful of objects only or of stacked spectra combined according to bins in global galaxy properties rather than individual galaxies due to low signal-to-noise for single-galaxy spectra. Most notably here is the work by Erb et al. (2006a) presenting an investigation of the stellar mass-metallicity relation by spectral stacking analysis of 87 galaxies divided into 6 mass bins at  $z \sim 2.2$  and spanning a stellar mass range of  $\sim 10^{9.3} - 10^{11.2} M_{\odot}$ .

In most work presented so far for  $z \sim 1.5 - 2.5$  objects, only two nebular emission lines were observed, [NII] $\lambda 6584$  and  $H\alpha$ , from which the [O/H] abundance was calculated according to calibrations derived for star-forming sources (such as, e.g., the 'N2' index by Pettini & Pagel 2004). A few studies (e.g., Shapley et al. 2005; Liu et al. 2006; Yabe et al. 2011) have also observed the [OIII] $\lambda 5007$  and  $H\beta$  line to investigate the line excitation properties.

We here present individual measurements for 12 galaxies between  $z = 1.4 - 2.4$  derived from individual galaxy spectra data taken in two near-infrared bands for each galaxy. These data provide measurements of  $H\alpha$ ,  $H\beta$ , [NII] $\lambda 6584$ , and [OIII] $\lambda 5007$  allowing us to constrain the dominant nebular line excitation mechanism.

### 9.2.1. Integrated emission line fluxes

Table 9.1 lists the line fluxes and their respective errors for all observed galaxies. Except for three galaxies, all four emission lines,  $H\alpha$ , [NII] $\lambda 6584$ ,  $H\beta$ , and [OIII] $\lambda 5007$  could be detected. For D3a6397, both  $H\beta$  and [OIII] could not be detected and upper-limits were as described in Section 7.5.2. For BX663 and BX482,  $H\beta$  could not be detected and also a reliable upper limit could not be calculated as in both cases the spectrum around the wavelength of  $H\beta$  is severely contaminated by a nearby OH line. The size and shape of the region used for spectrum extraction varies between objects and, for some objects, only covers a part of the whole galaxy, as traced by the  $H\alpha$  emission. This is often due

## 9.2. Sources as a whole: integrated measurements

to OH-line contamination on the blue or red side of an emission line, which then makes the 'blue' or 'red' side of a galaxy (as defined from the velocity map) unusable for line fitting. For an individual galaxy, the extraction regions are the same for all four lines (see section 7.5.2 for details on the spectrum extraction and fit).

Table 9.1.: Measured line fluxes<sup>(a)</sup> for H $\alpha$ , [NII] $\lambda$ 6584, H $\beta$ , and [OIII] $\lambda$ 5007

Source	F(H $\alpha$ )	F([NII])	F(H $\beta$ )	F([OIII])
Fluxes in units of $10^{-16}$ erg/s/cm <sup>2</sup>				
BM1163	5.58 <sup>+0.14</sup> <sub>-0.14</sub>	0.93 <sup>+0.05</sup> <sub>-0.04</sub>	0.99 <sup>+0.08</sup> <sub>-0.06</sub>	2.30 <sup>+0.06</sup> <sub>-0.05</sub>
BX663	0.88 <sup>+0.04</sup> <sub>-0.04</sub>	0.30 <sup>+0.03</sup> <sub>-0.03</sub>	... <sup>(c)</sup>	0.23 <sup>+0.06</sup> <sub>-0.04</sub>
MD41	1.19 <sup>+0.03</sup> <sub>-0.03</sub>	0.11 <sup>+0.03</sup> <sub>-0.03</sub>	0.25 <sup>+0.03</sup> <sub>-0.04</sub>	1.08 <sup>+0.04</sup> <sub>-0.04</sub>
BX389	0.71 <sup>+0.02</sup> <sub>-0.02</sub>	0.08 <sup>+0.02</sup> <sub>-0.02</sub>	0.19 <sup>+0.03</sup> <sub>-0.02</sub>	0.50 <sup>+0.02</sup> <sub>-0.02</sub>
BX610	2.61 <sup>+0.08</sup> <sub>-0.07</sub>	1.03 <sup>+0.04</sup> <sub>-0.05</sub>	0.38 <sup>+0.03</sup> <sub>-0.03</sub>	0.71 <sup>+0.06</sup> <sub>-0.05</sub>
BX482	1.94 <sup>+0.07</sup> <sub>-0.05</sub>	0.24 <sup>+0.07</sup> <sub>-0.05</sub>	... <sup>(c)</sup>	1.11 <sup>+0.05</sup> <sub>-0.05</sub>
K20ID5	1.77 <sup>+0.07</sup> <sub>-0.09</sub>	1.04 <sup>+0.08</sup> <sub>-0.07</sub>	0.14 <sup>+0.03</sup> <sub>-0.03</sub>	1.38 <sup>+0.05</sup> <sub>-0.04</sub>
K20ID7	1.46 <sup>+0.05</sup> <sub>-0.05</sub>	0.32 <sup>+0.03</sup> <sub>-0.04</sub>	0.17 <sup>+0.02</sup> <sub>-0.03</sub>	0.40 <sup>+0.03</sup> <sub>-0.03</sub>
D3a6004	0.15 <sup>+0.01</sup> <sub>-0.01</sub>	0.06 <sup>+0.01</sup> <sub>-0.01</sub>	0.02 <sup>+0.01</sup> <sub>-0.01</sub>	0.04 <sup>+0.01</sup> <sub>-0.01</sub>
D3a6397	2.10 <sup>+0.10</sup> <sub>-0.11</sub>	0.86 <sup>+0.06</sup> <sub>-0.07</sub>	<0.17 <sup>(b)</sup>	<0.09 <sup>(b)</sup>
D3a15504	0.93 <sup>+0.04</sup> <sub>-0.04</sub>	0.33 <sup>+0.03</sup> <sub>-0.03</sub>	0.12 <sup>+0.02</sup> <sub>-0.02</sub>	0.86 <sup>+0.03</sup> <sub>-0.04</sub>
ZC782941	1.86 <sup>+0.08</sup> <sub>-0.06</sub>	0.44 <sup>+0.04</sup> <sub>-0.04</sub>	0.28 <sup>+0.03</sup> <sub>-0.03</sub>	0.59 <sup>+0.03</sup> <sub>-0.02</sub>

<sup>(a)</sup> The fluxes are extracted from common regions across the object in which all four lines are detected; the regions do not cover the whole object (as traced by the H $\alpha$  emission) in all cases.

<sup>(b)</sup>  $1\sigma$  upper limit

<sup>(c)</sup> unreliable upper limit due to partly overlapping OH line

All line fluxes (table 9.1) have been derived using integral field observations. Thus there has been no need for an aperture correction factor, which accounts for undetected emission of the source due to slit losses and slit misalignment. Such corrections have been used in various previous studies (e.g., Erb et al. 2006). With the full 2D mapping, we recover the total fluxes of the sources irrespective of their sizes, P.A., or morphologies. This makes calculations involving lines from two observing bands such as H $\alpha$ /H $\beta$  significantly more robust. Uncertainties in the absolute flux calibrations are further reduced with SINFONI as we get a full coverage of the atmospheric bands with each of the gratings,

allowing us to synthesize the broad-band fluxes of our telluric standards.

We used the data in table 9.1 to derive the region-integrated [NII]/H $\alpha$  and [OIII]/H $\beta$  ratios, listed in table 9.2. From those ratios, we calculated the N2 and O3N2 based oxygen abundance (table 9.3) in units of  $12+\log(\text{O}/\text{H})$  as defined by Pettini & Pagel (2004). The two hydrogen lines H $\alpha$  and H $\beta$  were used to calculate the Balmer decrement H $\alpha$ /H $\beta$ . The integrated [NII]/H $\alpha$  and [OIII]/H $\beta$  ratios were plotted in the BPT diagnostic diagram as discussed below in 9.2.2. We also investigated the relations between metallicity and other known global source properties such as stellar mass and star formation rate. These results are discussed in section 9.2.3. Results from the Balmer decrement measurements are discussed in chapter 10.

Table 9.2.: [NII]/H $\alpha$  and [OIII]/H $\beta$  ratios calculated from table 9.1

Source	[NII] $\lambda$ 6584/H $\alpha$	[OIII] $\lambda$ 5007/H $\beta$
BM1163	0.17 $^{+0.01}_{-0.01}$	2.33 $^{+0.20}_{-0.16}$
BX663	0.34 $^{+0.04}_{-0.04}$	... <sup>(a)</sup>
MD41	0.09 $^{+0.02}_{-0.02}$	4.41 $^{+0.60}_{-0.67}$
BX389	0.12 $^{+0.03}_{-0.03}$	2.62 $^{+0.37}_{-0.29}$
BX610	0.39 $^{+0.02}_{-0.02}$	1.88 $^{+0.20}_{-0.21}$
BX482	0.12 $^{+0.03}_{-0.02}$	... <sup>(a)</sup>
K20ID5	0.59 $^{+0.05}_{-0.05}$	10.22 $^{+2.21}_{-2.39}$
K20ID7	0.22 $^{+0.03}_{-0.03}$	2.28 $^{+0.36}_{-0.42}$
D3a6004	0.41 $^{+0.07}_{-0.07}$	1.78 $^{+0.48}_{-0.44}$
D3a6397	0.41 $^{+0.03}_{-0.04}$	... <sup>(b)</sup>
D3a15504	0.35 $^{+0.03}_{-0.04}$	6.96 $^{+1.11}_{-1.14}$
ZC782941	0.24 $^{+0.02}_{-0.02}$	2.06 $^{+0.24}_{-0.22}$

<sup>(a)</sup> unreliable lower limit (OH line near H $\beta$ )

<sup>(b)</sup> both H $\beta$  and [OIII] fluxes are limits

### 9.2.2. The BPT diagram at $z \sim 2$

#### Line excitation diagnostics

Various diagnostic diagrams have been devised to distinguish the dominant excitation sources of the line-emitting gas in galaxies (e.g., photoionization by hot young stars in HII regions, i.e., 'star formation', Type 2 AGN, LINERs, shocks). Most notably, Baldwin, Phillips, & Terlevich (1981), introduced diagrams based on various line ratios including  $[\text{NII}] \lambda 6584 / \text{H}\alpha$ ,  $[\text{OIII}] \lambda 5007 / \text{H}\beta$ ,  $[\text{SII}] \lambda \lambda 6716, 6731 / \text{H}\alpha$ ,  $[\text{OI}] \lambda 6300 / \text{H}\alpha$ . Veilleux & Osterbrock (1987) expanded on this work, and classification schemes based on the BPT diagrams were subsequently updated by Kewley et al. (2001b; 2006) and Kauffmann et al. (2003). The basic principle behind the construction of such diagrams is to combine pairs of line ratios that are sensitive to different physical parameters, which in turn are indicative of the excitation mechanisms. Ideally, each line ratio involves lines which are close in wavelength, such that the effects of dust extinction are minimized (Section 10.1).

The  $[\text{OIII}] \lambda 5007 / \text{H}\beta$  versus  $[\text{NII}] \lambda 6584 / \text{H}\alpha$  diagram is perhaps the most commonly used, and is the one that we employ in our analysis below. For simplicity, this diagram is hereafter referred to as the BPT diagram. Because of the different ionization potentials of  $\text{O}^{++}$  and  $\text{H}^+$  (35.1 and 13.6 eV, respectively), the  $[\text{OIII}]/\text{H}\beta$  ratio is very sensitive to the hardness of the ionizing spectrum; it also varies with the ionization parameter and the gas-phase abundances. In contrast, the  $[\text{NII}]/\text{H}\alpha$  ratio, which also depends on the ionization parameter, is far less sensitive to the hardness of the ionizing radiation because of the  $\text{N}^+$  ionization potential of 14.5 eV but is more sensitive to the gas-phase abundances.

Empirically, emission line galaxies in the local universe define two main regions in BPT diagram, as illustrated in Figure 9.1. (Baldwin 1981; Veilleux & Osterbrock 1987; Kewley et al. 2001a, 2006; Kewley & Dopita 2002; Kauffmann et al. 2003).

Purely star-forming galaxies (as well as individual HII regions in the Milky Way and nearby galaxies) follow a fairly tight sequence correlated with gas-phase abundances, from high  $[\text{OIII}]/\text{H}\beta$ , low  $[\text{NII}]/\text{H}\alpha$  ratios (low abundances) to low  $[\text{OIII}]/\text{H}\beta$ , high  $[\text{NII}]/\text{H}\alpha$  ratios (high abundances). The distribution of galaxies along the star-forming sequence is primarily driven by metallicity effects through the key difference that O production in stars is primary, while N production is both primary and secondary. Detailed photoionization modeling allows to follow the behavior of the line ratios along the sequence (e.g., Kewley & Dopita 2002; Kewley et al. 2006; Levesque et al. 2010). Low metallicity objects, where O and N are of primary origin, populate the high  $[\text{OIII}]/\text{H}\beta$ , low  $[\text{NII}]/\text{H}\alpha$  part due to the harder radiation from low-metallicity OB stars, lower gas-phase abundances, and correspondingly higher  $T_e$  of the HII regions. As the abundances increase, cooling

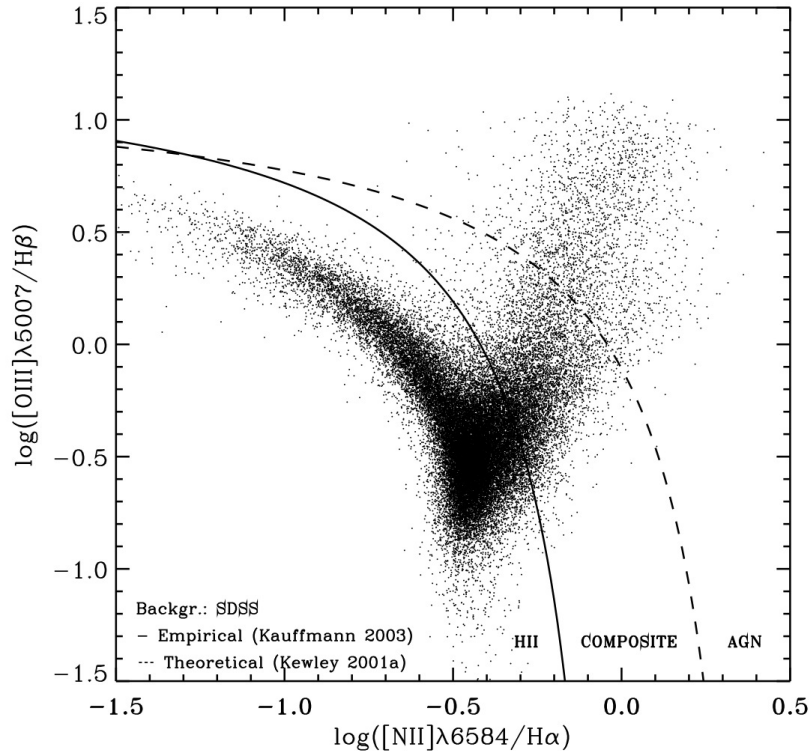


Figure 9.1.: The  $[\text{OIII}]\lambda 5007/\text{H}\beta$  vs.  $[\text{NII}]\lambda 6584/\text{H}\alpha$  BPT Diagram. Local SDSS galaxies are plotted and form a characteristic v-shape defining two main regions: the star-forming branch towards the left and the AGN branch towards the top-right. On the x-axis, the  $[\text{NII}]/\text{H}\alpha$  ratio describes the metallicity, the y-axis is a measure for the excitation hardness, higher  $[\text{OIII}]/\text{H}\beta$  implying harder excitation. Three demarcation lines are over-plotted, which separate different types of galaxies: The solid and dashed line separate AGN and Star-forming galaxies (excitation dominated by HII regions) based on empirical classification or theoretical modeling. In the region in between the two lines, composite galaxies are located.

of the nebular gas also increases, reducing the number of thermal electrons of appropriate energies for collisional excitation of forbidden lines. The bluer  $[\text{OIII}]\lambda 5007$  line is somewhat more affected than  $[\text{NII}]\lambda 6584$  because of its comparatively higher collisional excitation energy. However, the secondary production of N starts to dominate and, by mitigating the effects of increased cooling, enhances  $[\text{NII}]/\text{H}\alpha$  whereas  $[\text{OIII}]/\text{H}\beta$  further decreases. At the highest abundances, N itself becomes the dominant coolant and the  $T_e$  drops sufficiently to drive  $[\text{OIII}]/\text{H}\beta$  to yet lower values and to compensate for the N secondary production, so that the  $[\text{NII}]/\text{H}\alpha$  ratio “saturates” at around  $\log([\text{NII}]/\text{H}\alpha) \approx -0.5$ . Type 2 AGN sources lie on a separate branch at higher  $[\text{NII}]/\text{H}\alpha$  and  $[\text{OIII}]/\text{H}\beta$  ratios, reflecting the harder ionizing radiation from the nuclear power-law source (e.g., Dopita et al. 2002; Groves et al. 2004a,b). There is evidence that local AGN host galaxies gen-

erally have solar or higher metallicities (e.g., Heckman 1980; Pagel & Edmunds 1981; Diaz, Pagel, & Wilson 1984; Kauffmann et al. 2003), contributing to the high  $[\text{NII}]/\text{H}\alpha$  ratio. Line emission associated with shock activity significantly overlaps with the AGN region towards high  $[\text{NII}]/\text{H}\alpha$  and a wide range of  $[\text{OIII}]/\text{H}\beta$ . This is observed notably in large-scale galactic winds powered by intense starburst activity or an AGN, although photoionization by radiation escaping from the galaxy can also contribute to the excitation, especially at the base of the wind (e.g., Veilleux & Rupke 2002; Veilleux et al. 2003; Lipari et al. 2004; Monreal-Ibero et al. 2010; Rich et al. 2010; Sharp & Bland-Hawthorn 2010).

Kewley et al. (2001a) explored the theoretical upper limit in the BPT diagram above which star-forming galaxies are very unlikely to be found. This limit was obtained from stellar population synthesis coupled with photoionization modeling, computed for a wide range of physical parameters plausible for star-forming and starburst galaxies. The demarcation curve by Kauffmann et al (2003b) is based on the observed distribution of local line-emitting galaxies from the Sloan Digital Sky Survey and is more conservative in terms of defining purely star-forming galaxies. With this empirical criterion, only galaxies which have an AGN contribution to  $\text{H}\alpha$  of  $< 1\%$  are selected as non-AGN type.

The region between HII regions/star-forming galaxies and AGN-dominated objects, essentially between the two demarcation lines, is usually referred to as the “composite” region, where both AGN and star formation activity may contribute significantly to the excitation of emission lines (Kewley et al. 2006). It is, however, noteworthy that local starburst galaxies without AGN overlap with this “composite” region, reflecting elevated ionization parameters and electron densities associated with the enhanced star formation levels and surface densities (e.g. Kewley et al. 2011; Liu et al. 2008).

### Results

For 9 galaxies in our sample, we could detect all four emission lines  $\text{H}\alpha$ ,  $[\text{NII}]\lambda 6584$ ,  $\text{H}\beta$  and  $[\text{OIII}]\lambda 5007$ . BX663 and BX482 were omitted as their  $\text{H}\beta$  upper limit is unreliable. D3a-6397 has upper limits in both  $\text{H}\beta$  and  $[\text{OIII}]$  line fluxes and thus no  $[\text{OIII}]/\text{H}\beta$  ratio could be calculated. Having access to these four emission lines allows us to carry out an analysis of line excitation mechanisms present within the observed galaxies. Figure 9.2 shows the  $[\text{OIII}]\lambda 5007/\text{H}\beta$  vs.  $[\text{NII}]\lambda 6584/\text{H}\alpha$  ‘BPT’ diagram with source-integrated values for galaxies of this work. Results from other studies with measurements for individual galaxies are shown for comparison. In the background, the local galaxy population from the SDSS ( $0.04 \lesssim z \lesssim 0.1$ ) has been plotted for reference.

For the majority of the objects in our sample, we find an offset position, i.e., a slightly higher  $[\text{OIII}]/\text{H}\beta$  ratio compared to the average of local SDSS galaxies at a given  $[\text{NII}]/\text{H}\alpha$  ratio. The observed galaxies are mostly located in the region between the star-forming and AGN branch in the BPT diagram as traced out by the local SDSS galaxies,

a region, which is only very sparsely but still *is* populated by local galaxies. For a few other objects, the measured line ratios correspond to locations in the BPT diagram, which are well populated by SDSS galaxies. This is consistent with most findings of other recent work for smaller samples of galaxies selected by similar criteria as in this work. The observed offset suggests that various excitation mechanisms contribute in different proportions to the global line emission or, possibly, different physical conditions are prevailing in high- $z$  non-AGN actively star-forming systems compared to the bulk of local star-forming galaxies (see, e.g., the detailed discussion by Liu et al. 2008).

One galaxy (BX389) is located very close to the branch for local star-forming galaxies, with high  $[\text{OIII}]/\text{H}\beta$  and comparably low  $[\text{NII}]/\text{H}\alpha$  ratios, with only slightly higher  $[\text{OIII}]/\text{H}\beta$  ratio than the SDSS mean for the respective  $[\text{NII}]/\text{H}\alpha$  ratio. Two galaxies, K20-ID7 and ZC-782941, are more significantly offset above the star-forming branch very close to the empirical demarcation of Kauffmann et al. (2003). D3a-6004 and BX610 are located in the composite region at the left of the AGN branch. From the measured ratios, K20-ID5 appears to be a Seyfert-2 type AGN host galaxy. A very interesting object is D3a-15504, which shows a very unusual location at high  $[\text{OIII}]/\text{H}\beta$  but modest  $[\text{NII}]/\text{H}\alpha$  ratio, that places it between the star-forming galaxy- and AGN-branch. This galaxy could be spatially-resolved in all four BPT lines with high S/N and is discussed in detail in section 9.4. We will now discuss each object's BPT location, along with known properties from previous SINS work and papers.

### Summary:

Our results from the analysis of spatially-integrated line ratios combined with other source properties suggest that there is no single dominant mechanism common to all galaxies, which is causing the observed offset in the BPT diagram, compared to the location of local SDSS galaxies. On a case by case basis, we have found galaxies at  $z \sim 2$  with little offset relative to the distribution of local star-forming galaxies from SDSS at low  $[\text{NII}]/\text{H}\alpha$  and high  $[\text{OIII}]/\text{H}\beta$  ratios. Known AGNs are located in the Seyfert-2 and in the composite regions. The other sources show a similar offset as found in other high- $z$  studies, being located towards higher values in  $\log[\text{OIII}]/\text{H}\beta$  and in between the AGN and star-forming branch. For these objects, contributions from (possibly low-luminosity) AGN (e.g., Wright et al. 2009, 2010) as well as (possibly outflow-related) shocks or an ISM with higher electron density and ionization parameter may be possible (e.g., Shapley et al. 2005; Liu et al. 2008, Erb et al. 2006; Newman et al. 2012). None of our sources was found where the bulk of SDSS are located at the base of the V-shape distribution at low  $[\text{OIII}]/\text{H}\beta$  values. It should be noted that the offsets relative to the distribution of SDSS galaxies seen in this and other studies for the majority of the objects, are not offsets to regions that are entirely unpopulated by local galaxies: the offsets are still consistent with some local SDSS galaxies. In the section 9.4, we will demonstrate how a spatially-resolved analysis helps to rule out or confirm excitation scenarios that are otherwise indistinguishable in an analysis based on spatially-integrated measurements.

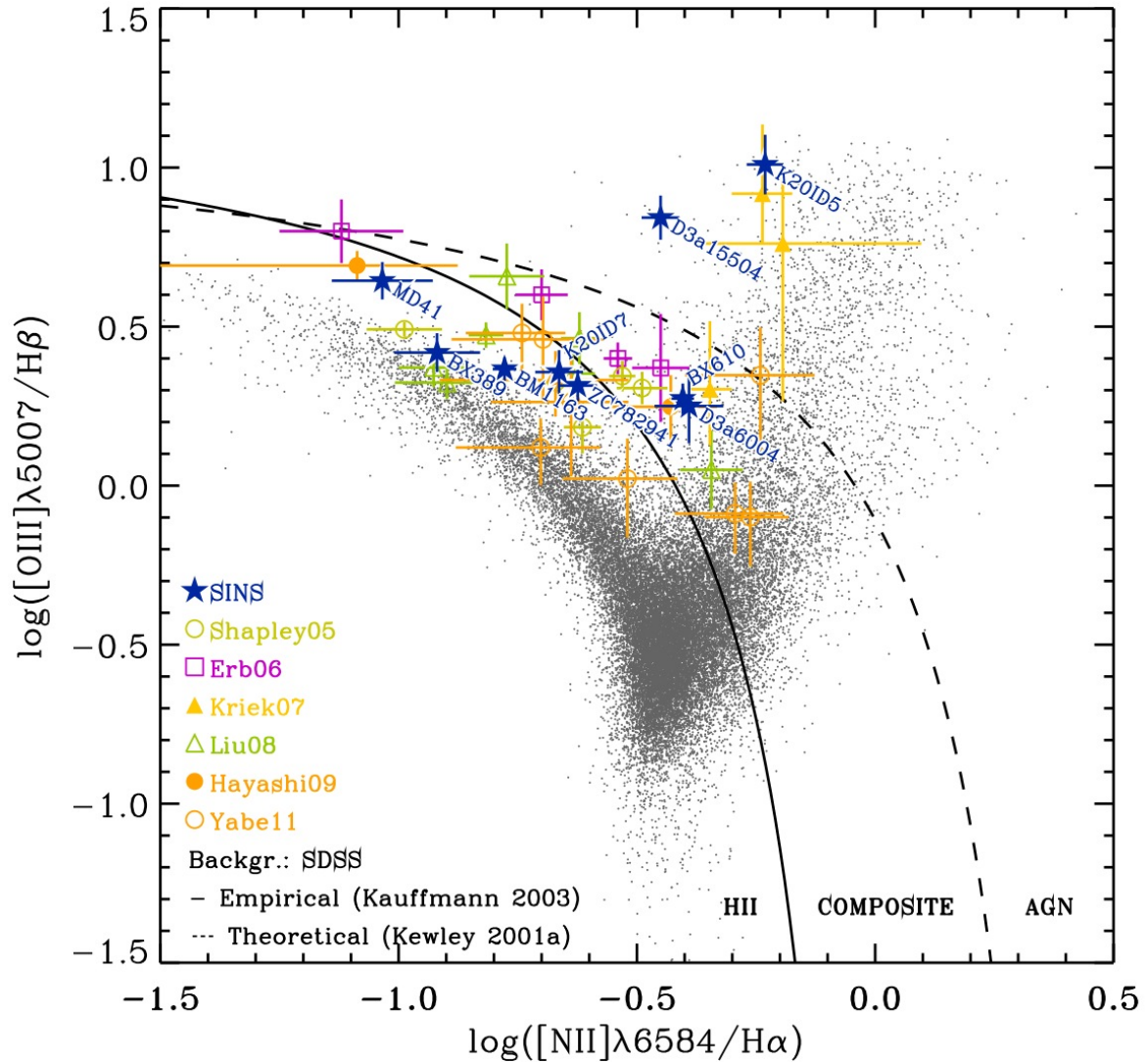


Figure 9.2.:  $[\text{NII}]\lambda 6584/\text{H}\alpha$  vs.  $[\text{OIII}]\lambda 5007/\text{H}\beta$  'BPT' diagram showing source-integrated values.

Background: local galaxy population from the SDSS. Star-forming galaxies and HII-regions are located on the left branch with decreasing gas-phase oxygen abundances towards lower  $[\text{NII}]/\text{H}\alpha$  and higher  $[\text{OIII}]/\text{H}\beta$  ratios. Galaxies with shocks and AGN dominating the gas excitation are located on the right branch. The blue 'star' data points show the source-integrated measurements from the SINS galaxies in this work. In other colors the results from selected studies with measurements for individual galaxies are shown for comparison. The SINS galaxies tend to be offset towards the region between the star-forming and AGN branches for local galaxies, suggesting that various excitation mechanisms contribute in different proportions to the global line emission or, possibly, different physical conditions are prevailing in non-AGN actively star-forming galaxies at high- $z$ .

**Individual objects:**

**MD41:** SSA22-MD41 at  $z=2.172$  is located in top left region of the star-forming branch with a low  $[\text{NII}]/\text{H}\alpha = 0.09 \pm 0.02$  and a high  $[\text{OIII}]/\text{H}\beta$  ratio of  $4.41 \pm 0.64$ . Its offset above the SDSS star-forming branch is comparable to most of our other galaxies. Together with the findings presented in section 8.2, MD41 is an actively star-forming galaxy with line ratios consistent with pure photoionization in HII regions and suggestive of low metallicity, which is in line with the young inferred stellar age of 50 Myr.

**BX389:** This  $z=2.17$  galaxy is located closest to the SDSS star-forming branch (only about 0.1 dex above) at an  $[\text{OIII}]/\text{H}\beta$  ratio of  $2.62 \pm 0.33$  and  $[\text{NII}]/\text{H}\alpha$  ratio of  $0.12 \pm 0.03$ . Its position suggests a metallicity of a somewhat more evolved system than MD41 backed by the SED based stellar age of 2.75 Gyr.

**BM1163:** With  $[\text{NII}]/\text{H}\alpha = 0.17 \pm 0.01$  and  $[\text{OIII}]/\text{H}\beta = 2.33 \pm 0.18$  this  $z=1.41$  galaxy is located above the SDSS star-forming branch offset by  $\sim 0.15$  dex. For BM1163 we have no SED modeling.

**K20-ID7:** ID7 is a  $z=2.23$  merger located offset from the star-forming galaxy branch by  $\sim 0.35$  dex in  $[\text{OIII}]/\text{H}\beta$  at the border between HII and composite regions as defined by Kauffman et al. (2003;  $[\text{NII}]/\text{H}\alpha = 0.22 \pm 0.03$ ,  $[\text{OIII}]/\text{H}\beta = 2.28 \pm 0.39$ ). As we do not see any sign supporting the presence of an AGN in this system, the offset may reflect contributions from merger-induced shocks or different ISM conditions.

**ZC782941:** This  $z=2.18$  galaxy at  $[\text{NII}]/\text{H}\alpha = 0.24 \pm 0.02$  and  $[\text{OIII}]/\text{H}\beta = 2.06 \pm 0.23$  is located offset by  $\sim 0.3$  dex in  $[\text{OIII}]/\text{H}\beta$  and, similarly to K20-ID7, is close to the boundary between HII and composite regions. For this galaxy, evidence for outflowing ionized gas (in the form of a low-amplitude broad Ha component) has been found in deep AO-assisted data (Genzel et al. 2011; Newman et al. in prep.). Shocks associated with this outflow might influence the line ratios and be responsible for the observed offset.

**BX610:** BX610 is located at  $[\text{NII}]/\text{H}\alpha = 0.39 \pm 0.02$  and  $[\text{OIII}]/\text{H}\beta = 1.88 \pm 0.21$  in the composite region. We have inferred an age of 2.75 Gyr from SED modeling, thus the high  $[\text{NII}]/\text{H}\alpha$  ratio likely reflects the high metallicity of an evolved galaxy.

**D3a-6004:** For this  $z = 2.39$  disk galaxy, we could only measure a reliable  $[\text{OIII}]/\text{H}\beta$  ratio in the region west of the nucleus where the line emission peaks. The  $[\text{NII}]/\text{H}\alpha = 0.41 \pm 0.07$  and  $[\text{OIII}]/\text{H}\beta = 1.78 \pm 0.47$  places this region in the composite regime of the BPT diagram, very close to the integrated values for BX610. The off-center location of peak Ha and  $[\text{OIII}]$  emission in D3a6004 (see Figure 8.7) would disfavor an AGN as causing the offset away from the purely star-forming branch. The comparably high integrated  $[\text{NII}]/\text{H}\alpha$  ratio and a stellar age of  $\sim 640$  Myr suggest that D3a-6004 is quite evolved, so that enhanced enrichment of the ISM could plausibly account at least in part for the observed line ratios of the off-center star-forming complex.

**K20-ID5:** At  $[\text{NII}]/\text{H}\alpha = 0.59 \pm 0.05$ ,  $[\text{OIII}]/\text{H}\beta = 4.41 \pm 0.64$ , ID5 is located on the Seyfert-2 side of the AGN branch. The rest-frame optical emission characteristics of K20-ID5 were argued by van Dokkum et al. (2005) to be more consistent with shock excitation rather than AGN activity because of their spatial extent. The spatially-resolved line ratios (see 9.3.2) support the presence of an AGN but also show that for extra nuclear regions the rest-frame optical emission line spectrum and thus the measured line ratios likely include a large and perhaps dominant contribution from shock excitation.

**D3a-15504** This object is located comparably far off all our other sources and the local SDSS galaxies at  $[\text{NII}]/\text{H}\alpha = 0.35 \pm 0.03$  and  $[\text{OIII}]/\text{H}\beta = 6.96 \pm 1.12$ . The clue to its very puzzling location is revealed once a spatially-resolved pixel-to-pixel BPT analysis is done (see 9.4). D3a-15504's offset is caused by the superposition of two excitation mechanisms, hence two sets of ratios, as the spatial dominance of its AGN is limited to the center, showing a typical AGN branch ratio, whereas the (outer) disk shows ratios typical of star-forming galaxies.

### Results of other studies

Results from selected studies with measurements for individual galaxies are shown in figure 9.2 for comparison. We summarize their findings in the next paragraphs.

#### *Shapley 05 (open circles):*

Shapley et al. (2005) have observed a sample of 72 star-forming galaxies at  $1.0 < z < 1.5$  drawn from the DEEP2 Galaxy redshift survey. Five were detected in all 4 BPT lines. Two at  $z \sim 1.0$  are located roughly on the local star-forming branch, showing slightly higher  $[\text{OIII}]/\text{H}\beta$  still. The three others are at a slightly higher redshift  $z \sim 1.4$  and are significantly offset, two into the composite region. In a short comparison with SDSS, they find higher SFRs for the five galaxies relative to typical SDSS values, from which they argue that this leads to an increase in the ionization parameter. They further report on higher electron densities from earlier  $[\text{OII}]$  measurements for these galaxies, which they find to be similar to local starbursts. They conclude that a combination of higher ionization parameter and higher electron densities likely causes the offset.

#### *Erb 06 (open squares):*

Erb et al. (2006) have studied a sample of 87 rest-UV selected star-forming galaxies at  $z \gtrsim 2$ , focussing on the mass-metallicity relation at high redshifts. They also observed the full BPT line set for four galaxies. All four objects are offset from the local SDSS sequence and fall in the composite region above the star-forming branch. Erb et al. could exclude any AGN contribution to their sample based on X-ray and UV properties.  $[\text{SII}]$  line measurements from their composite spectra indicate an elevated electron density of  $n_e \sim 500 \text{cm}^{-3}$  which could contribute to the observed shift in the BPT diagram.

*Kriek 07 (filled triangles):*

Kriek et al. (2007) presented measurements of 10 K-selected galaxies at  $z \sim 2.3$  with integral field spectroscopy using SINFONI at the VLT. For three of them, they could detect all four BPT lines. One is located in the composite region and does not exhibit signs of AGN activity based on its mid-IR SED shape. For this object, they regard a starburst-driven outflow as a likely scenario. The second galaxy is located well in the AGN Seyfert-2 regime. They report on a compact emission line region in this object and low SFR, and conclude the observed line ratios are not caused by a starburst-driven wind. They classify this object as an AGN. Kriek et al. also include the measurements of K20-ID5 obtained with the Gemini/GNIRS spectrograph, reported by van Dokkum et al. (2005). Compared to our measurements, the GNIRS-based  $[\text{NII}]/\text{H}\alpha$  ratio is in excellent agreement and the  $[\text{OIII}]/\text{H}\beta$  ratio is higher but still consistent at the  $2\text{-}\sigma$  level. The differences could be due to aperture effects for the long-slit GNIRS data.

*Liu 08 (open triangles):*

In a follow up of Shapley et al. (2005), Liu et al. (2008) have analyzed 20 star-forming galaxies at  $1.0 < z < 1.5$  drawn from the DEEP2 Galaxy redshift survey. The 7 galaxies for which they could detect all four BPT lines are significantly offset from the excitation sequence of SDSS emission line galaxies and nearby HII regions. To assess the offset's cause, they examined the properties of the small fraction of local SDSS galaxies that show BPT ratios similar to their DEEP-2 sample. For these offset SDSS objects they find two likely causes for the offset: a contribution by shocks and/or AGN at a level of  $\sim 20\%$  and different physical conditions in HII regions showing significantly larger ionization parameters due to higher electron densities and temperatures. They speculate that the cause for this might be connected to the host galaxies being smaller in size and featuring higher star formation rate surface densities.

*Hayashi 09 (filled circles):*

Hayashi et al. (2009) presented spectra of 15 star-forming BzK-color selected  $((z - K) - (B - z) > -0.2)$  galaxies ("sBzK's") at  $z \sim 2$ . Three galaxies could be detected in all four lines. Two metal-poor galaxies are located  $\sim 0.2$  dex above the local relation. One is located in the composite region towards the Seyfert-2 regime. They argue, however, that due to the comparably weak  $[\text{NII}]$  line, this object is more likely a metal-poor star-forming galaxy. They crosscheck for the presence of AGN using long wavelength SED fitting finding that one of the three galaxies (the one at  $\log[\text{NII}]/\text{H}\alpha \sim 0.7$  in fig. 9.2) could be consistent with a power-law fit possibly indicating the presence of a Seyfert-2 nucleus.

*Yabe 11 (open circles)*

Yabe et al. (2011) have observed a K-band ( $K \leq 23.9$  mag) selected sample of 71 objects with a photometric redshift of  $1.2 \leq z_{ph} \leq 1.6$  with the fiber-fed multi-object spectrograph FMOS at Subaru. Seven sources could be reliably detected in all four BPT lines. Their sources show a distribution across the BPT diagram similar to our findings. One is lo-

cated well within the star-forming branch, three are offset towards higher  $[OIII]/H\beta$  just below the boundary between HII regions and composite sources, two are located in the composite region in the AGN branch, and one is likely an AGN located right at the theoretical demarcation line between starburst and AGN systems derived by Kewley et al. (2001).

### The effect of $H\beta$ absorption

The measured  $H\beta$  fluxes might be biased by underlying stellar  $H\beta$  absorption (e.g. Dufour et al. 1980). We discuss this effect in more detail in section 10.2 as this is especially important when calculating the extinction from the Balmer decrement  $H\alpha/H\beta$ . In figure 9.3, we show the effect of correcting for  $H\beta$  absorption on the location of our SINS targets in the BPT diagram (for details on the calculation see section 10.2). We do see a noticeable down-shift in  $[OIII]/H\beta$  of  $\sim 0.02$  to  $0.21$  dex (mean  $0.12$  dex). Nevertheless, accounting for  $H\beta$  absorption does not reconcile our data with the distribution of local galaxies from the SDSS. Our estimated corrections for  $H\beta$  absorption are fairly similar to those of Shapley et al. (2005) who reported a maximum down-shift of  $0.1$  dex and also found that unaccounted-for  $H\beta$  absorption is likely not causing the observed offset in  $[OIII]/H\beta$  for their DEEP2 sample.

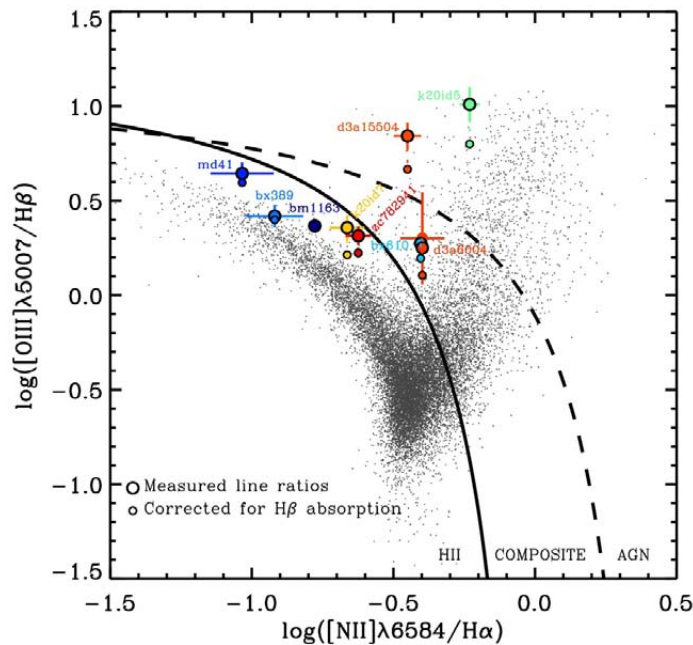


Figure 9.3.: Impact of accounting for underlying stellar  $H\beta$  absorption on the  $[OIII]/H\beta$  ratios measured for our 9 SINS galaxies. The mean effect is a decrease in ratio by  $0.12$  dex.

### 9.2.3. Integrated line ratios and metallicities

One of the most important properties of galaxies is their metallicity. Practically all existing chemical elements heavier than hydrogen, helium and lithium, which are largely of primordial origin, have been produced by stellar nucleosynthesis at some point in the past. The observed chemical composition of a galaxy, the spatial distribution, and relative abundances of heavy non-primordial elements, is not a snapshot of current conditions in these systems but is a property, which is integrated over the objects past. As such, it is a record of all preceding processes that influence the global chemical composition and the distribution of metals within galaxies.

The detailed star formation history (SFH) of galaxies will be reflected in their overall metallicity, as well as in their abundance patterns since stars of different initial mass have different lifetimes and different chemical yields. Metals are dispersed within galaxies through supernova explosions and stellar winds. They can be lost through galactic scale outflows, which in turn enrich the IGM. Gas accretion, gas infall of metal-poor gas into galaxies, dilutes the gas-phase metallicity. Mergers and internal mixing processes change the spatial distribution of metals. Metals play a critical role in cooling processes, which in turn directly affect timescales of gas infall onto galaxies and star formation within galaxies. Measurements of chemical abundances of galaxies and gradients thereof can thus provide constraints on the interplay, relative role and timescales of various processes.

#### Metallicity diagnostics

Empirically, the most reliable abundance diagnostics utilize the intensity ratio of an auroral line transition to a nebular line transition of the same ion sensitive to the electron temperature  $T_e$ . In the local universe and at low redshifts, the classical auroral line used for this measurement is the Oxygen [OIII] $\lambda$ 4363 line and is usually coupled with the nebular line of [OIII] $\lambda$ 5007. The [OIII] $\lambda$ 4363 line is however intrinsically weak and is detected only in the hottest, most metal-poor HII regions. It is absent at metallicities above about half solar. The faintness of the line makes it inaccessible for high-z studies in most cases. An alternative to the use of faint lines is the "strong-line method". It uses brighter rest-frame optical nebular emission lines such as  $H\alpha$ ,  $H\beta$ , [OII], [OIII], [NII], [SII] and [SIII] from bright HII regions (Kobulnicky et al. 1999; Pettini et al. 2001). The calibration of the strong emission line ratios to chemical abundances has been done against photoionization models or empirical  $T_e$ -based measurements of local HII regions (Pagel et al. 1979, Evans & Dopita 1985, Pettini & Pagel 2004). Comparing various strong line methods, studies have found in part substantial biases and offsets between the methods as well as between calibrations of the same method (Kennicutt et al. 2003; Kobulnicky & Kewley 2004). Nevertheless, consistent comparisons based on the same indicators and

calibrations provide useful constraints between different galaxies, or different regions within them. We here introduce those that are used in this work.

One of the most common methods for measuring metallicity of  $z \sim 1-3$  galaxies is the **N2-method**, introduced by Storchi-Bergmann et al. (1994). It uses the ratio between the singly ionized nitrogen [NII] $\lambda$ 6584 line and  $H\alpha$ ,

$$N2 := \log \left( \frac{[NII]}{H\alpha} \right). \quad (9.1)$$

The N2-index has the advantage of being insensitive to reddening and flux calibration and requires only one observation since [NII] and  $H\alpha$  line are spectrally close with a separation of  $21\text{\AA}$  in the restframe. For sources at  $0.7 \leq z \leq 2.7$ , the line pair can be observed in J, H, or K band. The dependence on metallicity results from various effects: with increasing metallicity, cooling of the nebular gas also increases, the ionizing stellar spectrum softens and as such the overall ionization decreases. Furthermore, [NII]/[NIII] increases since the number of more highly ionized states drops. The [NII]/ $H\alpha$  ratio increases monotonically up to solar metallicity. For relative oxygen abundances above solar,  $[O/H] \geq [O/H]_{\odot}$ , [NII]/ $H\alpha$  tends to saturate because [NII] comes to dominate the cooling (Kewley & Dopita 2002). Various calibrations between the N2 index and the oxygen abundance, expressed as  $12 + \log(O/H)$ , have been proposed in the literature. In this work, we adopt the calibration of Pettini & Pagel (2004), hereafter ‘‘PP04’’,

$$12 + \log(O/H) = 8.90 + 0.57 \times N2 \quad (9.2)$$

which is valid over the range  $7.50 < 12 + \log(O/H) < 8.75$ . For consistency, we also adopt the same solar abundance as PP04:  $12 + \log(O/H) = 8.66$  (Asplund et al. 2004). If N2 saturates above roughly solar abundances, AGN and shock excitation can contaminate metallicity measurements done with the N2 method, resulting in higher values than observed for pure star-forming regions.

The **O3N2 method** proposed by Pettini & Pagel in their same work, combines the ratios of four emission lines:

$$O3N2 := \log \left( \frac{[OIII] / H\beta}{[NII] / H\alpha} \right). \quad (9.3)$$

Like the N2 index, it is independent of reddening and flux calibrations. However, it relies on two line ratios for which the emission lines fall in different atmospheric windows for sources at  $z \sim 1-3$ . The calibration derived by PP04,

$$12 + \log(O/H) = 8.73 - 0.32 \times O3N2, \quad (9.4)$$

is valid in the range of  $8.12 < 12 + \log(O/H) < 9.05$ . As mentioned, [NII]/ $H\alpha$  saturates for super-solar metallicities, [OIII]/ $H\beta$  however continues to decrease thus the O3N2-index decreases also. AGN or shocks can also contaminate the O3N2-based metallicities. It is also important to note that the scatter of the data used by PP04 around their calibrations is significant ( $1-\sigma$  scatter of  $\pm 0.18\text{dex}$  and  $\pm 0.14\text{dex}$  for N2 and O3N2), as in general for other calibrations (e.g. Kewley & Ellison 2008).

Table 9.3.: N2 and O3N2 metallicities

Source	$12+\log[\text{O}/\text{H}]^{(a)}$	
	N2-index	O3N2-index
BM1163	$8.46^{+0.01}_{-0.01}$	$8.36^{+0.03}_{-0.02}$
BX389	$8.38^{+0.05}_{-0.05}$	$8.30^{+0.06}_{-0.06}$
BX482	$8.38^{+0.07}_{-0.07}$	... <sup>(b)</sup>
BX610	$8.67^{+0.01}_{-0.01}$	$8.51^{+0.03}_{-0.03}$
BX663	$8.63^{+0.03}_{-0.03}$	... <sup>(b)</sup>
D3a6004	$8.68^{+0.04}_{-0.04}$	$8.52^{+0.08}_{-0.07}$
D3a6397	$8.68^{+0.02}_{-0.02}$	... <sup>(c)</sup>
D3a15504	$8.64^{+0.02}_{-0.02}$	$8.32^{+0.05}_{-0.05}$
ZC782941	$8.54^{+0.02}_{-0.02}$	$8.43^{+0.04}_{-0.04}$
K20ID5	$8.77^{+0.02}_{-0.02}$	$8.33^{+0.06}_{-0.06}$
K20ID7	$8.52^{+0.03}_{-0.03}$	$8.40^{+0.05}_{-0.06}$
MD41	$8.31^{+0.06}_{-0.06}$	$8.19^{+0.07}_{-0.07}$

<sup>(a)</sup> Calibration after Pettini & Pagel (2004)

<sup>(b)</sup> Unreliable limit for  $\text{H}\beta$

<sup>(c)</sup> Both  $\text{H}\beta$  and  $[\text{OIII}]$  are limits

### Metallicity relations

Correlations between metallicity and mass or luminosity are long known to exist and have been studied extensively in the local universe. First observations of a correlation between heavy-element abundances and total galaxy mass were reported by Lequeux et al. in 1979. Subsequent studies focussed mostly on metallicity-luminosity correlations since luminosity is far easier to obtain than mass. A strong correlation between rest-frame optical luminosity and the degree of chemical enrichment has been observed to exist for both star-forming and early-type galaxies in the local universe (e.g. Garnett 1987; Skillmann et al. 1989; Brodie 1991; Salzer et al. 2005). The luminosity ( and M/L ratios) of galaxies is however highly sensitive to stellar evolutionary effects and star formation history, such that relationships between Z and stellar mass are preferable for comparisons between high and low redshift samples.

Tremonti et al. (2004) derived the gas-phase oxygen abundance and stellar mass from the Sloan Digital Sky Survey of  $\sim 53,000$  star-forming galaxies out to  $z \sim 0.1$ . They found

a tight correlation between stellar mass and metallicity spanning over 3 orders of magnitude in stellar mass and a factor 10 in metallicity, showing that galaxies with higher stellar mass have higher metallicities. The relation is relatively steep between  $10^{8.5}$  to  $10^{10.5} M_{\odot}$  and flattens above  $10^{10.5} M_{\odot}$ . Two main processes have been invoked to drive the correlation. Firstly metal loss through feedback from massive stars winds and supernova explosions, which expel metal-rich gas outside the galaxies, eventually enriching the IGM (Ellison et al 2000, Adelberger et al. 2003, 2005a). Further, higher gas outflow rates (and therefore higher metal ejection) are observed in low-mass systems (Larson 1974, Tremonti 1994). Secondly, metal buildup, i.e., the enrichment of the gas and a change in gas fraction when gas is converted into stars. Other effects shaping the mass-metallicity relation are related to “downsizing” whereby low-mass systems form their stars later and on longer timescales than high-mass systems, therefore show lower metallicities at a given time (Ellison et al. 2008), and possibly IMF variations (Köppen et al. 2007). Increasing star formation efficiency with increasing mass has also been proposed as an explanation for the correlation (Calura et al. 2009).

The first investigation of the mass-metallicity relation at  $z > 1$  was done by Erb et al. (2006a), hereafter Erb06, through a spectral stacking analysis of 87 high- $z$  galaxies divided into 6 mass bins at  $z \sim 2.2$  spanning a stellar mass range of  $\sim 10^{9.3} - 10^{11.2} M_{\odot}$ . The relation found by Erb et al. shows a similar trend of increasing metallicity at higher stellar masses, as found at  $z \sim 0-1$  but with an offset: compared to local universe, at high-redshifts, galaxies of a given mass tend to be more metal poor, by roughly 0.2 dex in oxygen abundance ( $12 + \log[\text{O}/\text{H}]$ ). The offset likely reflects an overall enrichment and gas depletion of galaxies at progressively later cosmic epochs. Using the empirical relation between star formation rate and gas surface density to infer the gas mass fraction, Erb et al. find an increase in gas fraction with decreasing stellar mass. Furthermore, contrary to the local universe, the effective yield  $y_{\text{eff}}^1$  (defined as  $y_{\text{eff}} := Z_{\text{obs}} / \ln f_{\text{gas}}^{-1}$ ;) shows a slight increase with decreasing baryonic mass. The shape and position of the  $M_{*}$ - $Z$  relation at  $z \sim 2$  cannot be explained by the simple model where outflows are more efficient at driving enriched gas out of galaxies in low-mass systems. Significant accretion of metal-poor gas at  $z \sim 2$  appears to play an important role, with estimates of the effective yield suggesting that the gas fraction is the driving factor at  $z \sim 2$  although metal loss via outflows might play a role as well (Erb et al. 2006, 2007; Pettini et al. 2001, 2002, 2003; also Savaglio et al. 2005; Kriek et al. 2007; Liu et al. 2008; Hainline et al. 2009; Law et al. 2009 for  $z \sim 0.5-2.5$ ). Maiolino et al. (2008) and Mannucci et al. (2009) have extended the mass metallicity relation up to  $z \sim 3.5$ .

It has further been shown that the mass-metallicity relation does evolve over time. Maiolino et al. (2008) investigated the evolution of the  $M_{*}$ - $Z$  relation from  $z \sim 3.5$  to  $z \sim 0.07$ . They find a consistent decrease in metallicity for a given mass with higher redshift. The

---

<sup>1</sup>The effective yield is an important probe of the effects of outflows or dilution by the infall of metal poor gas on the chemical enrichment history of galaxies (e.g. Edmunds 1990)

evolution is fastest and most extreme at early times between  $z \sim 3.5$  and  $z \sim 2.2$ . Low-mass systems ( $\sim 10^{8.5} M_{\odot}$ ) show a stronger evolution in metallicity of up to  $\sim 1.1$  dex between  $z \sim 3.5$  and  $z \sim 0.07$ , compared to 0.5 dex for high-mass systems ( $\sim 10^{11} M_{\odot}$ ). This could be an indication that massive galaxies build up metals more quickly. It is important to note, however, that the various  $M_*$ -Z evolution studies at the various redshifts do not probe the same but different galaxy populations.

Recently, Mannucci et al. (2010) have proposed that the mass-metallicity relation is only one aspect of a more fundamental relation between stellar mass, gas-phase metallicity and star formation rate, which they dubbed the ‘‘Fundamental Metallicity Relation’’ (FMR). They found that local galaxies define a tight surface in this 3D parameter space. According to this FMR, the oxygen abundance of galaxies at a given mass would decrease with increasing SFR. The tightest projection found for SDSS galaxies is

$$\mu = \log(M_*) - 0.32 \log(\text{SFR}). \quad (9.5)$$

Mannucci et al. (2010) proposed that the observed shift of the M-Z relation with redshift could simply reflect the evolution of the SFR of galaxies at given stellar mass, shifting them along a universal (constant in time) M-Z-SFR relation. They used average measurements for samples at  $z > 1$  to show tentative evidence in support of this statement, although clearly consistent metallicity estimates of significantly larger and unbiased samples will be required to test the FMR at  $z > 1$ . It is also important to note that the actual high SFR regime ( $\sim 1$ –several  $100$ 's of  $M_{\odot}/\text{yr}$ ) of massive galaxies at  $z > 1$  is essentially unconstrained in the Mannucci et al. analysis, since the local population probed by the SDSS sample only reaches up to  $\text{SFR} \sim 1 M_{\odot}/\text{yr}$ .

In the following paragraphs, we compare the inferred oxygen abundance (hereafter simply ‘‘metallicity’’) for our SINS galaxies with the previous measurements at  $z \sim 2$  by Erb06, and further explore relationships with other parameters. To improve the assessment of trends, or lack thereof, we complement our multi-line sample with [NII]/ $H\alpha$  measurements of the whole SINS  $H\alpha$  sample. All data were derived with the same procedure, and within elliptical apertures of PA and axis ratio based on the  $H\alpha$  morphologies. The measured  $H\alpha$  and [NII] $\lambda 6584$  line fluxes and [NII]/ $H\alpha$  values are listed in table 9.4. The line fluxes (and thus the [NII]/ $H\alpha$  ratios) for the 12 ‘four-line’ galaxies analyzed in this work differ slightly from their respective [NII]/ $H\alpha$  values shown in table 9.1, still they are consistent within  $1\sigma$ . The difference results from the different data extraction regions. The data for the [NII]/ $H\alpha$  values in table 9.1 were extracted from regions where all four BPT lines,  $H\alpha$ , [NII] $\lambda 6584$ ,  $H\beta$ , and [OIII] $\lambda 5007$  were detected to compare [NII]/ $H\alpha$  and [OIII]/ $H\beta$  ratio in the BPT diagram. The BPT analysis in the previous section has confirmed the AGN that were known, and, in general, shows that the line emission in most of the galaxies with multi-line measurements is dominated by star formation. We mark AGN sources in the following figures for reference, and assume all others from the  $H\alpha$  sample are also dominated by star-formation.

## 9.2. Sources as a whole: integrated measurements

Table 9.4.:  $H\alpha$  and  $[\text{NII}]\lambda 6584$  line flux,  $[\text{NII}]/H\alpha$  ratio and oxygen abundance for the sources of the SINS  $H\alpha$  sample with non-limit measurements

Source	$F(H\alpha)$ Fluxes <sup>(a)</sup> in units of $10^{-16}\text{erg/s/cm}^2$	$F([\text{NII}])$	$[\text{NII}]/H\alpha$	$12+\log[\text{O}/\text{H}]^{(b)}$ via N2
BM1163	$5.58^{+0.14}_{-0.14}$	$0.93^{+0.05}_{-0.04}$	$0.17^{+0.01}_{-0.01}$	$8.46^{+0.01}_{-0.01}$
BX528	$0.82^{+0.03}_{-0.03}$	$0.21^{+0.04}_{-0.04}$	$0.25^{+0.04}_{-0.05}$	$8.56^{+0.04}_{-0.05}$
BX599	$2.52^{+0.06}_{-0.05}$	$0.60^{+0.07}_{-0.06}$	$0.24^{+0.03}_{-0.02}$	$8.54^{+0.03}_{-0.02}$
BX663	$0.88^{+0.04}_{-0.04}$	$0.30^{+0.03}_{-0.03}$	$0.34^{+0.04}_{-0.04}$	$8.63^{+0.03}_{-0.03}$
MD41	$1.19^{+0.03}_{-0.03}$	$0.11^{+0.03}_{-0.03}$	$0.09^{+0.02}_{-0.02}$	$8.31^{+0.06}_{-0.06}$
BX389	$1.45^{+0.04}_{-0.03}$	$0.25^{+0.03}_{-0.03}$	$0.17^{+0.02}_{-0.02}$	$8.46^{+0.03}_{-0.03}$
BX513	$0.55^{+0.06}_{-0.05}$	$0.15^{+0.03}_{-0.04}$	$0.27^{+0.07}_{-0.07}$	$8.58^{+0.06}_{-0.07}$
BX610	$2.61^{+0.08}_{-0.07}$	$1.03^{+0.04}_{-0.05}$	$0.39^{+0.02}_{-0.02}$	$8.67^{+0.01}_{-0.01}$
BX404	$0.87^{+0.02}_{-0.02}$	$0.12^{+0.01}_{-0.01}$	$0.13^{+0.01}_{-0.02}$	$8.40^{+0.03}_{-0.03}$
BX405	$1.11^{+0.03}_{-0.02}$	$0.12^{+0.02}_{-0.02}$	$0.10^{+0.02}_{-0.01}$	$8.34^{+0.05}_{-0.04}$
BX416	$1.04^{+0.04}_{-0.03}$	$0.15^{+0.03}_{-0.03}$	$0.15^{+0.03}_{-0.03}$	$8.42^{+0.04}_{-0.05}$
BX482	$1.94^{+0.07}_{-0.05}$	$0.24^{+0.07}_{-0.05}$	$0.12^{+0.03}_{-0.02}$	$8.38^{+0.07}_{-0.05}$
K20-ID5	$1.34^{+0.05}_{-0.07}$	$0.81^{+0.06}_{-0.06}$	$0.61^{+0.05}_{-0.05}$	$8.78^{+0.02}_{-0.02}$
K20-ID6	$0.40^{+0.02}_{-0.02}$	$0.13^{+0.01}_{-0.01}$	$0.32^{+0.03}_{-0.04}$	$8.62^{+0.03}_{-0.03}$
K20-ID7	$1.46^{+0.05}_{-0.05}$	$0.32^{+0.03}_{-0.04}$	$0.22^{+0.03}_{-0.03}$	$8.52^{+0.03}_{-0.03}$
K20-ID8	$0.73^{+0.03}_{-0.03}$	$0.20^{+0.02}_{-0.03}$	$0.27^{+0.03}_{-0.04}$	$8.57^{+0.03}_{-0.04}$
ZC772759	$0.85^{+0.07}_{-0.05}$	$0.18^{+0.05}_{-0.06}$	$0.21^{+0.06}_{-0.07}$	$8.52^{+0.07}_{-0.08}$
ZC782941	$1.68^{+0.07}_{-0.05}$	$0.42^{+0.03}_{-0.03}$	$0.25^{+0.02}_{-0.02}$	$8.56^{+0.02}_{-0.02}$
D3a-6004	$1.39^{+0.05}_{-0.04}$	$0.61^{+0.04}_{-0.05}$	$0.44^{+0.03}_{-0.04}$	$8.69^{+0.02}_{-0.02}$
D3a-6397	$2.10^{+0.10}_{-0.11}$	$0.86^{+0.06}_{-0.07}$	$0.41^{+0.03}_{-0.04}$	$8.68^{+0.02}_{-0.02}$
D3a-7144	$0.91^{+0.08}_{-0.06}$	$0.65^{+0.03}_{-0.03}$	$0.71^{+0.07}_{-0.06}$	$8.82^{+0.02}_{-0.02}$
D3a-12556	$1.65^{+0.03}_{-0.03}$	$0.54^{+0.06}_{-0.06}$	$0.32^{+0.04}_{-0.04}$	$8.62^{+0.03}_{-0.03}$
D3a-15504	$1.76^{+0.06}_{-0.05}$	$0.52^{+0.04}_{-0.05}$	$0.30^{+0.02}_{-0.03}$	$8.60^{+0.02}_{-0.02}$
GK1084	$0.17^{+0.01}_{-0.01}$	$0.07^{+0.01}_{-0.01}$	$0.39^{+0.04}_{-0.04}$	$8.67^{+0.03}_{-0.03}$
GK2438	$0.49^{+0.02}_{-0.01}$	$0.15^{+0.04}_{-0.03}$	$0.31^{+0.08}_{-0.05}$	$8.61^{+0.07}_{-0.04}$
SA12-8768	$0.67^{+0.02}_{-0.03}$	$0.13^{+0.02}_{-0.02}$	$0.20^{+0.02}_{-0.03}$	$8.50^{+0.03}_{-0.03}$

<sup>(a)</sup> Integrated emission line fluxes extracted from elliptical apertures covering the whole source

<sup>(b)</sup> Calibration after Pettini & Pagel (2004)

The distribution of metallicity versus stellar mass we have derived from our data is shown in figure 9.4. Stellar masses have been calculated from SED fitting (see Förster Schreiber 2009 and 2011a). The metallicity is expressed as the oxygen abundance in units of  $12+\log[\text{O}/\text{H}]$ , calibrated via Pettini & Pagel 2004 ( $12 + \log(\text{O}/\text{H}) = 8.90 + 0.57 \times \text{N2}$ ). Our SINS data are shown as blue (the ‘BPT’ galaxies in this work) and black (other SINS  $\text{H}\alpha$  sample sources) circles. Filled circles denote  $z \sim 2.2$  and open circles  $z \sim 1.5$  objects. Throughout we assume a solar abundance of 8.66 (Asplund et al. 2004). Typical errors for stellar mass and metallicity are shown in the lower right in each plot. ‘Data’ refers to the propagated error for the line fluxes, ‘Cal’ is the uncertainty of the used metallicity calibrator (PP04).

Our choice of PP04 as the metallicity calibrator and the adopted solar value of 8.66 is to get a consistent comparison with the work of Erb06. Other choices would alter the absolute offset relative to solar and somewhat the shape of relations but would qualitatively preserve relative metallicities among galaxies (see Kewley & Ellison 2008). This is illustrated in figure 9.5 where we have plotted O3N2 versus N2-based metallicity of our galaxies using three different calibrations. “PP04” (blue filled circles) denotes the adopted Pettini & Pagel 2004 calibration, “T04” (black open circles) refers to the calibration presented by Tremonti et al. 2004, and “D02” (green triangles) is the one by Denicoló et al. 2002.

The deviation from the 1:1 relation is reminiscent of the offset above the SDSS star-forming sequence in the BPT diagram (see 9.2.2), which could reflect different physical conditions, perhaps small AGN contribution, driving the line excitation. Also note that the calibration by PP04 is defined for *local* galaxies, hence if different conditions prevail in *high-z* star-forming galaxies, one might expect some deviations. Nonetheless, relative measurements among galaxies remain unaltered and the use of one or the other indicator would lead to similar conclusions. If we account for stellar  $\text{H}\beta$  absorption, as previously shown in figure 9.3 for the BPT diagram, the deviation from the 1:1 relation decreases but not enough to get to a 1:1 relation within  $3\sigma$ . This effect is shown in figure 9.6.

The M-Z values in figure 9.4 obtained for the individual SINS sources (black and blue circles) are in reasonable agreement with the Erb06 relation (dotted line), albeit with larger scatter. The known AGN tend to lie mostly above the Erb et al. M-Z relation at higher stellar mass, but there is also a scatter with three sources being closer to this relation: D3a-15504, D3a-6397 and BX663, all of which have significant contribution from star formation to their integrated  $\text{H}\alpha$  and [NII] line emission. There is a hint of some systematic deviation with respect to Erb06. We find that at lower masses the M-Z relation traced by the SINS sources is similar to the result of Erb06. However, rather few galaxies from the SINS  $\text{H}\alpha$  sample probe this regime with well-measured [NII]/ $\text{H}\alpha$  ratios (with the typical sensitivities and exposure times of a few hours, most of the low-mass SINS galaxies only have upper limits on [NII] and provide weak constraints on the M-Z relation). At higher masses, at  $M_{\odot} \gtrsim 10^{10.5}$ , however, we find an “excess” in metallicity,

## 9.2. Sources as a whole: integrated measurements

---

which is not driven by known AGN. This is further illustrated in figure 9.7 where we plot the scatter of the metallicity of our sources around the M-Z relation as fitted from the Erb et al. data points. The SINS objects are plotted again as (filled/open) circles, and the reference data of Erb et al. lie on the dotted  $\Delta Z=0$  line. The mean scatter around the Erb relation is  $\sim 0.1$  dex.

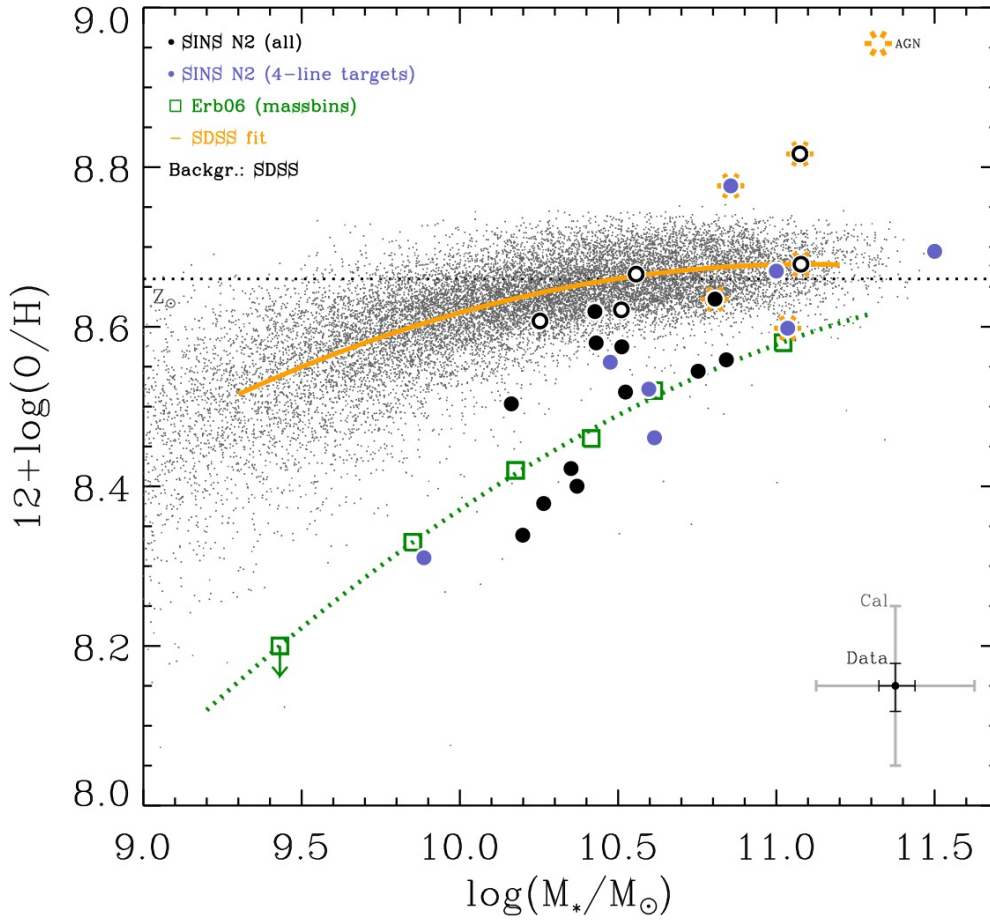


Figure 9.4.: Mass-Metallicity relation for the SINS sources with detection in both H $\alpha$  and [NII] lines. Circles: SINS sources. Filled circles denote sources with a redshift  $\sim 2$ - $2.5$ , open circles sources with a redshift  $\sim 1.5$ . The blue labeled circles are the targets used in this work for which all four BPT lines have been observed. Black circles denote the rest of the SINS H $\alpha$  sources. Sources with known AGN are marked with rays. The  $z \sim 2.2$  mass-metallicity relation from Erb et al. (2006a) is plotted as open squares. The dotted line is a 2nd order fit to the Erb et al. data. The local SDSS galaxies are plotted in the background and a corresponding 2nd order fit as a solid orange line. The metallicity of the SDSS sample plotted here is derived from the same N2 index as used for the SINS and Erb et al.  $z \sim 2$  samples. Typical errors for stellar mass and metallicity are shown in the lower right. 'Data' refers to the propagated error for the line fluxes, 'Cal' is the uncertainty of the metallicity calibrator (PP04). The horizontal dotted line marks solar metallicity ( $12 + \log[\text{O}/\text{H}] = 8.66$ , Asplund et al. 2004).

## 9.2. Sources as a whole: integrated measurements

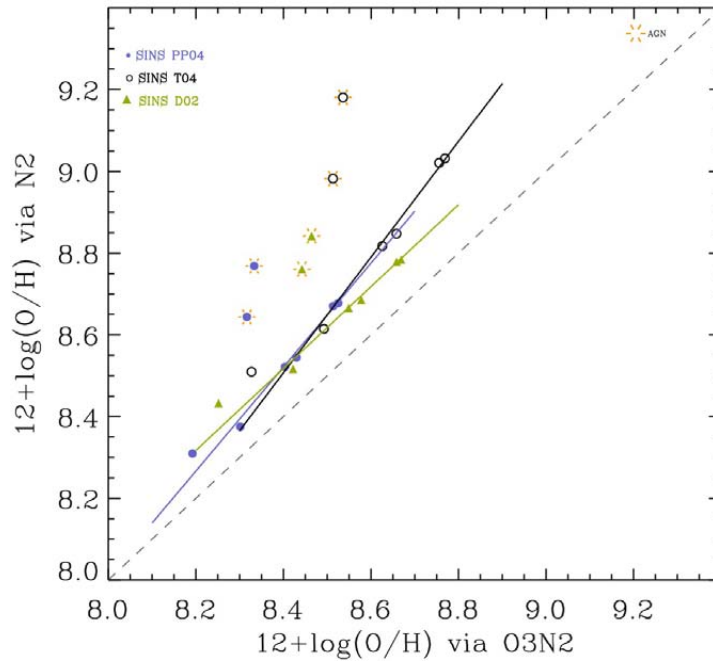


Figure 9.5.: Comparison of N2 and O3N2 metallicity for different calibrations (after Kewley & Ellison 2008). The linear fits exclude AGN systems.

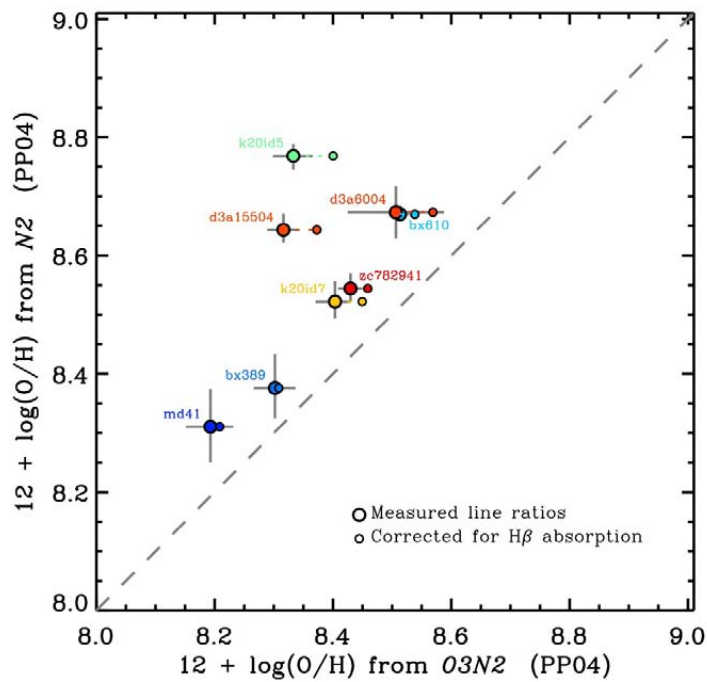


Figure 9.6.: Same as Figure 9.5, showing the impact of accounting for stellar  $H\beta$  absorption on the oxygen abundance derived from the O3N2 index.

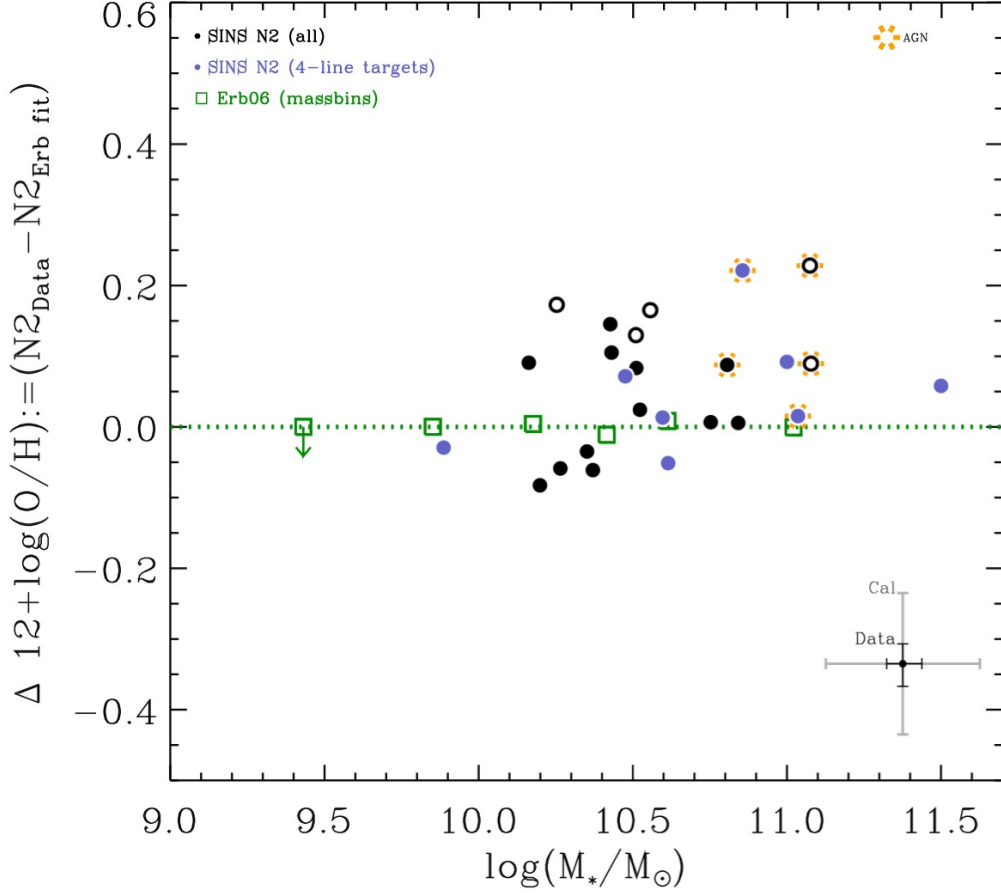


Figure 9.7.: Mass-Metallicity residuals around the M-Z relation as fitted from the Erb et al. data points. Mean scatter is  $\sim 0.09$  dex

Over the stellar mass range  $\sim 10^{10} - 10^{11} M_{\odot}$  where the SINS galaxies with detected [NII] and Ha overlap with the mass range probed by the Erb et al. (2006) sample, we find a slight excess of on average  $\sim 0.1$  dex. On one hand, this reflects sensitivity limits, which will bias measurements towards higher [NII]/Ha ratios for a given  $M_*$  (so that  $S/N > 3$  for [NII]), whereas objects with undetected [NII] were included in the stacked spectra of Erb et al. (2006). On the other hand, it can also reflect intrinsic differences in the sample properties. We find, however, no trend of a higher ‘excess’ in metallicity with increasing stellar mass. Note that in figure 9.4 and 9.7 all measurements are based on the same metallicity indicator, [NII]/ $H\alpha$ , and the same calibration (PP04). The difference in metallicity for the same mass between Erb’s and our data can not be attributed to systematic differences in metallicity indicator or calibration adopted.

We now explore the origin of the “excess” abundance we found in our data. The SINS data set includes a significant fraction of NIR-selected objects. It should therefore be less biased towards bluer, i.e., younger and less dusty, objects than the rest-UV BM/BX sample of Erb et al. (see Förster Schreiber et al. 2009 and references therein). It is

possible that the excess reflects the higher probability of older and dustier objects in the SINS sample. We therefore explore trends of oxygen abundance with  $J - K$  and  $B - K$  colors (which both show a dependence with stellar age and dust extinction  $A_V$ ), and best-fit stellar age and extinction from SED modeling.  $J - K$  is relatively more sensitive to age as it has a shorter wavelength coverage and brackets the Balmer/4000Å break, which is useful as a diagnostic for age in stellar population studies (e.g. Hamilton 1985; Kauffmann 2003a).  $B - K$  is more sensitive to extinction as it spans a larger wavelength interval. The strongest and only significant correlations we find are between  $B - K$  color and metallicity, and  $A_V$  and metallicity. These findings are illustrated in figures 9.8 and 9.9. In both figures, the upper panel shows the absolute relation, in the lower panel we plot  $B - K$  and  $A_V$  versus the residual metallicity  $\Delta(12 + \log[O/H])$  as presented in figure 9.7.

The  $B - K$  color versus  $\Delta(12 + \log[O/H])$  plot in figure 9.8 shows a clear trend of higher oxygen abundance with increasing  $B - K$ , i.e. redder objects. If we remove the mass-metallicity by subtracting the M-Z fit to the Erb et al. data (lower panel), the trend remains, albeit there might be a hint of flattening towards the reddest objects.

A similar positive trend can be seen in figure 9.9 where we plot  $A_V$  color versus oxygen abundance. Dustier, more obscured systems, i.e. higher  $A_V$  show higher metallicities, the scatter is however comparably higher than when plotting  $B - K$  color vs. oxygen abundance. The bottom panel shows  $A_V$  versus  $\Delta(12 + \log[O/H])$ . The reduced scatter in this plot makes the trend more readily visible. The regular spacing of the data in x-direction is due to the grid in  $A_V$  values (with spacing of  $\Delta(A_V) = 0.2$  mag) employed in the SED modeling.

The trends we find for the inferred oxygen abundance (and offset above the Erb relationship) with observed  $B - K$  color and  $A_V$  derived from SED modeling support a higher proportion of massive, dustier –hence likely more metal rich– objects in our sample to explain the observed difference in abundance in our data with respect to Erb et al.

9.2. Sources as a whole: integrated measurements

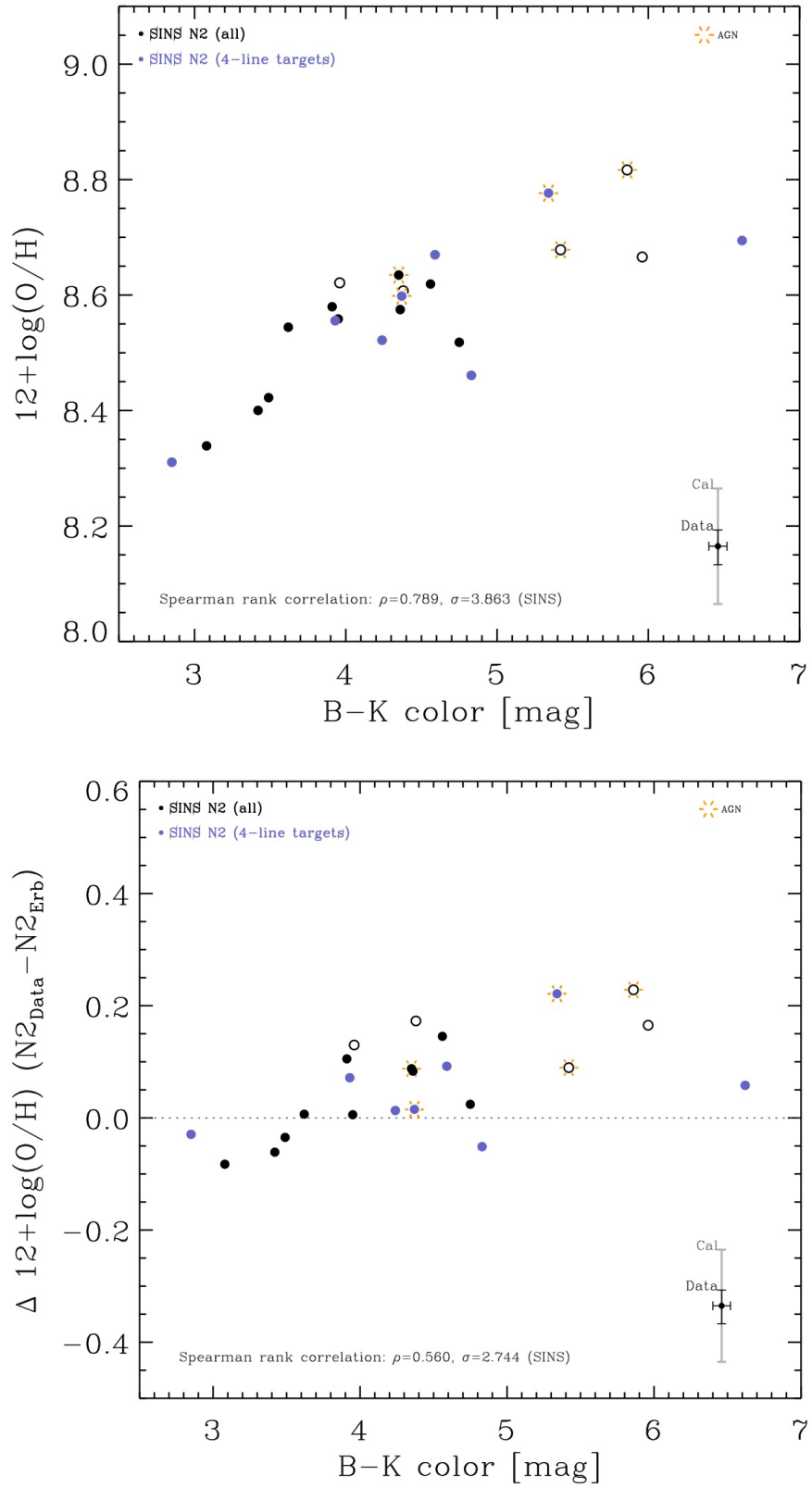


Figure 9.8.:  $B - K$  color vs.  $(\Delta)12+\log[O/H]$

## 9.2. Sources as a whole: integrated measurements

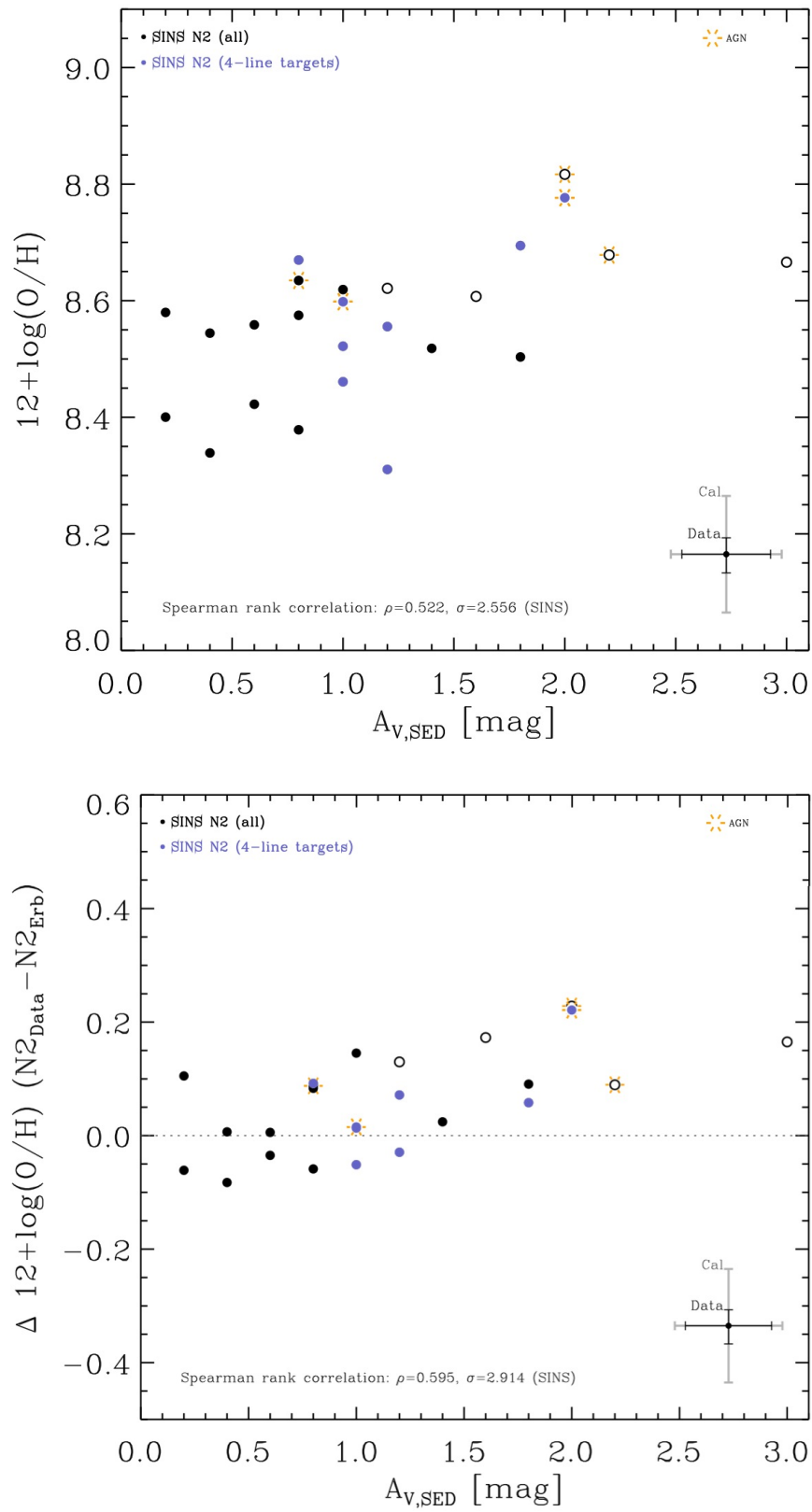


Figure 9.9.:  $A_{V,SED}$  vs.  $(\Delta)12+\log[O/H]$

We now turn to explore the impact of the SFR on the metallicity relationship. Mannucci et al. (2010) found, for local star-forming galaxies from the SDSS, that the distribution of points in the  $M_*$ -SFR-Z space was minimized for the projection  $\mu = \log M_* - 0.32 \log(\text{SFR})$ . We plot our SINS galaxies in the  $12+\log[\text{O}/\text{H}]$  vs.  $\mu$  diagram in figure 9.10, using the SFR as derived from SED modeling (Förster Schreiber et al. 2009, 2011a). The same SDSS sample as used in figure 9.4 is also plotted, along with a second order polynomial fit to these SDSS measurements. The SDSS range in  $\mu$  is not quite the same as in SINS. This reflects the higher star formation rates at higher redshift for galaxies in the same stellar mass range. Again, for consistency between the low- and high-redshift samples, we use the N2-based metallicities for the SDSS galaxies. In the analysis presented by Mannucci et al. (2009), metallicities were derived from other indicators, so it is of interest to verify whether the scatter of the SDSS measurements is also reduced between the M-Z and  $\mu$ -Z relationships as calculated from N2. The median scatter of the SDSS data around the SDSS mass-metallicity fit is 0.07. The scatter is reduced in the  $\mu$ -metallicity fit is 0.05.

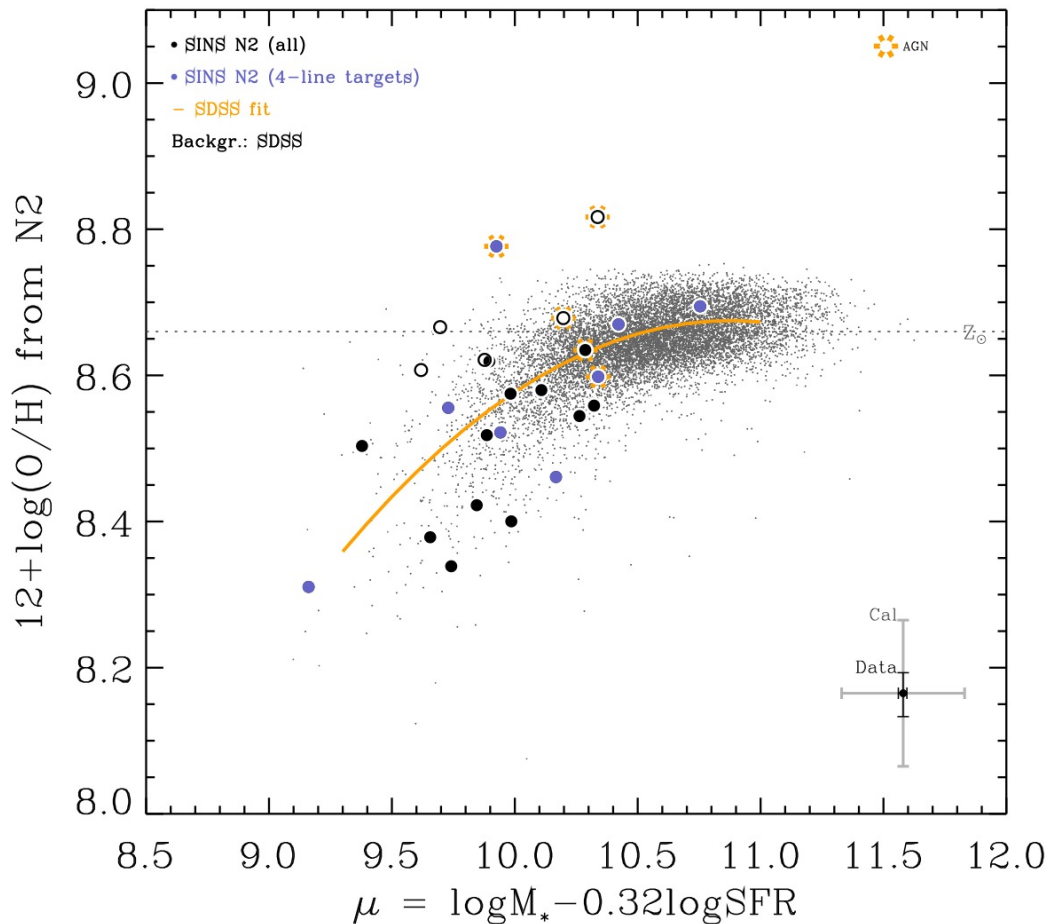


Figure 9.10.:  $\mu$ -Z relation. SINS data as blue and black circles, SDSS in the background. The orange line is a 2nd order fit to the SDSS data. The scatter of the SINS sources is 0.11).

Our measurements for the  $z \sim 2$  SINS galaxies tend to lie around the extrapolation towards lower  $\mu$ -values of the fit to the SDSS galaxies. As such, that is a similar argument as used by Mannucci et al. (2010) to hypothesize that the FMR, as derived from SDSS, might hold out to  $z \sim 3$ , where the large discrepancy for their  $z > 3$  Lyman-break galaxies might suggest it breaks down. At face value, our measurements would broadly support the FMR. However, we find that the scatter of individual the  $z \sim 2$  SINS points is still significant with a value of 0.11. Again, a small contribution by AGN and/or shocks could have some influence, even in targets not individually identified as AGN.

### 9.3. Zooming in: spatially-resolved line ratios and metallicity

Since all galaxies in this study have been observed with an integral field spectrometer, it is possible to explore the spatial distribution of the emission line fluxes across the objects, provided its spatial extent is greater than the typical PSF.

We first investigate variations along the major and minor axis of galaxies, as well as azimuthally averaged radial profiles. In a second step, emission line maps –created by fitting the line emission for each spatial pixel spectrum– are used to derive line ratio and metallicity maps for the galaxies with the best quality and S/N data. Since the aperture- / annuli-spectra are of higher S/N than the spectra for individual pixels, they can generally extend further out, i.e., to larger radii, whereas maps could only be derived for the brighter objects and are generally limited to the brighter central parts. In turn, spectra for apertures -and especially annuli- might integrate over a ‘clumpy’ metal distribution and thus show different trends in variations of line ratios.

In present-day spiral galaxies, negative radial metallicity gradients –with the inner disk regions more metal-rich than the outer parts– have long been established (e.g. Searle 1971; Shields 1974; Zaritsky et al. 1994). Nebular abundances derived from optical line emission from HII regions in the outer disk of our own Milky Way indicate a radial gradient  $\Delta \log(\text{O}/\text{H})/\Delta R \approx -0.07 \text{ dex kpc}^{-1}$  (Shaver et al. 1983). The range among nearby disks is significant ( $\sim -0.2$  to  $\sim 0.0 \text{ dex kpc}^{-1}$ ; e.g. Zaritsky et al. 1994), with trends of shallower gradients towards both the latest spiral types and irregulars, and early-type spirals (see also e.g. Pagel & Edmunds 1981; Henry & Worthey 1999). Barred spirals exhibit typically shallower gradients than non-barred ones of the same Hubble type, usually explained by “dilution” resulting from inflow of metal-poor gas from the outer disk parts towards the central regions. Interestingly, local interacting / merging systems also tend to show lower global gas-phase abundances and shallower gradients than isolated galaxies of the same mass, suggesting that strong interaction-induced gas flows bring less enriched material into the central regions (e.g. Rupke 2008, 2010b; Ellison et al. 2008; Kewley et al. 2010). This explanation appears to be supported by theoretical simulations (e.g. Montuori et al. 2010; Rupke 2010a).

At  $z > 1$ , empirical constraints are still scarce. Arguably, the best constraints on abundance gradients can be obtained for strongly-lensed objects. Jones et al. (2010) derived  $\Delta \log(\text{O}/\text{H})/\Delta R = -0.27 \pm 0.05 \text{ dex kpc}^{-1}$  from both  $[\text{NII}]/\text{H}\alpha$  and  $[\text{OIII}]/\text{H}\alpha$ , in a  $z=2.001$  lensed disk galaxy resolved on source-plane scales of 300 pc. They argue that if the physical gradient is fairly steep compared to local disks of similar mass, it is rather comparable when normalizing in terms of the effective radius. Yuan et al. (2011) also derived a rather steep  $-0.16 \text{ dex kpc}^{-1}$  in a  $z=1.49$  strongly lensed spiral from  $[\text{NII}]/\text{H}\alpha$  measurements resolved on 170 pc scales in the source plane. Both results were argued to support inside-out scenarios for disk formation, whereby early gas infall and mass assembly builds the central disk regions first with earlier chemical enrichment, and subsequent accretion builds the outer disk parts with resulting slower enrichment. Other studies focussed on unlensed galaxies with typical resolution of 4-5 kpc (seeing-limited) or 1-2 kpc (AO-assisted). In Förster Schreiber et al. (2006), we reported our first seeing-limited  $[\text{NII}]/\text{H}\alpha$  map, with a line ratios peaking at the center attributed to an increase by 20% in oxygen abundance relative to the outer regions (see also Genzel et al. 2008). At  $z \sim 3$ , Cresci et al. (2010) reported “inverted”, i.e. positive radial gradients in three isolated disk-like star-forming objects, from  $[\text{OIII}]$ ,  $\text{H}\beta$ ,  $[\text{NeIII}]$ , and  $[\text{OII}]$  maps obtained at seeing-limited resolution of  $0.5''$ , (corresponding to  $\sim 4 \text{ kpc}$ ). They interpreted these variations as the result of accretion of metal-poor gas from the halo through “cold flows” into the central regions of the galaxies. At  $z \sim 1-1.4$ , Queyrel et al. (2012) presented  $[\text{NII}]/\text{H}\alpha$  based gradients in 26 galaxies from the MASSIV survey, mostly conducted in seeing-limited mode. They found a range of inferred oxygen abundance gradients from negative to flat and even positive for a significant fraction (7 of 26). The prevalence of interacting / kinematically disturbed systems among the subset with positive gradients led these authors to suggest, in analogy with findings in local galaxies, that interaction-induced gas inflows might be responsible for the shallower/positive gradients. They also find that low-metallicity objects in their sample tend to show the shallowest or positive gradients while the more metal-rich ones show the steepest negative gradients, which they argue could be explained by the infall of metal-poor gas onto the galaxy centers.

Clearly, if empirical determinations of abundance gradients would in principle provide constraints on disk formation and evolution models (e.g. Chiappini et al. 1997; Molla et al. 1996,1997; Fu et al. 2009; Prantzos & Boissier 2000), this remains currently extremely challenging observationally. Important limitations stem notably from the very small samples for which such measurements can be made (OH avoidance largely hampers multi-line measurements of faint distant objects) and often the S/N on all necessary lines for a given diagnostic is sufficient only over a small number of resolution elements. The complex emission line morphologies can further complicate the interpretation.

In this light, we examine our best data sets in order to quantify gradients and compare with similar studies at high redshift. The  $z \sim 2$  regime has been so far rather little explored in terms of spatially-resolved line ratios and metallicities. Albeit small, our sample thus

makes a significant addition, with very well characterized high- $z$  galaxies in terms of their stellar and kinematic properties. We note that our data indicate in some cases significant asymmetries along the major or minor axis profiles, such that the interpretation of azimuthally-averaged radial gradients may not be straightforward.

#### 9.3.1. Metallicity profiles from discrete apertures and annuli

We have extracted two kinds of profiles. Profiles along the major and minor axes were based on circular apertures, having a size slightly larger than the PSF, and radial profiles were based on concentric elliptical annuli centered on the galaxy's center. All fluxes for the radial profiles were normalized by the area of the annuli considered, for surface brightness measurements. In some cases, where the morphology of the object did not favor a perpendicular placement of the aperture-axes (mainly due to low SN in individual pixels or OH line contamination of one side of the galaxy), one axis was placed roughly along the kinematic major axis and the other was placed to maximize the coverage of the object to probe different regions. Since the analysis aims at detecting and quantifying metallicity gradients in the galaxies, a linear fit to the  $[\text{NII}]/\text{H}\alpha$  based metallicity versus radius data was calculated. All gradients are expressed in units of the oxygen abundance based on calibration by Pettini & Pagel 2004:  $12 + \log(\text{O}/\text{H}) = 8.90 + 0.57 \times \text{N2}$ .

Table 9.5 lists the derived metallicity gradients and their uncertainties for the 7 objects for which meaningful measurements could be obtained, i.e., with at least 3 data points with sufficient S/N. The two left columns list the gradients and their errors as inferred from measurements in concentric annuli. The other two columns list the gradients as measured from apertures along major (middle) and minor (right) axis. Listed are the maximum gradients in one axis direction outward from the center. As the apertures along major and minor axis are often roughly the size of the PSF and therefore integrating over 10-20 pixel only, the S/N in these apertures tends to be lower than in the annuli, which typically encompass a larger area. Therefore, we cannot measure gradients along the major or minor axis for all our galaxies.

Figures 9.11 to 9.13 show the detailed analysis of each of the galaxies in table 9.5 for which meaningful results could be obtained. For each galaxy, two panels are plotted: on the left are the N2 metallicity measurements in apertures along major (black) or minor axis (blue). The maximum gradient in one direction was fit for minor and major axis where enough useful data points were available, the measured slope is noted at the bottom. Upper limits are  $3\sigma$ . The right panel shows the N2 metallicity measurements in annuli, as well as the fit for deriving the metallicity gradient (violet) and the calculated slope. The measured values are noted at the bottom of the plot. The orange line shows the global metallicity estimated from the source-integrated  $[\text{NII}]/\text{H}\alpha$  ratio (Table 9.4). The scale on the right in each plot is in units of  $12 + \log[\text{O}/\text{H}]$  with dashed lines indicating

Table 9.5.: Metallicity gradients from the N2 index measurements in concentric annuli and apertures along major or minor kinematic axes.

Source	Concentric annuli	Major axis <sup>(a)</sup>	Minor axis <sup>(a)</sup>
	$\Delta Z_{N2}/\Delta R$ [dex/kpc]	$\Delta Z_{N2}/\Delta R$ [dex/kpc]	$\Delta Z_{N2}/\Delta R$ [dex/kpc]
BX610	$-0.02 \pm 0.01$	$-0.01 \pm 0.01$	...
D3a-6004	$-0.01 \pm 0.02$	$-0.02 \pm 0.01$	$-0.02 \pm 0.01$
D3a-6397	$< 0.02$	$< -0.02$	...
D3a-15504	$-0.05 \pm 0.02$	$-0.03 \pm 0.01$	$-0.03 \pm 0.01$
ZC-782941	$-0.02 \pm 0.05$	$-0.02 \pm 0.01$	...
ZC-782941-AO	$< -0.02$	$< -0.01$	$< -0.04$
K20-ID7	$-0.01 \pm 0.02$	...	...

<sup>(a)</sup>maximum gradient in one direction outward from center

solar and half solar metallicity. The exact placement of the apertures is shown in figures B.1 to B.7 in Appendix B, p.225ff. where we also plot the fluxes in each aperture.

We find all metallicity gradients to be negative, ranging from  $-0.045$  to  $-0.014$  dex/kpc with a confidence level of  $1-2\sigma$ . The mean gradient of our sample is  $-0.02$  dex/kpc. Table 9.5 and the corresponding figures 9.11 to 9.13 show that the gradients are overall comparably shallow. The limit value for D3a-6397 along the major axis ( $<0.02$  dex/kpc) and all annuli ( $<0.02$  dex/kpc) could imply a steeper gradient which is supported by the measurement over only the three inner concentric annuli for the same object of  $-0.05$  dex/kpc.

We measure some differences between axis and radial profiles, however, in every case the values agree within  $1-\sigma$ . For D3a6004, D3a6397, and ZC782941, we find significant asymmetries between major and minor axis or for the two directions along the same axis outward from the center of the galaxy. The figures in appendix B show this more prominently. K20-ID7 seems to show a particularly complex behavior, although the variations are consistent with no gradient within  $\approx 1$ -sigma. major axis. The asymmetries, also for the other objects, are averaged out in the radial profile. The radial gradient in ID7, the only major merger measured here, is  $-0.01$  dex/kpc, comparable to the one measured in D3a6004, which is a massive disk with regular kinematics and no sign of ongoing or recent merger activity. The peak in metallicity of ZC782941 is confirmed in the higher resolution AO data set to be towards the north-east between the galaxy's center and a bright compact source on the north eastern edge (cf. figure 8.5). This can also be seen in the metallicity map in figure 9.17.

### 9.3. Zooming in: spatially-resolved line ratios and metallicity

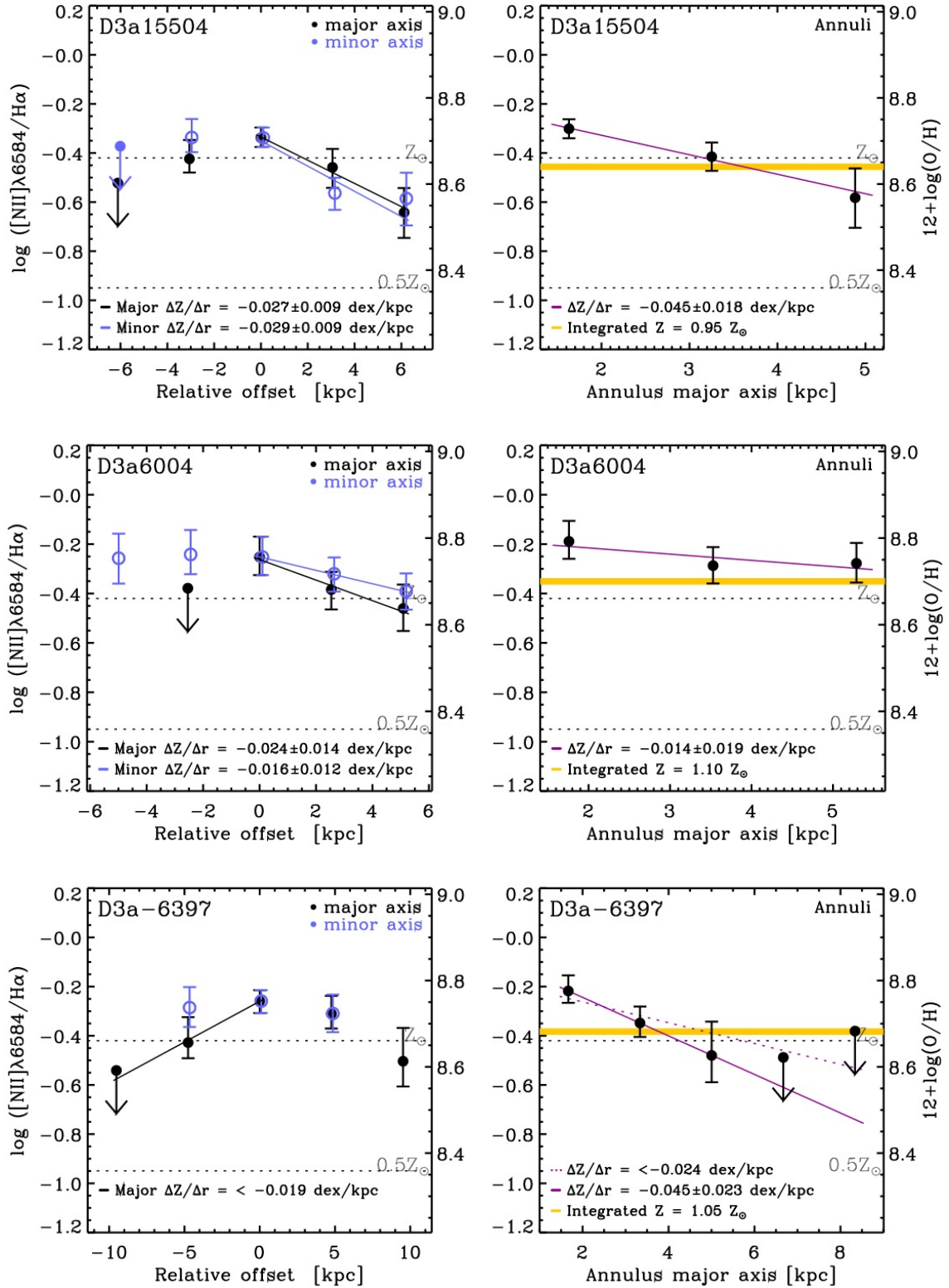


Figure 9.11.: [NII]/H $\alpha$  aperture cuts along major and minor axes (left column) and profiles for concentric annuli (right column) for D3a-15504 (top), D3a-6004 (middle) and D3a-6397 (bottom). The integrated metallicity from section 9.2.3 is shown in orange. See Appendix B for details on line flux and regions.

9.3. Zooming in: spatially-resolved line ratios and metallicity

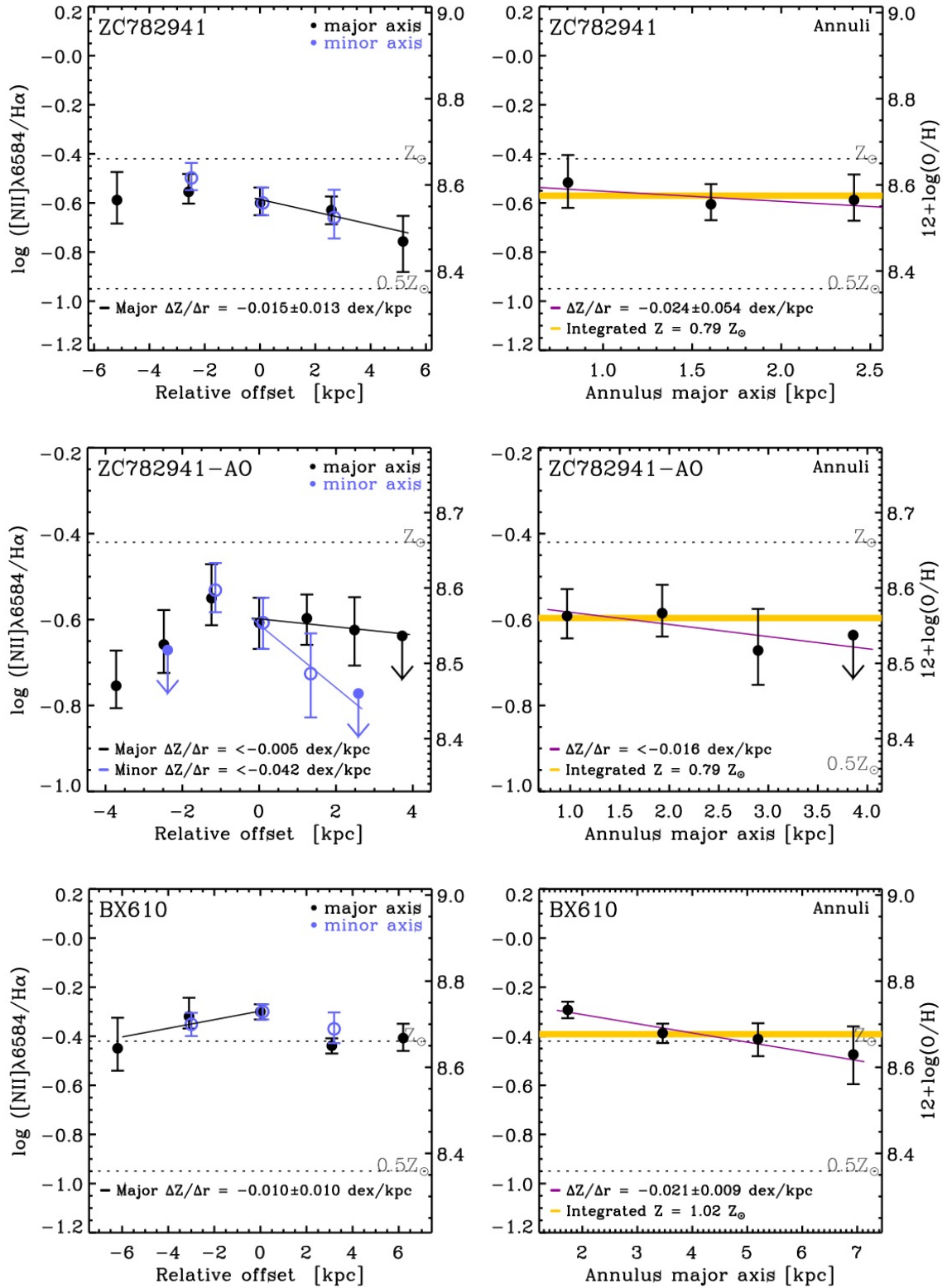


Figure 9.12.: As figure 9.11. Here: ZC-782941 (top), ZC-782941-AO (middle) and BX-610 (bottom).

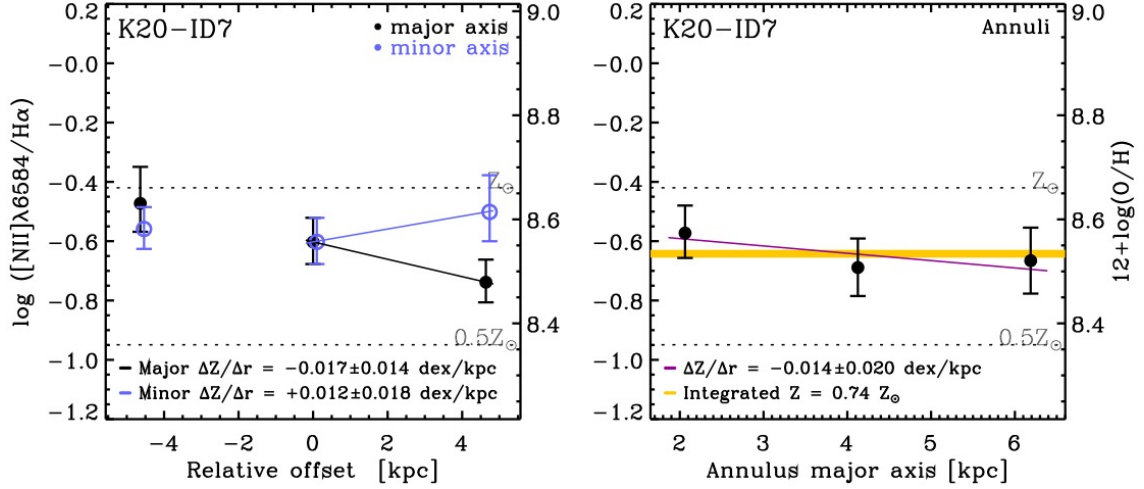


Figure 9.13.: As figure9.12. Here: K20-ID7

The range for our negative gradients is comparable to the set of negative gradients found by Queyrel et al. (2012). Contrary to these authors, we do not find any positive radial gradients. Both our gradients and the ones presented by Queyrel et al. (2012) are much shallower than those found in a lensed  $z \sim 1.5$  face on spiral galaxy presented by Yuan et al. (2011), who measured  $-0.16 \pm 0.02$  dex/kpc, and the reported  $-0.27 \pm 0.05$  dex/kpc found in another lensed  $z \sim 2$  galaxy by Jones et al. (2010). Also, in general, the inferred gradients in our disk galaxies (excluding ID7 which is a merger system) tend to be shallower than found in local spirals (e.g.,  $-0.07$  dex/kpc the Milky Way). The comparison with Queyrel et al. (2012) is the most consistent one, as the seeing-limited resolution for most of our and their data is similar and the metallicity indicator is the same. Comparisons with local galaxies or high- $z$  lensed disks, however, are hampered by the beam-smearing of our data. Although the gradient or limits for ZC782941 at non-AO and AO resolution are in encouraging agreement, this cannot be generalized. Because galaxies tend to be bright in their centers and [NII] is fainter than  $H\alpha$ , beam-smearing over a few kpc for objects with a given intrinsic negative gradient will result in a shallower observed gradient.

### 9.3.2. Line ratio and metallicity maps

Line ratio and metallicity maps provide the highest possible spatial resolution. Due to the faint nature of emission lines in high redshift galaxies and the long integration times needed to achieve a decent signal-to-noise level in each pixel, full object maps could only be derived for the brightest of our galaxies. For the fainter ones, the maps are limited to the brighter center or regions. Another limiting factor is OH line contamination. In some cases, a map could only be derived for a part of the object because of one or more of the emission lines of interest shifting in wavelength (due to velocity gradients) into regions

more heavily contaminated by OH line emission. Also, for some of the galaxies, only one ratio map (in these cases  $[\text{NII}]/\text{H}\alpha$ ) could be derived. These galaxies have either very low surface brightness or two or more emission lines are contaminated by OH lines. We here present the five best cases.

For each target, the  $[\text{NII}]/\text{H}\alpha$  map is shown on the left and (if available) the  $[\text{OIII}]/\text{H}\beta$  map on the right. These are maps generated from the pixel-to-pixel emission line flux maps as discussed in section 8.2 (figures 8.1 to 8.11). For comparison, the spatial distribution of the  $\text{H}\alpha$  flux is overlaid as intensity contours. The color coding shows the logarithm of the line flux ratio,  $\log([\text{NII}]/\text{H}\alpha)$  and  $\log([\text{OIII}]/\text{H}\beta)$ . Grey pixels/areas denote pixels/areas for which the S/N in both lines is too low (i.e  $\text{S/N} < 3$ ) but where  $\text{H}\alpha$  flux has a  $\text{S/N} > 5$ . The FWHM of the PSF is shown as a circle, a white line shows the scale: 8kpc for seeing-limited and 1kpc for AO maps.

### D3a-15504

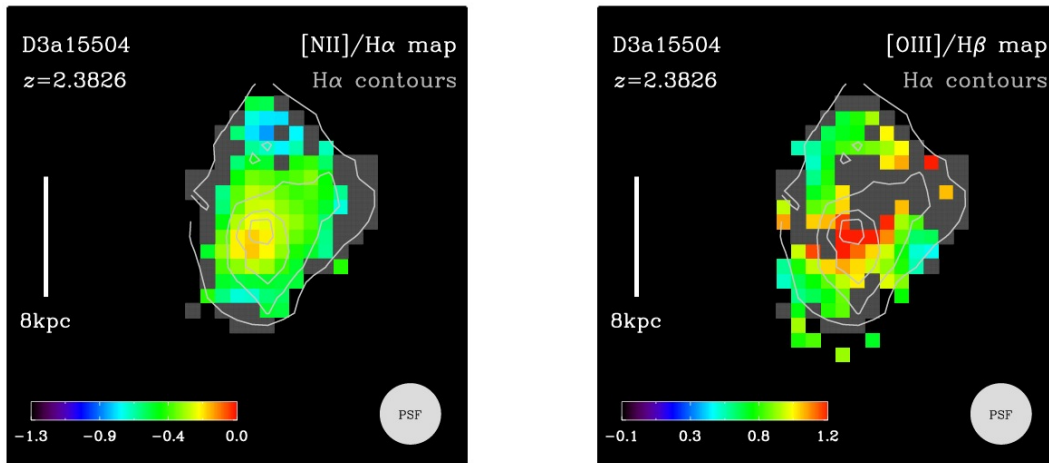


Figure 9.14.:  $[\text{NII}]/\text{H}\alpha$  and  $[\text{OIII}]/\text{H}\beta$  maps for D3a-15504

As described above, D3a-15504 is a rotating disk galaxy at  $z=2.38$ , which hosts an AGN. The effect of the AGN can be clearly seen in both the  $[\text{NII}]/\text{H}\alpha$  and  $[\text{OIII}]/\text{H}\beta$  map: it is the dominant excitation mechanism in the inner part of the galaxy where both  $[\text{NII}]/\text{H}\alpha$  and  $[\text{OIII}]/\text{H}\beta$  peak in the same region at ratios typical for AGN:  $[\text{NII}]/\text{H}\alpha \sim 0.6$ ,  $[\text{OIII}]/\text{H}\beta \sim 15$ . The AGN dominates the line excitation only locally in the central part of the galaxy. Towards the outer disk, we measure  $[\text{NII}]/\text{H}\alpha$  and  $[\text{OIII}]/\text{H}\beta$  ratios consistent with those found in star-forming regions ( $[\text{NII}]/\text{H}\alpha \sim 0.1$  and  $[\text{OIII}]/\text{H}\beta \sim 4.5$ ). This is consistent with the findings of Genzel et al. (2006). For a more detailed discussion see section 9.4, where we combine the two maps in a pixel-to-pixel BPT analysis.

**D3a-6004**

The  $[\text{NII}]/\text{H}\alpha$  map of D3a-6004 (Fig. 9.15, left) shows a compact, unresolved, peak in the center of the galaxy. The high N2 value of  $\sim -0.1$  and the small spatial extent of this region are indicative for the presence of an AGN. D3a-6004 shows a notable  $[\text{NII}]/\text{H}\alpha$  gradient from the peak center toward the outer parts of the galaxy. Towards the southeastern outer region, the  $[\text{NII}]/\text{H}\alpha$  ratio rises again. The significance of this effect is weakened by the fact that the S/N of the  $[\text{NII}]$  line in particular declines rapidly in this region. The available optical spectrum and optical to mid-infrared SED of D3a-6004 show no sign of AGN activity. It remains, however, possible that a low-luminosity AGN is present in its nucleus, as our data suggests. The peak in  $[\text{NII}]/\text{H}\alpha$  seen in the maps is smeared out in our axis and radial profiles. The implication of an AGN contribution at the center is that the N2-based metallicity gradient of D3a-6004 is overestimated. We note that such modest but non negligible AGN contribution have also been found and discussed by Wright et al. (2010) in some large  $z\sim 1.5$  disks.

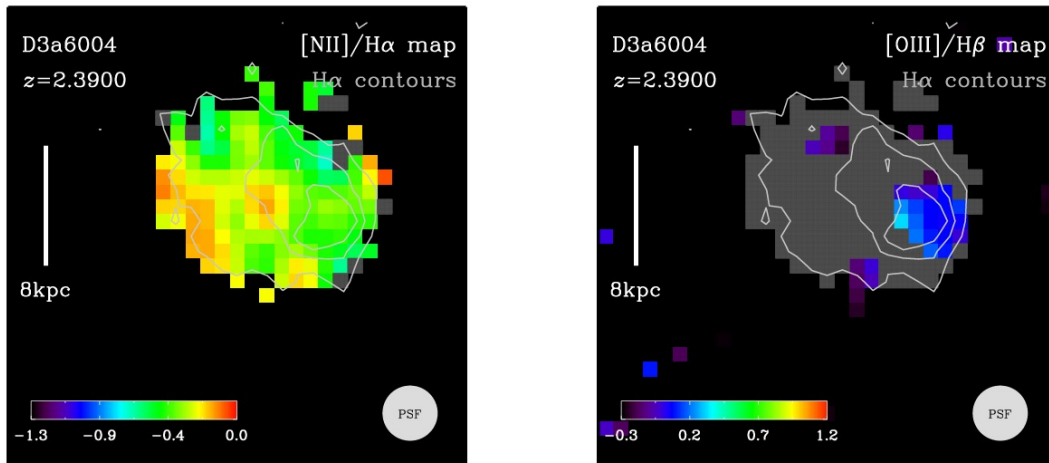


Figure 9.15.: D3a-6004: a possible low-luminosity AGN host galaxy at  $z=2.39$ .

**D3a-6397**

Similarly to D3a-6004, D3a-6397 shows no sign of AGN activity in its optical spectrum or optical to mid-infrared SED. Our  $[\text{NII}]/\text{H}\alpha$  map, however, clearly reveals a compact, unresolved peak reaching an  $[\text{NII}]/\text{H}\alpha \approx 0.77$ . Again, this indicates a contribution by an AGN, which also means that the actual observed N2-based metallicity gradient could be shallower than inferred from the profile analysis. The rise of metallicity towards the outer part of the galaxy, seen in all directions, is less affected by low  $[\text{NII}]$  S/N as in D3a-6004. Still, deeper data is needed to reliably confirm this finding.

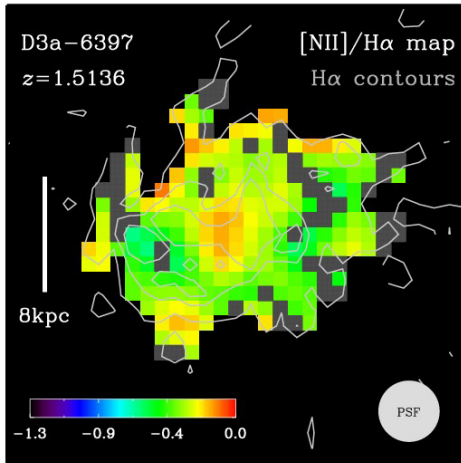


Figure 9.16.: D3a-6397: another possible AGN host galaxy.

### ZC782941

This object is another disk galaxy with a small companion galaxy or giant clump to the north-east, which is not resolved in seeing-limited data set (figure 9.17, upper panel) but is in the AO observation shown in the same figure in the lower panel. Both integrated and spatially-resolved line ratios are consistent with pure photoionization in HII regions, with somewhat higher abundances. Interestingly, the  $[\text{NII}]/\text{H}\alpha$  map shows another peak between the main body part of the galaxy and the north-east lower metallicity region. As this is clearly offset from the morphological and dynamical center of the galaxy, and the  $[\text{NII}]/\text{H}\alpha$  values are  $\sim 0.3$ , the ratio enhancement in this region may reflect some contribution from shock excitation. The AO based  $[\text{NII}]/\text{H}\alpha$  map reveals that the metallicity shows significant variations on small scales. Thus the seeing-limited map or the integrated value clearly provide only a limited description of the object.

### BX610

For BX610,  $[\text{NII}]/\text{H}\alpha$  peaks at its morphological and kinematic center. The values are consistent with roughly solar abundances and do not require or indicate AGN contribution as in the case of D3a-6004 and D3a-6397. This is consistent with the lack of AGN signatures in both the  $[\text{NII}]/\text{H}\alpha$  and  $[\text{OIII}]/\text{H}\beta$  map, and in its optical spectrum and mid-infrared SED (e.g. Erb et al 2006; Förster Schreiber et al. 2011b).

### 9.3. Zooming in: spatially-resolved line ratios and metallicity

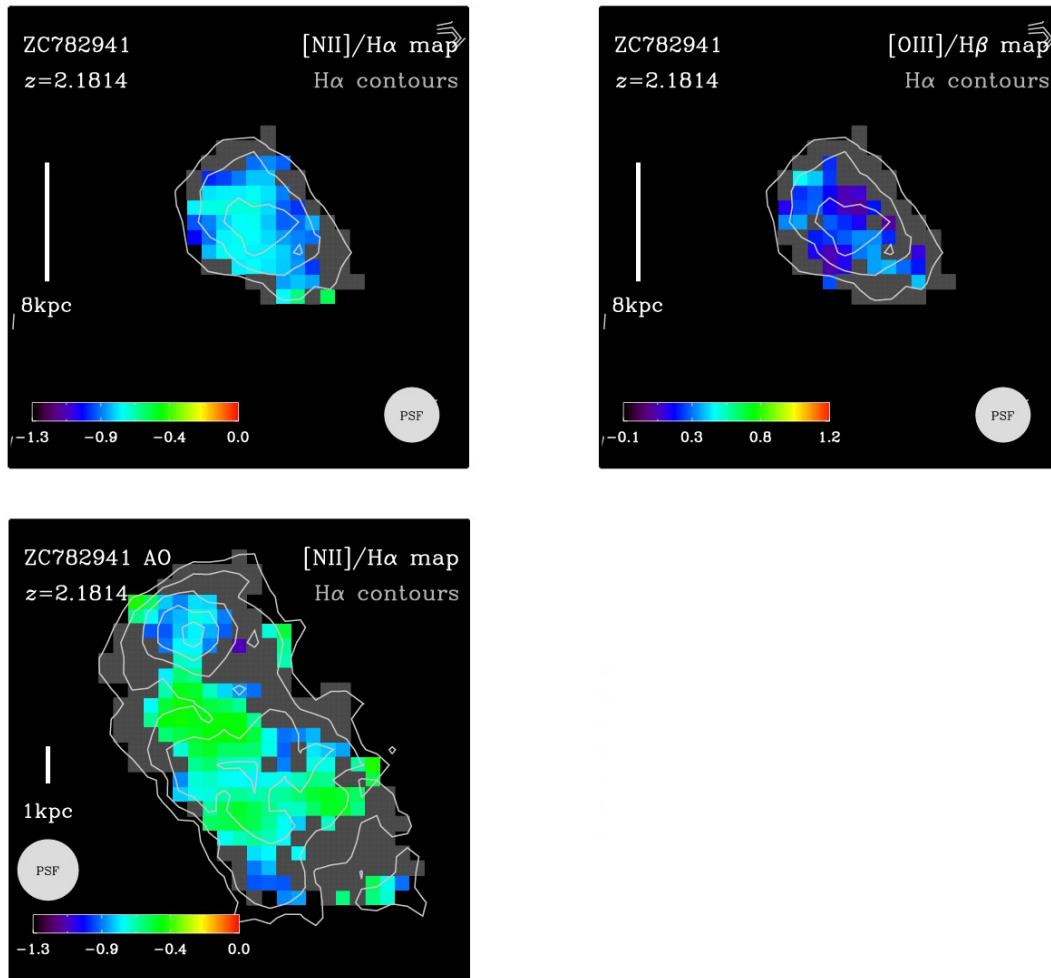


Figure 9.17.: ZC782941: A  $z = 2.18$  galaxy consistent with the star-forming branch of the BPT diagram

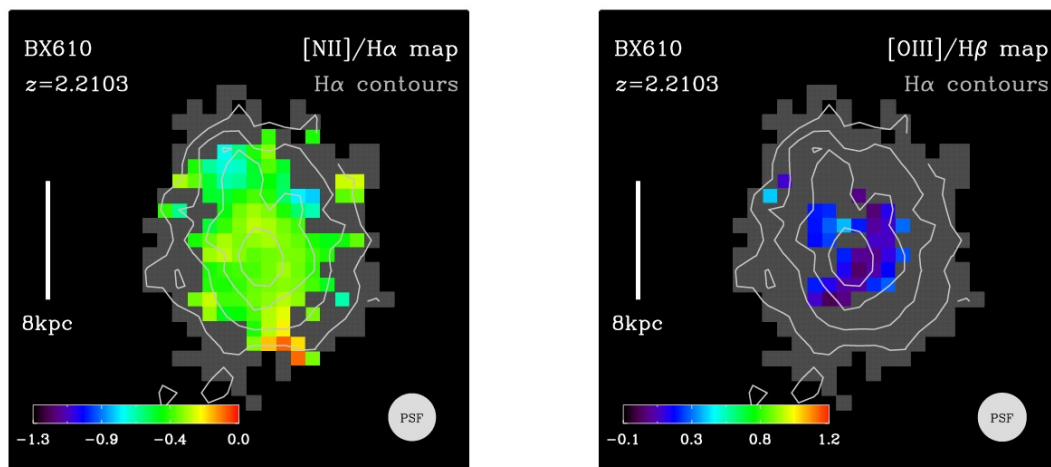


Figure 9.18.: BX610: a disk galaxy in the "composite type" region of the BPT diagram

## 9.4. Spatially-resolved BPT diagnostics

### 9.4.1. Pixel-to-Pixel BPT diagram

The axis and radial profiles as well as the line ratio maps presented in the previous subsections highlight the complexity of, and variations among individual objects, and thus the importance of spatially-resolved information for a fuller picture in terms of the line excitation and properties of nebular gas. With the full spatial mapping afforded by SINFONI, we can take the ultimate step and investigate the prevailing conditions across objects, relate them more directly with morphological and kinematic features, and better interpret the spatially-integrated emission line properties. This is illustrated here with two galaxies, D3a-15504 and ZC-782941 for which the S/N in all four BPT lines is sufficient over a large enough area to potentially cover different regions. Figures 9.19 and 9.20 show the distribution of all individual pixels with  $S/N > 3$  in each of  $H\alpha$ ,  $H\beta$ ,  $[\text{NII}]\lambda 6584$ , and  $[\text{OIII}]\lambda 5007$  in the BPT diagram. The data points are color-coded according to different physical regions as indicated in the third inset at the bottom of each figure: from red in the immediate vicinity of the kinematic and morphological center of the galaxy to blue for the outer disk parts.

For D3a-15504, the central AGN-dominated (red and yellow symbols) and outer star-forming disk regions (green and blue pixel) separate clearly and the ratios suggest gas-phase oxygen abundances of  $\sim 1/3$  to  $1/2$  solar in the outer disk. It is obvious, that the high excitation due to the AGN at the center drives the integrated ratios to values that lie between the loci of purely star-forming sources and the Seyfert-2 regime defined by the local SDSS sample. As noted previously, the AGN contribution also implies that the inferred N2-based metallicity gradient derived in section 9.3 represents an upper limit.

In contrast, for the non-AGN disk galaxy ZC782941, all pixels are consistent with excitation as observed in pure star-forming objects, and very similar to the integrated line ratio. This reflects the fairly uniform line ratio maps from the seeing-limited SINFONI data. At this resolution ( $0.6'' \text{FWHM} = 4.9 \text{kpc}$  at  $z=2.18$ ), the possible companion or large clump to the north-east is barely resolved, and so is the region between it and the main emission source where higher resolution AO K-band data reveals more clearly an enhanced  $[\text{NII}]/H\alpha$  ratio. Since this region does not coincide with the galaxy center nor with the north-eastern clump/companion, contribution by an AGN appears unlikely, and instead shocks or simply enhanced metallicity may cause this  $[\text{NII}]/H\alpha$  variation. The extension towards higher  $[\text{NII}]/H\alpha$  but similar  $[\text{OIII}]/H\beta$  values of some yellow and green points in figure 9.20, encompassing this region, possibly reflects this effect although higher resolution  $[\text{OIII}]/H\beta$  maps will be required for confirmation.

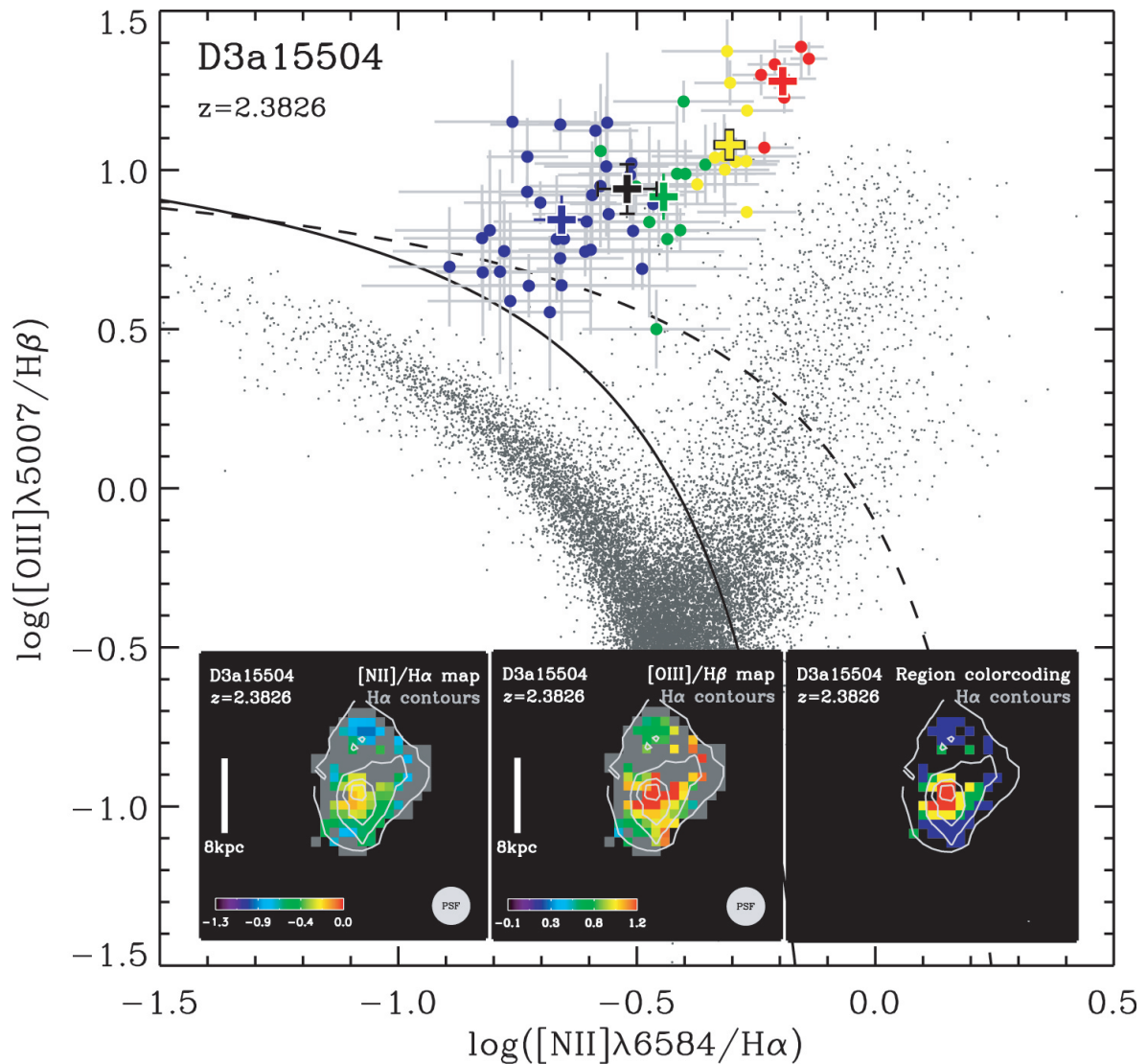


Figure 9.19.: Spatially-resolved BPT diagram for D3a-15504

The  $[\text{NII}]/\text{H}\alpha$  vs.  $[\text{OIII}]/\text{H}\beta$  ratio of individual spatial pixels is plotted in the BPT diagram, color coded according to their spatial location as indicated in the bottom right map (from red in the immediate vicinity of the center of the galaxy to blue for the outer disk parts). The maps of  $[\text{NII}]/\text{H}\alpha$  and  $[\text{OIII}]/\text{H}\beta$  ratios are shown as insets at the bottom left and middle. Pixels with  $\text{S/N} < 3$  are masked out. The mean BPT values for the individual regions are over-plotted as bold crosses in colors corresponding to their regions. The total mean BPT value over all pixel is denoted as a black cross.

In both figures, the black cross denotes the average BPT ratio over all pixels in the plot. In both cases it does not exactly correspond to the value found for the integrated analysis in section 9.2.3 and given in table 9.2, but it agrees within  $1.5\sigma$ . The reason for this mismatch is likely a flux weighting effect in the spectra from which the integrated measurements are derived. Brighter pixels contribute more to the integrated flux than dimmer ones. The simple average over ratios in individual pixels is not affected by this. Additionally, the integrated ratios are derived over a slightly different set of pixels where no single pixels are masked out within the main aperture. This in turn leads to slight differences in the probed regions and hence a difference in the integrated vs. pixel averaged ratios.

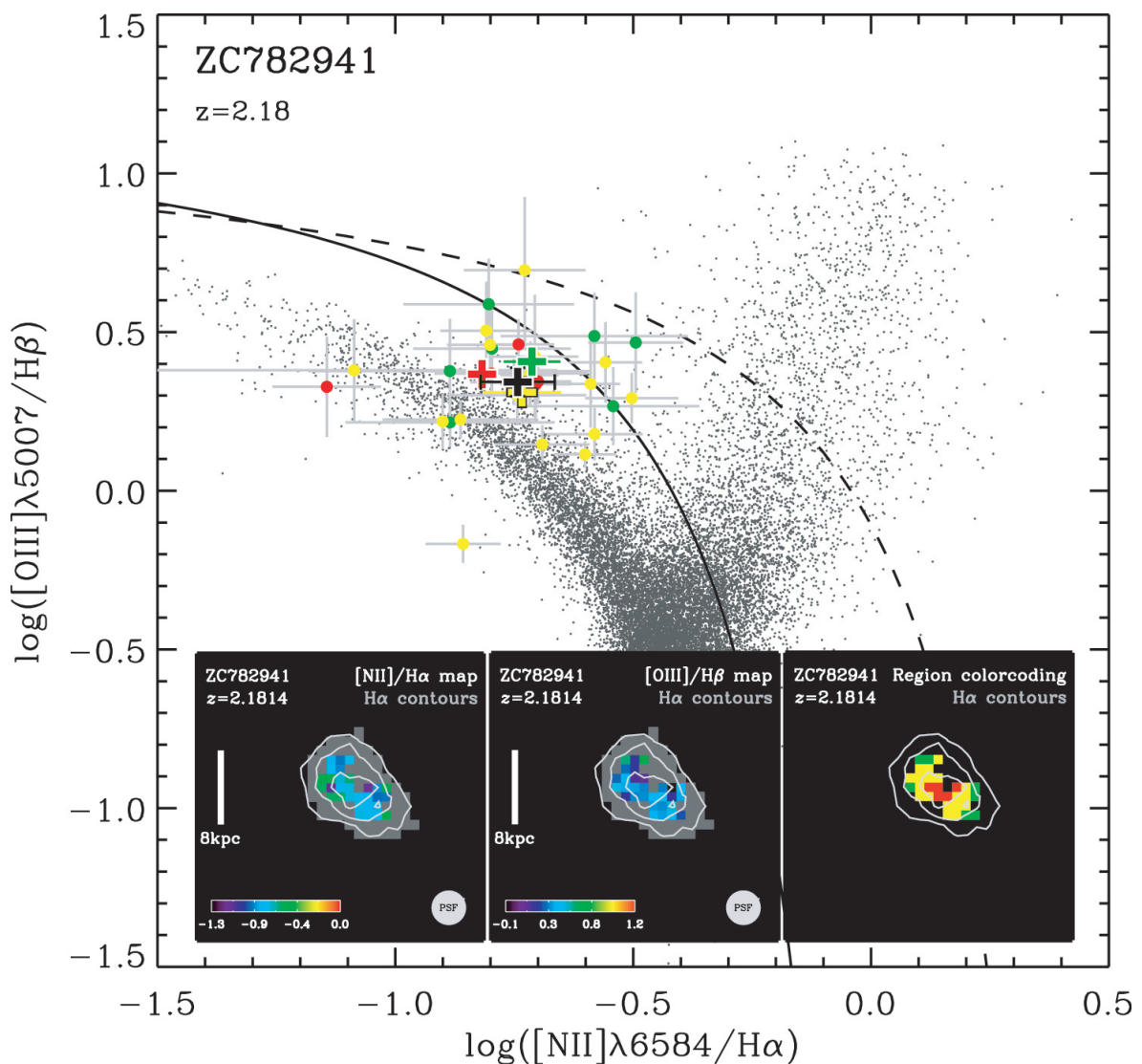


Figure 9.20.: Same as Fig. 9.19 but for ZC782941



# Chapter 10.

## Interstellar extinction at high redshift

In this chapter, we analyze the  $H\alpha/H\beta$  line ratio to measure the interstellar extinction. After a general discussion on extinction, its measurement and open questions in the high redshift universe, we start out in the first part with source-integrated nebular extinction measurements and compare our results with extinction derived from SED fitting to address the question of whether HII regions are generally more obscured than the bulk of stars in  $z\sim 2$  star-forming galaxies as found for  $z\sim 0$  actively star-forming systems. In the second part, we present spatially-resolved extinction measurements in a case study of one galaxy, BX610, which gives for the first time direct information on the spatial distribution of obscuring dust towards the HII regions in a  $z\sim 2$  galaxy.

### 10.1. Extinction

Interstellar extinction is a crucial parameter for deriving intrinsic properties such as the star formation rate. Being relatively well known and measurable in the local universe, for the epochs of most active star-forming activity between  $z\sim 1-2$  it is still comparatively poorly constrained because measurements typically rely on integrated colors or optical to mid-infrared SEDs that are degenerate with other properties such as stellar age and star-formation history. The more robust alternative method based on relative intensities of Hydrogen emission lines, such as  $H\alpha/H\beta$ , is hampered by the faintness of the lines (especially  $H\beta$ ) such that very few measurements exist at  $z\gtrsim 1$ .

The extinction,  $A(\lambda)$ , is the attenuation of light through absorption and scattering by gas or dust particles present along the line of sight between emitter and observer. It depends on the kind and size of the obscuring particles and the wavelength of the incident radiation. The extinction generally decreases with increasing wavelength. It is related to the optical depth  $\tau_\lambda$  by

$$A(\lambda)[mag] = 2.5 \log(e) \tau_\lambda = 1.086 \tau_\lambda. \quad (10.1)$$

## 10.1. Extinction

---

The extinction at wavelength  $\lambda$  is often expressed relative to the extinction in the optical V-band as  $A_\lambda/A_V$  or in terms of the color excess  $E(B-V) = A(B) - A(V)$ , which is the difference in attenuation in the optical B and V band and referred to as selective extinction. The ratio  $A(V)/E(B-V)$  defines  $R(V)$ , the total to selective extinction. For our own galaxy, the general shape of the UV to NIR extinction curve is fairly well characterized and has a slope  $R(V)=3.1$  (e.g. Cardelli et al. 1989). For the more active local “starburst” galaxies, Calzetti et al. (2000) derived that  $R(V)=4.05\pm 0.80$ . Given a reddening curve  $k(\lambda)$ , the extinction can be written as

$$A(\lambda) = k(\lambda)E(B - V) = \frac{k(\lambda)A_V}{R_V}. \quad (10.2)$$

The effective attenuation of light further depends on the relative distribution of sources and obscuring dust. Two geometries are usually considered: a simple foreground screen and a homogeneous mix of attenuating dust and sources. In the first case, a uniform optically thin dust cloud is located between the source and the observer. The emerging radiation intensity is calculated from the incident intensity via

$$I(\lambda) = I_0(\lambda)e^{-\tau_\lambda}. \quad (10.3)$$

In the mixed model, where absorber and emitter are homogeneously distributed in the same volume, the exiting radiation is

$$I(\lambda) = I_0(\lambda)\frac{1 - e^{-\tau_\lambda}}{\tau_\lambda}. \quad (10.4)$$

In reality, for astronomical systems such as galaxies the geometry is more complicated e.g. with regions being more dust enshrouded than others, and the two cases above may be considered as two extreme, or limiting cases.

Many efforts have been devoted to derive an extinction law for extragalactic, notably starburst systems. One of the most commonly used extinction law for actively star-forming galaxies is the one derived by Calzetti et al. (1997, 2000, 2001) The Calzetti law assumes the uniform dust screen model and is an empirical attenuation curve given as piecewise polynomial fit of the NIR to UV spectral range (Calzetti et al. 2000), where for  $0.12\mu m \leq \lambda < 0.63\mu m$

$$k(\lambda) = 2.659(-2.156 + 1.509/\lambda - 0.198/\lambda^2 + 0.011/\lambda^3) + R_V,$$

and for  $0.63\mu m \leq \lambda \leq 2.20\mu m$

$$k(\lambda) = 2.659(-1.857 + 1.040/\lambda) + R_V. \quad (10.5)$$

Little constraints exist at  $z>1$  on the applicable geometry and extinction law, and the Calzetti law in the uniform foreground screen framework are commonly assumed. In what follows, we will adopt the same assumptions.

### 10.1.1. Measuring extinction

If the intrinsic energy distribution of an object is known, the differential extinction of two observed wavelength  $A_{\lambda_1} - A_{\lambda_2}$  can be calculated by just comparing the measured flux at the two wavelength. For instance, to measure the extinction towards HII regions the two brightest nebular Balmer recombination lines,  $H\alpha$   $\lambda 6564\text{\AA}$  and  $H\beta$   $\lambda 4862\text{\AA}$ , are often used in studies of local galaxies, and are the most easily accessible for more distant sources out to  $z \sim 3$ . For the conditions typically present in HII regions,  $T = 10^4\text{K}$  and  $n_e \sim 10^2 - 10^4\text{cm}^{-3}$  and if one assumes 'Case B recombination' (i.e. the emission in the Lyman lines is optically thick, and in all other lines, optically thin), the intrinsic ratio  $H\alpha/H\beta$ , the "Balmer decrement", is  $\approx 2.86$  (Osterbrock 1974). A measured ratio different from this intrinsic theoretical value indicates extinction effects. and the amount of extinction can thus be calculated.

For a uniform foreground screen model, the observed Balmer decrement is

$$\left(\frac{F_{H\alpha}}{F_{H\beta}}\right)^{\text{obs.}} = \left(\frac{F_{H\alpha}}{F_{H\beta}}\right)^{\text{intr.}} \cdot \frac{e^{-\frac{A_{H\alpha}}{1.086}}}{e^{-\frac{A_{H\beta}}{1.086}}} \quad (10.6)$$

$$(10.7)$$

leading to

$$2.5 \log_{10} \left[ \frac{\left(\frac{F_{H\alpha}}{F_{H\beta}}\right)^{\text{obs.}}}{2.86} \right] = A_{H\beta} - A_{H\alpha} \quad (10.8)$$

Adopting the Calzetti law (eq. 10.5), and with the vacuum rest-wavelengths of  $H\alpha$  ( $0.65646\mu\text{m}$ ) and  $H\beta$  ( $0.48627\mu\text{m}$ ), this can be written as

$$A_V = 7.96 \log_{10} \left[ \frac{\left(\frac{F_{H\alpha}}{F_{H\beta}}\right)^{\text{obs.}}}{2.86} \right] \quad (10.9)$$

Being a reliable extinction tracer, and in principle relatively easy to measure, determinations of the Balmer decrement in high redshift galaxies faces however various complications: The measured separation of  $H\alpha$  and  $H\beta$  ( $1702\text{\AA}$  at restframe) at e.g a redshift of 2.4 is already  $5790\text{\AA}$  and thus the two lines fall in different atmospheric observing bands. Further complications arise due to seeing variations and OH line contamination. Therefore special care must be taken of the inter-band flux calibration.  $H\alpha$  has a typical emission line flux of the order of  $10^{-17} - 10^{-16}\text{erg s}^{-1}\text{cm}^{-2}$ , which dictates exposure times of  $> 1\text{h}$  for a decent S/N.  $H\beta$  being 2.8 times fainter in the ideal case needs  $\sim 10\times$  longer integration times to reach a comparable S/N.

### 10.1.2. Differential extinction towards HII regions and stars

Different methods for deriving the extinction probe physically different regions in the observed object. The extinction from broad-band SED modeling applies to a more evolved stellar population, the bulk of stars, while nebular line based extinction probes HII regions tracing recent or on-going star formation. Therefore, the SED-derived extinction can be significantly off from the attenuation towards HII regions, implying in particular large uncertainties in intrinsic SFRs derived from  $H\alpha$  if one uses  $A_{V,SED}$ .

Such “differential extinction” is found in local star-forming and starburst galaxies (e.g., Calzetti et al. 1994, 2000; Cid-Fernandes et al. 2005). In particular, Calzetti et al. (2000) derived a typical difference such that  $A_{V,SED} = 0.44 A_{V,neb}$ , where  $A_{V,SED}$  is the extinction towards the bulk of stars and  $A_{V,neb}$  is that towards the HII regions. At  $z \sim 2$ , results rely mostly on indirect arguments. In Förster Schreiber et al. (2009), a comparison of the measured  $H\alpha$  luminosities  $L(H\alpha)$  and rest-frame equivalent widths  $\omega(H\alpha)$  from SINFONI observations of  $\sim 60$  star-forming galaxies at  $1.3 < z < 2.6$  with model predictions from the best-fit parameters from the SED modeling of each galaxy, showed evidence for differential extinction between HII regions and stars. Similar findings are also reported by other groups in other (small) samples at  $z \sim 2$  (e.g. van Dokkum et al. 2004; Kriek et al. 2007; Mancini et al. 2011). In contrast, Erb et al. (2006) found no need for an extra attenuation towards HII regions relative to stars but their long-slit data are subject to potential errors from uncertain aperture correction and slit losses (see discussion in Förster Schreiber et al. 2009, Law et al. 2009).

The very first direct tests using the Balmer decrement at  $z \sim 2$  appear to support extra attenuation towards HII regions but still rely on rather noisy measurements of individual objects or stacked spectra (e.g. Yoshikawa et al. 2010).

## 10.2. Nebular extinction and comparison with extinction from broad-band SED modeling

Among our sample, we can derive robust integrated  $H\alpha/H\beta$  ratios for six objects. The line fluxes are measured from the co-added spectra of individual pixels with  $S/N > 3$  in each line, after shifting them to the systemic velocity, just as described in section 7.5.2. In doing so, we neglected possible underlying stellar absorption features at  $H\alpha$  and  $H\beta$ . This has little impact for  $H\alpha$  since for a range of star formation histories and ages and for plausible initial mass functions, the equivalent width of  $H\alpha$  in absorption is always  $< 5 \text{ \AA}$  (e.g. Brinchmann et al. 2004), which is small compared to the restframe equivalent width of  $H\alpha$  in emission for our galaxies (in the range  $45\text{--}206 \text{ \AA}$ , see Förster Schreiber et al. 2009). On the other hand, this can be more of a concern for the weaker  $H\beta$  emission

## 10.2. Nebular extinction and comparison with extinction from broad-band SED modeling

line, with inferred equivalent widths of  $\sim 11\text{--}29\text{\AA}$ , since stellar  $H\beta$  absorption can reach values between  $\sim 5\text{--}10\text{\AA}$ . To assess the impact on our Balmer decrement, we estimated the underlying  $H\beta$  absorption using the best-fit ages and star formation histories from SED modeling (Förster Schreiber et al. 2009, 2011a) with the same solar metallicity and Bruzual & Charlot (2003) synthesis code. We estimated the  $H\beta$  emission line equivalent width using our flux measurements and either the measured broad-band magnitudes in the same band as  $H\beta$ , or in magnitudes interpolated from available photometry in adjacent bands. Since broad-band photometry refers to the entire source as measured over a large ( $\gtrsim 2''$ ) aperture, we applied an aperture correction to the  $H\beta$  emission line fluxes based on the ratio of the total  $H\alpha$  flux and that measured over the common regions used for the Balmer decrement. This is a simplifying assumption for lack of better constraints for  $H\beta$  itself; the case of BX610 discussed in the next section shows that significant variations in  $H\alpha/H\beta$  ratios across the sources are likely. After correcting the equivalent width in emission for the underlying absorption (also assuming it is constant across each source), we calculate the corresponding corrected  $H\beta$  flux, and Balmer decrements.

Table 10.1.: Balmer decrement and derived nebular extinction

Source	$\frac{H\alpha}{H\beta}$	$A_{V,\text{neb}}$	$\left(\frac{H\alpha}{H\beta}\right)_{\text{abs.corr.}(a)}$	$A_{V,\text{neb}}^{\text{abs.corr.}(a)}$	$\frac{A_{V,\text{neb}}}{A_{V,\text{SED}}}$	$\frac{A_{V,\text{neb}}^{\text{abs.corr.}}}{A_{V,\text{SED}}}$
MD41	$4.86^{+0.72}_{-0.65}$	$1.83^{+0.52}_{-0.46}$	$4.34^{+0.59}_{-0.59}$	$1.44^{+0.47}_{-0.47}$	1.53	1.20
BX389	$3.67^{+0.41}_{-0.51}$	$0.86^{+0.38}_{-0.48}$	$3.51^{+0.63}_{-0.63}$	$0.71^{+0.62}_{-0.62}$	0.86	0.71
BX610	$6.92^{+0.63}_{-0.51}$	$3.06^{+0.31}_{-0.25}$	$5.78^{+0.59}_{-0.59}$	$2.43^{+0.36}_{-0.35}$	3.82	3.04
K20ID7	$8.39^{+1.46}_{-1.16}$	$3.72^{+0.60}_{-0.48}$	$6.03^{+0.76}_{-0.75}$	$2.58^{+0.44}_{-0.43}$	3.72	2.58
D3a15504	$7.54^{+1.25}_{-1.21}$	$3.35^{+0.57}_{-0.55}$	$5.03^{+0.72}_{-0.71}$	$1.95^{+0.49}_{-0.49}$	3.35	1.95
ZC782941	$6.55^{+0.71}_{-0.73}$	$2.86^{+0.37}_{-0.38}$	$5.31^{+0.56}_{-0.54}$	$2.14^{+0.36}_{-0.35}$	2.20	1.65

<sup>(a)</sup> after correcting for underlying stellar  $H\beta$  absorption as described in the text.

Table 10.1 lists the Balmer decrements and corresponding derived nebular extinction, both with and without correction for  $H\beta$  absorption. The nebular extinction values,  $A_{V,\text{neb}}$  are compared with the best fit  $A_V$  from SED modeling,  $A_{V,\text{SED}}$  in figure 10.1. Omitting  $H\beta$  absorption correction (large symbols and error bars in the figure) we find for all sources a ratio of  $A_{V,\text{neb}}/A_{V,\text{SED}} \gtrsim 1$ , (ranging from  $\sim 0.86$  for BX389 to 3.82 for BX610), supportive of extra attenuation towards HII regions. If we correct for  $H\beta$  absorption,  $A_{V,\text{neb}}$  decreases by 17 – 42%. Still, the  $A_{V,\text{neb}}/A_{V,\text{SED}} \gtrsim 1$ , BX389 being slightly lower than 1 at 0.71.

## 10.2. Nebular extinction and comparison with extinction from broad-band SED modeling

Various simplifying assumptions had to be made in our correction for  $H\beta$  absorption, and an additional possible caveat of our result is that we compare  $A_{V,SED}$  from modeling of SEDs for the entire source with  $A_{V,neb}$  from Balmer decrements measured over the smaller areas with sufficient S/N for  $H\alpha$  and  $H\beta$ . If the extinction in the central parts of our galaxies probed by our line measurements is higher, this could mimic extra attenuation towards HII regions in the diagram of figure 10.1. Better source-integrated Balmer decrements (higher S/N to larger radii and no OH contamination) and/or high resolution and high S/N optical to near-infrared imaging allowing spatially-resolved SED modeling (e.g. Wuyts et al. 2012) would enable more consistent  $A_{V,neb}$  versus  $A_{V,SED}$  comparisons, and, ultimately, a robust assessment of whether HII regions are on average more obscured than the bulk of stars in high- $z$  galaxies.

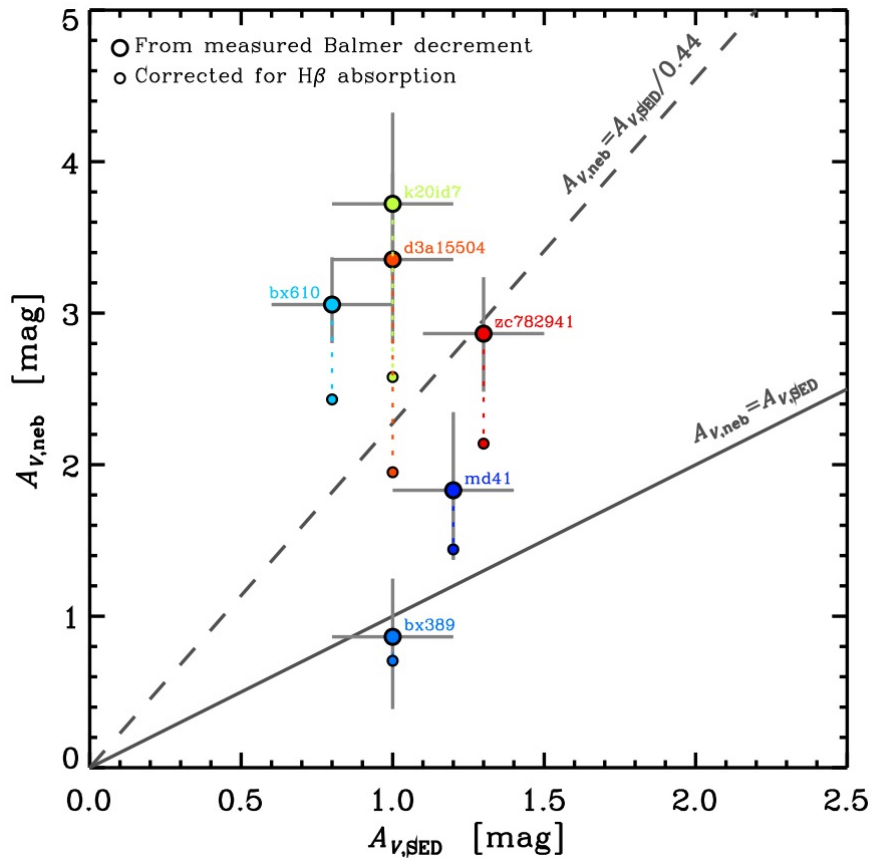


Figure 10.1.: Extinction based on SED modeling,  $A_{V,SED}$  plotted versus the Balmer Decrement 'nebular' extinction  $A_{V,nebular}$ . The dotted line denotes the 1:1 relation, the dashed line shows the relation if one assumes extra attenuation towards HII regions relative to the bulk of stars following Calzetti et al. (2000). Large symbols and error bars: no  $H\beta$  absorption correction. The connected small symbols below show how  $A_{V,neb}$  changes when accounting for  $H\beta$  stellar absorption as described in the text.

### 10.3. Case study: spatially-resolved extinction in BX610

From studies of spatially-resolved extinction in the local universe it is long known that the distribution of dust can be highly non-uniform. For higher- $z$  objects, comparing, for instance, broad-band morphologies at optical and near-infrared wavelength one can get an estimate of the dust distribution as optical observations probe the rest-UV, which is more affected by dust and obscuration than the rest-optical light observed in the near-IR (e.g., Cameron et al. 2010 at  $z \sim 0.4$ ). By comparing different estimates of the source-integrated extinction in the previous section, we presented evidence for a higher attenuation towards star-forming HII regions than towards the bulk of the stars, and thus evidence for global non-uniformity of the dust distribution.

In the following, we now take the ultimate step afforded by the full spatial mapping of SINFONI and present spatially-resolved extinction measurements in a case study of one galaxy, BX610, which gives – for the first time – direct information on the spatial distribution of obscuring dust towards the HII regions in a  $z \sim 2$  galaxy.

BX610 is our best object in terms of the quality of the data for the combined  $H\alpha$  and  $H\beta$  lines. In figure 10.2 we show the spatially-resolved extinction we have extracted from the BX610 data set. No data, however, exists to spatially correct for  $H\beta$  absorption as done for the spatially-integrated analysis in the previous section. In the upper row on the left, we show the  $H\alpha$  (black) and  $H\beta$  line flux (green) in major (solid line) and minor apertures (dotted line). The fluxes in concentric annuli is shown on the right. The  $H\alpha/H\beta$  ratios for the apertures and annuli are plotted below in the middle row. The actual placement of the apertures and annuli over the source is shown in small insets. The bottom row, left, shows a flux map of  $H\alpha$  and  $H\beta$ , where for  $H\alpha$  the intensity is color-coded and for  $H\beta$  over-plotted as contours. The resulting  $A_{V,neb}$  map is on its right.  $H\alpha$  intensity is over-plotted as contours. No extinction could be derived for the pixels shown in grey color as the measured  $H\beta$  line flux S/N is  $< 3$ .

All plots show a general increase in the derived  $A_{V,neb}$  towards the center of the galaxy. Comparing major and minor axis and the map, the spatial variations across the source are readily visible. The difference of major and minor value in the center is due to different coverage of the apertures within single pixels (see the  $A_{V,neb}$  map for masked pixels also in the center). The spatially-resolved  $[NII]/H\alpha$  data (cf. figure 9.12 and 9.18) show a peak in metallicity at the center, where  $A_{V,neb}$  peaks. Moreover, the molecular gas distribution traced by the CO(3-2) transition obtained at a resolution of  $\sim 0.9''$  with the IRAM Plateau de Bure interferometer is centrally concentrated (Tacconi et al. 2010). Given the general relationships between dust, molecular gas, and metal content (e.g. Leroy et al. 2011; Genzel et al. 2012) this additional evidence would support the increase in nebular extinction in the inner parts of BX610.

### 10.3. Case study: spatially-resolved extinction in BX610

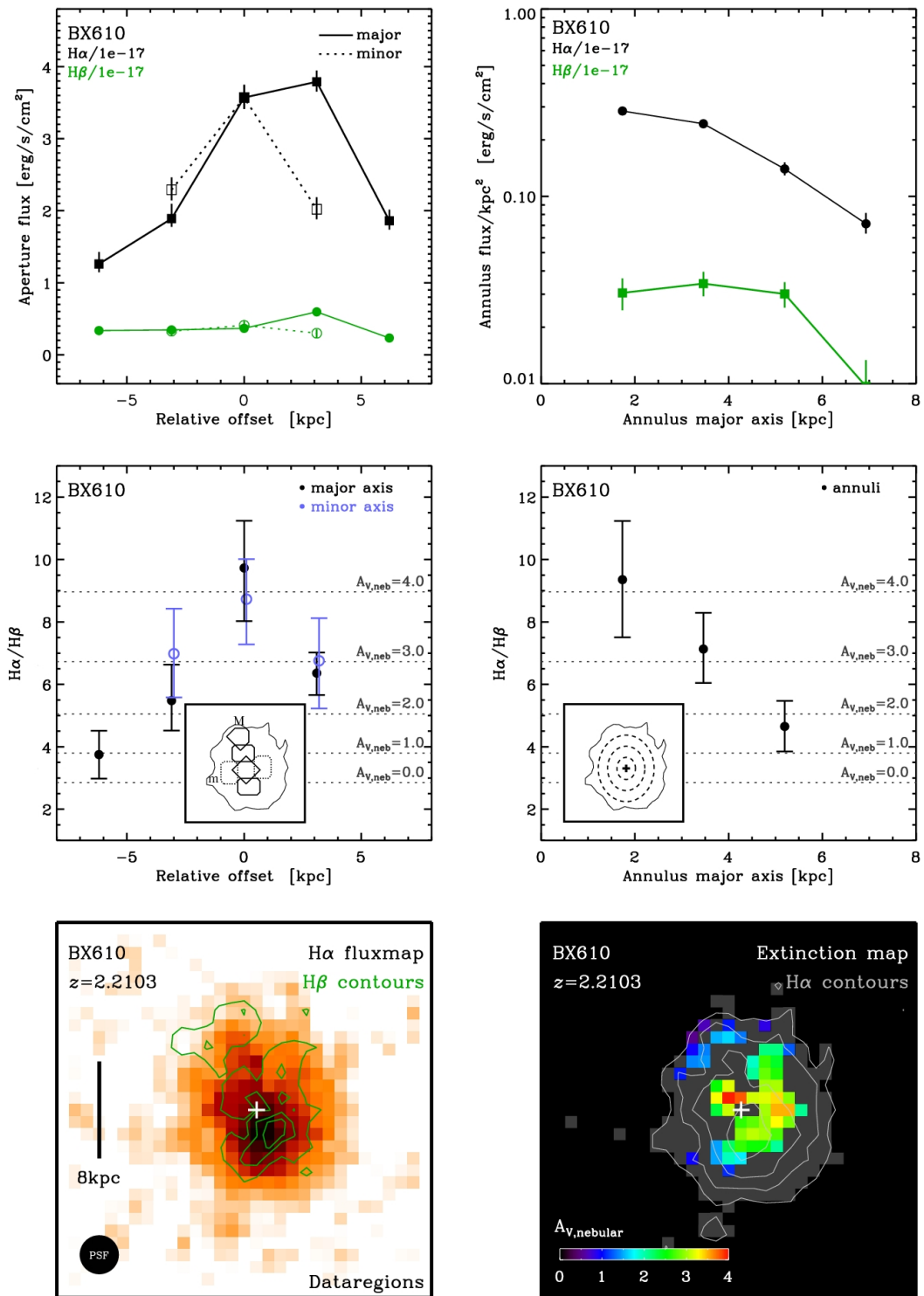


Figure 10.2.: Spatially-resolved extinction in BX610

Upper two rows:  $H\alpha$  and  $H\beta$  line flux, the  $H\alpha/H\beta$  ratio and corresponding nebular extinction  $A_{V,neb}$  in apertures along major and minor kinematic axis (left) and concentric annuli (right). Insets: location of apertures and annuli. Lower left:  $H\alpha$  line map with  $H\beta$  flux distribution contour overlay. Lower right: spatially-resolved extinction map. For map pixel in grey color no extinction could be derived as the  $H\beta$  line flux S/N is  $< 3$ .

# Chapter 11.

## Summary and outlook

### 11.1. Summary

The main findings from the analysis of the line emission properties of  $z \sim 2$  massive star-forming galaxies presented in the second part of this thesis can be summarized as follows:

#### **OH lines must be dealt with carefully - in observation planning and data analysis**

Particular attention needs to be given to the influence of night sky line contamination on emission line measurements in the near-infrared spectrum of faint high-redshift galaxies, even for source-integrated measurements. For instance, if one or more lines shift into a wavelength range strongly affected by a sky line for a sub-region of a galaxy due to its kinematic properties, the combination with other unaffected lines becomes less reliable and the different lines will effectively probe line emission from different regions of galaxy. This is exacerbated by the fact that the emission line properties of galaxies may not necessarily be symmetric about the center –even for disks– as our analysis of axis and radial profiles, and of line ratio maps showed for some of our sample galaxies.

Even in our very carefully selected objects –a subset of the full parent SINS  $H\alpha$  sample optimized for OH avoidance for  $H\alpha$  and the additional diagnostic lines of [NII], [OIII], and  $H\beta$ – one or more of these lines turned out to be significantly affected by a nearby OH line over some part of the galaxy, hampering full spatially-resolved analysis.

This work thus emphasizes how important the above considerations are for planning targets and strategies, and for exploiting the data from on-going and future near-infrared multi-object spectrographs and IFUs such as LUCIFER at the LBT, KMOS at the VLT, and MOSFIRE at Keck.

### **Evidence for significant spatial variations in line excitation mechanism, nebular oxygen abundances and/or extinction**

Of our sample of 12 galaxies with observations targeting multiple emission lines, 10 had sufficient S/N and little (3 objects) or no (7 objects) showed OH contamination for one or more of  $[\text{NII}]\lambda 6584$ ,  $[\text{OIII}]\lambda 5007$ , and  $\text{H}\beta$  to allow extraction of emission and kinematic maps. In general, the velocity fields and velocity dispersion maps are consistent with those derived from the (brighter) line of  $\text{H}\alpha$ . In terms of morphologies, noticeable differences between different emission lines were found in several cases, suggesting spatial variations in line excitation mechanism, nebular oxygen abundances and/or extinction.

### **The distribution of star-forming and AGN sources at $z\sim 2$ can be significantly offset from that of the bulk of local galaxies in the "BPT" line excitation diagram**

The emission line ratios of our sample of  $z\sim 2$  massive galaxies show a range of excitation, from ratios consistent with pure star-forming regions to high-excitation ratios indicative of an important contribution from AGN. For all our star-formation dominated sources we find an offset to higher  $[\text{OIII}]/\text{H}\beta$  compared to the mean  $[\text{OIII}]/\text{H}\beta$  for local SDSS galaxies at comparable  $[\text{NII}]/\text{H}\alpha$ . As such, our sample covers a similar area of the BPT diagram as other  $z\sim 1-3$  samples in other studies.

### **Diverse offset causes; AGN, different nebular conditions, and/or shocks**

A closer examination of the objects in our sample for which reliable line ratio maps and profiles could be extracted reveal that in some cases, the offset above the star-forming sequence of local SDSS galaxies can be due to the presence of a central AGN (sometimes of too low luminosity or too obscured to be identified in the rest-frame UV spectrum), with the magnitude of the offset reflecting the relative importance of star formation and AGN to the observed line emission. However, in other cases, our data resolved on scales of a few kpc indicate no sign for an AGN, such that the offset could be due to different nebular conditions (metallicity, ionization parameter, electron density) and/or contributions by shocks.

### **Mass-metallicity broadly consistent with previous studies; likely more dusty/metal rich objects in our sample**

Focussing on  $[\text{NII}]/\text{H}\alpha$  as metallicity indicator, our star-forming sample, augmented with the other non-AGN galaxies from the full SINS  $\text{H}\alpha$  sample, follows a similar mass-metallicity relation as reported previously at  $z\sim 2$  by Erb et al. (2006a). The only notable systematic difference is that at the high-mass end, our galaxies tend to lie at slightly higher metallicities than those of Erb et al. We cannot exclude that this could be due to a somewhat

more important contribution by low-luminosity or fairly obscured AGN unidentified even in our (mostly seeing-limited) data. However, our sample includes a larger proportion of objects selected from criteria less biased towards blue, mostly obscured  $z \sim 2$  galaxies compared to the Erb et al. (2006) sample. Consequently, a higher proportion of massive, dustier –hence likely more metal rich– objects in our sample could explain this difference as supported by the trends we find for the inferred oxygen abundance (and offset above the Erb relationship) with observed  $B - K$  color and  $A_V$  derived from SED modeling.

### **Our data are broadly consistent with the Fundamental Metallicity Relation**

Our  $[\text{NII}]/\text{H}\alpha$  based metallicities appear to be broadly consistent with a fundamental metallicity relation (FMR) relating  $M_*$ , SFR and metallicity as proposed by Mannucci et al. (2010). However the scatter in the data is, as for the mass-metallicity relation, very large.

### **Shallow, negative metallicity gradients; no evidence for positive gradients.**

Among the six objects for which we can extract reliable  $[\text{NII}]/\text{H}\alpha$  radial profiles, and excluding previously known AGN, we find no evidence for positive metallicity gradients, as has been reported in some  $z \sim 3$  and  $z \sim 1$  galaxies observed at similar (seeing-limited) resolution as our galaxies. In three cases, the negative gradients we measure may be biased towards steeper slopes by the possible presence of an AGN suggested by our  $[\text{NII}]/\text{H}\alpha$  maps. On the other hand, the significant beam-smearing of seeing-limited data may bias the observed gradients towards shallower slopes compared to intrinsic negative gradients. Higher S/N and resolution observations are necessary to overcome these limitations.

### **Evidence for extra attenuation towards HII regions, significant spatial extinction variations in one case study.**

From the Balmer decrement measured in six of our galaxies, we find evidence of possible extra attenuation towards HII regions with respect to the bulk of stars dominating the optical-near-IR SED, assuming that spatial variations in extinction across the objects can be neglected. Our best case object in terms of quality of spatially-resolved  $\text{H}\alpha$  and  $\text{H}\beta$  emission reveals however significant radial variations in  $\text{H}\alpha/\text{H}\beta$ , hence derived nebular extinction. The inferred extinction peaks at the center, which is also where the highest oxygen abundance and molecular gas concentration are inferred.

## 11.2. Outlook for future studies

SINS, and its extension with the zC-SINF sample, constitute is the largest integral field observation survey of high-redshift galaxies with  $z=1.5-2.5$  to date. More than 100 galaxies have been observed so far by our team in at least one emission line. Compared with local studies, however, the number of objects is still small and, for statistical analysis, data from many more objects over a wide range of galaxy properties are needed. Collecting IFU or even simply spectroscopic data for large samples in the high redshift universe is a very time consuming process as exposure times are of the order of several hours per target in the near-infrared where many key diagnostic –restframe optical– emission lines are redshifted to. Thus large NIR spectroscopic surveys can only be carried out efficiently using instruments that provide multi-object capabilities.

While no NIR multi-object integral-field spectrometer is commissioned yet (KMOS for the VLT is planned for commissioning in Fall 2012), multi-object slit-mask spectrometers, which provide 1D spectra, are now becoming available. With these instruments it is possible to obtain spatially-integrated data or limited resolution “cuts” across an object similar to the aperture data presented in this work. However, this comes with the important inherent limitation of slit-spectroscopy, i.e., slit losses. LUCIFER at the Large Binocular Telescope is one of three full cryogenic instruments at 8m class telescopes (the other two being MOIRCS at the Subaru telescope, MOSFIRE at Keck and FLAMINGOS-2 at Gemini-South) that are now on sky, delivering first data. There exists another instrument featuring a NIR multi-object unit, FMOS at Subaru, however this unit is non cryogenic and cannot be used for observations beyond  $2\mu\text{m}$  as the thermal background radiation becomes to high.

We aim to extend our SINS survey in two ways in the coming years. Obtaining large samples of spatially-integrated data with LUCIFER and –as soon as KMOS becomes available– spatially-resolved samples.

Our LUCIFER programs emphasize multi-line analysis from integrated or axis-profile ratios. First results on  $\sim 100$   $z\sim 1.5-2.5$  objects provide confirmation of those emerging from the more limited sample studied in this thesis on the distribution in the BPT diagram, mass-metallicity-star formation (M-Z-SFR) relationships, and nebular extinction (see section 5.5.1, figure 5.9, as well as Kurk et al., and Loose et al., in preparation).

The KMOS survey is being designed, with science goals taking advantage of the IFU capabilities (resolved kinematics amongst others). Results obtained as part of this thesis form a crucial basis in planning and exploiting these new surveys.

## Appendix A.

### Near-IR atmospheric OH line emission: origin and properties

OH airglow is the collective line emission from OH radicals in the Earth's atmosphere. These emission lines are prominent in the wavelength range of  $0.8 \lesssim \lambda \lesssim 2.4 \mu\text{m}$ , and are brightest and most numerous in the H band around  $1.5 \mu\text{m}$ . The emission is mainly caused by transitions with  $\Delta v = 2 - 5$  between vibrational states of the OH molecule. The lines are basically fine-structure doublets, triplets or quadruplets with an intrinsic line width of an individual line of  $\sim 0.1 \text{\AA}$  given a kinetic temperature around 220K. They originate in the upper atmosphere around an altitude of 87km as a product of reactions between hydrogen and ozone  $\text{H} + \text{O}_3 \rightarrow \text{OH}^* + \text{O}_2$ . Beyond  $\sim 2.4 \mu\text{m}$  the background is dominated by thermal emission (Baker et al. 1973, Oliva and Origlia 1992; Maihara et al. 1993; Osterbrock et al 1996; Rousselot et al. 2000; Ellis et al. 2008). For low resolution ( $R := \lambda/\Delta\lambda \lesssim 1000$ ) spectrographs only the P-branch lines (vibration-rotation transitions where  $\Delta J = -1$ ) can be resolved. Transitions with  $\Delta J = 0$  and  $\Delta J = 1$ , i.e. Q- and R-branch, are still blended together. To be able to resolve those blends and to look between the OH lines, thus getting more free spectral range where emission lines from astronomical objects can be observed and resolved, a spectral resolution of  $\gtrsim 3000$  is necessary.

The brightest OH lines in the H band have fluxes of the order of  $400 \text{ photons s}^{-1} \text{ m}^{-2} \text{ arcsec}^{-2}$  whilst the background continuum between these lines is only around  $600 \text{ photons s}^{-1} \text{ m}^{-2} \text{ arcsec}^{-2} \mu\text{m}^{-1}$ , as measured by Maihara et al. (1993). This implies the background on an OH line is 3 magnitudes higher than between them at  $R \sim 3000$ . Compared to the emission line fluxes of high-redshift galaxies as studied in this work, which are of the order  $10^{-16} \text{ W m}^2 \mu\text{m}^{-1}$ , the night-sky emission is brighter by a factor of  $\sim 100-1000$  than the objects.

Despite all the complications that arise from OH contamination, their presence in the spectra can also be put to scientific use: OH lines can serve as a wavelength calibration source, which is taken simultaneously with the observations of the astronomical source of interest. Extensive line lists have been compiled in the past (see e.g. Oliva 1991,

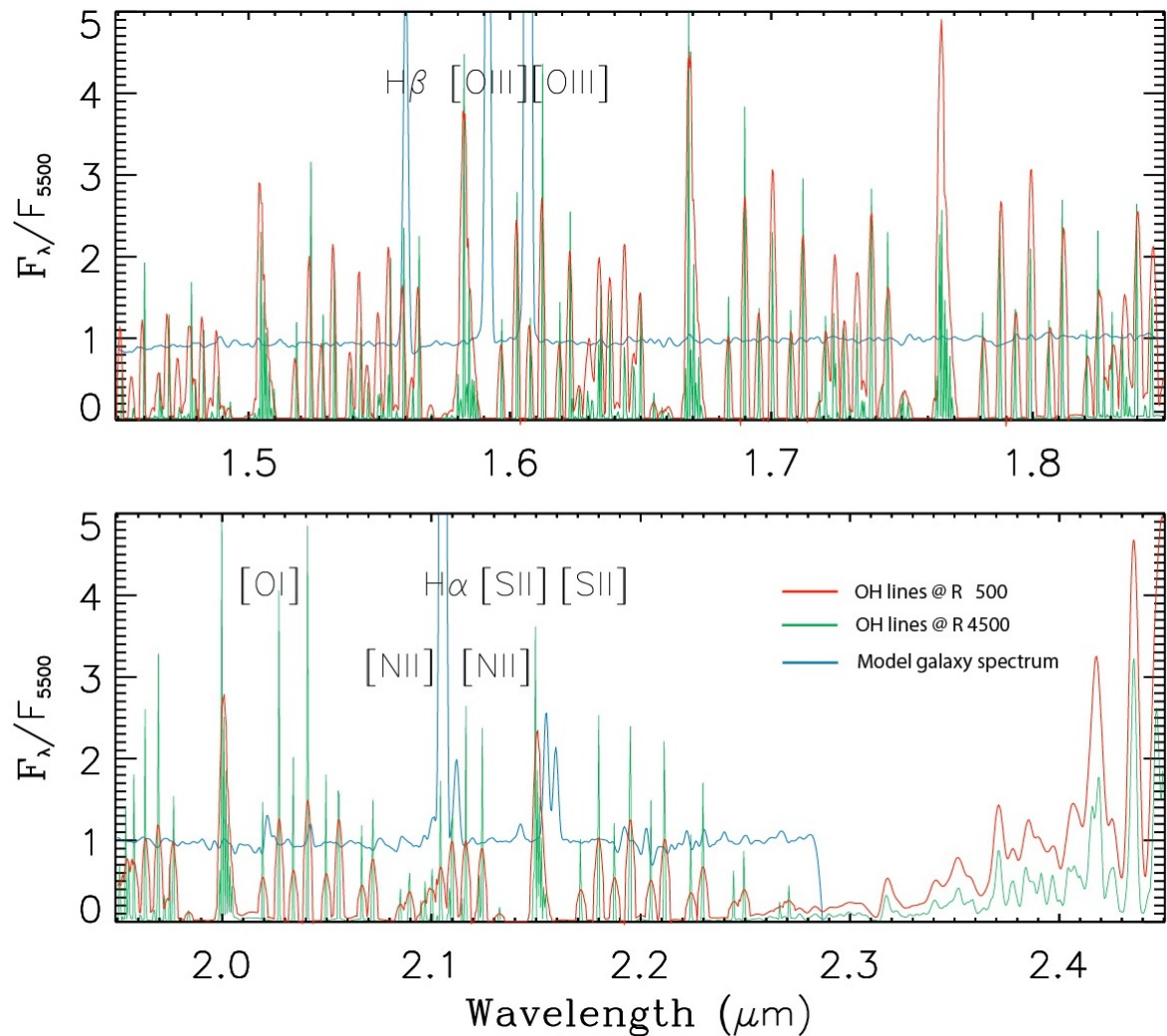


Figure A.1.: OH lines in the H and K band calculated for different spectral resolutions. Green: R=4500, red: R=500. A model galaxy spectrum at  $z=2.21$  is plotted in blue. At low resolution the OH lines blend together making it impossible to discern individual lines.

Maihara 1993, Rousselot 2000) listing approximately 100 bright OH lines that can be used for robust calibration purposes in the wavelength interval 1-2.2  $\mu\text{m}$ . The use of the OH lines in the science data themselves allows one to achieve higher accuracy in the wavelength calibration since subtle changes due, e.g., to instrument flexure from one exposure to the next can be tracked precisely.

## Appendix B.

### Plots - Apertures and Annuli used for the radial and axis profiles in emission line ratios

On the following pages, we show the detailed analysis plots behind the metallicity gradients presented in table 9.5 and in figures 9.11 and 9.12.

For each source, the left column shows the measurements and apertures along the minor and major axis, the right column shows those in concentric annuli. In each column we show (from top to bottom)  $H\alpha$  and  $[\text{NII}]\lambda 6584$  flux, the  $[\text{NII}]/H\alpha$  ratio and gradient, the placement of the extraction regions on top of the  $H\alpha$  flux map, and overlaid the  $H\alpha$  based velocity map.

In the flux plots, the major axis flux is shown as a solid line, the minor axis flux as a dotted line. For the concentric annuli, we plot the flux per  $\text{kpc}^2$ . Black symbols and lines correspond to  $H\alpha$ , green to  $[\text{NII}]$ .

The  $[\text{NII}]/H\alpha$  plots give the  $[\text{NII}]/H\alpha$  ratios in the corresponding regions. For the regions, for which only a limit could be derived, the  $3\sigma$  limit is given. The source-integrated metallicity is indicated as a solid orange horizontal line. Solar and half-solar metallicity is plotted for reference.

In the plots showing the extraction regions on the maps, the apertures along the minor and major axis are labeled M (major) and (m) minor in the corresponding leftmost region (most negative offset from the galaxy center). The  $H\alpha$  flux intensity is shown by the color image and the  $[\text{NII}]$  flux is overlaid as contours. We indicate the size of the PSF as well as the physical scale with a 8kpc (seeing-limited data) and 1kpc stick (AO data) for reference.

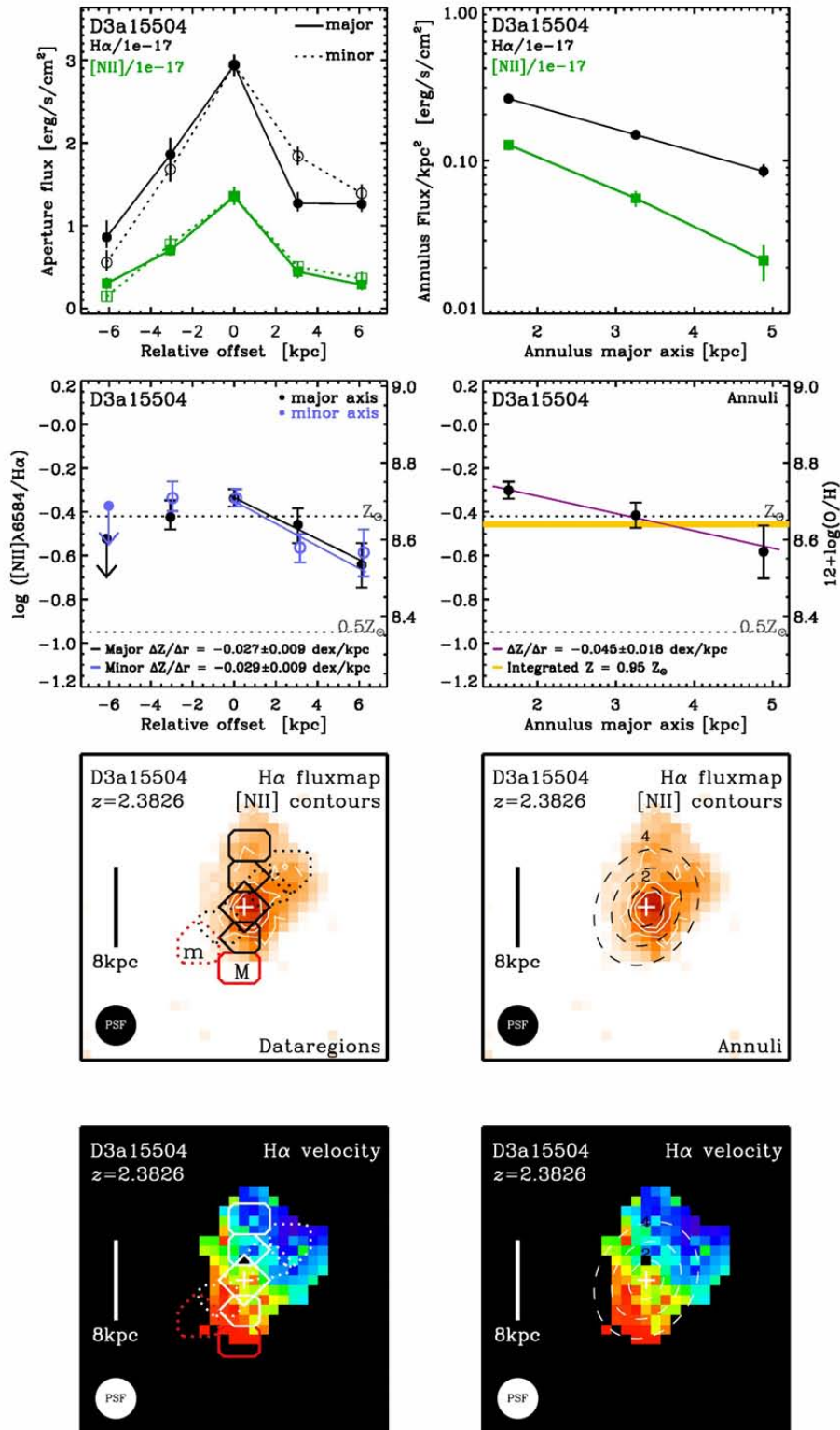


Figure B.1.: H $\alpha$  and [NII] $\lambda$ 6584 emission line fluxes and N2 metallicity in major and minor axis apertures and concentric annuli for D3a-15504.

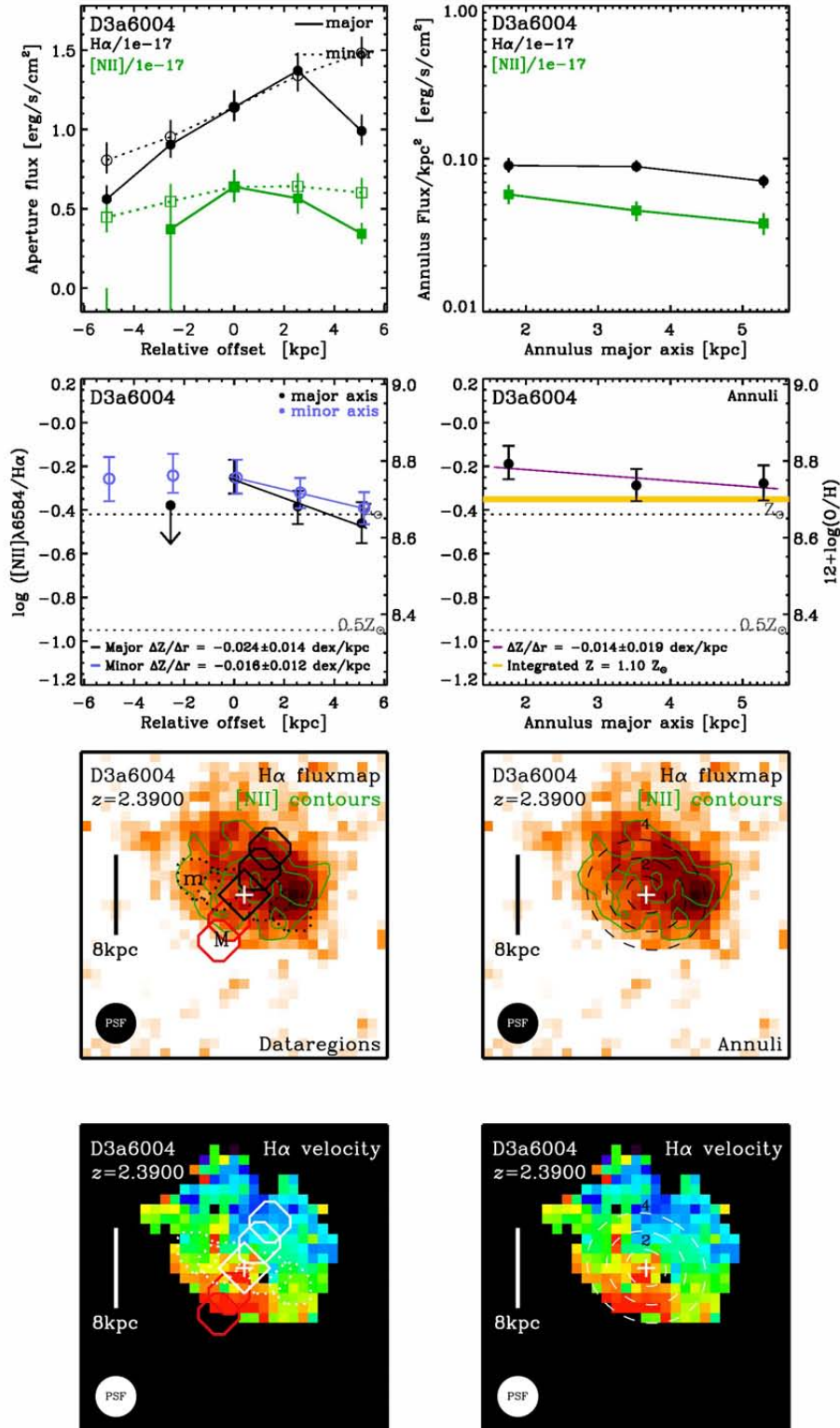


Figure B.2.:  $H\alpha$  and  $[NII]\lambda 6584$  emission line fluxes and  $N2$  metallicity in major and minor axis apertures and concentric annuli for D3a-6004. Details see text.

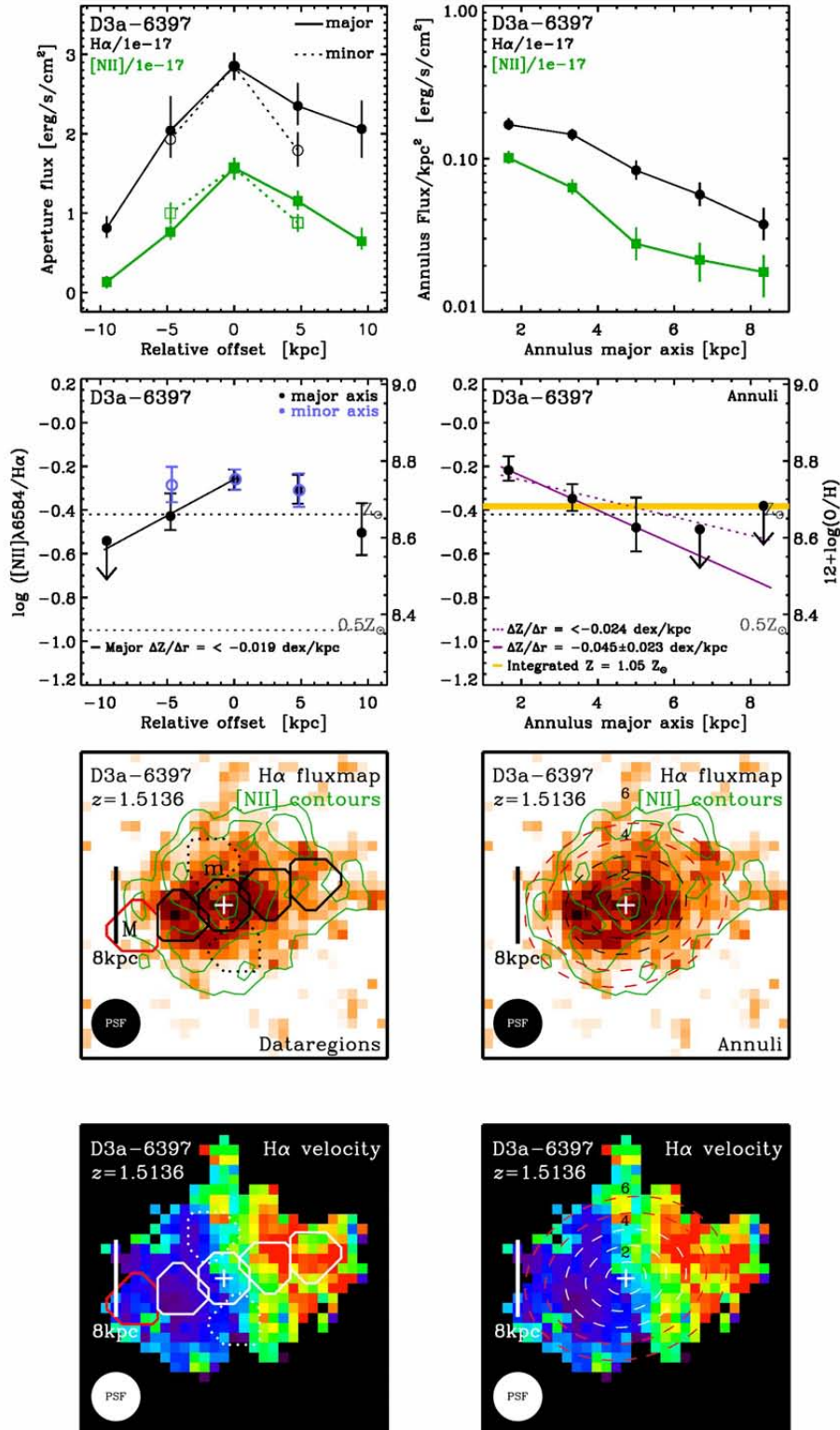


Figure B.3.: H $\alpha$  and [NII] $\lambda$ 6584 emission line fluxes and N2 metallicity in major and minor axis apertures and concentric annuli for D3a-6397. Details see text.

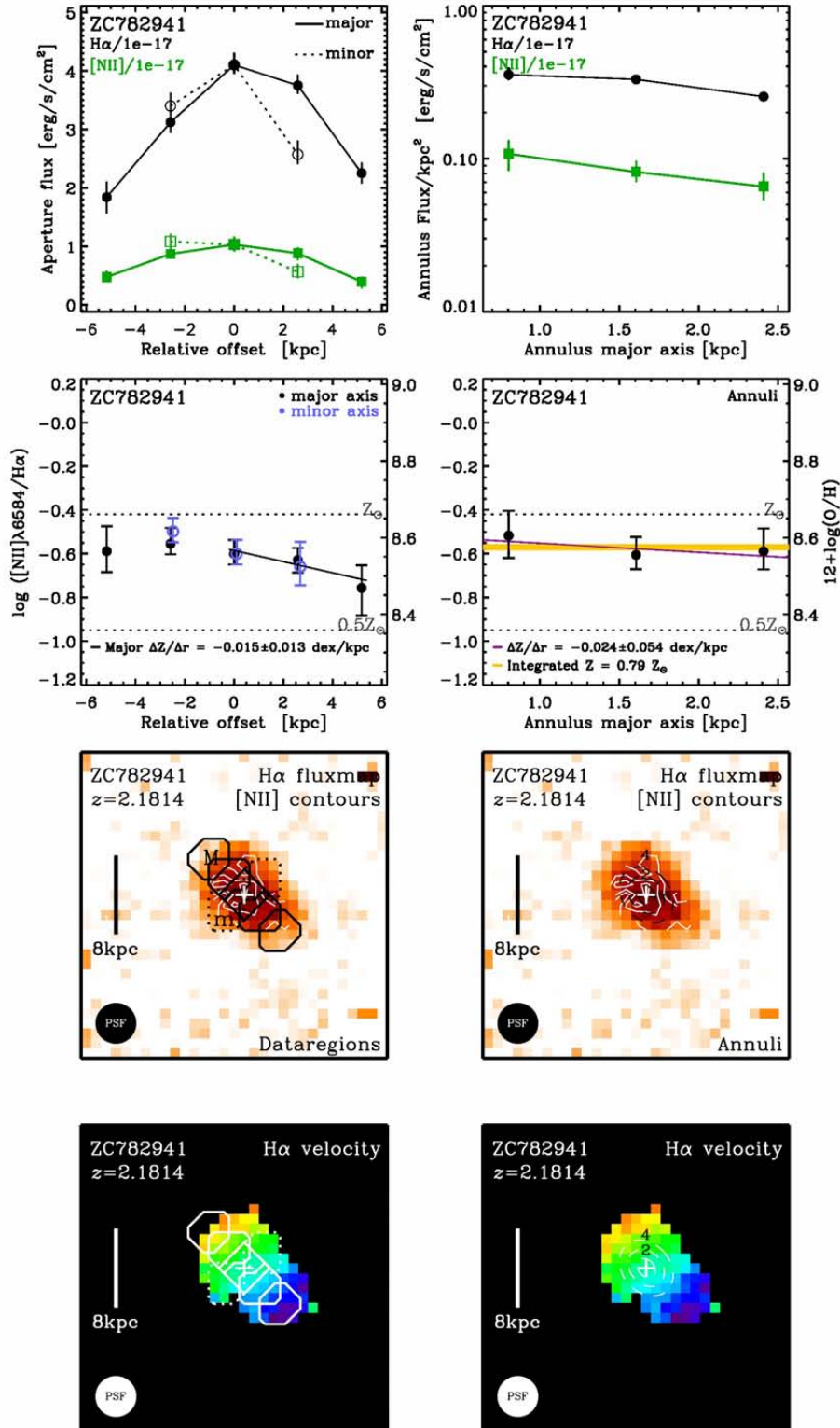


Figure B.4.: H $\alpha$  and [NII] $\lambda$ 6584 emission line fluxes and N2 metallicity in major and minor axis apertures and concentric annuli for ZC782941. Details see text.

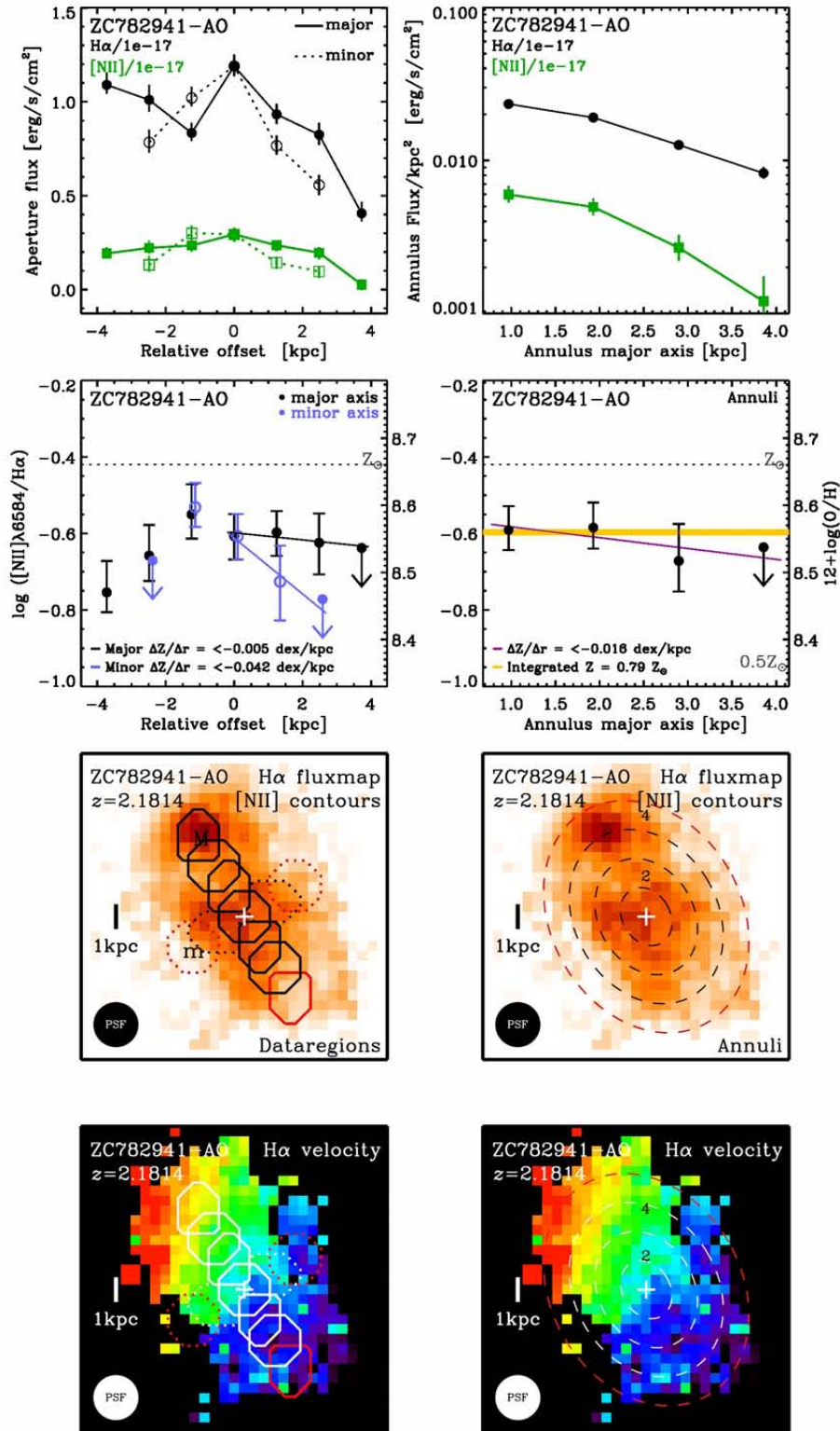


Figure B.5.: H $\alpha$  and [NII] $\lambda$ 6584 emission line fluxes and N2 metallicity in major and minor axis apertures and concentric annuli for ZC782941 AO Scale. Details see text.

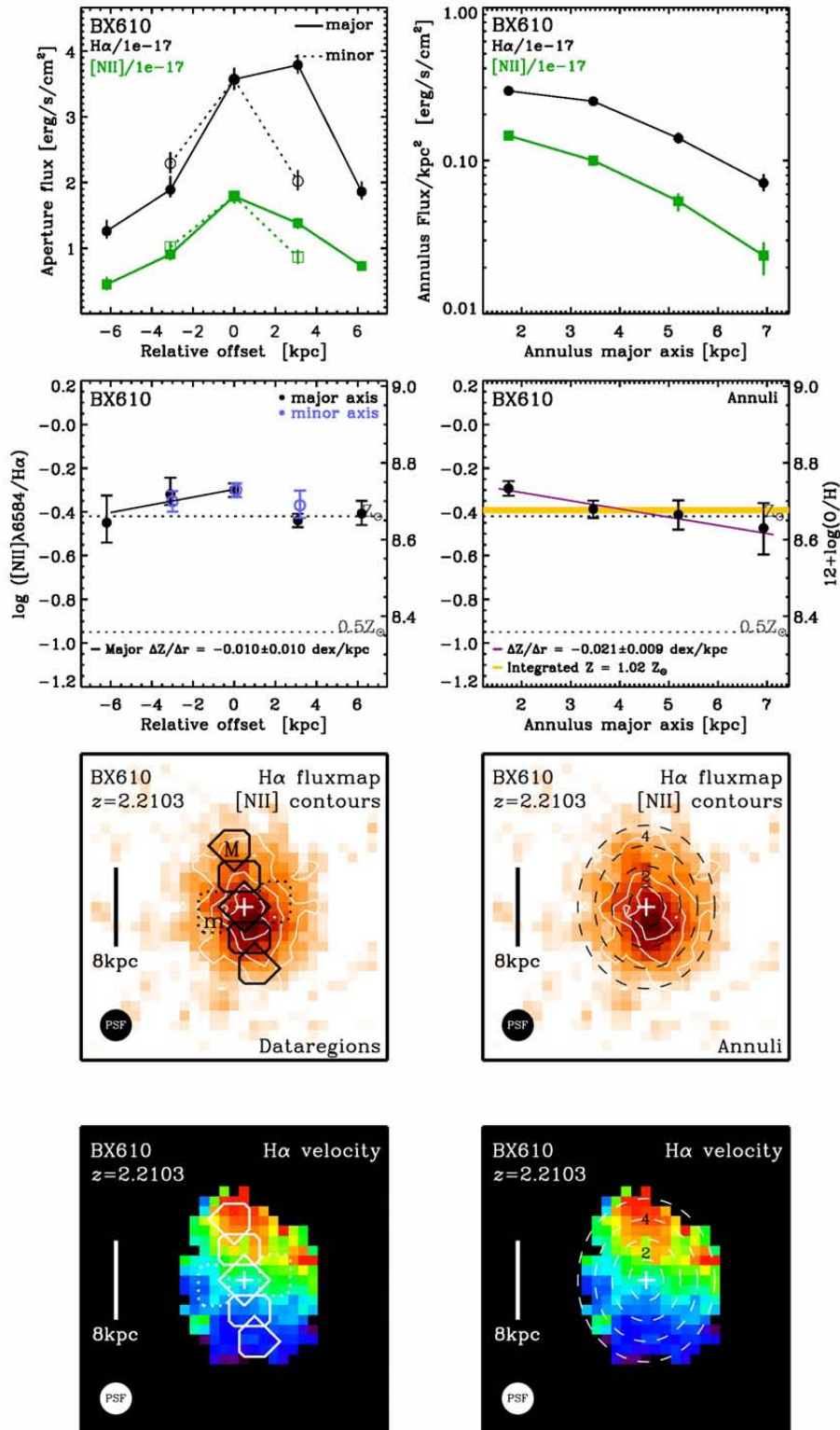


Figure B.6.: H $\alpha$  and [NII] $\lambda$ 6584 emission line fluxes and N2 metallicity in major and minor axis apertures and concentric annuli for BX610. Details see text.

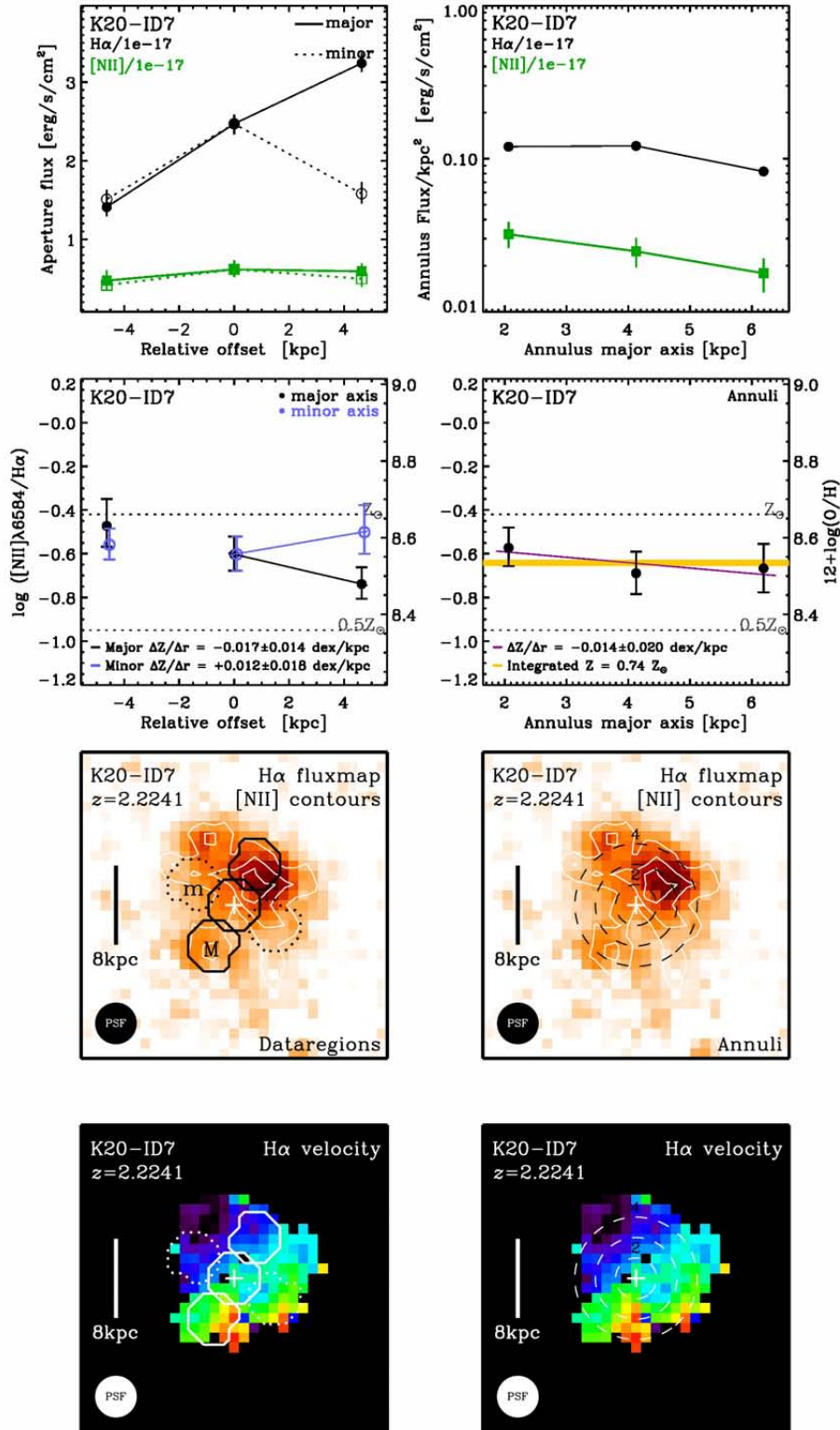


Figure B.7.: H $\alpha$  and [NII] $\lambda$ 6584 emission line fluxes and N2 metallicity in major and minor axis apertures and concentric annuli for ID7. Details see text.

## Appendix C.

### Adaptive Optics

Ground-based astronomy faces a major challenge if one wants to carry out observations with the full resolving power of an optical / near-IR instrument at large telescopes. The theoretical resolution of an optical system is defined by  $\Theta = 1.22\lambda/D$  where  $D$  is the diameter of the optical aperture. It is the angular radius of the first minimum in the Airy disc, the PSF in the case of a circular aperture and a point source at infinity. The FWHM of the central Airy profile is  $\Theta' = 0.98\lambda/D$ . For the VLT ( $D=8.2\text{m}$ ) the theoretical FWHM is  $0.054''$  at  $\lambda=2.2\text{micron}$ .

However, circulation and turbulence in the Earth's atmosphere distort the position and change the amplitude and phase of electromagnetic waves from the observed astronomical objects on timescales of milliseconds, an effect known as 'seeing'. This turbulence severely limits the achievable resolution to  $\lambda/r_0 \approx 1''$ , where  $r_0$  is the Fried parameter defined as the expected diameter over which the RMS of the phase distortion is 1rad. It is as such a measure of how large a segment of the wavefront can be treated as a plane wave, thus describing the diameter of a typical turbulence cell in the atmosphere. At 2.2 micron and for average observing conditions  $r_0$  is around 60cm. Under good to excellent observing conditions  $r_0$  can grow to  $\gtrsim 1\text{m}$ , leading to a FWHM of  $\sim 0.3\text{-}0.5''$  in the near-infrared. The value of  $r_0$  scales with wavelength as  $\lambda^{6/5}$ . With  $\text{FWHM} = 0.98 \lambda/D$  and replacing  $D$  by  $r_0$  one gets the dependence of the seeing on the observed wavelength. The seeing and thus the effective FWHM resolution scales with  $\lambda^{-1/5}$ . It is therefore slightly better in the NIR compared to visual wavelengths.

To partly overcome this limitation caused by the atmosphere, different techniques summarized under the name speckle imaging have been introduced. The distorted wavefront produced by the atmosphere can be approximated by a combination of different plane wavefronts each of which produces an Airy disk in the focal plane. The collection of Airy disks of all sub-wavefronts is the speckle pattern with the number of individual speckles being proportional to  $(D/r_0)^2$ . The pattern is dynamically changing due to the varying turbulence but can be frozen out with exposure times  $< 1/20\text{s}$ . In the shift-and-add technique, the individual speckle pattern exposures are mutually aligned by the bright-

est speckle and averaged. Combined with 'Lucky Imaging', i.e. selecting only the best  $\sim 10\%$  of the exposures, this technique can result in a near-diffraction limited quality image (e.g. Hofmann et al. 1995; Law et al. 2006).

Adaptive optics systems in turn correct the distorted wavefront itself in real time using deformable mirrors in the optical path. To analyze the incoming wavefront and to determine the correction that needs to be applied to the wavefront, a bright point source (e.g. nearby star) is observed using a wavefront sensor. The deformable mirror is driven in such a way that the incoming wavefront is artificially distorted in order to cancel out the distortion created by the atmospheric turbulence by varying the optical path length across the spatial extent of the incoming wavefront.

The rate at which the wavefront needs to be corrected is defined by the parameter  $\tau_0$ . It is the atmospheric time constant, defined as  $\tau_0 = 0.314 r_0/v$ , where  $v$  is the wind velocity averaged over the altitude. It stems from the simplified model of turbulence as fixed phase screens that are driven across the telescope aperture by wind. The performance of an AO system can be quantified by the Strehl ratio  $R_s$ . It is defined as the ratio of the central intensity of a PSF to the central intensity of the Airy function for the same source. For a perfect AO system  $R_s=1$ . Typical values that have been achieved in the NIR are  $R_s \sim 0.3$ . The distance between the science object and the star used for measuring the wavefront is limited. Their maximum separation is given by the isoplanatic angle  $\theta_0 = 0.314 r_0 \cos(\gamma)/\bar{h}$ , which is the largest angle for which the distortions differ by less than 1rad.  $\bar{h}$  is a characteristic average turbulence height and  $\gamma$  the angular distance of the object from zenith. The averaging for the height is done by weighting the refractive index structure constant  $C_n^2(h)$  with  $h^{5/3}$ . For small  $\theta$  the phase distortion for reference star and science object do not differ too much, but for  $\theta_0 \geq r_0/h$ , the phase distortions will be uncorrelated.

Since the probability of finding a suitable wavefront reference star within the isoplanatic angle is of the order of 1%, artificial guide stars projected by a laser system into the atmosphere have been developed. Since a laser guide star (LGS) can be placed arbitrarily near the object and is bright ( $\sim 12$ - $13$ mag), the probability of achieving a good AO correction rises significantly. However, the AO correction with laser guide stars is different from that using natural guide stars: the tip-tilt component can not be derived, since the laser is launched from ground and thus the light travels up and down through the atmosphere. This eliminates the displacement component of the laser guide star while the astronomical science object is still displaced by the atmospheric turbulence. A close-by Tip-Tilt reference star (TTS) needs to be observed in addition to the laser guide star to correct for the tip-tilt component. Another important limitation when using an LGS is induced by the cone-effect: because of the focus anisoplanatism, the LGS is not projected to infinity but to a distance of about 70 km into the atmosphere's sodium layer, and the cross section of the atmospheric turbulence that is sampled by the LGS is cone-shaped. The light from the science source, however, originates from infinity and thus the atmo-

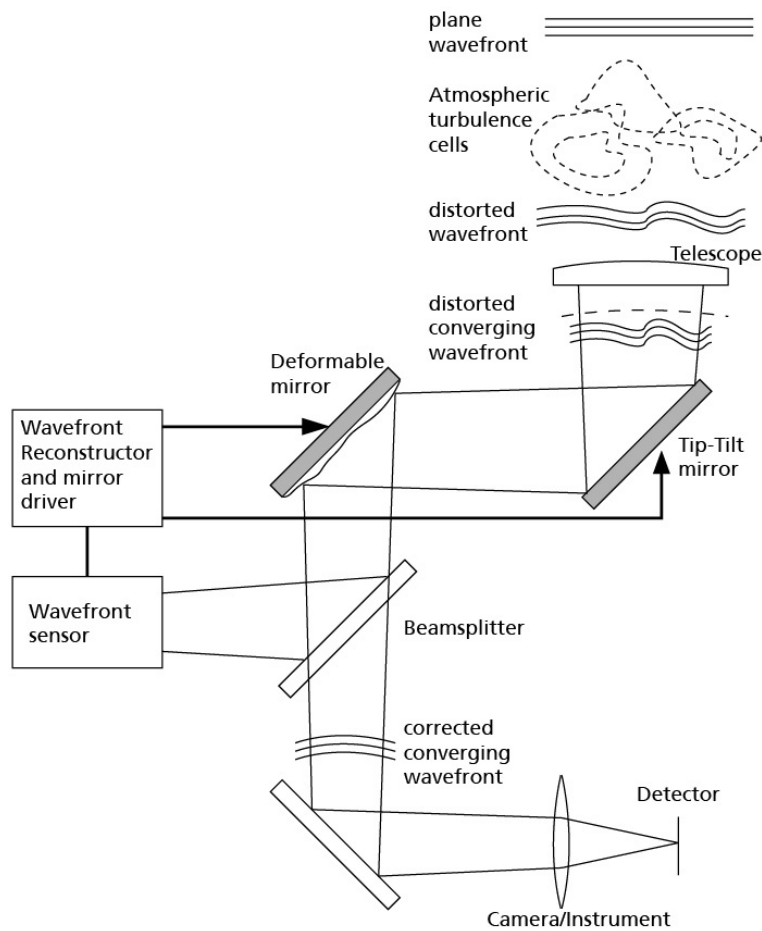


Figure C.1.: Block diagram of an adaptive optics (AO) system

spheric cross section is a cylinder with the diameter corresponding to the diameter of the primary telescope mirror. Therefore not all distortions of the science light wavefront are sampled. This leads to a phase-estimation error, which reduces the accuracy of the wavefront correction. The induced phase error in LGS mode is roughly equivalent to the error present when the NGS is  $10''$  away from the object, which is in H band already near to the edge of the circle described by the isoplanatic angle.



# Bibliography

- [1] R. Abuter et al. "SINFONI data reduction software". In: *New A Rev.* 50 (June 2006), pp. 398–400.
- [2] K. L. Adelberger et al. "Galaxies and Intergalactic Matter at Redshift  $z \sim 3$ : Overview". In: *ApJ* 584 (Feb. 2003), pp. 45–75.
- [3] V. L. Afanasiev et al. "Study of Central Regions of AGNs at 6-meter Telescope". In: *IAU Colloq. 149: Tridimensional Optical Spectroscopic Methods in Astrophysics*. Ed. by G. Comte & M. Marcelin. Vol. 71. Astronomical Society of the Pacific Conference Series. 1995, p. 261.
- [4] J. Afonso et al. "Dependence of Dust Obscuration on Star Formation Rates in Galaxies". In: *ApJ* 597 (Nov. 2003), pp. 269–273.
- [5] N. Ageorges et al. "LUCIFER1 commissioning at the LBT". In: *Society of Photo-Optical Instrumentation Engineers (SPIE) Conference Series*. Vol. 7735. Society of Photo-Optical Instrumentation Engineers (SPIE) Conference Series. July 2010.
- [6] O. Agertz, R. Teyssier, and B. Moore. "Disc formation and the origin of clumpy galaxies at high redshift". In: *MNRAS* 397 (July 2009), pp. L64–L68.
- [7] C. W. Allen. *Astrophysical Quantities*. 1976.
- [8] M. G. Allen et al. "The MAPPINGS III Library of Fast Radiative Shock Models". In: *ApJS* 178 (Sept. 2008), pp. 20–55.
- [9] J. Allington-Smith et al. "Integral Field Spectroscopy with the Gemini Multiobject Spectrograph. I. Design, Construction, and Testing". In: *PASP* 114 (Aug. 2002), pp. 892–912.
- [10] P. Amico, J. W. Beletic, and J. E. Beletic, eds. *Scientific detectors for astronomy : the beginning of a new era*. Vol. 300. Astrophysics and Space Science Library. 2004.
- [11] R. Antonucci. "Unified models for active galactic nuclei and quasars". In: *ARA&A* 31 (1993), pp. 473–521.
- [12] M. Asplund et al. "Line formation in solar granulation. IV. [O I], O I and OH lines and the photospheric O abundance". In: *A&A* 417 (Apr. 2004), pp. 751–768.
- [13] M. Aumer et al. "The Structure of Gravitationally Unstable Gas-rich Disk Galaxies". In: *ApJ* 719 (Aug. 2010), pp. 1230–1243.
- [14] R. Bacon et al. "The SAURON project - I. The panoramic integral-field spectrograph". In: *MNRAS* 326 (Sept. 2001), pp. 23–35.
- [15] D. J. Baker, A. J. Steed, and A. T. Stair Jr. "Ground observations of resolved hydroxyl ( $\Delta$   $\epsilon = 2$ ) airglow." In: *J. Geophys. Res.* 78 (1973), pp. 8859–8863.
- [16] J. A. Baldwin, M. M. Phillips, and R. Terlevich. "Classification parameters for the emission-line spectra of extragalactic objects". In: *PASP* 93 (Feb. 1981), pp. 5–19.
- [17] C. M. Baugh. "A primer on hierarchical galaxy formation: the semi-analytical approach". In: *Reports on Progress in Physics* 69 (Dec. 2006), pp. 3101–3156.
- [18] E. F. Bell and R. C. Kennicutt Jr. "A Comparison of Ultraviolet Imaging Telescope Far-Ultraviolet and  $H\alpha$  Star Formation Rates". In: *ApJ* 548 (Feb. 2001), pp. 681–693.

## Bibliography

---

- [19] E. F. Bell et al. "Nearly 5000 Distant Early-Type Galaxies in COMBO-17: A Red Sequence and Its Evolution since  $z \sim 1$ ". In: *ApJ* 608 (June 2004), pp. 752–767.
- [20] E. Bertschinger. "Simulations of Structure Formation in the Universe". In: *ARA&A* 36 (1998), pp. 599–654.
- [21] L. Binette et al. "Photoionization in elliptical galaxies by old stars". In: *A&A* 292 (Dec. 1994), pp. 13–19.
- [22] D. S. Birney, G. Gonzalez, and D. Oesper. *Observational Astronomy - 2nd Edition*. June 2006.
- [23] G. R. Blumenthal et al. "Formation of galaxies and large-scale structure with cold dark matter". In: *Nature* 311 (Oct. 1984), pp. 517–525.
- [24] H. Bonnet et al. "First light of SINFONI at the VLT". In: *The Messenger* 117 (Sept. 2004), pp. 17–24.
- [25] N. Bouché et al. "Dynamical Properties of  $z \sim 2$  Star-forming Galaxies and a Universal Star Formation Relation". In: *ApJ* 671 (Dec. 2007), pp. 303–309.
- [26] F. Bournaud, B. G. Elmegreen, and D. M. Elmegreen. "Rapid Formation of Exponential Disks and Bulges at High Redshift from the Dynamical Evolution of Clump-Cluster and Chain Galaxies". In: *ApJ* 670 (Nov. 2007), pp. 237–248.
- [27] R. J. Bouwens et al. "UV Continuum Slope and Dust Obscuration from  $z \sim 6$  to  $z \sim 2$ : The Star Formation Rate Density at High Redshift". In: *ApJ* 705 (Nov. 2009), pp. 936–961.
- [28] R. J. Bouwens and G. D. Illingworth. "Very Blue UV-Continuum Slopes of Star-Forming Galaxies at  $z \sim 7$  and the Evolution to  $z \sim 2-4$ ". In: *American Institute of Physics Conference Series*. Ed. by D. J. Whalen, V. Bromm, & N. Yoshida. Vol. 1294. American Institute of Physics Conference Series. Nov. 2010, pp. 208–210.
- [29] J. Brinchmann, M. Pettini, and S. Charlot. "New insights into the stellar content and physical conditions of star-forming galaxies at  $z = 2-3$  from spectral modelling". In: *MNRAS* 385 (Apr. 2008), pp. 769–782.
- [30] J. Brinchmann et al. "The physical properties of star-forming galaxies in the low-redshift Universe". In: *MNRAS* 351 (July 2004), pp. 1151–1179.
- [31] J. P. Brodie and J. P. Huchra. "Extragalactic globular clusters. III - Metallicity comparisons and anomalies". In: *ApJ* 379 (Sept. 1991), pp. 157–167.
- [32] G. Bruzual and S. Charlot. "Stellar population synthesis at the resolution of 2003". In: *MNRAS* 344 (Oct. 2003), pp. 1000–1028.
- [33] P. Buschkamp et al. "The LUCIFER MOS: a full cryogenic mask handling unit for a near-infrared multi-object spectrograph". In: *Society of Photo-Optical Instrumentation Engineers (SPIE) Conference Series*. Vol. 7735. Society of Photo-Optical Instrumentation Engineers (SPIE) Conference Series. July 2010.
- [34] F. Calura et al. "The evolution of the mass-metallicity relation in galaxies of different morphological types". In: *A&A* 504 (Sept. 2009), pp. 373–388.
- [35] D. Calzetti. "Measuring star formation in local and distant galaxies". In: *Nuovo Cimento B Serie* 122 (Sept. 2007), pp. 971–976.
- [36] D. Calzetti. "Reddening and Star Formation in Starburst Galaxies". In: *AJ* 113 (Jan. 1997), pp. 162–184.
- [37] D. Calzetti. "Star Formation and Starburst Galaxies in the Infrared". In: *American Astronomical Society Meeting Abstracts*. Vol. 33. Bulletin of the American Astronomical Society. Dec. 2001, p. 111.07.
- [38] D. Calzetti, A. L. Kinney, and T. Storchi-Bergmann. "Dust extinction of the stellar continua in starburst galaxies: The ultraviolet and optical extinction law". In: *ApJ* 429 (July 1994), pp. 582–601.

- [39] D. Calzetti, A. L. Kinney, and T. Storchi-Bergmann. "Dust Obscuration in Starburst Galaxies from Near-Infrared Spectroscopy". In: *ApJ* 458 (Feb. 1996), p. 132.
- [40] D. Calzetti et al. "The Dust Content and Opacity of Actively Star-forming Galaxies". In: *ApJ* 533 (Apr. 2000), pp. 682–695.
- [41] E. Cameron et al. "Bars in early- and late-type discs in COSMOS". In: *MNRAS* 409 (Nov. 2010), pp. 346–354.
- [42] J. A. Cardelli, G. C. Clayton, and J. S. Mathis. "The relationship between infrared, optical, and ultraviolet extinction". In: *ApJ* 345 (Oct. 1989), pp. 245–256.
- [43] N. Cardiel et al. "A Multiwavelength Approach to the Star Formation Rate Estimation in Galaxies at Intermediate Redshifts". In: *ApJ* 584 (Feb. 2003), pp. 76–99.
- [44] D. Ceverino, A. Dekel, and F. Bournaud. "High-redshift clumpy discs and bulges in cosmological simulations". In: *MNRAS* 404 (June 2010), pp. 2151–2169.
- [45] D. Ceverino et al. "Rotational support of giant clumps in high- $z$  disc galaxies". In: *MNRAS* 420 (Mar. 2012), pp. 3490–3520.
- [46] D. Ceverino and A. Klypin. "The Role of Stellar Feedback in the Formation of Galaxies". In: *ApJ* 695 (Apr. 2009), pp. 292–309.
- [47] S. C. Chapman et al. "A Redshift Survey of the Submillimeter Galaxy Population". In: *ApJ* 622 (Apr. 2005), pp. 772–796.
- [48] C. Chiappini, F. Matteucci, and D. Romano. "Abundance Gradients and the Formation of the Milky Way". In: *ApJ* 554 (June 2001), pp. 1044–1058.
- [49] C. Chiappini, F. Matteucci, and R. Gratton. "The Chemical Evolution of the Galaxy: The Two-Infall Model". In: *ApJ* 477 (Mar. 1997), p. 765.
- [50] P. I. Choi et al. "Star Formation Rates and Extinction Properties of IR-luminous Galaxies in the Spitzer First Look Survey". In: *ApJ* 637 (Jan. 2006), pp. 227–241.
- [51] Frederick R. Chromey. *To Measure the Sky*. Cambridge University Press, 2010.
- [52] R. Cid Fernandes et al. "Semi-empirical analysis of Sloan Digital Sky Survey galaxies - I. Spectral synthesis method". In: *MNRAS* 358 (Apr. 2005), pp. 363–378.
- [53] C. J. Conselice et al. "The Hubble Space Telescope GOODS NICMOS Survey: overview and the evolution of massive galaxies at  $1.5 < z < 3$ ". In: *MNRAS* 413 (May 2011), pp. 80–100.
- [54] R. Content. "New design for integral field spectroscopy with 8-m telescopes". In: *Society of Photo-Optical Instrumentation Engineers (SPIE) Conference Series*. Ed. by A. L. Ardeberg. Vol. 2871. Society of Photo-Optical Instrumentation Engineers (SPIE) Conference Series. Mar. 1997, pp. 1295–1305.
- [55] T. Contini et al. "MASSIV: Mass Assembly Survey with SINFONI in VVDS. I. Survey description and global properties of the  $0.9 < z < 1.8$  galaxy sample". In: *A&A* 539, A91 (Mar. 2012), A91.
- [56] G. Courtes. "An Integral Field Spectrograph (IFS) for Large Telescopes". In: *IAU Colloq. 67: Instrumentation for Astronomy with Large Optical Telescopes*. Ed. by C. M. Humphries. Vol. 92. Astrophysics and Space Science Library. 1982, p. 123.
- [57] G. Cresci et al. "Galaxy morphology and evolution from SWAN adaptive optics imaging". In: *A&A* 458 (Nov. 2006), pp. 385–396.
- [58] G. Cresci et al. "Gas accretion as the origin of chemical abundance gradients in distant galaxies". In: *Nature* 467 (Oct. 2010), pp. 811–813.
- [59] G. Cresci et al. "The SINS Survey: Modeling the Dynamics of  $z \sim 2$  Galaxies and the High- $z$  Tully-Fisher Relation". In: *ApJ* 697 (May 2009), pp. 115–132.

## Bibliography

---

- [60] E. Daddi et al. "A New Photometric Technique for the Joint Selection of Star-forming and Passive Galaxies at  $1.4 < z < 2.5$ ". In: *ApJ* 617 (Dec. 2004), pp. 746–764.
- [61] E. Daddi et al. "Multiwavelength Study of Massive Galaxies at  $z \sim 2$ . I. Star Formation and Galaxy Growth". In: *ApJ* 670 (Nov. 2007), pp. 156–172.
- [62] E. Daddi et al. "Very High Gas Fractions and Extended Gas Reservoirs in  $z = 1.5$  Disk Galaxies". In: *ApJ* 713 (Apr. 2010), pp. 686–707.
- [63] R. Davé, K. Finlator, and B. D. Oppenheimer. "Galaxy evolution in cosmological simulations with outflows - II. Metallicities and gas fractions". In: *MNRAS* 416 (Sept. 2011), pp. 1354–1376.
- [64] R. I. Davies. "A method to remove residual OH emission from near-infrared spectra". In: *MNRAS* 375 (Mar. 2007), pp. 1099–1105.
- [65] M. Davis et al. "The evolution of large-scale structure in a universe dominated by cold dark matter". In: *ApJ* 292 (May 1985), pp. 371–394.
- [66] A. Dekel et al. "Cold streams in early massive hot haloes as the main mode of galaxy formation". In: *Nature* 457 (Jan. 2009), pp. 451–454.
- [67] A. Dekel and Y. Birnboim. "Galaxy bimodality due to cold flows and shock heating". In: *MNRAS* 368 (May 2006), pp. 2–20.
- [68] G. Denicoló, R. Terlevich, and E. Terlevich. "New light on the search for low-metallicity galaxies - I. The N2 calibrator". In: *MNRAS* 330 (Feb. 2002), pp. 69–74.
- [69] P. Di Matteo et al. "On the survival of metallicity gradients to major dry-mergers". In: *A&A* 499 (May 2009), pp. 427–437.
- [70] A. I. Diaz, B. E. J. Pagel, and I. R. G. Wilson. "Chemical abundances and the ionisation mechanisms in LINERs". In: *Active Galactic Nuclei*. 1985, pp. 171–177.
- [71] A. I. Diaz, B. E. J. Pagel, and I. R. G. Wilson. "The intensities of the sulphur III lines and the ionization mechanisms in Liners". In: *MNRAS* 212 (Feb. 1985), pp. 737–749.
- [72] S. Dib, E. Bell, and A. Burkert. "The Supernova Rate-Velocity Dispersion Relation in the Interstellar Medium". In: *ApJ* 638 (Feb. 2006), pp. 797–810.
- [73] M. A. Dopita. "Optical Emission from Shock Waves. II. Diagnostic Diagrams". In: *ApJS* 33 (Apr. 1977), p. 437.
- [74] M. A. Dopita et al. "Are the Narrow-Line Regions in Active Galaxies Dusty and Radiation Pressure Dominated?" In: *ApJ* 572 (June 2002), pp. 753–761.
- [75] M. A. Dopita and R. S. Sutherland. *Astrophysics of the diffuse universe*. 2003.
- [76] M. A. Dopita and S. D. Ryder. "On the law of star formation in disk galaxies". In: *ApJ* 430 (July 1994), pp. 163–178.
- [77] M. A. Dopita and R. S. Sutherland. "Spectral Signatures of Fast Shocks. I. Low-Density Model Grid". In: *ApJS* 102 (Jan. 1996), p. 161.
- [78] M. A. Dopita and R. S. Sutherland. "Spectral Signatures of Fast Shocks. II. Optical Diagnostic Diagrams". In: *ApJ* 455 (Dec. 1995), p. 468.
- [79] B. T. Draine and C. F. McKee. "Theory of interstellar shocks". In: *ARA&A* 31 (1993), pp. 373–432.
- [80] M. Dubbeldam et al. "Integral field unit for the Gemini near-infrared spectrograph". In: *Society of Photo-Optical Instrumentation Engineers (SPIE) Conference Series*. Ed. by M. Iye & A. F. Moorwood. Vol. 4008. Society of Photo-Optical Instrumentation Engineers (SPIE) Conference Series. Aug. 2000, pp. 1181–1192.
- [81] R. J. Dufour et al. "M83 II: Spectral characteristics and chemical abundances of H II regions". In: *ApJ* 236 (Feb. 1980), pp. 119–121.

- [82] M. G. Edmunds. "General Constraints on the Effect of Gas Flows in the Chemical Evolution of Galaxies". In: *MNRAS* 246 (Oct. 1990), p. 678.
- [83] S. S. Eikenberry et al. "FLAMINGOS-2: the facility near-infrared wide-field imager and multi-object spectrograph for Gemini". In: *Society of Photo-Optical Instrumentation Engineers (SPIE) Conference Series*. Ed. by A. F. M. Moorwood and M. Iye. Vol. 5492. Society of Photo-Optical Instrumentation Engineers (SPIE) Conference Series. Sept. 2004, pp. 1196–1207.
- [84] F. Eisenhauer et al. "SINFONI - Integral field spectroscopy at 50 milli-arcsecond resolution with the ESO VLT". In: *Society of Photo-Optical Instrumentation Engineers (SPIE) Conference Series*. Ed. by M. Iye & A. F. M. Moorwood. Vol. 4841. Society of Photo-Optical Instrumentation Engineers (SPIE) Conference Series. Mar. 2003, pp. 1548–1561.
- [85] F. Eisenhauer et al. "The Universe in 3D: First Observations with SPIFFI, the Infrared Integral Field Spectrometer for the VLT". In: *The Messenger* 113 (Sept. 2003), pp. 17–25.
- [86] D. Elbaz et al. "The reversal of the star formation-density relation in the distant universe". In: *A&A* 468 (June 2007), pp. 33–48.
- [87] R. S. Ellis. "Faint Blue Galaxies". In: *ARA&A* 35 (1997), pp. 389–443.
- [88] S. C. Ellis and J. Bland-Hawthorn. "The case for OH suppression at near-infrared wavelengths". In: *MNRAS* 386 (May 2008), pp. 47–64.
- [89] S. L. Ellison et al. "Clues to the Origin of the Mass-Metallicity Relation: Dependence on Star Formation Rate and Galaxy Size". In: *ApJ* 672 (Jan. 2008), pp. L107–L110.
- [90] S. L. Ellison et al. "The Enrichment History of the Intergalactic Medium-Measuring the C IV/H I Ratio in the Ly $\alpha$  Forest". In: *AJ* 120 (Sept. 2000), pp. 1175–1191.
- [91] B. G. Elmegreen, F. Bournaud, and D. M. Elmegreen. "Bulge Formation by the Coalescence of Giant Clumps in Primordial Disk Galaxies". In: *ApJ* 688 (Nov. 2008), pp. 67–77.
- [92] B. G. Elmegreen et al. "On the Origin of Exponential Disks at High Redshift". In: *ApJ* 634 (Nov. 2005), pp. 101–108.
- [93] D. M. Elmegreen et al. "Clumpy Galaxies in Goods and Gems: Massive Analogs of Local Dwarf Irregulars". In: *ApJ* 701 (Aug. 2009), pp. 306–329.
- [94] D. M. Elmegreen et al. "Galaxy Morphologies in the Hubble Ultra Deep Field: Dominance of Linear Structures at the Detection Limit". In: *ApJ* 631 (Sept. 2005), pp. 85–100.
- [95] B. Epinat et al. "Integral field spectroscopy with SINFONI of VVDS galaxies. I. Galaxy dynamics and mass assembly at  $1.2 < z < 1.6$ ". In: *A&A* 504 (Sept. 2009), pp. 789–805.
- [96] M. Eracleous, J. A. Hwang, and H. M. L. G. Flohic. "Spectral Energy Distributions of Weak Active Galactic Nuclei Associated with Low-Ionization Nuclear Emission Regions". In: *ApJS* 187 (Mar. 2010), pp. 135–148.
- [97] D. K. Erb. "Chemical Abundances in Star-Forming Galaxies at High Redshift". In: *IAU Symposium*. Ed. by K. Cunha, M. Spite, & B. Barbuy. Vol. 265. IAU Symposium. Mar. 2010, pp. 147–154.
- [98] D. K. Erb. "Galaxy Metallicities, Masses and Outflows at Redshifts  $1 \lesssim Z \lesssim 3$ : An Observational Perspective". In: *EAS Publications Series*. Ed. by E. Emsellem, H. Wozniak, G. Massacrier, J.-F. Gonzalez, J. Devriendt, & N. Champavert. Vol. 24. EAS Publications Series. 2007, pp. 191–202.
- [99] D. K. Erb. "The properties of star-forming galaxies at  $z$  [approximates] 2: Kinematics stellar populations, and metallicities". PhD thesis. California Institute of Technology, May 2006.
- [100] D. K. Erb et al. "H $\alpha$  Observations of a Large Sample of Galaxies at  $z \sim 2$ : Implications for Star Formation in High-Redshift Galaxies". In: *ApJ* 647 (Aug. 2006), pp. 128–139.
- [101] D. K. Erb et al. "H $\alpha$  Spectroscopy of Galaxies at  $z > 2$ : Kinematics and Star Formation". In: *ApJ* 591 (July 2003), pp. 101–118.

## Bibliography

---

- [102] D. K. Erb et al. "Physical Conditions in a Young, Unreddened, Low-metallicity Galaxy at High Redshift". In: *ApJ* 719 (Aug. 2010), pp. 1168–1190.
- [103] D. K. Erb et al. "The Mass-Metallicity Relation at  $z \sim 2$ ". In: *ApJ* 644 (June 2006), pp. 813–828.
- [104] D. K. Erb et al. "The Stellar, Gas, and Dynamical Masses of Star-forming Galaxies at  $z \sim 2$ ". In: *ApJ* 646 (July 2006), pp. 107–132.
- [105] A. Escala and R. B. Larson. "Stability of Galactic Gas Disks and the Formation of Massive Clusters". In: *ApJ* 685 (Sept. 2008), pp. L31–L34.
- [106] ESO. *E-ELT Spectroscopic Exposure Time Calculator*. URL: <http://www.eso.org/observing/etc/bin/elt/elt/script/eltsimusp>.
- [107] S. Esposito et al. "First Light Adaptive Optics System for Large Binocular Telescope". In: *Society of Photo-Optical Instrumentation Engineers (SPIE) Conference Series*. Ed. by P. L. Wizinowich and D. Bonaccini. Vol. 4839. Society of Photo-Optical Instrumentation Engineers (SPIE) Conference Series. Feb. 2003, pp. 164–173.
- [108] O. Fakhouri and C.-P. Ma. "The nearly universal merger rate of dark matter haloes in  $\Lambda$ CDM cosmology". In: *MNRAS* 386 (May 2008), pp. 577–592.
- [109] X. Fan et al. "High-Redshift Quasars Found in Sloan Digital Sky Survey Commissioning Data. IV. Luminosity Function from the Fall Equatorial Stripe Sample". In: *AJ* 121 (Jan. 2001), pp. 54–65.
- [110] G. J. Ferland and H. Netzer. "Are there any shock-heated galaxies". In: *ApJ* 264 (Jan. 1983), pp. 105–113.
- [111] E. L. Fitzpatrick. "Correcting for the Effects of Interstellar Extinction". In: *PASP* 111 (Jan. 1999), pp. 63–75.
- [112] N. Förster-Schreiber et al. "High Z Galaxy Kinematics and Star Formation". In: *American Astronomical Society Meeting Abstracts #214*. Vol. 214. American Astronomical Society Meeting Abstracts. May 2009, p. 257.03.
- [113] N. M. Förster Schreiber et al. "A Substantial Population of Red Galaxies at  $z > 2$ : Modeling of the Spectral Energy Distributions of an Extended Sample". In: *ApJ* 616 (Nov. 2004), pp. 40–62.
- [114] N. M. Förster Schreiber et al. "Constraints on the Assembly and Dynamics of Galaxies. I. Detailed Rest-frame Optical Morphologies on Kiloparsec Scale of  $z \sim 2$  Star-forming Galaxies". In: *ApJ* 731, 65 (Apr. 2011), p. 65.
- [115] N. M. Förster Schreiber et al. "Constraints on the Assembly and Dynamics of Galaxies. II. Properties of Kiloparsec-scale Clumps in Rest-frame Optical Emission of  $z \sim 2$  Star-forming Galaxies". In: *ApJ* 739, 45 (Sept. 2011), p. 45.
- [116] N. M. Förster Schreiber et al. "SINFONI Integral Field Spectroscopy of  $z \sim 2$  UV-selected Galaxies: Rotation Curves and Dynamical Evolution". In: *ApJ* 645 (July 2006), pp. 1062–1075.
- [117] N. M. Förster Schreiber et al. "The SINS Survey: SINFONI Integral Field Spectroscopy of  $z \sim 2$  Star-forming Galaxies". In: *ApJ* 706 (Dec. 2009), pp. 1364–1428.
- [118] R. Foy and F. C. Foy, eds. *Optics in Astrophysics*. Jan. 2005.
- [119] D. Friedli and W. Benz. "Secular evolution of isolated barred galaxies. II. Coupling between stars and interstellar medium via star formation." In: *A&A* 301 (Sept. 1995), p. 649.
- [120] J. Fu et al. "Origin and Evolution of the Abundance Gradient Along the Milky Way Disk". In: *ApJ* 696 (May 2009), pp. 668–675.
- [121] D. Gallieni et al. "LBT adaptive secondary units final design and construction". In: *Society of Photo-Optical Instrumentation Engineers (SPIE) Conference Series*. Ed. by P. L. Wizinowich and D. Bonaccini. Vol. 4839. Society of Photo-Optical Instrumentation Engineers (SPIE) Conference Series. Feb. 2003, pp. 765–771.

- 
- [122] D. R. Garnett et al. "Interstellar Abundance Gradients in NGC 2403: Comparison to M33". In: *ApJ* 489 (Nov. 1997), p. 63.
- [123] D. R. Garnett and G. A. Shields. "The composition gradient across M81". In: *ApJ* 317 (June 1987), pp. 82–101.
- [124] S. Genel et al. "Short-lived Star-forming Giant Clumps in Cosmological Simulations of  $z \sim 2$  Disks". In: *ApJ* 745, 11 (Jan. 2012), p. 11.
- [125] S. Genel et al. "The Growth of Dark Matter Halos: Evidence for Significant Smooth Accretion". In: *ApJ* 719 (Aug. 2010), pp. 229–239.
- [126] R. Genzel et al. "A study of the gas-star formation relation over cosmic time". In: *MNRAS* 407 (Oct. 2010), pp. 2091–2108.
- [127] R. Genzel et al. "From Rings to Bulges: Evidence for Rapid Secular Galaxy Evolution at  $z \sim 2$  from Integral Field Spectroscopy in the SINS Survey". In: *ApJ* 687 (Nov. 2008), pp. 59–77.
- [128] R. Genzel et al. "The Metallicity Dependence of the  $\text{CO} \rightarrow \text{H}_2$  Conversion Factor in  $z \geq 1$  Star-forming Galaxies". In: *ApJ* 746, 69 (Feb. 2012), p. 69.
- [129] R. Genzel et al. "The rapid formation of a large rotating disk galaxy three billion years after the Big Bang". In: *Nature* 442 (Aug. 2006), pp. 786–789.
- [130] R. Genzel et al. "The Sins Survey of  $z \sim 2$  Galaxy Kinematics: Properties of the Giant Star-forming Clumps". In: *ApJ* 733, 101 (June 2011), p. 101.
- [131] I. S. Glass. *Handbook of Infrared Astronomy*. Aug. 1999.
- [132] A. Gnerucci et al. "Dynamical properties of AMAZE and LSD galaxies from gas kinematics and the Tully-Fisher relation at  $z \sim 3$ ". In: *A&A* 528, A88 (Apr. 2011), A88.
- [133] A. Gnerucci et al. "Spectroastrometry of rotating gas disks for the detection of supermassive black holes in galactic nuclei. I. Method and simulations". In: *A&A* 511, A19 (Feb. 2010), A19.
- [134] M. Goetz and J. Koeppen. "On abundance gradients in spiral galaxies". In: *A&A* 262 (Sept. 1992), pp. 455–467.
- [135] A. Grazian et al. "A comparison of LBGs, DRGs, and BzK galaxies: their contribution to the stellar mass density in the GOODS-MUSIC sample". In: *A&A* 465 (Apr. 2007), pp. 393–404.
- [136] B. A. Groves, M. A. Dopita, and R. S. Sutherland. "Dusty, Radiation Pressure-Dominated Photoionization. I. Model Description, Structure, and Grids". In: *ApJS* 153 (July 2004), pp. 9–73.
- [137] B. A. Groves, M. A. Dopita, and R. S. Sutherland. "Dusty, Radiation Pressure-Dominated Photoionization. II. Multiwavelength Emission Line Diagnostics for Narrow-Line Regions". In: *ApJS* 153 (July 2004), pp. 75–91.
- [138] C. Gruppioni et al. "PEP: First Herschel probe of dusty galaxy evolution up to  $z \sim 3$ ". In: *A&A* 518, L27 (July 2010), p. L27.
- [139] S. Günster, D. Ristau, and R. Davies. "Band-pass and OH-suppression filters for the E-ELT: design and prototyping". In: *Society of Photo-Optical Instrumentation Engineers (SPIE) Conference Series*. Vol. 8168. Society of Photo-Optical Instrumentation Engineers (SPIE) Conference Series. Sept. 2011.
- [140] Y. Guo et al. "Multi-Wavelength View of Kiloparsec-Scale Clumps in Star-Forming Galaxies at  $z \sim 2$ ". In: *ArXiv e-prints* (Oct. 2011).
- [141] K. N. Hainline et al. "Rest-Frame Optical Spectra of Three Strongly Lensed Galaxies at  $z \sim 2$ ". In: *ApJ* 701 (Aug. 2009), pp. 52–65.
- [142] J. P. Halpern and J. E. Steiner. "Low-ionization active galactic nuclei - X-ray or shock heated?" In: *ApJ* 269 (June 1983), pp. L37–L41.

## Bibliography

---

- [143] D. Hamilton. "The spectral evolution of galaxies. I - an observational approach". In: *ApJ* 297 (Oct. 1985), pp. 371–389.
- [144] M. Hayashi et al. "Star Formation Rates and Metallicities of K-Selected Star-Forming Galaxies at  $z \sim 2$ ". In: *ApJ* 691 (Jan. 2009), pp. 140–151.
- [145] T. M. Heckman. "The broad line region in active nuclei and quasars - Correlations with luminosity and radio emission". In: *A&A* 88 (Aug. 1980), pp. 311–316.
- [146] T. M. Heckman, L. Armus, and G. K. Miley. "On the nature and implications of starburst-driven galactic superwinds". In: *ApJS* 74 (Dec. 1990), pp. 833–868.
- [147] R. B. C. Henry and G. Worthey. "The Distribution of Heavy Elements in Spiral and Elliptical Galaxies". In: *PASP* 111 (Aug. 1999), pp. 919–945.
- [148] H. Hirashita, V. Buat, and A. K. Inoue. "Star formation rate in galaxies from UV, IR, and  $H\alpha$  estimators". In: *A&A* 410 (Oct. 2003), pp. 83–100.
- [149] L. C. Ho. "LINERs as low-luminosity active galactic nuclei". In: *Advances in Space Research* 23 (1999), pp. 813–822.
- [150] L. C. Ho. "Origin and Dynamical Support of Ionized Gas in Galaxy Bulges". In: *ApJ* 699 (July 2009), pp. 638–648.
- [151] L. C. Ho, A. V. Filippenko, and W. L. W. Sargent. "A Search for "Dwarf" Seyfert Nuclei. III. Spectroscopic Parameters and Properties of the Host Galaxies". In: *ApJS* 112 (Oct. 1997), p. 315.
- [152] R. Hofmann et al. "High-angular-resolution NIR astronomy with large arrays (SHARP I and SHARP II)". In: *Society of Photo-Optical Instrumentation Engineers (SPIE) Conference Series*. Ed. by A. M. Fowler. Vol. 2475. Society of Photo-Optical Instrumentation Engineers (SPIE) Conference Series. June 1995, pp. 192–202.
- [153] Hopkins. "Test". In: *ApJ* 1 (2011), p. 1.
- [154] A. M. Hopkins and J. F. Beacom. "On the Normalization of the Cosmic Star Formation History". In: *ApJ* 651 (Nov. 2006), pp. 142–154.
- [155] P. F. Hopkins et al. "The effects of gas on morphological transformation in mergers: implications for bulge and disc demographics". In: *MNRAS* 397 (Aug. 2009), pp. 802–814.
- [156] D. G. Hummer and P. J. Storey. "Recombination-line intensities for hydrogenic ions. I - Case B calculations for H I and He II". In: *MNRAS* 224 (Feb. 1987), pp. 801–820.
- [157] T. Ichikawa et al. "MOIRCS: multi-object infrared camera and spectrograph for SUBARU". In: *Society of Photo-Optical Instrumentation Engineers (SPIE) Conference Series*. Vol. 6269. Society of Photo-Optical Instrumentation Engineers (SPIE) Conference Series. July 2006.
- [158] A. Immeli et al. "Gas physics, disk fragmentation, and bulge formation in young galaxies". In: *A&A* 413 (Jan. 2004), pp. 547–561.
- [159] A. Immeli et al. "Subgalactic Clumps at High Redshift: A Fragmentation Origin?" In: *ApJ* 611 (Aug. 2004), pp. 20–25.
- [160] C. Iserlohe. "Inbetriebnahme und Charakterisierung des abbildenden Nahinfrarot-Spektrographen SPIFFI und Beobachtung der ultraleuchtkraeftigen Galaxie IRAS06206-6315". PhD thesis. LMU München: Faculty of Physics, 2006.
- [161] C. Iserlohe et al. "On-sky performance of SPIFFI: the integral field spectrometer for SINFONI at the VLT". In: *Society of Photo-Optical Instrumentation Engineers (SPIE) Conference Series*. Ed. by A. F. M. Moorwood & M. Iye. Vol. 5492. Society of Photo-Optical Instrumentation Engineers (SPIE) Conference Series. Sept. 2004, pp. 1123–1134.
- [162] F. A. Jenkins and H. E. White. *Fundamentals of Optics 4th edition*. Ed. by Jenkins, F. A. & White, H. E. 1976.

- [163] T. Jones et al. "Measurement of a Metallicity Gradient in a  $z = 2$  Galaxy: Implications for Inside-out Assembly Histories". In: *ApJ* 725 (Dec. 2010), pp. L176–L180.
- [164] T. A. Jones et al. "Resolved spectroscopy of gravitationally lensed galaxies: recovering coherent velocity fields in subluminoous  $z \sim 2$ -3 galaxies". In: *MNRAS* 404 (May 2010), pp. 1247–1262.
- [165] G. Kauffmann et al. "Stellar masses and star formation histories for  $10^5$  galaxies from the Sloan Digital Sky Survey". In: *MNRAS* 341 (May 2003), pp. 33–53.
- [166] G. Kauffmann et al. "The host galaxies of active galactic nuclei". In: *MNRAS* 346 (Dec. 2003), pp. 1055–1077.
- [167] R. C. Kennicutt Jr. "The Global Schmidt Law in Star-forming Galaxies". In: *ApJ* 498 (May 1998), p. 541.
- [168] D. Kereš et al. "How do galaxies get their gas?" In: *MNRAS* 363 (Oct. 2005), pp. 2–28.
- [169] L. J. Kewley, R. A. Jansen, and M. J. Geller. "Aperture Effects on Star Formation Rate, Metallicity, and Reddening". In: *PASP* 117 (Mar. 2005), pp. 227–244.
- [170] L. J. Kewley and S. L. Ellison. "Metallicity Calibrations and the Mass-Metallicity Relation for Star-forming Galaxies". In: *ApJ* 681 (July 2008), pp. 1183–1204.
- [171] L. J. Kewley et al. "Metallicity Gradients and Gas Flows in Galaxy Pairs". In: *ApJ* 721 (Sept. 2010), pp. L48–L52.
- [172] L. J. Kewley et al. "Optical Classification of Southern Warm Infrared Galaxies". In: *ApJS* 132 (Jan. 2001), pp. 37–71.
- [173] L. J. Kewley et al. "The  $H\alpha$  and Infrared Star Formation Rates for the Nearby Field Galaxy Survey". In: *AJ* 124 (Dec. 2002), pp. 3135–3143.
- [174] L. J. Kewley et al. "The host galaxies and classification of active galactic nuclei". In: *MNRAS* 372 (Nov. 2006), pp. 961–976.
- [175] L. J. Kewley et al. "Theoretical Modeling of Starburst Galaxies". In: *ApJ* 556 (July 2001), pp. 121–140.
- [176] L. J. Kewley and M. A. Dopita. "Using Strong Lines to Estimate Abundances in Extragalactic H II Regions and Starburst Galaxies". In: *ApJS* 142 (Sept. 2002), pp. 35–52.
- [177] É. Y. Khachikyan and D. W. Weedman. "A spectroscopic study of luminous galactic nuclei". In: *Astrophysics* 7 (July 1971), pp. 231–240.
- [178] M. Kimura et al. "Fibre Multi-Object Spectrograph (FMOS) for the Subaru Telescope". In: *PASJ* 62 (Oct. 2010), pp. 1135–1147.
- [179] C. R. Kitchin. *Astrophysical techniques*. 1984.
- [180] C. Kobayashi. "GRAPE-SPH chemodynamical simulation of elliptical galaxies - I. Evolution of metallicity gradients". In: *MNRAS* 347 (Jan. 2004), pp. 740–758.
- [181] H. A. Kobulnicky and L. J. Kewley. "Metallicities of  $0.3 < z < 1.0$  Galaxies in the GOODS-North Field". In: *ApJ* 617 (Dec. 2004), pp. 240–261.
- [182] J. Koeppen. "The evolution of abundance gradients in spiral galaxies". In: *A&A* 281 (Jan. 1994), pp. 26–34.
- [183] E. Komatsu et al. "Seven-year Wilkinson Microwave Anisotropy Probe (WMAP) Observations: Cosmological Interpretation". In: *ApJS* 192, 18 (Feb. 2011), p. 18.
- [184] X. Kong et al. "A Wide Area Survey for High-Redshift Massive Galaxies. I. Number Counts and Clustering of BzKs and EROs". In: *ApJ* 638 (Feb. 2006), pp. 72–87.
- [185] J. Köppen, C. Weidner, and P. Kroupa. "A possible origin of the mass-metallicity relation of galaxies". In: *MNRAS* 375 (Feb. 2007), pp. 673–684.

## Bibliography

---

- [186] M. Kriek et al. "A Near-Infrared Spectroscopic Survey of K-selected Galaxies at  $z \sim 2.3$ : Redshifts and Implications for Broadband Photometric Studies". In: *ApJ* 677 (Apr. 2008), pp. 219–237.
- [187] M. Kriek et al. "An Ultra-Deep Near-Infrared Spectrum of a Compact Quiescent Galaxy at  $z = 2.2$ ". In: *ApJ* 700 (July 2009), pp. 221–231.
- [188] M. Kriek et al. "The Detection of a Red Sequence of Massive Field Galaxies at  $z \sim 2.3$  and Its Evolution to  $z \sim 0$ ". In: *ApJ* 682 (Aug. 2008), pp. 896–906.
- [189] M. Kriek et al. "The Hubble Sequence Beyond  $z = 2$  for Massive Galaxies: Contrasting Large Star-forming and Compact Quiescent Galaxies". In: *ApJ* 705 (Nov. 2009), pp. L71–L75.
- [190] M. Kriek et al. "The Origin of Line Emission in Massive  $z \sim 2.3$  Galaxies: Evidence for Cosmic Downsizing of AGN Host Galaxies". In: *ApJ* 669 (Nov. 2007), pp. 776–790.
- [191] M. T. Kriek. "The many phases of massive galaxies. A Near-Infrared spectroscopic study of galaxies in the early universe". PhD thesis. Leiden Observatory, Leiden University, 2007.
- [192] M. R. Krumholz and A. Dekel. "Survival of star-forming giant clumps in high-redshift galaxies". In: *MNRAS* 406 (July 2010), pp. 112–120.
- [193] F. Lamareille et al. "Physical properties of galaxies and their evolution in the VIMOS VLT Deep Survey. I. The evolution of the mass-metallicity relation up to  $z \sim 0.9$ ". In: *A&A* 495 (Feb. 2009), pp. 53–72.
- [194] D. Larson et al. "Seven-year Wilkinson Microwave Anisotropy Probe (WMAP) Observations: Power Spectra and WMAP-derived Parameters". In: *ApJS* 192, 16 (Feb. 2011), p. 16.
- [195] R. B. Larson and B. M. Tinsley. "Star formation rates in normal and peculiar galaxies". In: *ApJ* 219 (Jan. 1978), pp. 46–59.
- [196] D. R. Law, C. C. Steidel, and D. K. Erb. "Predictions and Strategies for Integral-Field Spectroscopy of High-Redshift Galaxies". In: *AJ* 131 (Jan. 2006), pp. 70–83.
- [197] D. R. Law et al. "The Kiloparsec-scale Kinematics of High-redshift Star-forming Galaxies". In: *ApJ* 697 (June 2009), pp. 2057–2082.
- [198] D. R. Law et al. "The Physical Nature of Rest-UV Galaxy Morphology during the Peak Epoch of Galaxy Formation". In: *ApJ* 656 (Feb. 2007), pp. 1–26.
- [199] N. M. Law, C. D. Mackay, and J. E. Baldwin. "Lucky imaging: high angular resolution imaging in the visible from the ground". In: *A&A* 446 (Feb. 2006), pp. 739–745.
- [200] D. Le Borgne et al. "Cosmic star-formation history from a non-parametric inversion of infrared galaxy counts". In: *A&A* 504 (Sept. 2009), pp. 727–740.
- [201] J. Lequeux et al. "Chemical composition and evolution of irregular and blue compact galaxies". In: *A&A* 80 (Dec. 1979), pp. 155–166.
- [202] A. Leroy et al. "The Molecular Interstellar Medium of Dwarf Galaxies on Kiloparsec Scales: A New Survey for CO in Northern, IRAS-detected Dwarf Galaxies". In: *ApJ* 625 (June 2005), pp. 763–784.
- [203] A. K. Leroy et al. "The CO-to-H<sub>2</sub> Conversion Factor from Infrared Dust Emission across the Local Group". In: *ApJ* 737, 12 (Aug. 2011), p. 12.
- [204] E. M. Levesque, L. J. Kewley, and K. L. Larson. "Theoretical Modeling of Star-Forming Galaxies. I. Emission-Line Diagnostic Grids for Local and Low-Metallicity Galaxies". In: *AJ* 139 (Feb. 2010), pp. 712–727.
- [205] S. Lilly et al. "Hubble Space Telescope Imaging of the CFRS and LDSS Redshift Surveys. II. Structural Parameters and the Evolution of Disk Galaxies to  $Z$  approximately 1". In: *ApJ* 500 (June 1998), p. 75.
- [206] S. J. Lilly, C. M. Carollo, and A. N. Stockton. "The Metallicities of Star-forming Galaxies at Intermediate Redshifts  $0.47 < z < 0.92$ ". In: *ApJ* 597 (Nov. 2003), pp. 730–750.

- [207] S. L pari et al. "Infrared mergers and infrared quasi-stellar objects with galactic winds - II. NGC5514: two extranuclear starbursts with LINER properties and a supergiant bubble in the rupture phase". In: *MNRAS* 355 (Dec. 2004), pp. 641–681.
- [208] X. Liu et al. "Metallicities and Physical Conditions in Star-forming Galaxies at  $z \sim 1.0$ -1.5". In: *ApJ* 678 (May 2008), pp. 758–779.
- [209] Steven D. Lord. *A New Software Tool for Computing Earth's Atmospheric Transmission of Near- and Far-Infrared Radiation*. Technical Memorandum 103957. NASA, Dec. 1992.
- [210] J. M. Lotz et al. "The Evolution of Galaxy Mergers and Morphology at  $z < 1.2$  in the Extended Groth Strip". In: *ApJ* 672 (Jan. 2008), pp. 177–197.
- [211] C. Ly et al. "The Luminosity Function and Star Formation Rate between Redshifts of 0.07 and 1.47 for Narrowband Emitters in the Subaru Deep Field". In: *ApJ* 657 (Mar. 2007), pp. 738–759.
- [212] P. Madau et al. "High-redshift galaxies in the Hubble Deep Field: colour selection and star formation history to  $z \sim 4$ ". In: *MNRAS* 283 (Dec. 1996), pp. 1388–1404.
- [213] L. Magrini et al. "The metallicity gradient of M 33: chemical abundances of H II regions". In: *A&A* 470 (Aug. 2007), pp. 865–874.
- [214] T. Maihara et al. "Observations of the OH airglow emission". In: *PASP* 105 (Sept. 1993), pp. 940–944.
- [215] R. Maiolino et al. "AMAZE. I. The evolution of the mass-metallicity relation at  $z > 3$ ". In: *A&A* 488 (Sept. 2008), pp. 463–479.
- [216] A. H. Maller et al. "The Intrinsic Properties of SDSS Galaxies". In: *ApJ* 691 (Jan. 2009), pp. 394–406.
- [217] A. Mampaso, M. Prieto, and F. S nchez. *Infrared Astronomy*. Jan. 2004.
- [218] C. Mancini et al. "The zCOSMOS-SINFONI Project. I. Sample Selection and Natural-seeing Observations". In: *ApJ* 743, 86 (Dec. 2011), p. 86.
- [219] F. Mannucci et al. "A fundamental relation between mass, star formation rate and metallicity in local and high-redshift galaxies". In: *MNRAS* 408 (Nov. 2010), pp. 2115–2127.
- [220] F. Mannucci et al. "LSD: Lyman-break galaxies Stellar populations and Dynamics - I. Mass, metallicity and gas at  $z \sim 3.1$ ". In: *MNRAS* 398 (Oct. 2009), pp. 1915–1931.
- [221] I. M rquez et al. "Rotation curves and metallicity gradients from H II regions in spiral galaxies". In: *A&A* 393 (Oct. 2002), pp. 389–407.
- [222] M. Martig and F. Bournaud. "Triggering of merger-induced starbursts by the tidal field of galaxy groups and clusters". In: *MNRAS* 385 (Mar. 2008), pp. L38–L42.
- [223] C. L. Martin. "UV Diagnostics of the Interaction between Starburst Galaxies and the Intergalactic Medium". In: *Ultraviolet-Optical Space Astronomy Beyond HST*. Ed. by J. A. Morse, J. M. Shull, & A. L. Kinney. Vol. 164. Astronomical Society of the Pacific Conference Series. 1999, p. 66.
- [224] F. Matteucci and C. Chiappini. "Abundance Gradients in the Galactic Disk: a Clue to Galaxy Formation". In: *Chemical Evolution from Zero to High Redshift*. Ed. by J. R. Walsh & M. R. Rosa. 1999, p. 83.
- [225] F. Matteucci and P. Francois. "Galactic chemical evolution - Abundance gradients of individual elements". In: *MNRAS* 239 (Aug. 1989), pp. 885–904.
- [226] Francesca Matteucci, ed. *Chemical Evolution of Galaxies*. Springer-Verlag, 2012.
- [227] Y. D. Mayya et al. "Star Formation History and Extinction in the Central Kiloparsec of M82-like Starbursts". In: *ApJ* 600 (Jan. 2004), pp. 188–203.
- [228] C. F. McKee and D. J. Hollenbach. "Interstellar shock waves". In: *ARA&A* 18 (1980), pp. 219–262.

## Bibliography

---

- [229] I. S. McLean et al. "Design and development of MOSFIRE: the multi-object spectrometer for infrared exploration at the Keck Observatory". In: *Society of Photo-Optical Instrumentation Engineers (SPIE) Conference Series*. Vol. 7735. Society of Photo-Optical Instrumentation Engineers (SPIE) Conference Series. July 2010.
- [230] S. Mengel. "Merger induced star formation in the antennae and the SPIFFI near infrared integral field spectrometer". PhD thesis. LMU München: Faculty of Physics, 2001.
- [231] G. R. Meurer, T. M. Heckman, and D. Calzetti. "Dust Absorption and the Ultraviolet Luminosity Density at  $Z \sim 3$  as Calibrated by Local Starburst Galaxies". In: *ApJ* 521 (Aug. 1999), pp. 64–80.
- [232] M. Mignoli et al. "The K20 survey. VII. The spectroscopic catalogue: Spectral properties and evolution of the galaxy population". In: *A&A* 437 (July 2005), pp. 883–897.
- [233] J. C. Mihos and L. Hernquist. "Gasdynamics and Starbursts in Major Mergers". In: *ApJ* 464 (June 1996), p. 641.
- [234] M. Molla, F. Ferrini, and A. I. Diaz. "Evolution of Spiral Galaxies. VI. Radial Distributions of Abundances in External Galaxies". In: *ApJ* 466 (Aug. 1996), p. 668.
- [235] M. Molla, F. Ferrini, and A. I. Diaz. "Evolution of Spiral Galaxies. VII. Time Evolution of the Radial Distributions of Abundances". In: *ApJ* 475 (Feb. 1997), p. 519.
- [236] A. Monreal-Ibero et al. "VLT-VIMOS integral field spectroscopy of luminous and ultraluminous infrared galaxies. II. Evidence for shock ionization caused by tidal forces in the extra-nuclear regions of interacting and merging LIRGs". In: *A&A* 517, A28 (July 2010), A28.
- [237] M. Montuori et al. "The dilution peak, metallicity evolution, and dating of galaxy interactions and mergers". In: *A&A* 518, A56 (July 2010), A56.
- [238] A. Moorwood et al. "ISAAC sees first light at the VLT." In: *The Messenger* 94 (Dec. 1998), pp. 7–9.
- [239] A. F. M. Moorwood et al. " $H\alpha$  emitting galaxies and the cosmic star formation rate at  $z \sim 2.2$ ". In: *A&A* 362 (Oct. 2000), pp. 9–18.
- [240] N. Murray, E. Quataert, and T. A. Thompson. "The Disruption of Giant Molecular Clouds by Radiation Pressure & the Efficiency of Star Formation in Galaxies". In: *ApJ* 709 (Jan. 2010), pp. 191–209.
- [241] T. Naab and J. P. Ostriker. "A simple model for the evolution of disc galaxies: the Milky Way". In: *MNRAS* 366 (Mar. 2006), pp. 899–917.
- [242] T. Naab, S. Khochfar, and A. Burkert. "Properties of Early-Type, Dry Galaxy Mergers and the Origin of Massive Elliptical Galaxies". In: *ApJ* 636 (Jan. 2006), pp. L81–L84.
- [243] T. Naab and A. Burkert. "Statistical Properties of Collisionless Equal- and Unequal-Mass Merger Remnants of Disk Galaxies". In: *ApJ* 597 (Nov. 2003), pp. 893–906.
- [244] T. Nagao, R. Maiolino, and A. Marconi. "Gas metallicity diagnostics in star-forming galaxies". In: *A&A* 459 (Nov. 2006), pp. 85–101.
- [245] N. Nesvadba. "Integral-Field Spectroscopy of High-Redshift Galaxies: Implications for Early Galaxy Evolution". PhD thesis. LMU München: Faculty of Physics, 2006.
- [246] N. P. H. Nesvadba et al. "Integral-field spectroscopy of a Lyman-break galaxy at  $z = 3.2$ : evidence for merging". In: *A&A* 479 (Feb. 2008), pp. 67–73.
- [247] N. P. H. Nesvadba et al. "Intense Star Formation and Feedback at High Redshift: Spatially Resolved Properties of the  $z = 2.6$  Submillimeter Galaxy SMM J14011+0252". In: *ApJ* 657 (Mar. 2007), pp. 725–737.
- [248] K. G. Noeske et al. "Star Formation in AEGIS Field Galaxies since  $z=1.1$ : The Dominance of Gradually Declining Star Formation, and the Main Sequence of Star-forming Galaxies". In: *ApJ* 660 (May 2007), pp. L43–L46.

- [249] M. Noguchi. "Early Evolution of Disk Galaxies: Formation of Bulges in Clumpy Young Galactic Disks". In: *ApJ* 514 (Mar. 1999), pp. 77–95.
- [250] E. Oliva and L. Origlia. "The OH Airglow Spectrum - a Calibration Source for Infrared Spectrometers". In: *A&A* 254 (Feb. 1992), p. 466.
- [251] M. Onodera et al. "A Wide Area Survey for High-Redshift Massive Galaxies. II. Near-Infrared Spectroscopy of BzK-Selected Massive Star-Forming Galaxies". In: *ApJ* 715 (May 2010), pp. 385–405.
- [252] D. E. Osterbrock. *Astrophysics of gaseous nebulae*. 1974.
- [253] D. E. Osterbrock. *Astrophysics of gaseous nebulae and active galactic nuclei*. 1989.
- [254] D. E. Osterbrock et al. "Night-Sky High-Resolution Spectral Atlas of OH and O2 Emission Lines for Echelle Spectrograph Wavelength Calibration". In: *PASP* 108 (Mar. 1996), p. 277.
- [255] B. E. J. Pagel and M. G. Edmunds. "Abundances in stellar populations and the interstellar medium in galaxies". In: *ARA&A* 19 (1981), pp. 77–113.
- [256] B. E. J. Pagel and B. E. Patchett. "Metal abundances in nearby stars and the chemical history of the solar neighborhood". In: *MNRAS* 172 (July 1975), pp. 13–40.
- [257] B. E. J. Pagel et al. "On the composition of H II regions in southern galaxies. I - NGC 300 and 1365". In: *MNRAS* 189 (Oct. 1979), pp. 95–113.
- [258] C. Palmer and E. Loewen. *Diffraction Grating Handbook*. Newport Corporation, 2006.
- [259] C. Papovich et al. "The Assembly of Diversity in the Morphologies and Stellar Populations of High-Redshift Galaxies". In: *ApJ* 631 (Sept. 2005), pp. 101–120.
- [260] S. Pascual et al. "H $\alpha$  emitting galaxies and the star formation rate density at  $z \sim 0.24$ ". In: *A&A* 379 (Dec. 2001), pp. 798–806.
- [261] M. S. Peeples, R. W. Pogge, and K. Z. Stanek. "Outliers from the Mass-Metallicity Relation. II. A Sample of Massive Metal-Poor Galaxies from SDSS". In: *ApJ* 695 (Apr. 2009), pp. 259–267.
- [262] J. Perez, L. Michel-Dansac, and P. B. Tissera. "Chemical evolution during gas-rich galaxy interactions". In: *MNRAS* 417 (Oct. 2011), pp. 580–590.
- [263] P. G. Pérez-González et al. "Exploring the Evolutionary Paths of the Most Massive Galaxies since  $z \sim 2$ ". In: *ApJ* 687 (Nov. 2008), pp. 50–58.
- [264] P. G. Pérez-González et al. "The Stellar Mass Assembly of Galaxies from  $z = 0$  to  $z = 4$ : Analysis of a Sample Selected in the Rest-Frame Near-Infrared with Spitzer". In: *ApJ* 675 (Mar. 2008), pp. 234–261.
- [265] E. Pérez-Montero et al. "Physical properties of galaxies and their evolution in the VIMOS VLT Deep Survey. II. Extending the mass-metallicity relation to the range  $z \sim 0.89$ -1.24". In: *A&A* 495 (Feb. 2009), pp. 73–81.
- [266] M. Pettini. "Early galactic chemical evolution with UVES". In: *The Messenger* 111 (Mar. 2003), pp. 13–17.
- [267] M. Pettini et al. "New Observations of the Interstellar Medium in the Lyman Break Galaxy MS 1512-cB58". In: *ApJ* 569 (Apr. 2002), pp. 742–757.
- [268] M. Pettini and B. E. J. Pagel. "[OIII]/[NII] as an abundance indicator at high redshift". In: *MNRAS* 348 (Mar. 2004), pp. L59–L63.
- [269] M. Pettini et al. "The Rest-Frame Optical Spectra of Lyman Break Galaxies: Star Formation, Extinction, Abundances, and Kinematics". In: *ApJ* 554 (June 2001), pp. 981–1000.
- [270] S. Phillipps and M. G. Edmunds. "On the cause of metallicity gradients in spiral galaxies". In: *MNRAS* 251 (July 1991), pp. 84–92.
- [271] A. J. Pickles. "A Stellar Spectral Flux Library: 1150-25000 Å". In: *PASP* 110 (July 1998), pp. 863–878.

## Bibliography

---

- [272] L. S. Pilyugin, J. M. Vílchez, and T. Contini. “Oxygen and nitrogen abundances in nearby galaxies. Correlations between oxygen abundance and macroscopic properties”. In: *A&A* 425 (Oct. 2004), pp. 849–869.
- [273] K. L. Polsterer. “The LUCIFER Control Software: The Core System, Instrument Control and Scientific Applications”. PhD thesis. Fakultät für Physik und Astronomie der Ruhr-Universität Bochum, 2011.
- [274] N. Prantzos and S. Boissier. “Chemo-spectrophotometric evolution of spiral galaxies - III. Abundance and colour gradients in discs”. In: *MNRAS* 313 (Apr. 2000), pp. 338–346.
- [275] J. Queyrel et al. “Integral field spectroscopy with SINFONI of VVDS galaxies. II. The mass-metallicity relation at  $1.2 < z < 1.6$ ”. In: *A&A* 506 (Nov. 2009), pp. 681–687.
- [276] J. Queyrel et al. “MASSIV: Mass Assembly Survey with SINFONI in VVDS. III. Evidence for positive metallicity gradients in  $z \sim 1.2$  star-forming galaxies”. In: *A&A* 539, A93 (Mar. 2012), A93.
- [277] S. Rabien et al. “Design of PARSEC the VLT laser”. In: *Society of Photo-Optical Instrumentation Engineers (SPIE) Conference Series*. Ed. by P. L. Wizinowich & D. Bonaccini. Vol. 4839. Society of Photo-Optical Instrumentation Engineers (SPIE) Conference Series. Feb. 2003, pp. 393–401.
- [278] S. Ravindranath et al. “The Evolution of Disk Galaxies in the GOODS-South Field: Number Densities and Size Distribution”. In: *ApJ* 604 (Mar. 2004), pp. L9–L12.
- [279] J. C. Raymond. “Shock waves in the interstellar medium”. In: *ApJS* 39 (Jan. 1979), pp. 1–27.
- [280] N. A. Reddy et al. “A Census of Optical and Near-Infrared Selected Star-forming and Passively Evolving Galaxies at Redshift  $z \sim 2$ ”. In: *ApJ* 633 (Nov. 2005), pp. 748–767.
- [281] N. A. Reddy and C. C. Steidel. “A Steep Faint-End Slope of the UV Luminosity Function at  $z \sim 2$ -3: Implications for the Global Stellar Mass Density and Star Formation in Low-Mass Halos”. In: *ApJ* 692 (Feb. 2009), pp. 778–803.
- [282] N. A. Reddy et al. “Dust Obscuration and Metallicity at High Redshift: New Inferences from UV,  $H\alpha$ , and  $8 \mu\text{m}$  Observations of  $z \sim 2$  Star-forming Galaxies”. In: *ApJ* 712 (Apr. 2010), pp. 1070–1091.
- [283] J. A. Rich et al. “NGC 839: Shocks in an M82-like Superwind”. In: *ApJ* 721 (Sept. 2010), pp. 505–517.
- [284] G. Rieke. *Detection of Light*. Dec. 2002.
- [285] R. H. Ritchie et al. “Surface-Plasmon Resonance Effect in Grating Diffraction”. In: *Phys. Rev. Lett.* 21 (22 1968), pp. 1530–1533.
- [286] B. Robertson et al. “A Merger-driven Scenario for Cosmological Disk Galaxy Formation”. In: *ApJ* 645 (July 2006), pp. 986–1000.
- [287] G. Rodighiero et al. “The Lesser Role of Starbursts in Star Formation at  $z = 2$ ”. In: *ApJ* 739, L40 (Oct. 2011), p. L40.
- [288] P. Rousselot et al. “Night-sky spectral atlas of OH emission lines in the near-infrared”. In: *A&A* 354 (Feb. 2000), pp. 1134–1150.
- [289] G. Rudnick et al. “Measuring the Average Evolution of Luminous Galaxies at  $z < 3$ : The Rest-Frame Optical Luminosity Density, Spectral Energy Distribution, and Stellar Mass Density”. In: *ApJ* 650 (Oct. 2006), pp. 624–643.
- [290] G. Rudnick et al. “The Rest-Frame Optical Luminosity Density, Color, and Stellar Mass Density of the Universe from  $z = 0$  to  $z = 3$ ”. In: *ApJ* 599 (Dec. 2003), pp. 847–864.
- [291] D. Rupke, L. Kewley, and J. Barnes. “Redistribution of Metals in Interacting Galaxies”. In: *Galaxy Wars: Stellar Populations and Star Formation in Interacting Galaxies*. Ed. by B. Smith et al. Vol. 423. Astronomical Society of the Pacific Conference Series. June 2010, p. 355.

- [292] D. S. N. Rupke, L. J. Kewley, and J. E. Barnes. "Galaxy Mergers and the Mass-Metallicity Relation: Evidence for Nuclear Metal Dilution and Flattened Gradients from Numerical Simulations". In: *ApJ* 710 (Feb. 2010), pp. L156–L160.
- [293] D. S. N. Rupke, L. J. Kewley, and L.-H. Chien. "Gas-phase Oxygen Gradients in Strongly Interacting Galaxies. I. Early-stage Interactions". In: *ApJ* 723 (Nov. 2010), pp. 1255–1271.
- [294] D. S. N. Rupke, S. Veilleux, and A. J. Baker. "The Oxygen Abundances of Luminous and Ultraluminous Infrared Galaxies". In: *ApJ* 674 (Feb. 2008), pp. 172–193.
- [295] J. J. Salzer et al. "Metal Abundances of KISS Galaxies. IV. Galaxian Luminosity-Metallicity Relations in the Optical and Near-Infrared". In: *ApJ* 624 (May 2005), pp. 661–679.
- [296] D. B. Sanders and I. F. Mirabel. "Luminous Infrared Galaxies". In: *ARA&A* 34 (1996), p. 749.
- [297] M. Sarzi et al. "The SAURON project - XVI. On the sources of ionization for the gas in elliptical and lenticular galaxies". In: *MNRAS* 402 (Mar. 2010), pp. 2187–2210.
- [298] S. Savaglio et al. "The Gemini Deep Deep Survey. VII. The Redshift Evolution of the Mass-Metallicity Relation". In: *ApJ* 635 (Dec. 2005), pp. 260–279.
- [299] M. Schmidt. "The Rate of Star Formation. II. The Rate of Formation of Stars of Different Mass." In: *ApJ* 137 (Apr. 1963), p. 758.
- [300] P. Schneider. *Einführung in die extragalaktische Astronomie und Kosmologie*. 2006.
- [301] N. M. Schreiber. "Near-infrared imaging spectroscopy and mid-infrared spectroscopy of M 82: revealing the nature of star formation activity in the archetypal starburst galaxy". PhD thesis. LMU München, Faculty of Physics, 1999.
- [302] L. Searle. "Evidence for Composition Gradients across the Disks of Spiral Galaxies". In: *ApJ* 168 (Sept. 1971), p. 327.
- [303] L. Searle and W. L. W. Sargent. "Inferences from the Composition of Two Dwarf Blue Galaxies". In: *ApJ* 173 (Apr. 1972), p. 25.
- [304] W. Seifert et al. "LUCIFER1: performance results". In: *Society of Photo-Optical Instrumentation Engineers (SPIE) Conference Series*. Vol. 7735. Society of Photo-Optical Instrumentation Engineers (SPIE) Conference Series. July 2010.
- [305] K. L. Shapiro et al. "Kinometry of SINS High-Redshift Star-Forming Galaxies: Distinguishing Rotating Disks from Major Mergers". In: *ApJ* 682 (July 2008), pp. 231–251.
- [306] A. E. Shapley et al. "Chemical Abundances of DEEP2 Star-forming Galaxies at  $z \sim 1.0$ -1.5". In: *ApJ* 635 (Dec. 2005), pp. 1006–1021.
- [307] A. E. Shapley et al. "Evidence for Solar Metallicities in Massive Star-forming Galaxies at  $z > 2$ ". In: *ApJ* 612 (Sept. 2004), pp. 108–121.
- [308] A. E. Shapley et al. "Rest-Frame Ultraviolet Spectra of  $z \sim 3$  Lyman Break Galaxies". In: *ApJ* 588 (May 2003), pp. 65–89.
- [309] A. E. Shapley et al. "Ultraviolet to Mid-Infrared Observations of Star-forming Galaxies at  $z \sim 2$ : Stellar Masses and Stellar Populations". In: *ApJ* 626 (June 2005), pp. 698–722.
- [310] R. G. Sharp and J. Bland-Hawthorn. "Three-Dimensional Integral Field Observations of 10 Galactic Winds. I. Extended Phase (gsim10 Myr) of Mass/Energy Injection Before the Wind Blows". In: *ApJ* 711 (Mar. 2010), pp. 818–852.
- [311] R. Sharples et al. "Design of the KMOS multi-object integral-field spectrograph". In: *Society of Photo-Optical Instrumentation Engineers (SPIE) Conference Series*. Vol. 6269. Society of Photo-Optical Instrumentation Engineers (SPIE) Conference Series. July 2006.
- [312] R. Sharples et al. "Recent Progress on the KMOS Multi-object Integral Field Spectrometer". In: *The Messenger* 139 (Mar. 2010), pp. 24–27.

## Bibliography

---

- [313] R. Sharples et al. "Surveying the High-Redshift Universe with KMOS". In: *The Messenger* 122 (Dec. 2005), pp. 2–5.
- [314] P. A. Shaver et al. "The galactic abundance gradient". In: *MNRAS* 204 (July 1983), pp. 53–112.
- [315] G. A. Shields. "Composition gradients across spiral galaxies". In: *ApJ* 193 (Oct. 1974), pp. 335–341.
- [316] J. C. Shields. "Normal O stars in dense media generate LINERs". In: *ApJ* 399 (Nov. 1992), pp. L27–L30.
- [317] P. L. Shopbell and J. Bland-Hawthorn. "The Asymmetric Wind in M82". In: *ApJ* 493 (Jan. 1998), p. 129.
- [318] E. D. Skillman. "Chemical Evolution of the ISM in Nearby Galaxies". In: *Stellar astrophysics for the local group: VIII Canary Islands Winter School of Astrophysics*. Ed. by A. Aparicio, A. Herrero, & F. Sánchez. 1998, p. 457.
- [319] E. D. Skillman, R. Terlevich, and J. Melnick. "Abundances in southern Local Group dwarf irregular galaxies". In: *MNRAS* 240 (Oct. 1989), pp. 563–572.
- [320] E. D. Skillman, R. C. Kennicutt, and P. W. Hodge. "Oxygen abundances in nearby dwarf irregular galaxies". In: *ApJ* 347 (Dec. 1989), pp. 875–882.
- [321] S. J. Smartt and W. R. J. Rolleston. "The Galactic Oxygen Abundance Gradient". In: *ApJ* 481 (May 1997), p. L47.
- [322] L. S. Sparke and J. S. Gallagher III. *Galaxies in the Universe - 2nd Edition*. Apr. 2006.
- [323] H. Spinrad. *Galaxy Formation and Evolution*. 2005.
- [324] M. Spolaor et al. "The Mass-Metallicity Gradient Relation of Early-Type Galaxies". In: *ApJ* 691 (Feb. 2009), pp. L138–L141.
- [325] V. Springel, C. S. Frenk, and S. D. M. White. "The large-scale structure of the Universe". In: *Nature* 440 (Apr. 2006), pp. 1137–1144.
- [326] S. A. Stanford et al. "The Evolution of Early-Type Field Galaxies Selected from a NICMOS Map of the Hubble Deep Field North". In: *AJ* 127 (Jan. 2004), pp. 131–155.
- [327] D. P. Stark et al. "The formation and assembly of a typical star-forming galaxy at redshift  $z \sim 3$ ". In: *Nature* 455 (Oct. 2008), pp. 775–777.
- [328] G. Stasińska. "What can emission lines tell us?" In: *ArXiv e-prints* (Apr. 2007).
- [329] G. Stasińska et al. "Can retired galaxies mimic active galaxies? Clues from the Sloan Digital Sky Survey". In: *MNRAS* 391 (Nov. 2008), pp. L29–L33.
- [330] C. C. Steidel et al. "A Survey of Star-forming Galaxies in the  $1.4 \lesssim z \lesssim 2.5$  Redshift Desert: Overview". In: *ApJ* 604 (Apr. 2004), pp. 534–550.
- [331] T. Storchi-Bergmann, D. Calzetti, and A. L. Kinney. "Ultraviolet to near-infrared spectral distributions of star-forming galaxies: Metallicity and age effects". In: *ApJ* 429 (July 1994), pp. 572–581.
- [332] M. Sullivan et al. "A Comparison of Independent Star Formation Diagnostics for an Ultraviolet-selected Sample of Nearby Galaxies". In: *ApJ* 558 (Sept. 2001), pp. 72–80.
- [333] R. Suzuki et al. "Multi-Object Infrared Camera and Spectrograph (MOIRCS) for the Subaru Telescope I. Imaging". In: *PASJ* 60 (Dec. 2008), pp. 1347–.
- [334] A. M. Swinbank et al. "The Interstellar Medium in Distant Star-forming Galaxies: Turbulent Pressure, Fragmentation, and Cloud Scaling Relations in a Dense Gas Disk at  $z = 2.3$ ". In: *ApJ* 742, 11 (Nov. 2011), p. 11.
- [335] L. J. Tacconi et al. "High molecular gas fractions in normal massive star-forming galaxies in the young Universe". In: *Nature* 463 (Feb. 2010), pp. 781–784.

- [336] M. Tecza et al. "SPIFFI Image Slicer: High-Precision Optics at Cryogenic Temperatures". In: *Society of Photo-Optical Instrumentation Engineers (SPIE) Conference Series*. Ed. by E. Atad-Ettinger & S. D'Odorico. Vol. 4842. Society of Photo-Optical Instrumentation Engineers (SPIE) Conference Series. Feb. 2003, pp. 375–383.
- [337] M. Tecza et al. "SPIFFI Observations of the Starburst SMM J14011+0252: Already Old, Fat, and Rich by  $z=2.565$ ". In: *ApJ* 605 (Apr. 2004), pp. L109–L112.
- [338] J. Tennyson. *Astronomical spectroscopy : an introduction to the atomic and molecular physics of astronomical spectra*. 2005.
- [339] R. Terlevich and J. Melnick. "Warmers - The missing link between Starburst and Seyfert galaxies". In: *MNRAS* 213 (Apr. 1985), pp. 841–856.
- [340] N. Thatte et al. "The Nuclear Stellar Core, the Hot Dust Source, and the Location of the Nucleus of NGC 1068". In: *ApJ* 490 (Nov. 1997), p. 238.
- [341] B. M. Tinsley and R. B. Larson. "Chemical evolution and the formation of galactic disks". In: *ApJ* 221 (Apr. 1978), pp. 554–561.
- [342] A. Toomre. "On the gravitational stability of a disk of stars". In: *ApJ* 139 (May 1964), pp. 1217–1238.
- [343] A. Toomre. "Theories of spiral structure". In: *ARA&A* 15 (1977), pp. 437–478.
- [344] P. Torrey et al. "The Metallicity Evolution of Interacting Galaxies". In: *ApJ* 746, 108 (Feb. 2012), p. 108.
- [345] C. A. Tremonti et al. "The Origin of the Mass-Metallicity Relation: Insights from 53,000 Star-forming Galaxies in the Sloan Digital Sky Survey". In: *ApJ* 613 (Oct. 2004), pp. 898–913.
- [346] C. M. Urry and P. Padovani. "Unified Schemes for Radio-Loud Active Galactic Nuclei". In: *PASP* 107 (Sept. 1995), p. 803.
- [347] S. van den Bergh et al. "A Morphological Catalog of Galaxies in the Hubble deep Field". In: *AJ* 112 (Aug. 1996), p. 359.
- [348] S. van den Bergh, J. G. Cohen, and C. Crabbe. "Caltech Faint Galaxy Redshift Survey. XV. Classifications of Galaxies with  $0.2 < Z < 1.1$  in the Hubble Deep Field North and its Flanking Fields". In: *AJ* 122 (Aug. 2001), pp. 611–620.
- [349] P. G. van Dokkum. "Cosmic-Ray Rejection by Laplacian Edge Detection". In: *PASP* 113 (Nov. 2001), pp. 1420–1427.
- [350] P. G. van Dokkum et al. "Gemini Near-Infrared Spectrograph Observations of a Red Star-forming Galaxy at  $z=2.225$ : Evidence of Shock Ionization Due to a Galactic Wind". In: *ApJ* 622 (Mar. 2005), pp. L13–L16.
- [351] P. G. van Dokkum et al. "Stellar Populations and Kinematics of Red Galaxies at  $z > 2$ : Implications for the Formation of Massive Galaxies". In: *ApJ* 611 (Aug. 2004), pp. 703–724.
- [352] P. G. van Dokkum et al. "The Growth of Massive Galaxies Since  $z = 2$ ". In: *ApJ* 709 (Feb. 2010), pp. 1018–1041.
- [353] L. van Zee et al. "Spectroscopy of Outlying H II Regions in Spiral Galaxies: Abundances and Radial Gradients". In: *AJ* 116 (Dec. 1998), pp. 2805–2833.
- [354] S. Veilleux et al. "A Search for Very Extended Ionized Gas in Nearby Starburst and Active Galaxies". In: *AJ* 126 (Nov. 2003), pp. 2185–2208.
- [355] S. Veilleux and D. S. Rupke. "Identification of Galactic Wind Candidates Using Excitation Maps: Tunable-Filter Discovery of a Shock-excited Wind in the Galaxy NGC 1482". In: *ApJ* 565 (Jan. 2002), pp. L63–L66.
- [356] S. Veilleux and D. E. Osterbrock. "Spectral classification of emission-line galaxies". In: *ApJS* 63 (Feb. 1987), pp. 295–310.

## Bibliography

---

- [357] K. Viironen et al. "Spatially resolved properties of the grand-design spiral galaxy UGC 9837: a case for high-redshift 2-D observations". In: *A&A* 538, A144 (Feb. 2012), A144.
- [358] M. B. Vila-Costas and M. G. Edmunds. "The relation between abundance gradients and the physical properties of spiral galaxies". In: *MNRAS* 259 (Nov. 1992), pp. 121–145.
- [359] G. M. Voit and M. Donahue. "A Deep Look at the Emission-Line Nebula in Abell 2597". In: *ApJ* 486 (Sept. 1997), p. 242.
- [360] L. Weitzel et al. "3D: The next generation near-infrared imaging spectrometer." In: *A&AS* 119 (Nov. 1996), pp. 531–546.
- [361] S. D. M. White and M. J. Rees. "Core condensation in heavy halos - A two-stage theory for galaxy formation and clustering". In: *MNRAS* 183 (May 1978), pp. 341–358.
- [362] R. J. Williams et al. "Detection of Quiescent Galaxies in a Bicolor Sequence from  $Z = 0-2$ ". In: *ApJ* 691 (Feb. 2009), pp. 1879–1895.
- [363] E. Wisnioski et al. "The WiggleZ Dark Energy Survey: high-resolution kinematics of luminous star-forming galaxies". In: *MNRAS* 417 (Nov. 2011), pp. 2601–2623.
- [364] S. A. Wright. "A spatially resolved kinematic study of high redshift star forming galaxies: Development and use of adaptive optics instrumentation". PhD thesis. University of California, Los Angeles, 2008.
- [365] S. A. Wright et al. "Dynamics of Galactic Disks and Mergers at  $z \sim 1.6$ : Spatially Resolved Spectroscopy with Keck Laser Guide Star Adaptive Optics". In: *ApJ* 699 (July 2009), pp. 421–440.
- [366] S. A. Wright et al. "Integral Field Spectroscopy of a Candidate Disk Galaxy at  $z \sim 1.5$  Using Laser Guide Star Adaptive Optics". In: *ApJ* 658 (Mar. 2007), pp. 78–84.
- [367] S. A. Wright et al. "The Presence of Weak Active Galactic Nuclei in High Redshift Star-forming Galaxies". In: *ApJ* 711 (Mar. 2010), pp. 1291–1296.
- [368] S. Wuyts et al. "On Star Formation Rates and Star Formation Histories of Galaxies Out to  $z \sim 3$ ". In: *ApJ* 738, 106 (Sept. 2011), p. 106.
- [369] S. Wuyts et al. "Smooth(er) Stellar Mass Maps in CANDELS: Constraints on the Longevity of Clumps in High-redshift Star-forming Galaxies". In: *ArXiv e-prints* (Mar. 2012).
- [370] K. Yabe et al. "NIR Spectroscopy of Star-Forming Galaxies at  $z \sim 1.4$  with Subaru/FMOS: The Mass-Metallicity Relation". In: *ArXiv e-prints* (Dec. 2011).
- [371] L. Yan et al. "The  $H\alpha$  Luminosity Function and Global Star Formation Rate from Redshifts of 1-2". In: *ApJ* 519 (July 1999), pp. L47–L50.
- [372] R. M. Yates, G. Kauffmann, and Q. Guo. "The relation between metallicity, stellar mass and star formation in galaxies: an analysis of observational and model data". In: *MNRAS* (Mar. 2012), p. 2572.
- [373] C.-W. Yip et al. "Extinction in Star-forming Disk Galaxies from Inclination-dependent Composite Spectra". In: *ApJ* 709 (Feb. 2010), pp. 780–790.
- [374] T. Yoshikawa et al. "MOIRCS Deep Survey. VI. Near-infrared Spectroscopy of K-Selected Star-forming Galaxies at  $z \sim 2$ ". In: *ApJ* 718 (July 2010), pp. 112–132.
- [375] T.-T. Yuan and L. J. Kewley. "First Direct Metallicity Measurement Of a Lensed Star-Forming Galaxy at  $z = 1.7$ ". In: *ApJ* 699 (July 2009), pp. L161–L164.
- [376] T.-T. Yuan et al. "Metallicity Gradient of a Lensed Face-on Spiral Galaxy at Redshift 1.49". In: *ApJ* 732, L14 (May 2011), p. L14.
- [377] H. J. Zahid, L. J. Kewley, and F. Bresolin. "The Mass-Metallicity and Luminosity-Metallicity Relations from DEEP2 at  $z \sim 0.8$ ". In: *ApJ* 730, 137 (Apr. 2011), p. 137.
- [378] D. Zaritsky, R. C. Kennicutt Jr., and J. P. Huchra. "H II regions and the abundance properties of spiral galaxies". In: *ApJ* 420 (Jan. 1994), pp. 87–109.





# Acknowledgements

First and foremost I thank my supervisor Natascha M. Förster Schreiber and my co-supervisor Frank Eisenhauer. Natascha, Frank, your help and advice, continuous interest, encouragements and support during the years I have worked on this thesis were invaluable and I deeply thank you for all of it.

I wish to thank Reinhard Genzel for giving me the the opportunity to carry out my research work in his group at MPE. Thank you, Reinhard, for giving valuable advice and the occasional incentive at times, for clearing the way, for steering the ship.

Thanks go to the LUCI and MOS team... Hans Gemperlein, Reiner Hofman, Reinhard Lederer, Nancy Ageorges, Mathias Honsberg, Marcus Haug from MPE and Walter Seifert from Landessternwarte Heidelberg and Kai Polsterer from the Ruhr Universität Bochum. Thank you for being a very good team –in building and and getting the MOS and LUCI running– and for fun and exciting times and nights in the lab and at the LBT.

Of course I would have not gotten far without the other current and former MPE gang members, especially, the infrared-gang... Thanks go to Katie Dodds-Eden, Oliver Pfuhl, Thomas Ott, Sebastian Rabien, Jaron Kurk, Sascha Trippe, Linda Tacconi and all the others. Thank you for your friendship, occasional advice and help, for roaming the earth, for important “backstage work ”, and for all the little things on the way.

The world is not just the MPE or the LBT, despite that during long hours there it sometimes felt like it. No, it would not have worked without my friends “outside”:

Elisabeth Peters, who moved from Bielefeld over the “Weisswurstäquator” with me to pursue her PhD thesis at the MPQ. Thanks, Elisabeth, for our weekly lunch, for hanging out, for continuous discussions and for listening to my laments at times.

Aurora Simionescu. Thank you, Aurora, for adding new perspectives and for our discussions about live and everything.

Ralitsa Angelova. Thank you, Rali, for all your time and support, for being around. For the raccoons et al. and the new adventures Birne could and will take because of you.

Caroline Justen, Kai Hübner, Steffi and Björn Kähler. Thanks for being there when needed although I have managed to not see some of you far less frequently than I should have.

And of course my parents, Friedchen and Horst, and my sister Sonja. Thank you for your love and unconditional support in all the years, and beyond. Danke.

Thank you all.



Cover:

Background: Detail of the constellation Virgo; Johann Bayer, *URANOMETRIA*, 1603, Augsburg

Inset images (left to right): LBT, LUCI, MOS, D3a15504, VLT; by the author

